# THREE-DIMENSIONAL MAGNETOTELLURIC MODELING AND INVERSION WITH APPLICATIONS TO THE CALIFORNIA BASIN AND RANGE PROVINCE

by

RANDALL LEE MACKIE

B.S. Geophysical Engineering
Colorado School of Mines
(1984)

Submitted to the Department of Earth,
Atmospheric, and Planetary Sciences
in Partial Fullfillment of the Requirements
for the Degree of

DOCTOR OF PHILOSOPHY

at the

MASSACHUSETTS INSTITUTE OF TECHNOLOGY

February, 1991



Signature of Author _____
Department of Earth, Atmospheric, and Planetary Sciences
January 11, 1991

Certified by _____
Theodore R. Madden
Department of Earth, Atmospheric, and Planetary Sciences
Thesis Supervisor

Accepted by _____
Thomas H. Jordan
Department Chairman

# THREE-DIMENSIONAL MAGNEOTELLURIC MODELING AND INVERSION WITH APPLICATIONS TO THE CALIFORNIA BASIN AND RANGE PROVINCE

by

RANDALL LEE MACKIE

Submitted to the Department of Earth, Atmospheric, and Planetary Sciences
on January 11, 1991 in Partial Fullfillment of the Requirements
for the Degree of Doctor of Philosophy.

## ABSTRACT

Three-dimensional modeling and inversion algorithms are required to properly interpret magnetotelluric data because the Earth's conductivity structure is inherently heterogeneous. Furthermore, these modeling algorithms must be able to incorporate regional features far away from the actual area of interest since local electromagnetic fields can be perturbed by these distant features. In this thesis, we have developed three-dimensional modeling algorithms that meet these needs, and we have made considerable progress in implementing a three-dimensional magnetotelluric inversion algorithm. Finally, we interpret magnetotelluric data taken in the California Basin and Range Province. This data is very three-dimensional and regional in nature, and it requires three-dimensional modeling algorithms to interpret.

Our three-dimensional modeling algorithms are difference equation algorithms that are based on the integral forms of Maxwell's Equations rather than the differential forms. This formulation does not lead to the problem of approximating derivatives of Earth properties or derivatives of the electromagnetic fields. We investigated exact and approximate solutions of these difference equations.

The exact solution method is similar to propagator methods and Ricatti equation methods. Results from the exact solution compare very well with those determined from the integral equation solution of *Wannamaker* (1990). The relaxation solutions are conjugate direction algorithms that iteratively obtain an approximate solution to the system of equations. The relaxation solutions can incur significant errors due to the eigenvalue spread of the system. A multiple-scaling approach is used to counteract these errors.

The three-dimensional inversion scheme is a relaxation solution of the maximum-likelihood inverse equations. At each iteration of the non-linear inversion, conjugate gradient relaxation is used to obtain an approximate solution for the model perturbations with which to update the model. Using conjugate gradient relaxation schemes allows one to bypass the construction of the sensitivity matrix, or the inversion of a large matrix at each iteration of the non-linear inversion procedure. Instead, one only needs to know the effect of the sensitivity matrix, and its transpose, operating on an arbitrary vector. We show that these two operations are equivalent to one forward problem each per frequency with sources distributed either on the surface (for the transpose operation), or distributed throughout the volume. This procedure cuts down tremendously on the computation time involved in non-linear inversions, and begins to make 3D magnetotelluric inversions feasible.

Finally, we interpret magnetotelluric data from the California Basin and Range Province that we collected over the past two years. The principal (maximum) mode of the impedance in this region is perturbed by excess ocean electrical currents trapped in the continental upper crust. Following the leakage of these excess currents allows us to place bounds on the integrated lower crustal resistivity properties for the California Basin and Range. Three-dimensional modeling of the data requires a lower crust in the California Basin and Range that has 16 times less integrated resistance (resistivity-thickness product) than the lower crust further to the west in California. Such low resistivities for this region can be explained by an increase in the connected porosity of the lower crust. This may well be related to the extension presently occurring there, but more importantly, it probably indicates that some small component of brittle failure is occurring in the lower crust even though it deforms ductilely as a whole (this is semi-brittle deformation). The exact relationships and interactions between fluids in the lower crust, fluid pressures, and deformation processes in the lower crust is, however, not completely understood.

Thesis supervisor: Theodore R. Madden

Title: Professor of Geophysics

## Table of Contents

# Chapter 1
# Introduction

"In spite of the simplicity of Ohm's law, the theory of current flow in the Earth is very complex."

-*Cagniard* (1953)

## *Thesis objectives*

The objectives of this thesis are threefold: 1) develop three-dimensional magnetotelluric modeling algorithms, 2) develop three-dimensional magnetotelluric inversion algorithms, and 3) study the electrical properties of the California Basin and Range Province using magnetotelluric measurements. This data set is very three-dimensional in nature and requires three-dimensional modeling algorithms to interpret.

One-dimensional and two-dimensional modeling and inversion methods have existed for some time, but to date, no practical three-dimensional modeling algorithms, and certainly no three-dimensional inversion algorithms, have been developed. A practical modeling algorithm is one that is capable of modeling fully inhomogeneous media quickly and accurately without the use of a supercomputer. In this thesis, we detail our attempts at solving this difficult problem. Specifically, our modeling algorithms are based on the difference equations derived from the integral forms of Maxwell's equations rather than from the differential forms. In order to solve these difference equations quickly and efficiently, we employ conjugate direction relaxation methods in conjunction with a multiple scaling technique. Our three-dimensional inversion algorithm uses conjugate direction relaxation techniques to solve the maximum likelihood inverse equations. This approach eliminates the need for a sensitivity analysis and the need for inverting large matrices, and it makes three-dimensional inversions feasible. Much work remains to be done, however, before the inversion algorithm is practical. Finally, we use our forward modeling algorithms to interpret magnetotelluric data taken in the California Basin and Range Province to gain insight into the processes that govern extension in the region.

***Background***

Complex interactions between the Earth's magnetic field and the solar wind give rise to a time-varying magnetic field that induces electrical currents in the conductive Earth. Magnetotellurics (MT) is the geophysical technique that uses measurements of these naturally-occurring electromagnetic fields on the Earth's surface to infer the electrical properties of its crust and mantle. The total amount of current flowing in the conductive Earth is determined from the magnetic field measurement while the distribution of that current with depth, which is dependent on the conductivity structure, is determined from the electric field measurement.

Introduced by *Cagniard* (1953) and *Tikhonov* (1950), magnetotellurics involves measurements of the horizontal electric and magnetic fields at the Earth's surface to determine its conductivity structure. Although all of the magnetotelluric concepts and formulae can be derived from the theory of electromagnetic wave propagation, it must be remembered that physically, the process is one of diffusion. The fields induced by a time-varying external magnetic field diffuse through the conductive Earth and decay with depth (*Price*, 1962). Consequently, fields with different frequencies penetrate to different depths in the Earth. Lower frequency fields penetrate deeper than higher frequency fields. By making measurements at several frequencies, one can make a determination of the Earth's conductivity structure with depth. If measurements are made over an array of sites, one can also map out the lateral variations of conductivity.

The electrical conductivity of the Earth's crust and mantle is related to its mechanical, thermal, lithologic, fluid, and partial melt properties. The Earth's electrical conductivity structure can be quite complicated because the Earth is inherently inhomogeneous, and its electrical conductivities can range over ten orders of magnitude from $10^5$ S/m in the core to $10^{-5}$ S/m in the lower crust. Electrical conductivity in the Earth results from many different mechanisms. In the crust, conductivity is due primarily to the movement of ions through a fluid-filled, connected pore space (this pore space also

includes fractures, cracks, faults, etc.), although some minerals such as sulphides and graphite are highly conductive. The connectivity of fluids in the lower crust is controversial because it is thought that the wetting angles, which may be related to the connectivity (*Watson and Brenan*, 1987), might be too high (*Madden*, 1990, pers. comm.). Laboratory measurements, however, show that the wetting angles are reduced when the fluids contain saline components (*Watson and Brenan*, 1987). Since fluids in the lower crust are probably highly saline (*Orville*, 1963; *Ellis and Mahon*, 1964), it is likely they will form a connected phase. High fluid pressures may also be another mechanism for enhancing the connectivity in the lower crust (*Etheridge et al.*, 1984). In the mantle, temperatures are high enough so that thermally-activated semi-conduction processes take over resulting in conductivities dramatically higher than those found in the crust. The composition of the mantle also plays a role in its electrical conductivity. Olivine, which is 90% forsterite ($Mg_2SiO_4$) and 10% fayalite ($Fe_2SiO_4$), is believed to be the major phase of the Earth's upper mantle (*Duba*, 1972). Laboratory studies show (*Duba*, 1972; *Duba et al.*, 1974) that the conductivity of mantle-like olivine increases with increasing iron content. Additionally, partial melt in the upper mantle may explain high conductivity anomalies in the upper mantle that have been inferred from long-period magnetotelluric measurements and geomagnetic deep soundings (*Shankland and Waff*, 1977).

In magnetotelluric surveys, one is mainly concerned with the conductivity structure of the crust and upper mantle. Even though at these depths the conductivity is controlled primarily by connected pore fluids, there are still large variations in conductivity both laterally and vertically. For example, sedimentary rocks tend to be more conductive than igneous rocks because of their generally higher porosities. The lower crust should be more resistive than the upper crust because the lower crust deforms ductilely, and this tends to eliminate much of the porosity. Ductile deformation in the lower crust is due primarily to the higher temperatures found there as compared to the upper crust. Additionally, conductivities in sedimentary basins are often highly anisotropic because of interbedded

shales and sandstones, or the inclusion of clay layers, which are also anisotropic. In short, the heterogeneous nature of the Earth's conductivity structure necessitates three-dimensional modeling algorithms to properly interpret magnetotelluric data.

The California Basin and Range Province is very three-dimensional in nature and requires three-dimensional modeling algorithms to interpret the data we have collected there. We became particularly interested in this region after analyzing magnetotelluric data we had collected during the MIT Geophysics Field Camp at Panamint Valley, California, in January of 1987. We were suprised to find that the current system at Panamint Valley was still being influenced by the ocean some 300 km away in the period range of 10-300s. Near ocean-continent boundaries, ocean-like electrical currents get trapped in the continental upper crust at periods where they should be in the mantle in typical continental areas. These excess currents gradually leak across the resistive lower crust into the mantle as one moves away from the ocean-continent boundary. This effect is manifested in magnetotelluric data by the retardation of the mantle response to longer periods. In typical continental areas, one starts to see the mantle response (this part of the magnetotelluric spectrum is termed the mantle branch) at periods from 10-100s. In an ocean regime, the mantle is not seen until periods of 12h or greater. In the region around the ocean-continent boundary, the mantle branch is seen at periods that are a compromise between the ocean and the continental responses. For instance, at Hollister, California some 75 km away from the ocean, the mantle branch begins at a period of about 8h (*Mackie et al.*, 1988). At Panamint Valley, we find the mantle branch at periods of around 100-300s, and at stations further south in Searles Valley, the mantle branch is retarded to even longer periods. Particularly surprising, however, is that this ocean effect is present in the north-south currents, but absent in the east-west currents. This is a feature that we continue to observe at other stations throughout the California Basin and Range. It seems as if the Sierra Nevada block off the current from the west, but that current from south of the Sierra Nevada comes up

into the Basin and Range Province. Obviously, it will take three-dimensional modeling to fully understand these data.

### *Three-dimensional magnetotelluric modeling*

Interpretation methods for magnetotellurics largely involve the use of one-dimensional and two-dimensional modeling and inversion algorithms. One-dimensional geometries are modeled quite simply by using the analytic solution to Maxwell's equations for a layered earth (*Kaufman and Keller,* 1981). Except for a few special cases, such as a quarter space model (*d'Erceville and Kuntz,* 1962), two-dimensional geometries must be modeled with numerical methods. These include network analogs (*Madden,* 1972), finite differences (*Brewitt-Taylor and Weaver*, 1976; *Oristaglio and Hohmann*, 1984), finite elements (*Coggan*, 1971; *Wannamaker et al.*, 1987), or integral equation techniques (*Hohmann*, 1971; *Lee*, 1975). The Earth, however, is three-dimensional, and its electrical properties are much more variable than most of its other physical properties. Even though there are certain special situations where three-dimensional responses can be accurately modeled by two-dimensional TM mode responses (*Wannamaker et al.*, 1984), three-dimensional modeling routines are clearly needed.

In recent years, a lot of effort has been put into developing three-dimensional magnetotelluric modeling algorithms. Much of this work has gone into the integral equation approach (*Hohmann,* 1975; *Wannamaker et al.*, 1984; *San Filipo et al.*, 1985; *Wannamaker*, 1990). This method is computationally quick when there are only a few inhomogeneous bodies in an otherwise layered earth. As the complexity of the model increases, so also does the computation time. Other algorithms work in the Fourier domain (*Park,* 1985; *Fornberg,* 1987), but these implicitly involve periodicity assumptions that can bias the computations. Finite difference and finite element algorithms (*Adhidjaja and Hohmann*, 1989; *Reddy et al.*, 1977) lead to very large systems of equations to be solved for realistic earth models, but advances in solving large sparse matrices by relaxation

techniques (e.g., *Reid*, 1971) make these methods more appealing. Finally, there are some hybrid algorithms (*Lee et al.*, 1981; *Best et al.*, 1985) that involve combinations of these solution methods, but it remains to be seen whether they offer any improvements over the more traditional methods.

The goal, then, is to develop an algorithm that can model complex, fully inhomogeneous, three-dimensional media quickly and accurately. Integral equation techniques are not well suited for situations in which there are more than just a few inhomogeneities in an otherwise layered earth because they become too time-consuming. Fourier methods, while similar to finite differences or finite elements, implicitly assume periodicity, and are unable to include regional boundary conditions on the three-dimensional model. Therefore, one is led to use either finite differences or finite elements to model complex media, but finite differences are simpler to implement. Our modeling algorithms are finite difference algorithms that are actually based on the integral forms of Maxwell's equations rather than the differential forms. This bypasses the difficulties associated with approximating derivative operators or taking derivatives of Earth properties. Arguably, discretized Earth models can still lead to large, sparse systems of equations, but these sparse systems can often be solved quickly and efficiently with certain approximate and direct solution techniques.

We investigate several relaxation and direct solution techniques for solving the system of equations that arise from our finite difference formulation of Maxwell's equations. The relaxation algorithms are conjugate direction algorithms (*Hestenes and Stiefel*, 1952) and are quick, simple to implement, and do not require large amounts of computer storage. Conjugate direction algorithms, in theory, exactly solve a system of equations in no more than $n$ steps where $n$ is the dimension of the system. Relaxation solutions are approximate solutions, but one of the drawbacks to using them is that one never really knows when to stop the relaxation process. Unfortunately, the residual, which is the only measure one has of the error in the solution, is not always a good indicator of

when the relaxation process should be terminated. An additional problem with relaxation methods is that they have difficulty resolving the component of the solution that is associated with the small eigenvalues of the system (*Reid*, 1971). We have implemented a relaxation algorithm that uses a multiple scaling technique, and this appears to give better results compared to the relaxation algorithm without multiple scaling. This technique condenses the model into a smaller scale model (horizontally and not vertically) that is solved using an exact solution of the difference equations. These fields are then interpolated onto a larger scale model that is solved iteratively by a conjugate direction relaxation method. This process is continued until the original model is reached. This technique has the advantage that the regional **H** field structure is imprinted onto the starting field values for the larger scale relaxation solutions. The results from this technique appear to be superior to those obtained from the conventional relaxation of the original model, which are started with 2D TM mode **H** field values.

The direct solution technique is an exact solution of the difference equations that is similar to propagator methods (*Gilbert and Backus*, 1966; *Haskell*, 1953; *Thomson*, 1950) and Ricatti equation solutions (*Eckhardt*, 1963). With this technique, a matrix is computed for each earth layer that relates the horizontal **E** fields to the horizontal **H** fields in that layer. This matrix is propagated up through the earth, and is dependent on all the interactions below that layer. This method is more time consuming than the relaxation methods since a matrix inversion has to be performed for each layer in the earth model, and it requires more computer storage space, but the resulting solution is more accurate.

### *Three-dimensional magnetotelluric inversion*

Our approach to the forward problem has always been influenced by the goal of implementing a three-dimensional inversion algorithm. We are motivated by the desire to have the ability to invert for a fully inhomogeneous model since the Earth is never as simplistic as layered media or a single inhomogeneous body buried in a layered media.

Inversion schemes can be catagorized as either direct or linearized schemes. Direct inversions involve well-defined operators acting on the data to produce a model that predicts the observed data. Linearized inversion schemes, on the other hand, are iterative approaches that make systematic changes in the model to reduce the error in the fit to the data, usually subject to certain constraints.

Direct inversions are known for several one-dimensional geophysical examples, the most famous being the seismic traveltime inversion, which is known as the Herglotz-Wiechert formula (*Aki and Richards,* 1980). Examples of other direct inversion schemes are the 'layer-stripping' algorithms. These algorithms systematically proceed from higher to lower frequencies (or equivalently from the surface on down) adding layers to a one-dimensional model until all the data has been predicted. They are called layer-stripping methods because when an additional layer had been added to the model, its effect is stripped away from the data in order to unmask the properties of the next layer, and so on. *Pekeris* (1940) derived a layer-stripping algorithm for the electrical resistivity problem. Such algorithms have also been applied to seismic data (*Yagle and Levy,* 1985). These algorithms have only dealt with one-dimensional models, although theoretically, they should be extendable to higher dimensional models.

Direct inversion methods also exist for the magnetotelluric problem, although these are restricted to one-dimensional geometries. *Weidelt* (1972) adapted the Gelfand-Levitan theory for the solution of the inverse Sturm-Liouville problem to the magnetotelluric problem for either a spherically symmetric or plane stratified earth. *Baily* (1970) derived an analytic solution for the geomagnetic induction problem in a spherically symmetric earth. He also proved that the resulting model was unique for a continuum of noise-free measurements if the conductivity distribution was a bounded, real analytic function of depth. The uniqueness proof was extended by *Loewenthal* (1975) to the magnetotelluric case for a one-dimensional geometry in which the conductivity distribution consisted of a finite number of discontinuities (i.e., the earth is composed of a finite number of layers,

each having isotropic conductivity). More recently, *Coen et al* (1983) obtained a direct solution for one-dimensional geometries by using the Born approximation to the electric field integral equation. Unfortunately, direct inversions tend to be unstable for noisy, band-limited data. Other iterative analytic methods have been developed to help stabilize the direct inversion of magnetotelluric data (*Fischer et al.*, 1981; *Parker and Whaler*, 1981), but again, they are limited to one-dimensional geometries.

Linearized inversion schemes, on the other hand, are not restricted to one-dimensional geometries, and they are used in a wide variety of geophysical and medical applications. These schemes involve linearizing a non-linear problem about some model, and solving for the model perturbations that minimize a pre-determined error functional. Since the problems are non-linear, the model is updated and the procedure is iterated until an acceptable fit to the data, perhaps subject to certain constraints, is obtained.

Examples of linearized inversion schemes for the magnetotelluric problem can be found, for example, in *Jupp and Vozoff* (1977) and *Pederson and Rasmussen* (1989). These inversion schemes typically employ non-linear least squares algorithms. For our inversions, we prefer to use the maximum likelihood inverse (*Mackie et al.*, 1988), which closely follows the work of *Tarantola* (1987) and *Tarantola and Valette* (1982). The maximum likelihood inverse is the inverse that minimizes a weighted sum of the variance of the data errors (misfit of the observed data to the predicted data) and the model errors (deviation of the solution model from an *a priori* model).

Most linearized inversion schemes involve a sensitivity analysis that determine how the observed parameters depend on changes in the properties of the Earth. These determinations, often called the Frechet derivatives, are grouped together into the sensitivity, or Jacobian, matrix (see *McGillivray and Oldenburg*, 1990, for a comparative study of sensitivity analyses). Carrying out the sensitivity analysis to create the sensitivity matrix involves doing one forward modeling run per frequency with sources at each observation site (reciprocity relationships guarantee that this is equivalent to putting sources

in the media and solving for the fields at each observation site). For one-dimensional and two-dimensional geometries, the actual sensitivity analysis poses no computational difficulty, especially with modern computers. However, because three-dimensional modeling algorithms are so computer-intensive, creating the sensitivity matrix for a three-dimensional model would be impractical, even with the use of a supercomputer. There is one additional problem for three-dimensional inversion schemes: most linearized inversion algorithms, including weighted least squares and maximum likelihood methods (*Tarantola*, 1987), require, after constructing the sensitivity matrix, the evaluation of a quantity like $(\mathbf{A}^H\mathbf{A})^{-1}$ where $\mathbf{A}$ is the sensitivity matrix. Evaluating the matrix $\mathbf{A}^H\mathbf{A}$ and inverting it is yet another large computational task. We circumvent these problems by using conjugate gradient relaxation methods to solve the maximum likelihood equations. This bypasses the need to create $\mathbf{A}$ or $\mathbf{A}^H\mathbf{A}$, and the need to invert $\mathbf{A}^H\mathbf{A}$, because all the relaxation method needs to know is the result of $\mathbf{A}$ or $\mathbf{A}^H$ operating on an arbitrary vector. We show that these operations are equivalent to one forward modeling run each with sources distributed throughout the volume (for the $\mathbf{A}$ calculation) or at the surface (for the $\mathbf{A}^H$ calculation). Relaxation solutions of the maximum likelihood equations work as well in one-dimensional and two-dimensional geometries as the direct solution of those equations (*Madden and Mackie*, 1989). In this thesis, these concepts are extended to three-dimensional geometries.

### *A magnetotelluric study of the California Basin and Range*

We have spent a fair amount of time during the past three years collecting magnetotelluric data in the California Basin and Range Province. We have collected data east to west from Death Valley to Owens Valley, and north to south from Eureka Valley to the northern Mojave Desert. Although the data are narrowly band-limited (10 sec to 300 sec periods) and of only moderate quality, they are sufficient to allow us to identify zones in the crust of increased conductance and electric current leakage. We find that even this far inland from the ocean, the local telluric fields are perturbed from their normal continental-

like values because of the excess ocean current still trapped in the upper crust. These perturbations occur in the **E** fields aligned along the valley, whereas the **E** fields aligned across the valley are not perturbed, but rather, contain information about the upper-crustal conductivity structure of the basins.

The total amount of current induced in the Earth is determined by the source field, which changes temporally and spatially. The vertical distribution of that current, however, is determined by the Earth's conductivity structure. In the oceans, most of the electric current is concentrated in the ocean itself even down to very long periods (12 h or greater) because of the high conductance of the ocean. In continental regimes, at these same long periods, the current is concentrated in the mantle. Since current is divergenceless, the current fields perpendicular to the ocean-continent boundary must readjust themselves in some region around the ocean-continent boundary. This readjustment, which is a leakage of the currents out of the upper crust into the mantle across the resistive lower crust, typically takes place over a distance of hundreds of kilometers and is dependent upon the resistivity of the lower crust and the conductivity of the upper crust (*Ranganayaki and Madden*, 1980). On the conductive side of a conductive-resistive contact, the current density near the surface is decreased near the contact (causing a decrease in the **E** field perpendicular to the contact), and the current density near the surface on the resistive side is higher than it would normally be if the conductive medium were not present (causing an increase in the **E** field perpendicular to the contact). In our situation, the contact is the ocean-continental boundary, the conductive side is the ocean, and the resistive side is the continent. The current fields found on the continent near the ocean-continent boundary, being divergenceless, are a mix between the oceanic current system and the continental current system. The effect of the oceanic current system is to retard the magnetotelluric response to longer periods (as occurs in the ocean because of its high conductance). That is, the part of the magnetotelluric spectrum that is termed the mantle branch (*Mackie et al.*, 1988) usually occurs at periods of 10-100s in typical continental regimes, but is retarded to

much longer periods nearer to the ocean. These are not subtle effects as they show up as dramatic changes in the phases and slopes of the apparent resistivity curves and do not require the highest quality data to follow.

This particular coast effect shows up in the current system perpendicular to the ocean-continent boundary and was first described by *Kasameyer* (1974). He found excess ocean currents in the upper crust across New England all the way to New York, some 500 km away from the continental margin. The more familiar coast effect was described by *Parkinson* (1962) and *Schmucker* (1963) where anomalies in the vertical component of the geomagnetic field near ocean-continent boundaries are due to electric currents running parallel to the coast in both the ocean and in the oceanic upper mantle.

In central and southern California, high current levels at long periods have been documented by *Bennett* (1985) and *Mackie et al.* (1988). The interpretation of that long-period magnetotelluric data requires a highly resistive oceanic crust (a resistivity-thickness product on the order of 1 x $10^6$ Ω-m-km). This value is consistent with that determined from ocean-bottom controlled-source electromagnetic measurements in the Pacific ocean (*Cox et al.*, 1986). These excess currents gradually leak into the mantle as one proceeds away from the ocean-continent boundary and are documented across the Great Valley in central California (*Park et al.*, 1990), and to a lesser extent in the California Basin and Range (*this thesis*). What is especially unusual about these studies is that there are zones in the lower crust that are more conductive than usual through which large amounts of the excess upper-crustal current leaks into the mantle. More intriguing, however, is that these zones appear to be correlated with certain tectonic features. For example, in central California, these zones are correlated with suture zones in the lower crust on the eastern and western edges of the Great Valley (*Park et al.*, 1990). In the California Basin and Range, these zones are correlated with the areas presently undergoing the most recent and dramatic extension (*this thesis*). The increased conductance in these zones may result from subducted sedimentary rocks (as postulated for the Great Valley suture zones), or may

result from other processes associated with the extension of continental crust as in the California Basin and Range. Such results may well aid us in our understanding of the tectonic evolution of the lower crust in such regimes.

### *Thesis organization*

This thesis is organized into three parts. The first part, chapter 2, details our algorithms for solving the three-dimensional magnetotelluric forward modeling problem. Included are both relaxation and direct approaches. Comparisons are made between our direct solution and another direct solution which uses the integral equation technique. Comparisons are also made between the relaxation algorithms and the direct algorithms. The second part of the thesis, chapter 3, details our solution of the three-dimensional magnetotelluric inversion problem. This solution technique uses conjugate gradient relaxation methods. Several examples are shown inverting synthetic noise-free magnetotelluric data. The third part of the thesis, chapter 4, is a magnetotelluric study of the California Basin and Range. The forward modeling algorithms developed in the first part are used to model these data. The results as well as the implications are presented. Conclusions and suggestions for further work are in Chapter 5.

***References***

Adhidjaja, J.I., and Hohmann, G.W., 1989. A finite-difference algorithm for the transient electromagnetic response of a three-dimensional body, *Geophys. J. Int.*, **98**, 233-242.

Aki, K., and Richards, P.G., 1980. *Quantitative Seismology: Theory and Methods*, New York, NY, W.H. Freeman and Co.

Baily, R.C., 1970. Inversion of the geomagnetic induction problem, *Proc. Roy. Soc. Lond.*, **A 315**, 185-194.

Bennett, B.R., 1985. A long-period magnetotelluric study in California, *S.M. dissertation*, MIT.

Best, M.E., Duncan, P., Jacobs, F.J., and Scheen, W.L., 1985. Numerical modeling of the electromagnetic response of three-dimensional conductors in a layered earth, *Geophysics*, **50**, 665-676.

Brewitt-Taylor, C.R., and Weaver, J.T., 1976. On the finite difference solution of two-dimensional induction problems, *Geophys. J. R. astr. Soc.*, **47**, 375-396.

Cagniard, L., 1953. Basic theory of the magnetotelluric method of geophysical prospecting, *Geophysics*, **18**, 605-635.

Coen, S., Franchesca, Q., and Mackiewicz, M., 1983. Direct inversion of one-dimensional magnetotelluric data, *J. Geophys. Res.*, **88**, 2407-2412.

Coggan, J.M., 1971. Electromagnetic and electrical modeling by the finite element method, *Geophysics*, **36**, 132-155.

Cox, C.S., Constable, S.C., Chave, A.D., and Webb, S.C., 1986. Controlled-source electromagnetic sounding of the oceanic lithosphere, *Nature*, **320**, 52-54.

Duba, A., 1972. Electrical conductivity of olivine, *J. Geophys. Res.*, **77**, 2483-2495.

Duba, A., Heard, H.C., and Schock, R.N., 1974. Electrical conductivity of olivine at high pressure and under controlled oxygen fugacity, *J. Geophys. Res.*, **79**, 1667-1673.

Eckhardt, D.H., 1963. Geomagnetic induction in a concentrically stratified earth, *J. Geophys. Res.*, **68**, 6273-6278.

d'Erceville, I., and Kunetz, G., 1962. The effect of a fault on the earth's natural electromagnetic field, *Geophysics*, **27**, 651-665.

Ellis, A.J., and Mahon, W.A.J., 1964. Natural hydrothermal systems and experimental hot water/rock interactions, *Geochim Cosmochim Acta*, **28**, 1323-1357.

Etheridge, M.A., Wall, V.J., Cox, S.F., and Vernon, R.H., 1984. High fluid pressures during regional metamorphism and deformation: implications for mass transport and deformation mechanisms, *J. Geophys. Res.*, **89**, 4344-4358.

Fischer, G., Schnegg, P.A., Peguiron, M., and Le Quang, B.V., 1981. An analytic one-dimensional magnetotelluric inversion scheme, *Geophys. J. R. astr. Soc.*, **67**, 257-278.

Fornberg, B., 1987. The pseudospectral method: comparisons with finite differences for the elastic wave equation, *Geophysics*, **52**, 483-501.

Gilbert, F., and Backus, G.E., 1966. Propagation matrices in elastic wave and vibration problems, *Geophysics*, **31**, 326-332.

Haskell, N.A., 1953. The dispersion of surface waves in multilayered media, *B. Seis. Soc. Am.*, **43**, 17-34.

Hestenes, M.R., and Stiefel, E., 1952. Methods of conjugate gradients for solving linear systems, *J. Res. Natl. Bureau Stand.*, **49**, 409-436.

Hohmann, G.W., 1971. Electromagnetic scattering from conductors in the earth near a line source of current, *Geophysics*, **36**, 101-131.

Hohmann, G.W., 1975. Three-dimensional induced polarization and electromagnetic modeling, *Geophysics*, **40**, 309-324.

Jupp, D.L.B., and Vozoff, K., 1977. Two-dimensional magnetotelluric inversion, *Geophys. J. R. astr. Soc.*, **50**, 333-352.

Kasameyer, P., 1974. Low frequency magnetotelluric survey of New England, *Ph.D. dissertation*, MIT.

Kaufman, A.A., and Keller, G.V., 1981. *The Magnetotelluric Sounding Method*, Elsevier Scientific Publishing Co.

Lee, K.H., Pridmore, D.F., and Morrison, H.F., 1981. A hybrid three-dimensional electromagnetic modeling scheme, *Geophysics*, **46**, 796-805.

Lee, T., 1975. An integral equation and its solution for some two-and-three dimensional problems in resistivity and induced polarisation, *Geophys. J. R. astr. Soc.*, **42**, 81-95.

Loewenthal, D., 1975. Theoretical uniqueness of the magnetotelluric inverse problem for equal penetration discretizable models, *Geophys. J. R. astr. Soc.*, **43**, 897-903.

Mackie, R.L., Bennett, B.R., and Madden, T.R., 1988. Long-period magnetotelluric measurements near the central California coast: a land-locked view of the conductivity structure under the Pacific Ocean, *Geophys. J.*, **95**, 181-194.

Madden, T.R., 1972. Transmission systems and network analogies to geophysical forward and inverse problems, *ONR Tech. Rep.*, **72-3**.

Madden, T.R., and Mackie, R.L., 1989. Three-dimensional magnetotelluric modeling and inversion, *Proc. IEEE*, **77**, 318-333.

McGillivray, P.R., and Oldenburg, D.W., 1990. Methods for calculating Frechet derivatives and sensitivities for the non-linear inverse problem: a comparative study, *Geophys. Pros.*, **38**, 499-524.

Oristaglio, M.L., and Hohmann, G.W., 1984. Diffusion of electromagnetic fields into a two-dimensional earth: a finite-difference approach, *Geophysics*, **49**, 870-894.

Orville, P.M., 1963. Alkali ion exchange between vapor and feldspar phases, *Am. J. Sci.*, **261**, 201-237.

Park, S.K., Orange, A.S., and Madden, T.R., 1983. Effects of three-dimensional structure on magnetotelluric sounding curves, *Geophysics*, **48**, 1402-1405.

Park, S.K., 1985. Distortion of magnetotelluric sounding curves by three-dimensional structures, *Geophysics*, **50**, 785-797.

Park, S.K., Biasi, G.P., Mackie, R.L., and Madden, T.R., 1990. Magnetotelluric evidence for crustal suture zones bounding the southern Great Valley, California, *J. Geophys. Res.*, **in press**.

Parker, R.L., and Whaler, K.A., 1981. Numerical methods for establishing solutions to the inverse problem of electromagnetic induction, *J. Geophys. Res.*, **86**, 9574-9584.

Parkinson, W.D., 1962. The influence of continents and oceans on geomagnetic variations, *Geophys. J.*, **6**, 441-449.

Pedersen, L.B., and Rasmussen, T.M., 1989. Inversion of magnetotelluric data: a non-linear least-squares approach, *Geophys. Pros.*, **37**, 669-695.

Pekeris, C.L., 1940. Direct method of interpretation in resistivity prospecting, *Geophysics*, **5**, 31-42.

Price, A.T., 1962. The theory of magnetotelluric methods when the source field is considered, *J. Geophys. Res.*, **67**, 1907-1918.

Ranganayaki, R.P., and Madden, T.R., 1980. Generalized thin sheet analysis in magnetotellurics, an extension of Price's analysis, *Geophys. J. R. astr. Soc.*, **60**, 445-457.

Reddy, I.K., Rankin, D., and Phillips, R.J., 1977. Three-dimensional modelling in magnetotelluric and magnetic variational sounding, *Geophys. J. R. astr. Soc.*, **51**, 313-325.

Reid, J.K., 1971. On the method of conjugate gradients for the solution of large sparse systems of linear equations, in *Large Sparse Sets of Linear Equations*, Academic Press, 231-254.

San Filipo, W.A., and Hohmann, G.W., 1985. Integral equation solution for the transient electromagnetic response of a three-dimensional body in a conductive half-space, *Geophysics*, **50**, 798-809.

Schmucker, U., 1963. Anomalies of geomagnetic variations in the southwestern United States, *J. Geomagn. Geoelectr.*, **15**, 193-221.

Shankland, T.J., and Waff, H.S., 1977. Partial melting and electrical conductivity anomalies in the upper mantle, *J. Geophys. Res.*, **82**, 5409-5417.

Tarantola, A., and Valette, B., 1982. Generalized nonlinear inverse problems solved using the least squares criterion, *Rev. Geophys. Space Phys.*, **20**, 219-232.

Tarantola, A., 1987. *Inverse Problem Theory: Methods for Data Fitting and Model Parameter Estimation*, Elsevier, New York.

Thomson, W.T., 1950. Transmission of elastic waves through a stratified solid, *J. Appl. Phys.*, **21**, 89-93.

Tikhonov, A.N., 1950. Determination of the electrical characteristics of the deep strata of the earth's crust, *Dokl. Akad. Nauk*, **73**, 295-297.

Wannamaker, P.E., Hohmann, G.W., and Ward, S.H., 1984. Magnetotelluric responses of three-dimensional bodies in layered earths, *Geophysics*, **49**, 1517-1533.

Wannamaker, P.E., Stodt, J.A., and Rijo, L., 1987. A stable finite element solution for two-dimensional magnetotelluric modeling, *Geophys. J. R. astr. Soc.*, **88**, 277-296.

Wannamaker, P.E., 1990. Modeling three-dimensional magnetotelluric responses using integral equations, *Geophysics*, **in review**.

Weidelt, P., 1972. The inverse problem of geomagnetic induction, *Z. Geophys.*, **38**, 257-289.

Yagle, A.E., and Levy, B.C., 1985. The layer stripping solution of the inverse problem for a one-dimensional elastic medium, *Geophysics*, **50**, 425-433.

# Chapter 2
# Three-dimensional magnetotelluric modeling methods

"Sometimes we have a blind trust in machines, a tendency to believe that whatever a computer tells us is gospel..."
-Dean R. Koontz, Midnight

## *Introduction*

In this chapter, we describe several approaches to solving a large system of equations for the electromagnetic response of a fully inhomogeneous, three-dimensional Earth model due to a uniform current source far above the Earth (this is the magnetotelluric response). We depart from most of the recent efforts that have been put into developing integral equation approaches (*Wannamaker et al.*, 1984a; *San Filipo et al.*, 1985; *Wannamaker,* 1990). We instead focus on the viability of using finite difference equations. Our difference equation algorithm, however, is based on the integral forms of Maxwell's equations. The traditional difference equation approach, working with the second-order system of equations derived from the differential equations, leads to the issue of approximating derivatives of Earth properties (*Adhidjaja and Hohmann,* 1989). Starting from the integral forms of Maxwell's equations, however, one only has to be concerned with issues of taking averages, and not in approximating derivatives.

Finite difference algorithms lead to very large systems of equations to be solved for realistic, three-dimensional Earth models. Therefore, the bulk of this chapter is concerned with solving these large systems of equations quickly, accurately, and efficiently. These algorithms are grouped into relaxation solution techniques and direct solution techniques.

The relaxation solutions use conjugate direction relaxation algorithms to obtain approximate solutions to the second order system of equations in **H**. These methods are quick, give reasonable answers, and do not require large amounts of computer storage space. The direct solutions, which are similar to propagator matrix algorithms, are more

computer-intensive because they can require large amounts of storage space and involve doing many matrix inversions. They do, however, give exact solutions to the difference equations up to roundoff and precision errors.

### *Difference Equations*

At the low frequencies involved in magnetotelluric exploration, conduction currents dominate over displacement currents. Therefore, if displacement currents are ignored and an $e^{-i\omega t}$ time dependence is assumed, then the integral forms of Maxwell's equations in *mks* units are given by:

$$\int \mathbf{H}\cdot d\mathbf{l} = \int\int \sigma\mathbf{E}\cdot d\mathbf{S} \qquad (2\text{-}1a)$$

$$\int \mathbf{E}\cdot d\mathbf{l} = \int\int i\omega\mu\mathbf{H}\cdot d\mathbf{S}\,, \qquad (2\text{-}1b)$$

where in general, $\sigma$ and $\mu$ are tensor quantities (*Stratton,* 1941). These integrals can be evaluated for any discretization of the Earth involving flat surfaces. We choose to divide the Earth model into rectangular blocks of arbitrary dimensions with the **H** field defined along block edges, and average **E** fields defined as normals across block faces, as shown in Figure 2-1. This is similar to the geometry for a finite difference scheme on a staggered grid. If adjoining blocks have differing conductivities, the actual **E** fields are discontinuous across the block faces, but the **J** fields are continuous because current is divergenceless. The **E** fields in our geometry, however, actually represent average **E** fields. Discontinuities in the **E** field do not pose any problems since these equations involve integrations rather than differentiations.

One can transform any unequally gridded earth to an equally gridded earth by making the appropriate transformations in the conductivity, permeability, and field values (*Madden and Mackie,* 1989). This is often quite useful in situations where equally spaced

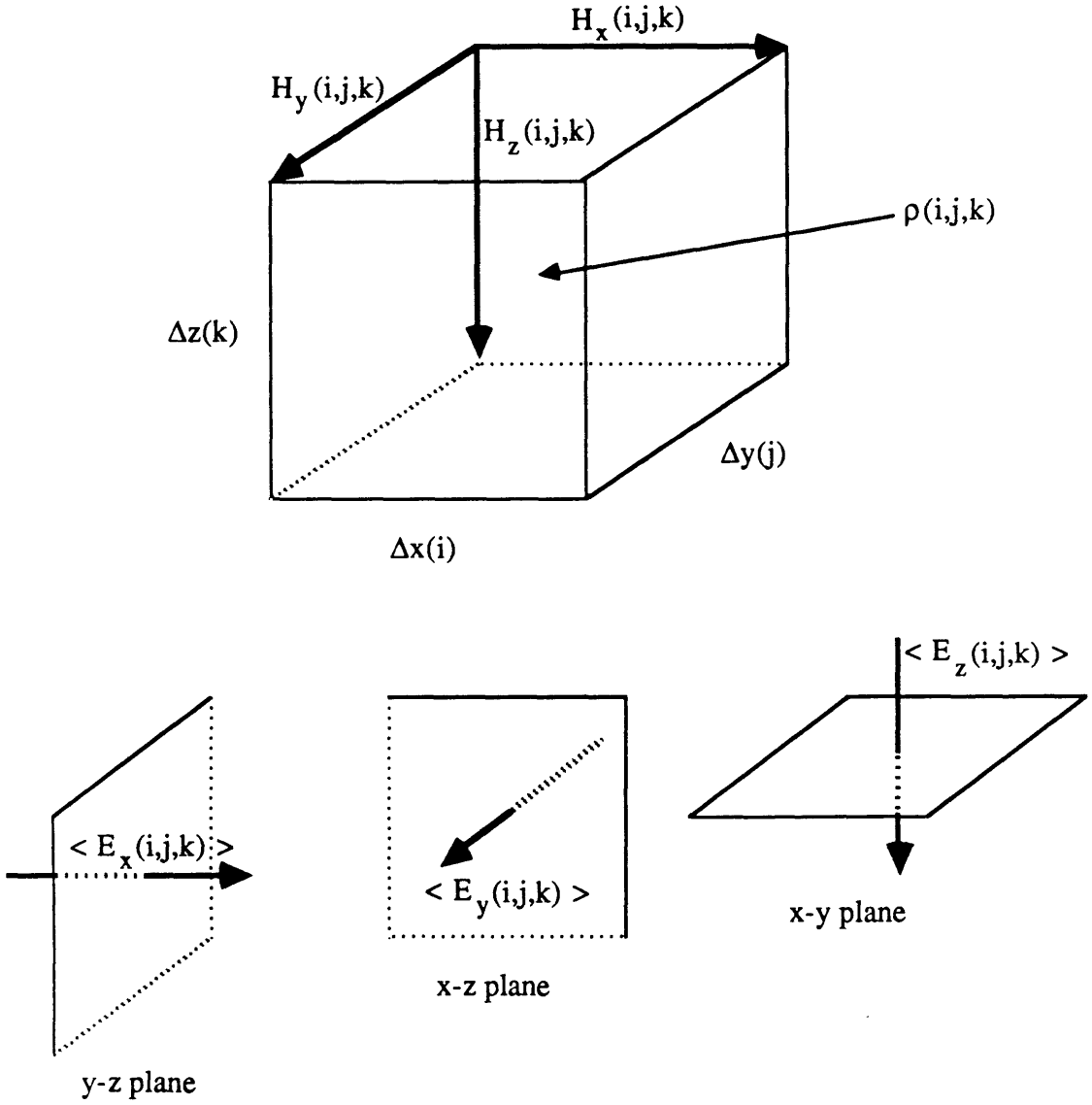


**Figure 2-1**. The difference equation geometry based on the integral forms of Maxwell's equations. The Earth model is divided into rectangular blocks of arbitrary dimensions. The **H** fields are defined as averages along block edges, and the **E** fields are defined as averages across block faces.

grids are needed such as Fourier applications. In addition, if one is using an equally gridded mesh, then the operator for the difference equations is symmetric, which would not generally be the case if the spacing was variable. This turns out to be an important issue when solving this problem by conjugate direction relaxation techniques, which assume symmetric operators.

If the transformed parameters are denoted with an apostrophe, then the scaling factors for the transformation are

$$C_x = \frac{\Delta x}{\Delta x'} \quad C_y = \frac{\Delta y}{\Delta y'} \quad C_z = \frac{\Delta z}{\Delta z'}, \tag{2-2}$$

and the transformed conductivity and permeability tensors are

$$\sigma' = \begin{bmatrix} \sigma \frac{C_y C_z}{C_x} & 0 & 0 \\ 0 & \sigma \frac{C_x C_z}{C_y} & 0 \\ 0 & 0 & \sigma \frac{C_x C_y}{C_z} \end{bmatrix} \tag{2-3}$$

$$\mu' = \begin{bmatrix} \mu \frac{C_y C_z}{C_x} & 0 & 0 \\ 0 & \mu \frac{C_x C_z}{C_y} & 0 \\ 0 & 0 & \mu \frac{C_x C_y}{C_z} \end{bmatrix}. \tag{2-4}$$

For our applications, we assume isotropic conductivity, but the generalization to anisotropic media is straightforward. We also assume that $\mu=\mu_o=4\pi \times 10^{-7}$ henry/m everywhere. The transformed **E**, **H**, and **J** fields are defined as

$$E'_x = C_x E_x \quad E'_y = C_y E_y \quad E'_z = C_z E_z \tag{2-5a}$$

$$H'_x = C_x H_x \quad H'_y = C_y H_y \quad H'_z = C_z H_z \tag{2-5b}$$

$$J'_x = C_y C_z J_x \quad J'_y = C_x C_z J_y \quad J'_z = C_x C_y J_z \,. \tag{2-5c}$$

Under these transformations, equations 2-1a and 2-1b remain invariant, so that solving the transformed system is equivalent to solving the original, or untransformed, system. Throughout the remainder of this chapter it will be assumed that we are dealing with the transformed variables, and the apostrophes will be dropped. Furthermore, to ensure symmetry, it is required that $\Delta x'=\Delta y'=\Delta z'=L$.

With this formulation and the geometry shown in Figure 2-1, the x, y, and z components of equation 2-1a are

$$\begin{aligned}
&\{[H_z(i,j+1,k) - H_z(i,j,k)] - [H_y(i,j,k+1) - H_y(i,j,k)]\}\, L = J_x(i,j,k)\, L^2 \\
&\{[H_x(i,j,k+1) - H_x(i,j,k)] - [H_z(i+1,j,k) - H_z(i,j,k)]\}\, L = J_y(i,j,k)\, L^2 \\
&\{[H_y(i+1,j,k) - H_y(i,j,k)] - [H_x(i,j+1,k) - H_x(i,j,k)]\}\, L = J_z(i,j,k)\, L^2 \,,
\end{aligned} \tag{2-6}$$

where the **J** fields are related to the average **E** fields by

$$\begin{aligned}
E_x(i,j,k) &= \frac{[\rho_{xx}(i,j,k) + \rho_{xx}(i-1,j,k)]}{2} J_x(i,j,k) \\
E_y(i,j,k) &= \frac{[\rho_{yy}(i,j,k) + \rho_{yy}(i,j-1,k)]}{2} J_y(i,j,k) \\
E_z(i,j,k) &= \frac{[\rho_{zz}(i,j,k) + \rho_{zz}(i,j,k-1)]}{2} J_z(i,j,k) \,.
\end{aligned} \tag{2-7}$$

The resistivities are subscripted because the transformed resistivity tensor is anisotropic even though the actual resistivities are isotropic (see equation 2-3). This likewise applies to the magnetic permeabilities. The components of equation 2-1b are given by

$$\begin{aligned}
&\{[E_z(i,j,k) - E_z(i,j-1,k)] - [E_y(i,j,k) - E_y(i,j,k-1)]\}\, L = i\omega\langle\mu_{xx}\rangle H_x(i,j,k)\, L^2 \\
&\{[E_x(i,j,k) - E_x(i,j,k-1)] - [E_z(i,j,k) - E_z(i-1,j,k)]\}\, L = i\omega\langle\mu_{yy}\rangle H_y(i,j,k)\, L^2
\end{aligned} \tag{2-8}$$

$$\{[E_y(i,j,k) - E_y(i-1,j,k)] - [E_x(i,j,k) - E_x(i,j-1,k)]\}\, L = i\omega\langle\mu_{zz}\rangle\, H_z(i,j,k)\, L^2 ,$$

where the average permeabilities are defined as

$$\langle\mu_{xx}\rangle = \frac{\mu_{xx}(i,j-1,k-1) + \mu_{xx}(i,j,k-1) + \mu_{xx}(i,j-1,k) + \mu_{xx}(i,j,k)}{4}$$

$$\langle\mu_{yy}\rangle = \frac{\mu_{yy}(i-1,j,k-1) + \mu_{yy}(i,j,k-1) + \mu_{yy}(i-1,j,k) + \mu_{yy}(i,j,k)}{4} \qquad (2\text{-}9)$$

$$\langle\mu_{zz}\rangle = \frac{\mu_{zz}(i-1,j-1,k) + \mu_{zz}(i-1,j,k) + \mu_{zz}(i,j-1,k) + \mu_{zz}(i,j,k)}{4} .$$

One can solve the first order system of equations, or one can algebraically eliminate either **E** or **H** to obtain a second order system of equations. The relaxation solution techniques that we discuss later in this chapter operate on the second order system of equations in **H**. Our direct solution technique solves the first order system of equations (after eliminating $H_z$ and $E_z$). No matter which solution technique is used, one is ultimately interested in the fields at the Earth's surface since these are the fields that are actually measured. The **E** and **H** fields are output on the Earth's surface at the top face center of each model block. Since the **H** fields are defined along block edges, the **H** fields in the center at the Earth's surface ($H_{xs}$ and $H_{ys}$) are simply taken to be the average of the adjacent **H** fields:

$$H_{xs}(i,j) = \frac{1}{2}[H_x(i,j,ksurf) + H_x(i,j+1,ksurf)]$$

$$H_{ys}(i,j) = \frac{1}{2}[H_y(i,j,ksurf) + H_y(i+1,j,ksurf)] . \qquad (2\text{-}10)$$

Since the **E** fields in the model are defined as normals across the block faces, a bit more care must be taken in computing the fields at the Earth's surface. First, the fields in the top model layer are averaged to give the **E** field in the block center ($E_{xc}$ and $E_{yc}$). Because the actual **E** fields are discontinuous across conductivity contrasts, the averages are weighted by the conductivities of the blocks (here, *k* refers to the top Earth layer):

$$E_{xc}(i,j) = \frac{\rho(i,j,k)}{\rho(i,j,k) + \rho(i-1,j,k)} E_x(i,j,k) + \frac{\rho(i,j,k)}{\rho(i,j,k) + \rho(i+1,j,k)} E_x(i+1,j,k)$$
$$E_{yc}(i,j) = \frac{\rho(i,j,k)}{\rho(i,j,k) + \rho(i,j-1,k)} E_y(i,j,k) + \frac{\rho(i,j,k)}{\rho(i,j,k) + \rho(i,j+1,k)} E_y(i,j+1,k) . \quad (2\text{-}11)$$

Then, the **E** fields are continued up to the Earth's surface using equation 2-8 and assuming that $E_z = 0$ at the Earth's surface.

***Boundary conditions, grading of models***

Proper treatment of the model boundaries is important in calculating the magnetotelluric response of 3D models. One common approach is to assume that the model is periodic in the horizontal directions. This approach is used in Fourier methods (*Park,* 1983) and Rayleigh-FFT methods (*Jiracek et al.*, 1989). It can also be used in difference equations, but even if the boundaries are extended a considerable distance away from the local 3D structure, there are still many situations where it would not be an accurate representation of the regional structure. Oftentimes, local magnetotelluric fields are biased by regional features far away from the local measurement site. The ocean-continent boundary is perhaps the most severe example of this (*Ranganayaki and Madden,* 1980).

To circumvent the potential problems associated with periodic models, one can assign the **H** fields on the boundaries of the model. This is in essence assigning the regional current field, both laterally and vertically, *a priori*. These values could be 1D values, or they could come from a larger scale 2D or 3D calculation. For example, all our algorithms, except the multiple scaling algorithm, currently use 2D TM mode **H** field values assigned on the boundaries of the 3D model. The 2D values are from a calculation where each vertical plane of the 3D model has been imbedded into a larger-scale 2D regional model. We have elected to use the 1D boundary values in the multiple scaling algorithm and to simply include the regional features in the 3D model. This results in larger 3D models to be solved, but the multiple scaling algorithm, which will be shown to be

superior to the other relaxation algorithms, is quick enough and accurate enough to include the regional features.

It is possible to extend the side boundaries to large distances without creating unmanageably large systems by grading the 3D model in the horizontal directions. Discretizing the model on a finer scale near regions of strong conductivity gradients allows one to obtain more accurate solutions. One can also grade the model in the vertical direction because 1) the diffuse nature of electromagnetic waves in conducting media smears the information content with depth, and 2) this allows one to use the same model for a wide range of frequencies without changing the vertical spacing at least up to some high frequency limit that is determined by the thickness and conductivity of the first layer. We found (*Madden and Mackie,* 1989) that geometrical grading factors of 2 in the vertical direction and factors of 3 in the horizontal directions gave results accurate to within 1% in amplitude and less than a degree in phase. These results applied to one- and two-dimensional geometries, but our own modeling experience has been that these results are probably valid for three-dimensional calculations.

Several graded air layers are added on top of the Earth model to account for perturbations in the **H** fields from current gathering effects. These air layers extend far above the Earth and are given a high but finite resistivity of $10^6$ ohm-m. All the results presented in this chapter are from computations with the air layers extending to 75 km above the Earth. We ran a test case with the air layers extending to 150 km above the Earth, but this produced no appreciable differences in the computed field values compared to those that had the air layers extending to 75 km above the Earth. All of the **H** field perturbations are required to be damped out by the top of the air layers. At the bottom of the model, a 1D impedance for a layered earth is used to relate the **E** field to the **H** field ($E_z$ is also assumed to be zero there). Thus, it helps to have the bottom of the model below the resistive lower crust, which acts to filter out shorter wavelength **H** field variations.

***Relaxation solution***

A second order system of equations in **H** is obtained by algebraically eliminating the **E** fields from the difference equations. This procedure produces a large system of equations to be solved, with a sparse coefficient matrix. Relaxation methods can then be used to iteratively obtain the solution to this second order system of equations. Relaxation algorithms have often been used to solve large sparse systems of equations that arise from numerical solutions of partial differential equations. Methods such as steepest descents, over-relaxation, and Gauss-Seidel have traditionally been used to solve such problems, and it has only been recently (*Reid,* 1971) that conjugate direction methods have been applied to the solution of these large sparse matrices. Conjugate direction methods encompass a whole class of algorithms, the most well known of which is the conjugate gradient algorithm (*Hestenes and Stiefel,* 1952).

Conjugate direction methods are iterative techniques that in theory exactly solve the system of equations $\mathbf{Ax} = \mathbf{b}$ in at most $n$ steps where $n$ is the dimension of the matrix **A**. Conjugate direction methods build up the solution vector **x** as a combination of linearly independent vectors **p** (also called the search directions). The amount of each vector **p** that is represented in the solution **x** is determined by satisfying certain orthogonality and conjugacy relations. The method fell into disfavor shortly after it was introduced because it was realized that due to roundoff errors and finite computer word lengths, the method could never be used as an exact method. However, it was shown (e.g., *Reid,* 1971) that when used as an iterative technique, accurate results were often obtained after only a modest number of iterations for several different problems.

Consider the system of equations $\mathbf{Ax} = \mathbf{b}$. For any trial vector $\mathbf{x}_k$, the corresponding *residual* is defined as $\mathbf{r}_k = \mathbf{b} - \mathbf{A}\mathbf{x}_k$. If **A** is real, symmetric, and positive definite, then the functional

$$\Phi(\mathbf{x}_k) = \frac{1}{2}\,\mathbf{r}_k^T\,\mathbf{A}^{-1}\,\mathbf{r}_k \qquad (2\text{-}12)$$

has a minimum value when $\mathbf{r}_k = 0$, or $\mathbf{x}_k = \mathbf{A}^{-1}\mathbf{b}$. Thus, the problem of minimizing $\Phi$ and solving $\mathbf{Ax} = \mathbf{b}$ are equivalent. Since any function decreases most rapidly in the direction of its negative gradient, it might seem logical to iterate to the minimum of $\Phi$ by moving at each step in the direction of its negative gradient, $-\nabla\Phi(\mathbf{x}_k) = \mathbf{r}_k$, to the point where $\Phi$ is locally minimized in that direction. This corresponds to moving to that point at which the residual vector is tangent to the level curves of $\Phi$. This is the basis of the relaxation method known as steepest descents. By construction of the algorithm, each residual vector is orthogonal to the previous residual vector, but not necessarily orthogonal to <u>all</u> previous residual vectors. If the eigenvalue spread of $\mathbf{A}$ is large, then the level curves of $\Phi$ are very elongated, and convergence is prohibitively slow. This is because one is forced to traverse back and forth across the valley defined by the level curves rather than down the valley (*Golub and VanLoan,* 1983). In fact, an infinite number of iterations are usually required to obtain the exact solution (*Jacobs,* 1981).

If, however, $\Phi$ is minimized along a set of directions $\{\mathbf{p}_1, \mathbf{p}_2, \ldots\}$ such that each $\mathbf{p}$ is linearly independent and each $\mathbf{x}_k$ satisfies the relation

$$\min_{\mathbf{x}_k \in \text{span}\{\mathbf{p}_1,\ldots,\mathbf{p}_k\}} \Phi(\mathbf{x}), \tag{2-13}$$

then not only is global convergence guaranteed, but the solution will be reached in at most $n$ steps (*Golub and VanLoan,* 1983). This is the basis of conjugate direction relaxation techniques.

To solve $\mathbf{Ax}=\mathbf{b}$, one starts with an initial estimate $\mathbf{x}_0$, the initial residual $\mathbf{r}_0$, and an initial search direction, which is given by $\mathbf{p}_0 = \mathbf{r}_0$. These vectors are updated at each iteration by the following relations:

$$\begin{aligned} \mathbf{x}_k &= \mathbf{x}_{k-1} + \alpha_k \mathbf{p}_{k-1} \\ \mathbf{r}_k &= \mathbf{b} - \mathbf{A}\mathbf{x}_k = \mathbf{r}_{k-1} - \alpha_k \mathbf{A}\mathbf{p}_{k-1} \end{aligned} \tag{2-14}$$

$$\mathbf{p}_k = \mathbf{r}_k + \beta_k \mathbf{p}_{k-1} ,$$

where $\alpha_k$ is chosen to require that $\mathbf{r}_k^T \mathbf{p}_{k-1} = 0$, and $\beta_k$ is chosen to require that $\mathbf{p}_k^T \mathbf{A}\mathbf{p}_{k-1} = 0$. It can be shown (*Golub and VanLoan,* 1983; *Hestenes and Stiefel,* 1952) that given these relations, the search directions $\mathbf{p}_k$ are A-conjugate, that is,

$$\mathbf{p}_k^T \mathbf{A}\mathbf{p}_i = 0 \qquad i \neq k , \tag{2-15}$$

and that the residuals are orthogonal, that is,

$$\mathbf{r}_i^T \mathbf{r}_j = 0 \qquad i \neq j . \tag{2-16}$$

From these relationships, it is clear that the vectors $\mathbf{p}_i$ and $\mathbf{r}_i$ both lie in the space $S_{i+1}=\{\mathbf{r}_o, \mathbf{A}\mathbf{r}_o, \ldots \mathbf{A}^i\mathbf{r}_o\}$. Because of the orthogonality and conjugacy conditions, the $\mathbf{p}_i$ and $\mathbf{r}_i$ vectors each form a set of linearly independent vectors, and thus, the space $S_{i+1}$ can also be represented by the vector bases $\{\mathbf{p}_o, \mathbf{p}_1, \ldots \mathbf{p}_i\}$ and $\{\mathbf{r}_o, \mathbf{r}_1, \ldots \mathbf{r}_i\}$.

Recall that in this algorithm, A is assumed to be real, symmetric, and positive-definite. For many problems, however, the operator A is not real, or symmetric, or positive-definite. For example, the operator for the three-dimensional electromagnetic equations is neither real nor positive-definite, but can be made symmetric by the proper transformations as described earlier. If an operator is complex, but hermitian and positive-definite, then the conjugate gradient algorithm, along with its properties, holds if all the dot products are simply changed to hermitian dot products. For situations in which an operator is real and symmetric, but not necessarily positive-definite, the minimum residual algorithm (also called the minimum variance algorithm) can be used (*Hestenes and Stiefel,* 1952; *Fletcher,* 1975; *Axelsson,* 1980). In this algorithm, the functional $\mathbf{r}^T\mathbf{r}$ is minimized rather than the functional $\mathbf{r}^T\mathbf{A}^{-1}\mathbf{r}$, and we will describe it shortly. In the complex case, naturally, the functional $\mathbf{r}^H\mathbf{r}$ must be minimized.

We mentioned earlier that one of the drawbacks to using conjugate direction techniques was that even though in theory they represented exact solutions, such results could never be obtained in practice because of finite computer word lengths and roundoff

errors. Another potential problem with any relaxation technique, let alone conjugate direction techniques, concerns the eigenvalue distribution of the operator. Both *Jennings* (1977) and *Jacobs* (1981) have pointed out that not only is the eigenvalue spread important, but so also is the distribution of the eigenvalues. That is, using exact arithmetic, conjugate gradients require one step for each distinct eigenvalue. This fact was clearly established by *Hestenes and Stiefel* (1952). What was not made clear in their original paper, however, was that conjugate gradient techniques are especially well suited for problems in which most of the eigenvalues are clustered in a small number of groups. The basis for this statement essentially comes from the relationships between the theory of orthogonal polynomials and conjugate gradient relaxation methods as described in *Hestenes and Stiefel* (1952) and *Stiefel* (1958).

*Jennings* (1977) pointed out that the residual vector could be written as a linear combination of the eigenvectors of the matrix **A**:

$$\mathbf{r} = \sum_i s_i \, \mathbf{q}_i \,, \tag{2-17}$$

where $\mathbf{q}_i$ is the eigenvector corresponding to the $i^{th}$ eigenvalue, and $s_i$ is a coefficient which is a measure of the amount of that particular eigenvector represented in the residual vector. *Jennings* (1977) proved that the coefficients $s_i$ at the $k^{th}$ iteration could be expressed as

$$s_i^{(k)} = \Gamma^{(k)}(\lambda_i) \, s_i^{(0)} \,, \tag{2-18}$$

where $\Gamma^{(k)}(\lambda_i)$ is a polynomial of order $k$ that satisfies $\Gamma^{(k)}(0) = 1$ and $\lambda_i$ is the $i^{th}$ eigenvalue. The residual vector, therefore, would be zero when $\Gamma^{(k)}(\lambda_i) = 0$ for all $\lambda_i$ for which $s_i^{(0)} \neq 0$. Consequently, it takes a polynomial of order equal to the number of eigenvalues to make $\Gamma^{(k)}(\lambda_i) \doteq 0$, and therefore make the residual equal to zero. If the eigenvalues are evenly distributed, it takes a very high order polynomial to have zeros on or near each distinct eigenvalue and hence give considerable error reduction. If, however, the eigenvalues are clustered in a few small groups, then the best-fitting low order polynomial

(order equal to the number of clusters) will give a small residual because that polynomial will have zeros either within or close to each cluster of eigenvalues. Therefore, only a small number of relaxation steps would be needed to give a considerable error reduction.

Unfortunately, finite difference and finite element schemes usually result in coefficient matrices whose eigenvalues are evenly distributed (*Jacobs,* 1981). Furthermore, matrices with large eigenvalue spreads (large condition numbers) are more difficult to relax than those with smaller eigenvalue spreads (e.g., *Jennings,* 1977). Consequently, in order to use conjugate gradients on such ill-conditioned systems, it is often necessary to precondition them. This is certainly the case for the 3D electromagnetic equations.

The idea behind the use of a preconditioner is to compact the eigenvalue spread of the original matrix because the smaller the eigenvalue spread, the more efficient the relaxation procedure (*Hestenes and Stiefel,* 1952). The preconditioner acts on the original matrix to produce a matrix that has a more compact eigenvalue spread and is given by

$$\mathbf{B} = \mathbf{C}^{-1}\mathbf{A}\mathbf{C}^{-1} . \qquad (2\text{-}19)$$

Preconditioners can be implemented without ever computing **B**, one only needs to be able to compute the effect of $\mathbf{C}^{-2} = \mathbf{M}^{-1}$ on a vector. One example of a common preconditioner is the matrix $\mathbf{M} = \mathrm{diag}(a_{11}, a_{22}, ..., a_{nn})$ where $a_{ii}$ refers to the diagonal elements of the **A** matrix (*Golub and Van Loan,* 1983). Other preconditioners that could be used are those based on certain classes of matrices (*Meijerink and Van der Vost,* 1977), or those that arise when the original coefficient matrix can be expressed in other more convenient forms (*Concus et al.*, 1976), or those that are based on certain 'incomplete' matrix decompositions (*Kershaw,* 1978). The best preconditioners, however, are those which are most closely related to the actual inverse of the matrix. If, for example, we used as a preconditioner the actual inverse of the matrix, $\mathbf{M}^{-1} = \mathbf{A}^{-1}$, the conjugate gradient algorithm would reach the solution in just one step. This is because that particular preconditioner

reduces the eigenvalue spread of the original matrix to just one eigenvalue ($\lambda = 1$). This is clearly an exaggerated example because if we had the actual inverse, there would be no need to use conjugate gradients. Nevertheless, it demonstrates the idea behind the use of a preconditioner.

We can examine how preconditioning is implemented by considering the minimum residual algorithm for real symmetric matrices in which $\mathbf{r}^T\mathbf{r}$ is minimized (*Fletcher,* 1975; *Axelsson,* 1980). Make the following definitions:

$$\mathbf{A}' = \mathbf{C}^{-1}\,\mathbf{A}\,\mathbf{C}^{-1} \qquad \mathbf{x}' = \mathbf{C}\,\mathbf{x} \qquad \mathbf{b}' = \mathbf{C}^{-1}\,\mathbf{b}\,. \tag{2-20}$$

Here we will also assume that $\mathbf{C}$, and therefore $\mathbf{C}^{-1}$, are symmetric. Therefore, the system $\mathbf{A}'\mathbf{x}' = \mathbf{b}'$ is equivalent to $\mathbf{C}^{-1}\mathbf{A}\mathbf{C}^{-1}\mathbf{C}\mathbf{x} = \mathbf{C}^{-1}\mathbf{b}$, or $\mathbf{A}\mathbf{x} = \mathbf{b}$. In other words, solving $\mathbf{A}'\mathbf{x}' = \mathbf{b}'$ also solves $\mathbf{A}\mathbf{x} = \mathbf{b}$. We now apply the minimum residual algorithm to the transformed system as it is better conditioned and should have improved convergence properties. The quantities with apostrophes will denote those that are related to the transformed system of equations. The equations for updating the solution vector and the search directions in the transformed system are

$$\begin{aligned} \mathbf{x}'_{i+1} &= \mathbf{x}'_i + \alpha_i\,\mathbf{p}'_i \quad \Rightarrow \quad \mathbf{C}\mathbf{x}_{i+1} = \mathbf{C}\mathbf{x}_i + \alpha_i\,\mathbf{p}'_i \\ \mathbf{r}'_{i+1} &= \mathbf{r}'_i - \alpha_i\,\mathbf{A}'\mathbf{p}'_i \quad \Rightarrow \quad \mathbf{r}'_{i+1} = \mathbf{r}'_i - \alpha_i\,\mathbf{C}^{-1}\mathbf{A}\mathbf{C}^{-1}\mathbf{p}'_i\,. \end{aligned} \tag{2-21}$$

Notice that if we set $\mathbf{p} = \mathbf{C}^{-1}\mathbf{p}'$ and $\mathbf{r} = \mathbf{C}\mathbf{r}'$, then we obtain

$$\begin{aligned} \mathbf{x}_{i+1} &= \mathbf{x}_i + \alpha_i\,\mathbf{p}_i \\ \mathbf{r}_{i+1} &= \mathbf{r}_i - \alpha_i\,\mathbf{A}\mathbf{p}_i\,. \end{aligned} \tag{2-22}$$

Furthermore, we obtain for $\alpha_i$ (by requiring that $(\mathbf{r}'_{i+1})^T\,\mathbf{A}'\mathbf{p}' = 0$ for the minimum residual algorithm)

$$\alpha_i = \frac{(\mathbf{r}'_i)^T\,\mathbf{A}'\mathbf{p}'_i}{(\mathbf{A}'\mathbf{p}'_i)^T\,\mathbf{A}'\mathbf{p}'_i} = \frac{\mathbf{r}_i^T\,\mathbf{C}^{-2}\mathbf{A}\mathbf{p}_i}{\mathbf{p}_i^T\,\mathbf{A}^T\mathbf{C}^{-2}\mathbf{A}\mathbf{p}_i}\,, \tag{2-23}$$

which, since **A** is symmetric, can also be written as

$$\alpha_i = \frac{\mathbf{r}_i^T \mathbf{C}^{-2}\mathbf{A}\mathbf{p}_i}{\mathbf{p}_i^T \mathbf{A}\mathbf{C}^{-2}\mathbf{A}\mathbf{p}_i} . \tag{2-24}$$

The search directions are updated as

$$\mathbf{p}'_{i+1} = \mathbf{r}'_{i+1} + \beta_i \mathbf{p}'_i \quad \Rightarrow \quad \mathbf{p}_{i+1} = \mathbf{C}^{-2}\mathbf{r}_{i+1} + \beta_i \mathbf{p}_i . \tag{2-25}$$

We obtain for $\beta_i$ (by requiring that $(\mathbf{A}'\mathbf{p}'_{i+1})^T \mathbf{A}'\mathbf{p}' = 0$ for the minimum residual algorithm)

$$\beta_i = \frac{-(\mathbf{A}'\mathbf{r}'_{i+1})^T \mathbf{A}'\mathbf{p}'_i}{(\mathbf{A}'\mathbf{p}'_i)^T \mathbf{A}'\mathbf{p}'_i} = \frac{-\mathbf{r}_{i+1}^T \mathbf{C}^{-2}\mathbf{A}\mathbf{C}^{-2}\mathbf{A}\mathbf{p}_i}{\mathbf{p}_i^T \mathbf{A}^T\mathbf{C}^{-2}\mathbf{A}\mathbf{p}_i} , \tag{2-26}$$

which again, since **A** is symmetric, can be written as

$$\beta_i = \frac{-\mathbf{r}_{i+1}^T \mathbf{C}^{-2}\mathbf{A}\mathbf{C}^{-2}\mathbf{A}\mathbf{p}_i}{\mathbf{p}_i^T \mathbf{A}\mathbf{C}^{-2}\mathbf{A}\mathbf{p}_i} . \tag{2-27}$$

Notice that we never have to compute the matrix $\mathbf{A}' = \mathbf{C}^{-1}\mathbf{A}\mathbf{C}^{-1}$, we only need to be able to compute $\mathbf{C}^{-2}\mathbf{r}$ and $\mathbf{C}^{-2}\mathbf{A}\mathbf{p}$. Clearly, for the preconditioned minimum residual algorithm to be an effective technique, we must be able to compute $\mathbf{C}^{-2}\mathbf{r}$ and $\mathbf{C}^{-2}\mathbf{A}\mathbf{p}$ quickly and efficiently. With a good preconditioner, rapid convergence can often be obtained, even after $O(\sqrt{n})$ iterations (*Golub and VanLoan,* 1983).

Up to this point, we have skirted the issue of dealing with complex systems of equations. As mentioned earlier, the algorithms discussed would still be valid for complex systems if the symmetry properties were changed to hermitian symmetry, and if all the dot products were changed to hermitian dot products. For general complex matrices however, we follow *Lanczos* (1961) and imbed the operator into a larger hermitian system

$$\mathbf{A}' = \begin{bmatrix} 0 & \mathbf{C}^{-1}\mathbf{A}\mathbf{C}^{-1} \\ (\mathbf{C}^{-1}\mathbf{A}\mathbf{C}^{-1})^H & 0 \end{bmatrix} \quad \mathbf{x}' = \begin{bmatrix} \mathbf{C}^H\mathbf{x}^* \\ \mathbf{C}\mathbf{x} \end{bmatrix} \quad \mathbf{b}' = \begin{bmatrix} \mathbf{C}^{-1}\mathbf{b} \\ \mathbf{C}^{H^{-1}}\mathbf{b}^* \end{bmatrix} . \tag{2-28}$$

Since this operator is hermitian symmetric, the minimum residual algorithm could be applied to this system provided all the dot products are changed to hermitian dot products. This would ensure that at each step we are reducing the functional $(\mathbf{r}')^H \mathbf{r}'$. There are, however, two potential problems associated with proceeding along these lines. The first is that because the larger hermitian system has a dimension of twice the original system, in theory it will take $2n$ steps to reduce the residual to zero. The second problem is that it is necessary to know $(\mathbf{C}^{-1})^H\mathbf{C}^{-1}$, which, unless $\mathbf{C}^{-1}$ is real, is generally not known. For situations in which $\mathbf{C}^{-1}$ is real and symmetric, however, and $\mathbf{A}$ is complex and symmetric, the minimum residual algorithm for the expanded system above is as follows:

$$\alpha_i = \frac{\mathrm{Re}\left[\mathbf{r}_i^H \mathbf{C}^{-2}\mathbf{A}\mathbf{p}_i\right]}{\mathrm{Re}\left[(\mathbf{A}\mathbf{p}_i)^H \mathbf{C}^{-2}\mathbf{A}\mathbf{p}_i\right]}$$

$$\mathbf{x}_{i+1} = \mathbf{x}_i + \alpha_i \mathbf{p}_i$$

$$\mathbf{r}_{i+1} = \mathbf{r}_i - \alpha_i \mathbf{A}\mathbf{p}_i \qquad (2\text{-}29)$$

$$\beta_i = \frac{-\mathrm{Re}\left[(\mathbf{A}\mathbf{C}^{-2}\mathbf{r}_{i+1}^*)^H \mathbf{C}^{-2}\mathbf{A}\mathbf{p}_i\right]}{\mathrm{Re}\left[(\mathbf{A}\mathbf{p}_i)^H \mathbf{C}^{-2}\mathbf{A}\mathbf{p}_i\right]}$$

$$\mathbf{p}_{i+1} = \mathbf{C}^{-2}\mathbf{r}_{i+1}^* + \beta_i \mathbf{p}_i \,.$$

We have entertained this long discourse on conjugate direction methods because many authors avoid the issues of dealing with complex indefinite matrices, and the ones who do try to deal with such systems in theory seem to never have dealt with such systems in practice. *Jacobs* (1986) derived a modification of the conjugate gradient method for general complex matrices that he called the 'complex biconjugate gradient method.' Although he was able to show that the algorithm terminated in at most $n$ steps ($n$ being the dimension of the matrix), he also stated that "... the monotonic decay of the residual measure [similar to the functional $\Phi$ as defined earlier] cannot be proved." Part of the appeal of the original conjugate gradient algorithm was that at each iteration, the functional $\mathbf{r}^T \mathbf{A}^{-1}\mathbf{r}$ was minimized over the entire subspace if $\mathbf{A}$ was positive-definite. It was this

property that oftentimes led to a rapid convergence to an acceptable error level after only a small number of iterations. Furthermore, since the residual is really the only measure of the error available to us, and hence the only way to ascertain the validity of the iterate $\mathbf{x}_k$, this minimization property is especially important when trying to decide when the error has been reduced enough to stop the relaxation procedure. Since the 3D electromagnetic equations are complex, but not hermitian symmetric nor necessarily positive-definite, the original form of the conjugate gradient algorithm cannot be used. *Jacobs'* (1986) complex biconjugate gradient algorithm could be used to solve the system, but unfortunately, the important minimization property does not hold. Therefore, since the 3D electromagnetic system is symmetric (or can be made to be hermitian symmetric by the Lanczos method), some form of the minimum residual algorithm is probably best suited for relaxing the electromagnetic system of equations. Recall that for the minimum residual algorithm, **A** was not required to be positive-definite. Again, the appeal of this algorithm was the fact that $\mathbf{r}^T\mathbf{r}$ was minimized at <u>each</u> iteration, leading one to perhaps expect reasonable answers after only a modest number of iterations as compared to the dimension of the matrix.

Before we get into the specifics of the relaxation algorithms developed for the 3D magnetotelluric problem, let us first return to the issue of preconditioners. We have explored the behavior of relaxation solutions to the 3D magnetotelluric problem using two different preconditioners. One preconditioner is the matrix $\mathbf{M} = \text{diag}(|a_{11}|, |a_{22}|, ..., |a_{nn}|)$, where $|\cdot|$ stands for absolute value. A better preconditioner might be one that is more closely related to the actual matrix to be inverted. The second order system of equations in **H** can be written as

$$\mathbf{A} = \begin{bmatrix} \mathbf{M}_{xx} & \mathbf{N}_{xy} & \mathbf{N}_{xz} \\ \mathbf{N}_{yx} & \mathbf{M}_{yy} & \mathbf{N}_{yz} \\ \mathbf{N}_{zx} & \mathbf{N}_{zy} & \mathbf{M}_{zz} \end{bmatrix}, \tag{2-30}$$

where the block diagonal matrices **M** are the same as the 2D operators for the TM mode in each direction. For example, $\mathbf{M}_{xx}$ describes the TM equations in the y-z plane for which $H_x$ is parallel to the strike direction, and the electric fields are perpendicular to the strike direction, in this case, the x-direction. These 2D operators can be inverted quickly and cheaply (*Swift,* 1967), so that it is feasible to use the operator

$$\mathbf{M}^{-1} = \begin{bmatrix} \mathbf{M}_{xx}^{-1} & 0 & 0 \\ 0 & \mathbf{M}_{yy}^{-1} & 0 \\ 0 & 0 & \mathbf{M}_{zz}^{-1} \end{bmatrix} \tag{2-31}$$

as a preconditioner. This preconditioner is complex and symmetric, but not hermitian. We have not explored any other preconditioners, although it is conceivable that a different decomposition of the matrix **A** might give better results than have been obtained with these two preconditoners.

Our first attempt at relaxing the 3D system of equations was based on using the preconditioner given in equation 2-31, and a good deal of naivety about what we were doing. We realized that since the matrix **A** for the 3D electromagnetic equations was not positive-definite, we could not use the original form of the conjugate gradient algorithm. And because the matrix was not hermitian symmetric, we knew we could not use the complex form of the minimum residual algorithm. Since the matrix and the preconditioner given in equation 2-31 were symmetric however, we thought we could use the preconditioned form of the minimum residual algorithm for real matrices. This algorithm, which is designated as the MINRTRACC algorithm (minimum $\mathbf{r}^T\mathbf{r}$ accelerated algorithm), is the preconditioned form of the algorithm which minimizes $\mathbf{r}^T\mathbf{r}$ at each iteration (actually it minimizes $\mathbf{r}^T\mathbf{M}^{-1}\mathbf{r}$, where $\mathbf{M}^{-1}$ is the preconditioner given above). However, this is not a strictly valid procedure because even though both the operator and preconditioner are symmetric, they are also complex and therefore the local minimization property is not absolutely valid. Minimizing $\mathbf{r}^T\mathbf{r}$ is not equivalent to minimizing $\mathbf{r}^H\mathbf{r}$ when dealing with

complex operators except that the solution is obtained when $\mathbf{r} = 0$. The functional $\mathbf{r}^T\mathbf{r}$ is still a 'measure' of the error in the solution, although it is not the true measure of the magnitude of the error, which is $\mathbf{r}^H\mathbf{r}$. However, this algorithm allowed us to use the preconditioner in its complex form, rather than having to use, say, the real part of the preconditioner. The MINRTRACC algorithm has been used widely by some people in the industry (Arnie Orange and Richard Sigal have been our biggest users) and seems to be the most robust relaxation algorithm we have developed. We have experimented with different preconditioners and different versions of the algorithms, but have not been completely satisfied with any of these modifications. What does show considerable promise, though, is a multiple scaling technique based on the unaccelerated form of the minimum residual algorithm, and this will be discussed shortly. We will also show results from another relaxation algorithm that is called the MINRTR (minimum $\mathbf{r}^T\mathbf{r}$ algorithm), which is basically the same algorithm as the MINRTRACC, except the preconditioner is that given by the absolute value of the complex diagonal components of the matrix **A**. We originally believed that the accelerated form of the algorithm would be superior to the unaccelerated form because it seemed to reduce the residual error measure much more quickly than the unaccelerated form of the algorithm. While this is indeed true, what has recently become apparent is that the solutions obtained from the MINRTRACC algorithm may not necessarily be superior to those obtained by the MINRTR algorithm. This will be discussed in more detail in the 'model responses' section.

The main problem with all these relaxation methods, besides those associated with the eigenvalue spread or distribution, is that one never really knows when to stop iterating the procedure. Hopefully, one would want to be able to stop after some modest number of iterations, especially if the system of equations is quite large. In addition, one would want the confidence that the answer obtained was fairly reasonable and close to the true answer. Unfortunately, there are no hard and fast rules that govern the number of iterations required to obtain reasonable answers. One must use care, good judgement, and experience to

determine when an accurate solution has been reached. There are, however, some common-sense 'rules of thumb' one can use. For example, the final error should be several orders of magnitude less than the starting error and should not be changing during the last several iterations. One could also look at the surface field values, or apparent resistivities and phases, to make sure that they are not changing during the last several iterations. Unfortunately, this does not necessarily guarantee that the results at such a point are reasonably accurate. Probably the most helpful suggestion, however, is to obtain some experience relaxing simple 3D models where one has a good idea of what to expect, or where one can compare the relaxation results to exact numerical calculations.

There is one last problem associated with these relaxation methods that is especially exacerbated with the preconditioner given in equation 2-31: the **H** field values in the air hardly get changed from their initial values. The problem is that eigenvectors associated with small eigenvalues are poorly represented in the initial residual $\mathbf{r}_0$. Since the residuals and search directions $\mathbf{r}_i$ and $\mathbf{p}_i$ both lie in the space $\mathbf{S}_{i+1}=\{\mathbf{r}_0, \mathbf{A}\mathbf{r}_0, \ldots \mathbf{A}^i\mathbf{r}_0\}$, the contributions from small eigenvalue eigenvectors are quickly lost in the roundoff errors. For the 3D MT problem, a small eigenvalue eigenvector is associated with the residuals in the air layers. Because of its uniform conductivity, there is little contribution to the initial residual from the air, and consequently, **H** does not get changed from its starting value in the air. Nevertheless, we have found that in many cases, the computed impedances are still fairly accurate. This must be due to the fact that the **E** fields are still fairly well determined because they involve differences of the **H** fields, and the **H** field in general is smoother and more regionally uniform than the **E** field.

One possible way to counteract the somewhat inaccurate **H** field determinations is to implement the Biot-Savart Law after several iterations. If the algorithm was then restarted with the updated **H** field values, much improved accuracy could be achieved. The Biot-Savart Law is given by (*Stratton,* 1941)

$$\mathbf{H}(x',y',z') = \frac{1}{4\pi}\int_v \mathbf{J} \times \nabla(\frac{1}{r})\, dV - \frac{1}{4\pi}\int_s (\mathbf{n} \times \mathbf{H}) \times \nabla(\frac{1}{r})\, dS - \frac{1}{4\pi}\int_s (\mathbf{n} \cdot \mathbf{H})\, \nabla(\frac{1}{r})\, dS \tag{2-32}$$

These integrals can be computed numerically given the boundary **H** values and the current density **J** within the Earth. The problem with this implementation is that it can be fairly time-consuming since it is a full matrix operation.

Another possible way to counteract the problem is to use a multiple scaling approach to get a better representation of the **H** field distribution. Multiple scaling, which is closely aligned to renormalization group theory approaches to critical phenomena, has been successfully applied to modeling the effects of crack interactions on the brittle failure of rocks, as described in *Madden* (1976, 1983) and *Lockner* (1990). The basic idea behind multiple scaling is that oftentimes the modeling of a heterogeneous system is not numerically tractable unless the problem is broken into a series of smaller problems. Specifically, the system under consideration is broken down into small subsections, whose properties are then numerically computed. Several of these subsections are then 'averaged' together and treated as part of a larger-scale subsection. The properties of this larger-scale subsection are determined, and the process is repeated up through several scales until one has determined the average properties of the largest-scale system. In this manner, one can numerically model large, complex, hetergeneous systems.

Multiple scaling has also been tried in 3D magnetotelluric modeling (*Ranganayaki,* 1978; *Park,* 1983), although the results, except in special cases, have been mostly negative. The motivation for multiple scaling in magnetotelluric modeling is that the local fields are influenced by regional features, so that to properly model local features, a large model must be constructed that accounts for the regional features. Unfortunately, this leads to very large systems of equations to be solved. If instead one solves a cruder 3D model that contains the 'essence' of the actual 3D model, one could perhaps use the values from the crude model as the regional field for the actual 3D model. Figure 2-2 is a

Simplified Multiple Scaling Geometry

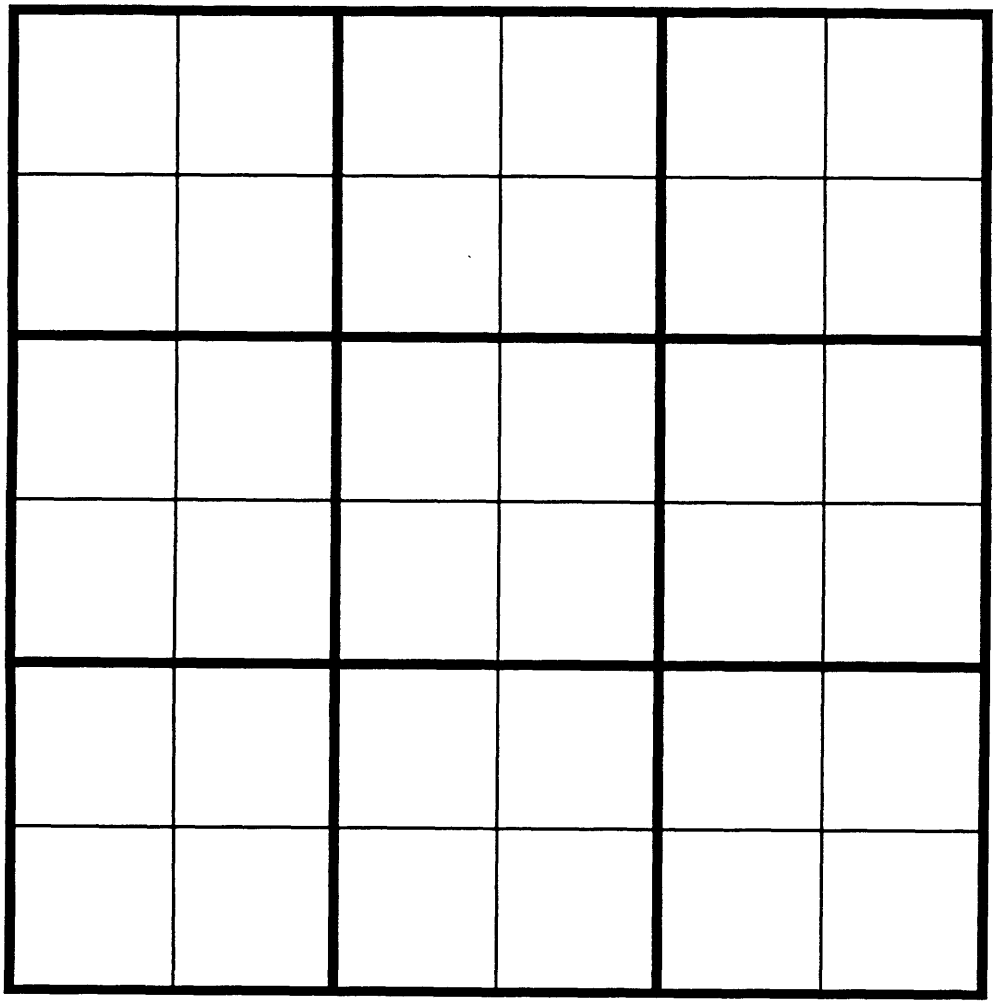

**Figure 2-2.** A simplified version of the multiple scaling geometry. The large scale model, which is six blocks by six blocks, is condensed into a smaller scale model (outlined by the bold lines) which is three blocks by three blocks. The resistivities of the larger scale blocks are averaged to give the resistivity of the block at the smaller scale.

simplified version of the multiple scaling geometry. The original model is six blocks by six blocks. These blocks are averaged to form a cruder model which is three blocks by three blocks (outlined by the bold lines) and which contains the average properties of the full-scale model. To avoid confusion, we will call the cruder 3D model the regional model, or small scale model (because it has a small number of model parameters), and the actual 3D model the full-scale model, or large scale model (since it has a large number of model parameters). *Park* and *Ranganayaki's* multiple scaling approach is a two scale method where the fields at the smaller regional scale are solved for, then interpolated onto the more detailed larger scale model. At the larger scale, only the fields inside the local 3D heterogeneity are solved for. All other fields are assumed to be equal to the interpolated values from the regional model.

Our multiple scale approach differs somewhat from these previous approaches in that we attempt to use multiple scales to improve the relaxation solution at the larger scales. Unlike *Park* and *Ranganayaki*, we use the interpolated field values only as starting values for the relaxation procedure at the next scale. Such an approach was originally suggested by *Southwell* (1946) for relaxing Laplace's equation. If these starting values are more 'correct' than the 2D TM mode starting values used earlier, it is hoped that a more accurate relaxation solution would be obtained. Our method goes as follows. First, the 3D model is scaled down horizontally to a model that is eight blocks by eight blocks (the number of vertical layers does not change). This model is solved exactly using the direct solution method outlined in the next section. The field values from this calculation are interpolated onto the next scale, which is 16 blocks by 16 blocks. These interpolated values serve as the starting point for the MINRTR relaxation procedure. It is hoped that these starting values are more representative of the regional features of the model, especially the **H** field values in the air, and that the relaxation will produce better results. At this scale, the MINRTR procedure is iterated some number of times to meet either a preset level of error reduction, or some maximum number of relaxation steps. The field values from this calculation are

then interpolated onto the next scale model, and the process is repeated. This is continued until we have reached the final scale, or the original 3D model to be solved. The results from this type of procedure are especially encouraging and will be shown in the upcoming model responses section.

The averaging of the model blocks must be done in such a way as to most accurately represent the true features of the original model at the smaller condensed scale. At the smaller scale, the resistivity in the x-direction is defined to be the geometric mean of the series and parallel average in the x-direction of the resistivities of those blocks at the larger scale which are to be condensed into that particular block at the smaller scale. Likewise, the resistivity in the y-direction is the geometric mean of the series and parallel average in the y-direction of the resistivities. Taking the geometric mean of the series and parallel averages is somewhat of a compromise, but is probably the best solution to handle the most general situations. And finally, the resistivity in the z-direction is simply taken to be the parallel average in the z-direction of the conductivities.

### *Direct solution: impedance matrix formulation*

Because of the difficulties associated with relaxation solutions, it is worthwhile to seek an alternate solution method, one that in principle would give an exact solution to the system of equations. Sparse matrix inversion routines do exist that take advantage of the structure and sparsity of the matrix. If, however, one examines the problem in terms of neighboring layer interactions, one can achieve perhaps the same efficiency as the sparse matrix methods without losing the insight of looking at the system as an EM system. An example of such an approach is the Greenfield Algorithm (*Greenfield,* 1965; *Swift,* 1967). This algorithm solves networks for unknown nodal voltages given a current source distribution. The algorithm analyzes one row or column of the network at a time. Instead of doing one large matrix inversion, it obtains its efficiency by computing several smaller matrix inversions, thus greatly decreasing the computation time. The algorithm is

essentially an algorithm for inverting block tridiagonal matrices (*Golub and Van Loan,* 1983).

Let's look at the 3D magnetotelluric problem in somewhat more detail. If $E_z$ and $H_z$ are eliminated from the discretized system of equations given earlier, then the horizontal **E** or **H** fields in one layer can be expressed in terms of the fields in that layer and one layer below that layer. For example, since by equation 2-8, $H_z$ is given by

$$H_z(i,j,k) = \frac{1}{i\omega L \langle \mu_{zz} \rangle}[E_y(i,j,k) - E_y(i-1,j,k) - E_x(i,j,k) + E_x(i,j-1,k)] , \qquad (2\text{-}33)$$

then $H_x$, by virtue of equations 2-6 and 2-7, can be written as

$$\begin{aligned} H_x(i,j,k) = {} & H_x(i,j,k+1) \\ & - \frac{1}{i\omega L \langle \mu_{zz}(i+1,j,k) \rangle}[E_y(i+1,j,k) - E_y(i,j,k) - E_x(i+1,j,k) + E_x(i+1,j-1,k)] \\ & + \frac{1}{i\omega L \langle \mu_{zz}(i,j,k) \rangle}[E_y(i,j,k) - E_y(i-1,j,k) - E_x(i,j,k) + E_x(i,j-1,k)] \\ & - \frac{2L}{[\rho_{yy}(i,j,k) + \rho_{yy}(i,j-1,k)]} E_y(i,j,k) , \end{aligned} \qquad (2\text{-}34)$$

where the *k+1* layer is beneath the $k^{th}$ layer. Similar equations can also be written for $H_y$, $E_x$, and $E_y$. These equations can be expressed in a much more compact form as

$$\mathbf{E_k} = \mathbf{A_k H_{k+1}} + \mathbf{E_{k+1}} + \mathbf{a_k} \qquad (2\text{-}35)$$

$$\mathbf{H_k} = \mathbf{B_k E_k} + \mathbf{H_{k+1}} \cdot \qquad (2\text{-}36)$$

Here, the matrices **A** and **B** are the coefficient matrices that arise from the elimination of $E_z$ and $H_z$ from the difference equations (for example the coefficients contained in the equation above for $H_x$), the vector **a** is the vector that contains the contributions from the boundary tangential **H** fields, and **E** and **H** are the vectors of the horizontal electric and magnetic fields respectively.

At the bottom of the 3D model, which has *n* layers, we assume that **E** is related to **H** by the 1D plane-wave impedance. This **E** is continued up to the *n-1* layer assuming that $E_z$=0. Consequently, no boundary **H** terms are involved with this initial step. Likewise, **H** is continued up to the *n-1* layer using equation 2-36. For the first propagation step, this gives the following equations:

$$\mathbf{E}_{n-1} = \mathbf{A}_{n-1}\mathbf{H}_n \tag{2-37}$$

$$\mathbf{H}_{n-1} = \mathbf{B}_{n-1}\mathbf{E}_{n-1} + \mathbf{H}_n \,. \tag{2-38}$$

One could compute an impedance matrix for the bottom layer that does not assume an infinite wavelength by using a Fourier Series approach. This, however, is very time-consuming and also includes an implicit repetition assumption that would be somewhat inconsistent with the rest of the model, which does not assume repetition.

We can express **E** for the bottom layer in terms of **H** for that layer only. Solving equation 2-38 for $\mathbf{H}_n$, and substituting this into equation 2-37 yields

$$\mathbf{E}_{n-1} = \mathbf{A}_{n-1}[\mathbf{H}_{n-1} - \mathbf{B}_{n-1}\mathbf{E}_{n-1}] \,. \tag{2-39}$$

Solving for $\mathbf{E}_{n-1}$ we arrive at:

$$\mathbf{E}_{n-1} = \mathbf{Z}_{n-1}\mathbf{H}_{n-1} \,, \tag{2-40}$$

where

$$\mathbf{Z}_{n-1} = [\mathbf{I} + \mathbf{A}_{n-1}\mathbf{B}_{n-1}]^{-1}\,\mathbf{A}_{n-1} \,. \tag{2-41}$$

A similar analysis is carried out for all of the other Earth layers, except that one has to keep track of the boundary terms. For each layer, the **E** fields are continued up from the previous layer using equation 2-35 and the **H** fields are continued up using equation 2-36. For example, for the *n-2* layer, which is the next higher layer, we would have:

$$\mathbf{E}_{n-2} = \mathbf{A}_{n-2}\mathbf{H}_{n-1} + \mathbf{E}_{n-1} + \mathbf{a}_{n-2} \tag{2-42}$$

$$\mathbf{H}_{n-2} = \mathbf{B}_{n-2}\mathbf{E}_{n-2} + \mathbf{H}_{n-1}. \tag{2-43}$$

The expression for $\mathbf{E}_{n-1}$ given in equation 2-40 is substituted into equation 2-42 giving:

$$\mathbf{E}_{n-2} = [\,\mathbf{A}_{n-2} + \mathbf{Z}_{n-1}\,]\,\mathbf{H}_{n-1} + \mathbf{a}_{n-2}. \tag{2-44}$$

Equation 2-43 is then solved for $\mathbf{H}_{n-1}$, and this is substituted into equation 2-44 giving us an equation with the unkowns $\mathbf{E}_{n-2}$ and $\mathbf{H}_{n-2}$. This can then be rearranged to give:

$$\mathbf{E}_{n-2} = \mathbf{Z}_{n-2}\mathbf{H}_{n-2} + \mathbf{z}_{n-2} \tag{2-45}$$

where

$$\mathbf{Z}_{n-2} = [\mathbf{I} + (\mathbf{A}_{n-2} + \mathbf{Z}_{n-1})\mathbf{B}_{n-2}]^{-1} [\mathbf{A}_{n-2} + \mathbf{Z}_{n-1}] \tag{2-46}$$

and

$$\mathbf{z}_{n-2} = [\mathbf{I} + (\mathbf{A}_{n-2} + \mathbf{Z}_{n-1})\mathbf{B}_{n-2}]^{-1} \mathbf{a}_{n-2} \tag{2-47}$$

The vector $\mathbf{z}$ contains the effects of the known boundary values. In this manner, an impedance matrix is computed for each layer in the model that relates the horizontal $\mathbf{E}$ fields to the horizontal $\mathbf{H}$ fields. A simple recursion formula gives the impedance information at each level:

For k = n-2 to ksurf (ksurf is top Earth layer)

$$\mathbf{Z}_k = [\mathbf{I} + (\mathbf{A}_k + \mathbf{Z}_{k+1})\mathbf{B}_k]^{-1} [\mathbf{A}_k + \mathbf{Z}_{k+1}]$$

$$\mathbf{z}_k = [\mathbf{I} + (\mathbf{A}_k + \mathbf{Z}_{k+1})\mathbf{B}_k]^{-1} [\mathbf{a}_k + \mathbf{z}_{k+1}]$$

$$\mathbf{E}_k = \mathbf{Z}_k\mathbf{H}_k + \mathbf{z}_k \, .$$

This recursion formula is stable and well-behaved. For the top Earth layer, the $\mathbf{E}$ fields are continued up to the Earth's surface assuming no $E_z$.

A somewhat similar procedure is used for the air layers. As we will explain shortly, a uniform current sheet at the Earth's surface is the source field for the direct solution. Consequently, there are no boundary $\mathbf{H}$ field terms in the air layers. Starting at the top air layers with a plane-wave impedance and $E_z = 0$, we have the equation:

$$\mathbf{E}_1 = \mathbf{Z}_1\mathbf{H}_1 \, . \tag{2-48}$$

For the next air layer down, we can write:

$$\mathbf{H}_2 = \mathbf{H}_1 - \mathbf{B}_1 \mathbf{E}_1 \qquad (2\text{-}49)$$

$$\mathbf{E}_2 = \mathbf{E}_1 - \mathbf{A}_1 \mathbf{H}_2 . \qquad (2\text{-}50)$$

We substitute the expression for $\mathbf{E}_1$, equation 2-48, into equations 2-49 and 2-50, solve equation 2-49 for $\mathbf{H}_1$ in terms of $\mathbf{H}_2$, then substitute this into equation 2-50 to obtain an equation for $\mathbf{E}_2$ in terms of $\mathbf{H}_2$:

$$\mathbf{E}_2 = \mathbf{Z}_2 \mathbf{H}_2 , \qquad (2\text{-}51)$$

where

$$\mathbf{Z}_2 = \mathbf{Z}_1 [\mathbf{I} - \mathbf{B}_1 \mathbf{Z}_1]^{-1} - \mathbf{A}_1 . \qquad (2\text{-}52)$$

A similar analysis is carried out for each air layer resulting in a simple recurrence formula for the air layers:

For k = 2 to ksurf-1 (ksurf is top Earth layer)

$$\mathbf{Z}_{k+1} = \mathbf{Z}_k [\mathbf{I} - \mathbf{B}_k \mathbf{Z}_k]^{-1} - \mathbf{A}_k .$$

In the air layer directly above the Earth's surface, the **E** field is continued down to the Earth's surface assuming $E_z = 0$, and the **H** field is continued down using equation 2-49 except with the 2 changed to *ksurf* and the 1 changed to *ksurf-1*.

We put a uniform current sheet at the Earth's surface, across which there is a jump in the **H** field. The **E** field is continuous across the current sheet. The tangential **H** field boundary terms in the air layers are zero, so that there are no sources above the Earth's surface. This means that the **H** field in the air is a secondary outgoing field and it is equal to the **H** field due to the Earth conductivity structure minus the uniform field at the Earth's surface. Since it is uniform, the current sheet can be put anywhere above the Earth's surface as long as one allows for the secondary outgoing fields above the current sheet. Therefore, we have at the Earth's surface the following relationships:

$$\mathbf{E}_{air} = \mathbf{Z}_{air}\mathbf{H}_{air}$$

$$\mathbf{E}_{earth} = \mathbf{Z}_e\mathbf{H}_{earth} + \mathbf{z}_e \qquad (2\text{-}53)$$

$$\mathbf{H}_{air} = \mathbf{H}_{earth} - \mathbf{J}_{cs},$$

where $\mathbf{J}_{cs}$ is the constant current sheet at the Earth's surface, $\mathbf{z}_e$ contains the effects of the boundary values, $\mathbf{E}_{air}$ and $\mathbf{H}_{air}$ correspond to the **E** and **H** fields just above the current sheet, and $\mathbf{E}_{earth}$ and $\mathbf{H}_{earth}$ correspond to the **E** and **H** fields just below the current sheet. Since **E** is continuous across the current sheet, we can write:

$$\mathbf{H}_{earth} = [\mathbf{I} - \mathbf{Y}_{air}\mathbf{Z}_e]^{-1}[\mathbf{J}_{cs} + \mathbf{Y}_{air}\mathbf{z}_e]. \qquad (2\text{-}54)$$

Once the **H** fields at the Earth's surface are known, then the **E** fields at the surface can be determined as well as the **E** and **H** fields everywhere in the model. Thus, solving the 3D model has been reduced to solving the EM interactions at each layer in the model rather than solving the EM interactions in the 3D model as a whole at one time. As with the Greenfield Algorithm, the algorithm just described has the advantages of directly solving the 3D MT equations by doing several smaller matrix inversions rather than one large matrix inversion. Since matrix inversions take $O(n^3)$ operations, this is seen as a tremendous time savings.

### *Model Responses*

We compare the computed responses between different modeling algorithms to judge the accuracy and flexibility of the different algorithms. Furthermore, since the relaxation algorithms are approximate solutions, it is necessary to compare them with other exact calculations. The model we have chosen for our comparisons is one proposed by Dr. M.S. Zhdanov of the USSR Academy of Sciences in his effort to compile 2D and 3D model responses by investigators worldwide. We directly compare our computed responses with those computed by *Wannamaker* (1990) for the same model. The *Wannamaker* (1990) responses were computed using the integral equation approach. This approach was originally outlined in *Wannamaker et al.* (1984a) and the recent modifications are described in *Wannamaker* (1990). We will also compare our direct solution results with the relaxation solution results. In this section we are striving merely to compare

responses from different modeling algorithms and we are not intending to explore in detail the 3D responses for complicated geometries. There are several studies that have concentrated on examining 3D field behavior (*Park*, 1985; *Park et al.*, 1983; *Wannamaker et al.*, 1984b)

The model under study consists of two adjacent rectangular blocks residing in a three-layer host (see Figure 2-3). One block is conductive (1 Ω-m) and the adjacent block is resistive (100 Ω-m). The rectangular blocks are imbedded in a layer of 10 Ω-m, and are each 20 km in width, 40 km in length, and 10 km in depth. The first layer is underlain by a second layer of 100 Ω-m and 20 km thickness. This layer is then underlain by a halfspace of resistivity 0.1 Ω-m. The responses were computed for periods of 10, 100, and 1000 seconds. The skin depths in the conductive block are 1.6 km, 5 km, and 16 km respectively, and 16 km, 50 km, and 160 km for the resistive block. We define the strike length to be the length of the conductive and resistive bodies in the y-direction. Therefore, the strike length is 40 km for all calculations except when we compare the 3D results with 2D results, for which case the strike length is increased to 200 km.

### Comparisons between direct solution and Wannamaker's solution

We first compare our direct solution technique, which uses difference equations, and Wannamaker's integral equation method. The model described above was discretized into 28 blocks in the x-direction, 19 blocks in the y-direction, and 11 layers in the z-direction. The model was more finely discretized near the conductivity contrasts (see Figure 2-4). We will show the apparent resistivities and phases for the $Z_{xy}$ and $Z_{yx}$ responses for profiles across the 3D body. The $Z_{xy}$ component of the surface impedance tensor is the $E_x$ field due to an applied $H_y$ field. Similarly, the $Z_{yx}$ component of the surface impedance tensor, is the $E_y$ field due to an applied $H_x$ field.

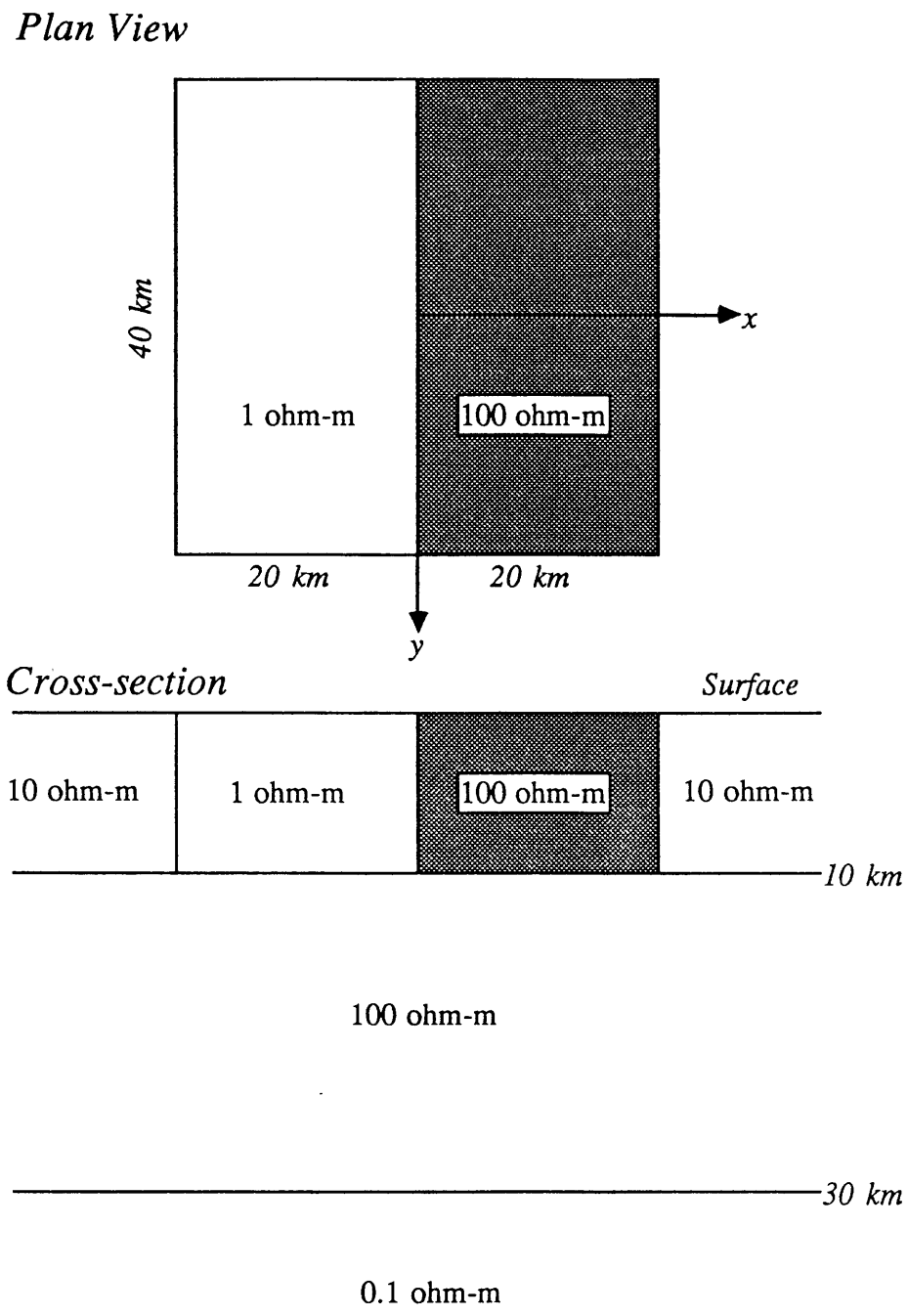


**Figure 2-3.** The 3D model used to make comparisons between our difference equation algorithms and *Wannamaker's* (1990) integral equation algorithm. This model is also used to compare the behavior of the relaxation solutions with the direct solutions.

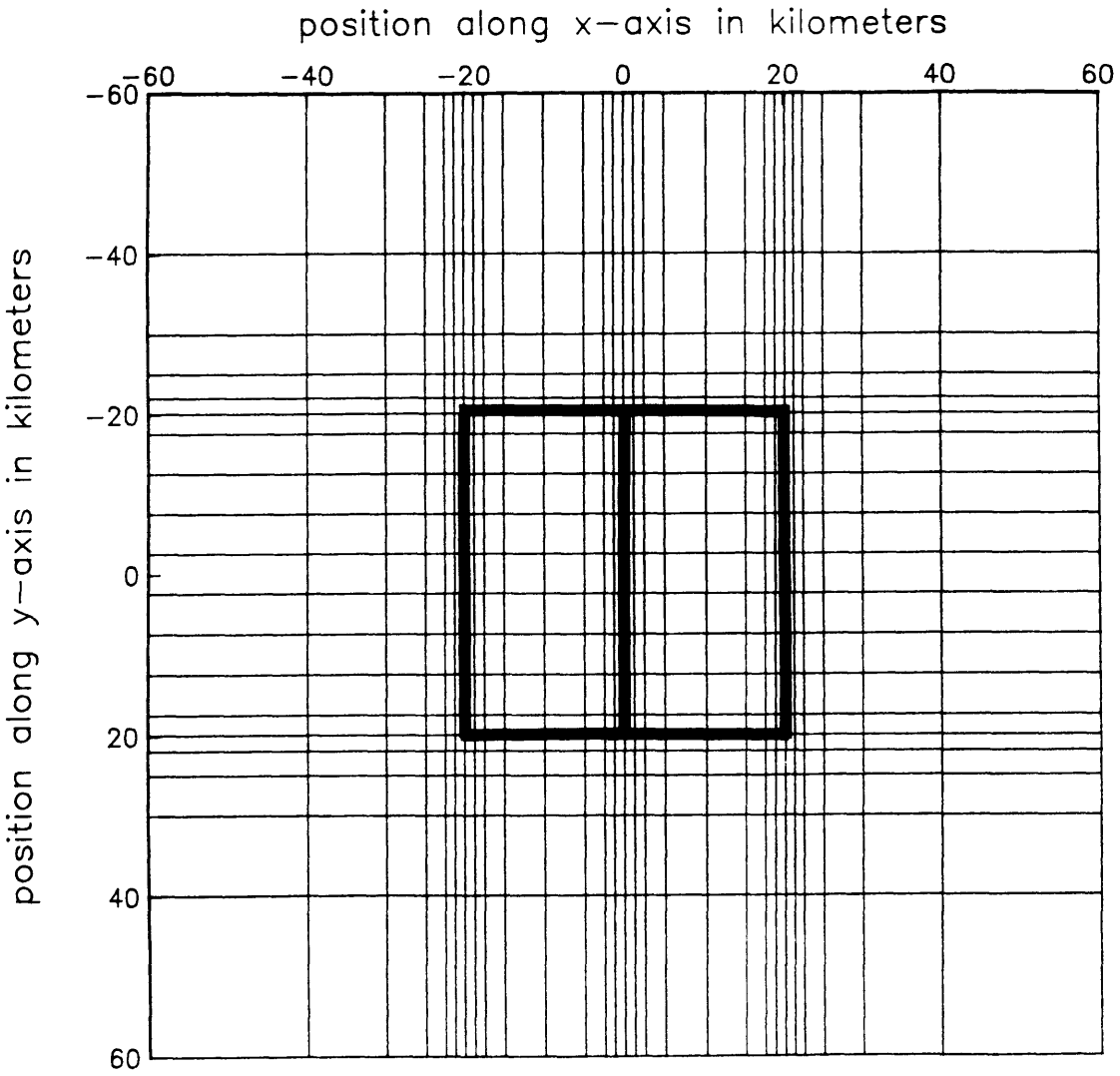


**Figure 2-4**. A plan view of the horizontal discretization used for the model of Figure 2-3. The model has been more finely discretized near the conductivity contrasts to obtain more accurate solutions in these areas.

Shown in Figures 2-5 and 2-6 are the $Z_{xy}$ mode and $Z_{yx}$ mode responses for the model at a 10 second period for a profile across the center of the body (along the x-axis of Figure 2-3). There is generally good agreement between Wannamaker's responses (labelled as *rhoxy.ie, phxy.ie,* etc. where the *.ie* stands for integral equation) and our difference equation responses (labelled *rhoxy.dir, phxy.dir,* etc. where the *.dir* stands for direct difference equation solution as opposed to relaxation solution). There are small discrepencies in the phases over the center of the resistive body and near conductivity contrasts. The phase differences near the boundaries are probably due to the differences in the **E** field geometry between our difference equation approach and Wannamaker's integral equation approach. As mentioned earlier, the **E** fields in our algorithm actually represent averages across block faces, whereas in Wannamaker's algorithm, the **E** fields represent averages for a block and not across block faces. Near conductivity contrasts, the **E** fields are changing rapidly, and the issue is how the **E** field is averaged to obtain a value which is called the field at that particular location. Finer discretization can be used to obtain more accurate results in areas where strong gradients in the **E** field exist. The phase discrepencies over the center of the resistive body may arise because the integral equation algorithm typically has more difficulty computing the fields over resistive bodies as compared to conductive bodies (*Wannamaker* , 1990, pers. comm.). Figures 2-7 and 2-8 show that the difference equation $Z_{xy}$ and $Z_{yx}$ mode responses at this period agree almost exactly with 2D TM and TE mode responses when the strike length of the 3D body is increased from 40 km to 200 km (effectively making the response across the center of the body a 2D response since the ends of the 3D body are many skin depths away from the center).

The $Z_{xy}$ and $Z_{yx}$ mode responses for the model at a 100 second period are shown in Figures 2-9 and 2-10 respectively, and the $Z_{xy}$ and $Z_{yx}$ mode responses at a 1000 second period are shown in Figures 2-11 and 2-12 respectively. There is excellent overall agreement between Wannamaker's integral equation responses and our difference equation

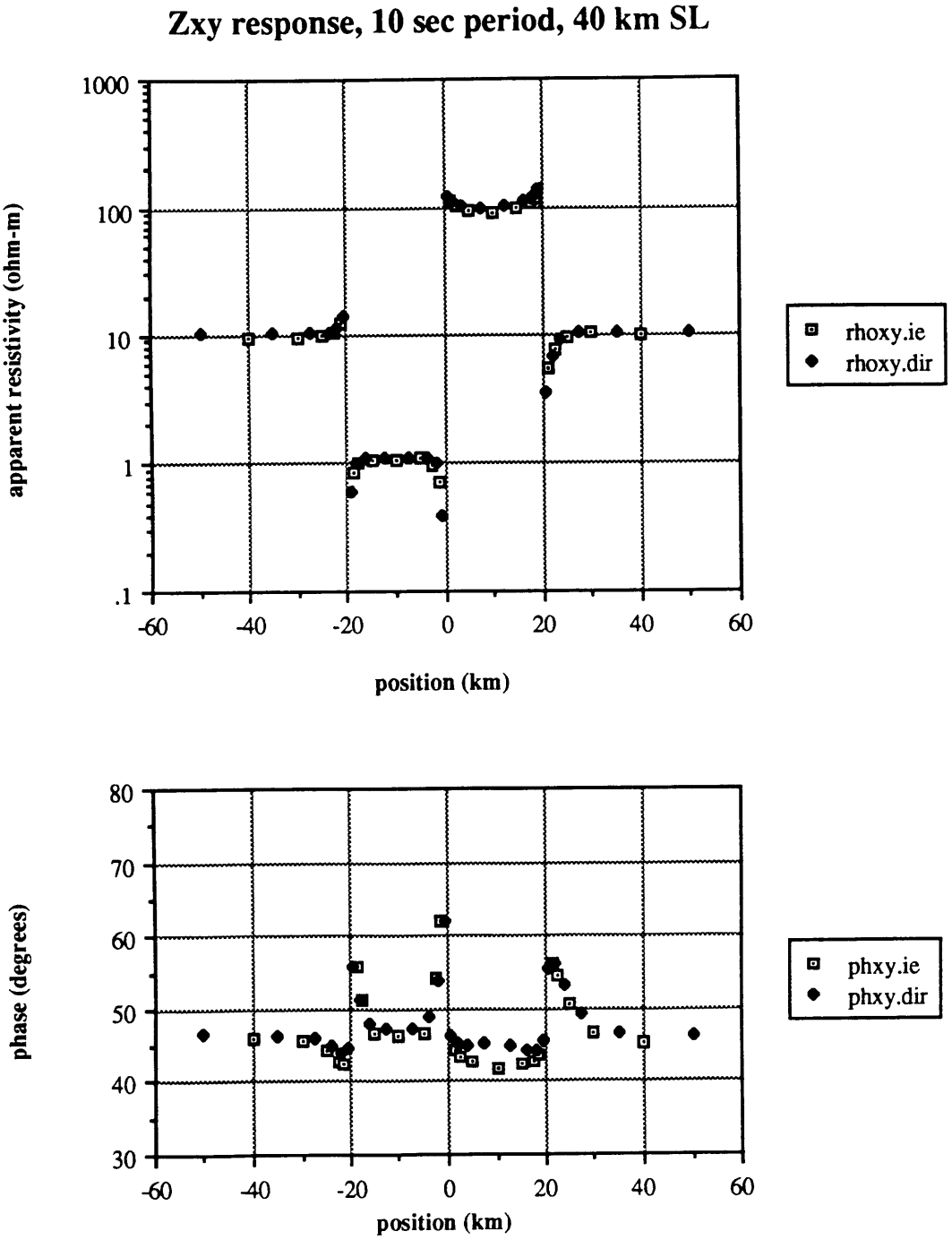


**Figure 2-5**. The $Z_{xy}$ response along a profile across the center of the bodies at a period of 10 seconds, and a strike length of 40 km (this is the width of the bodies in the y-direction). The responses labelled *rhoxy.ie, phxy.ie,* etc are those from *Wannamaker's* (1990) integral equation solution. The responses labelled *rhoxy.dir, phxy.dir,* etc are those from our direct solution of the difference equations.

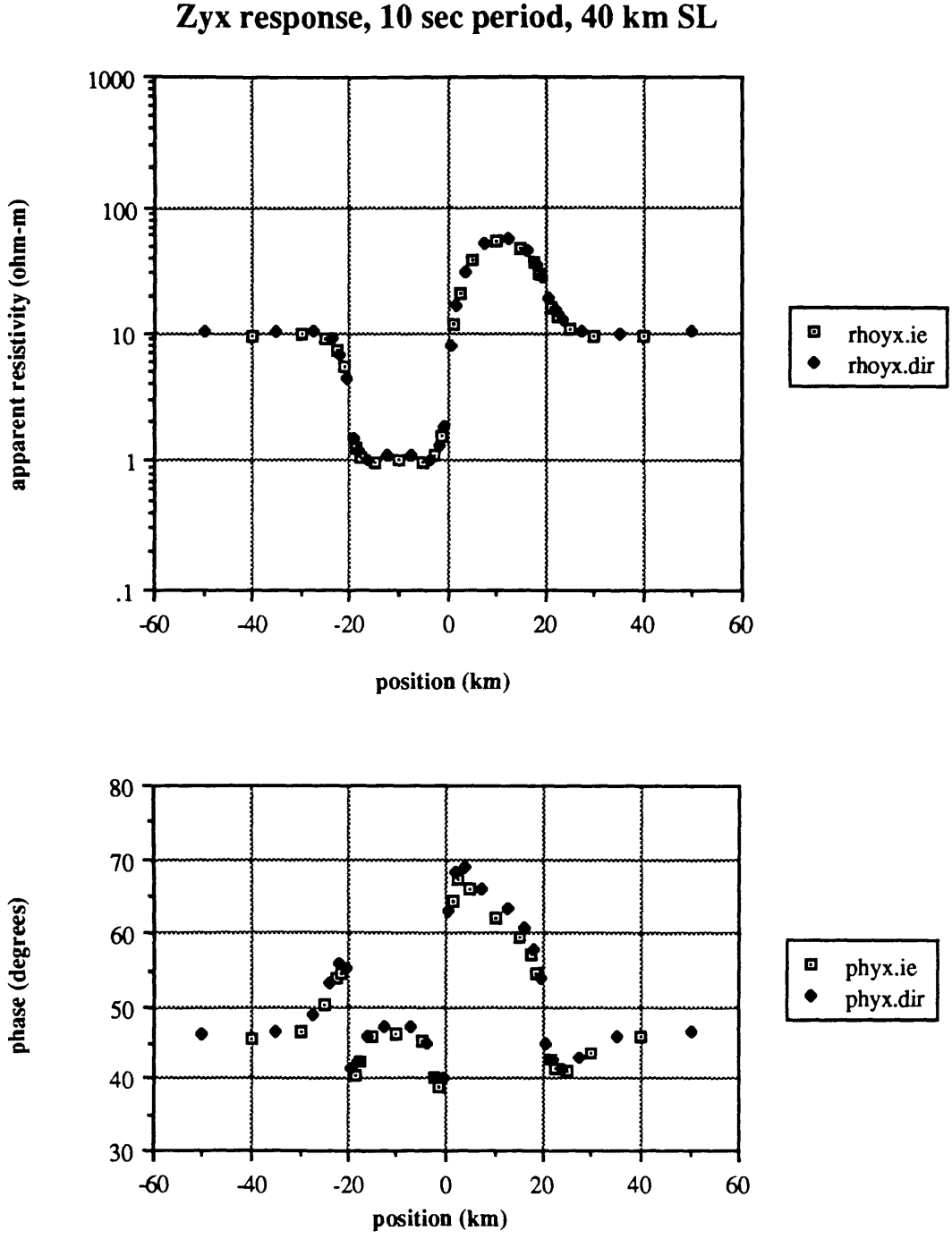


**Figure 2-6.** The $Z_{yx}$ response along a profile across the center of the bodies at a period of 10 seconds and a strike length of 40 km comparing the integral equation solutions with the direct difference equation solutions.

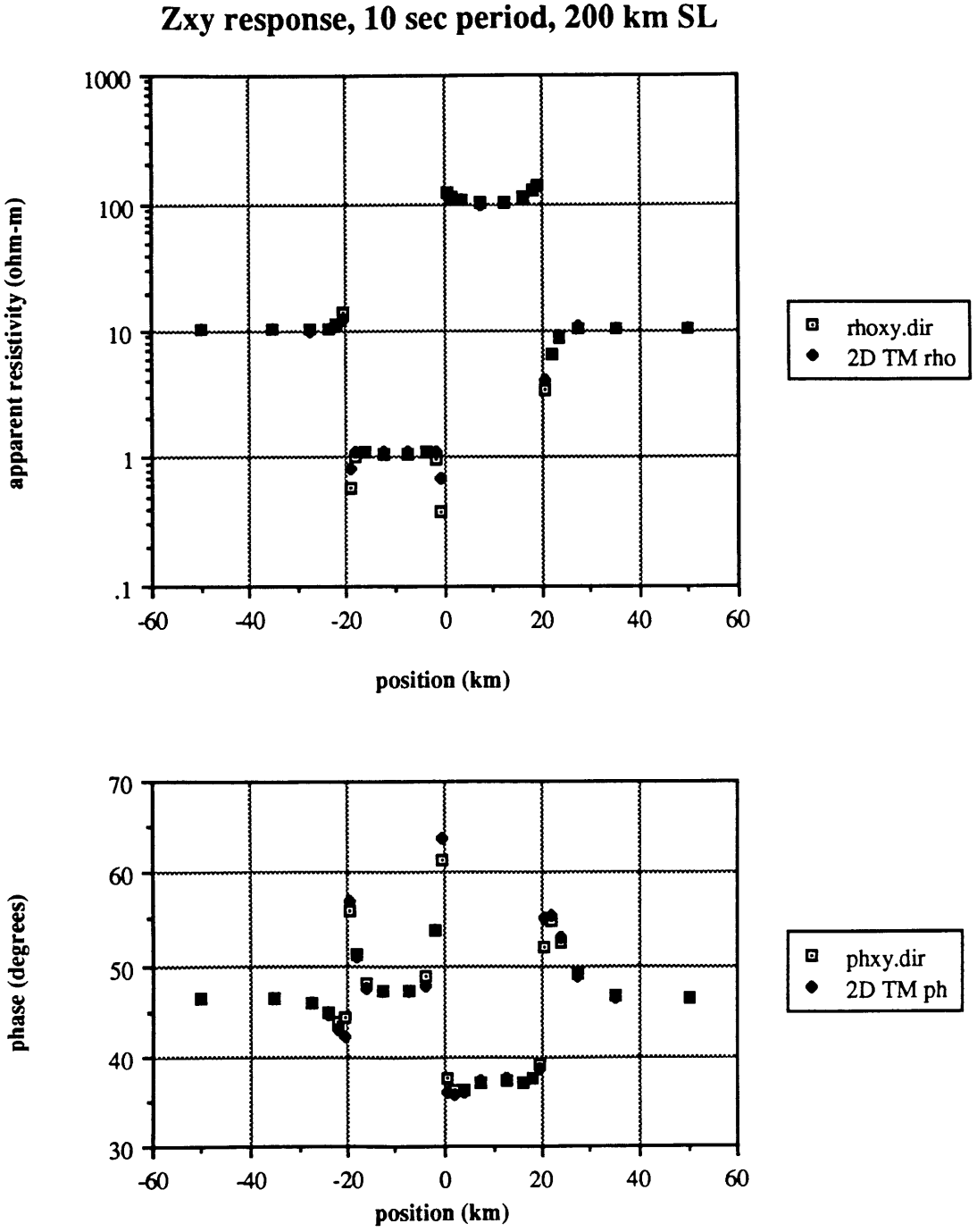


**Figure 2-7.** The $Z_{xy}$ response along a profile across the center of the bodies when the strike length of the bodies is increased to 200 km. The results are for a period of 10 seconds. Here we are comparing the 3D difference equation direct solution results along this profile with the 2D TM results for the profile computed using a 2D finite difference (transmission analog) algorithm.

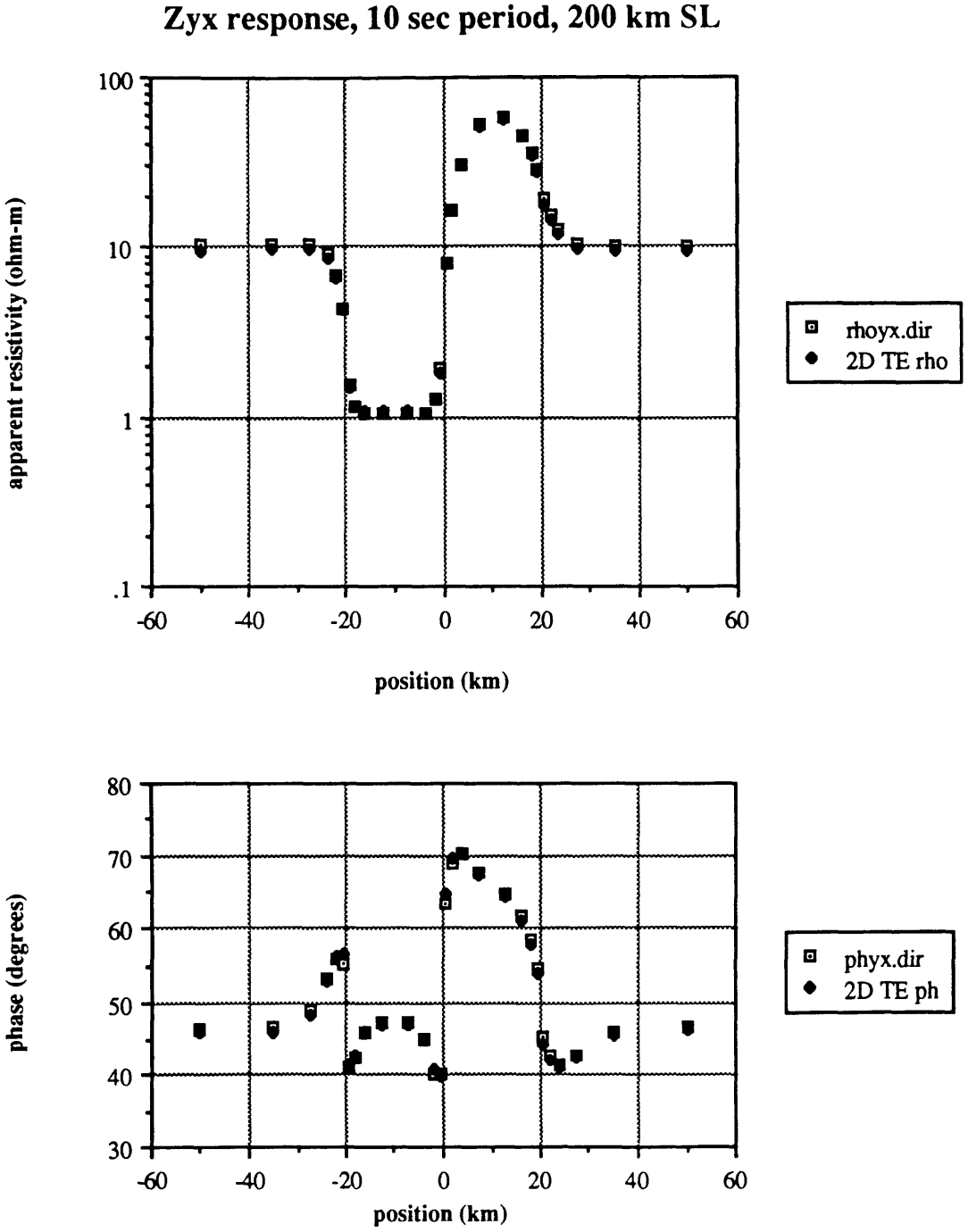


**Figure 2-8.** The $Z_{yx}$ response along a profile across the center of the bodies when the strike length of the bodies is increased to 200 km. The results are for a period of 10 seconds. Here we are comparing the 3D difference equation direct solution results along this profile with the 2D TE results for the profile computed using a 2D finite difference (transmission analog) algorithm.

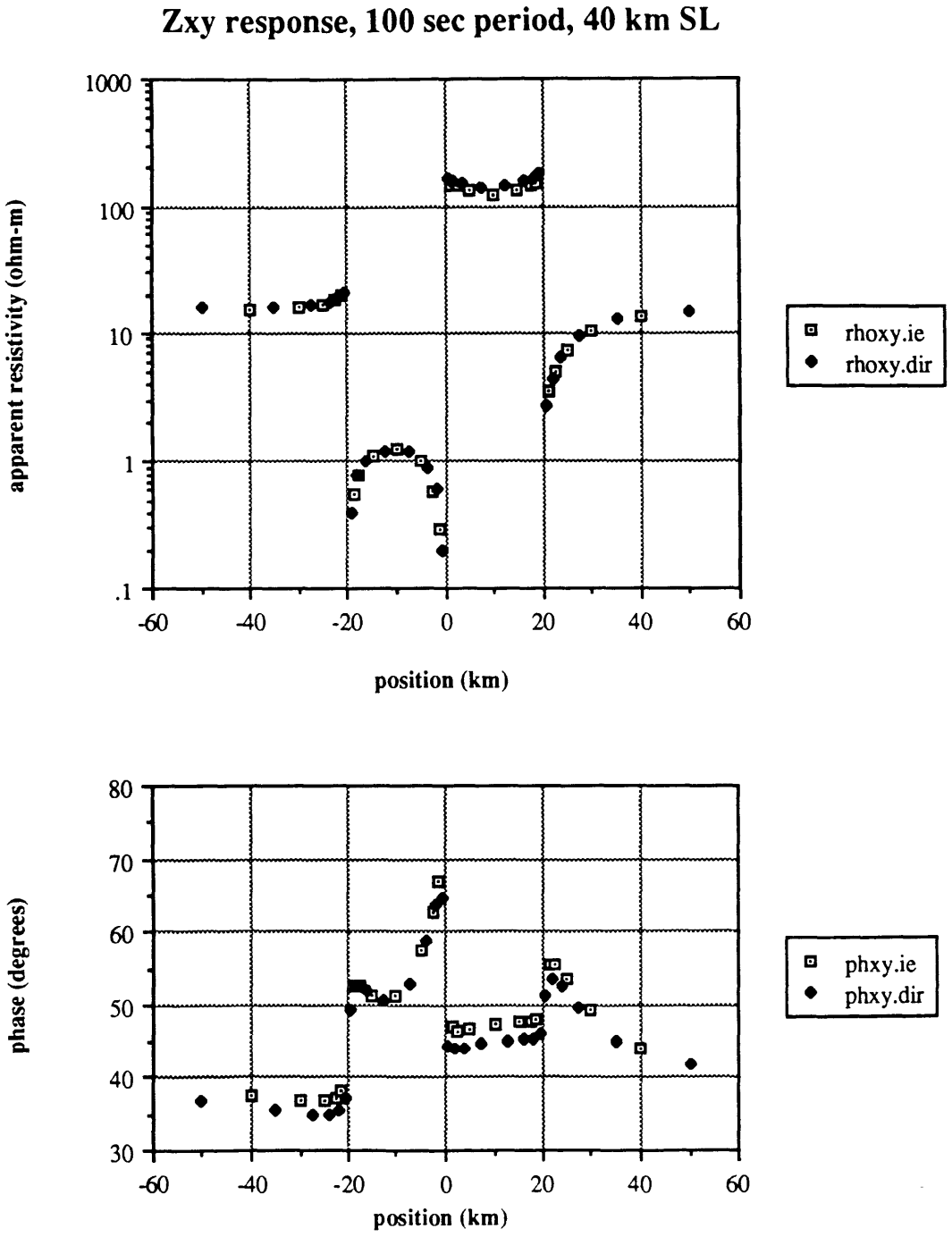


**Figure 2-9**. The $Z_{xy}$ response along a profile across the center of the bodies at a period of 100 seconds comparing the integral equation solutions with the direct difference equation solutions.

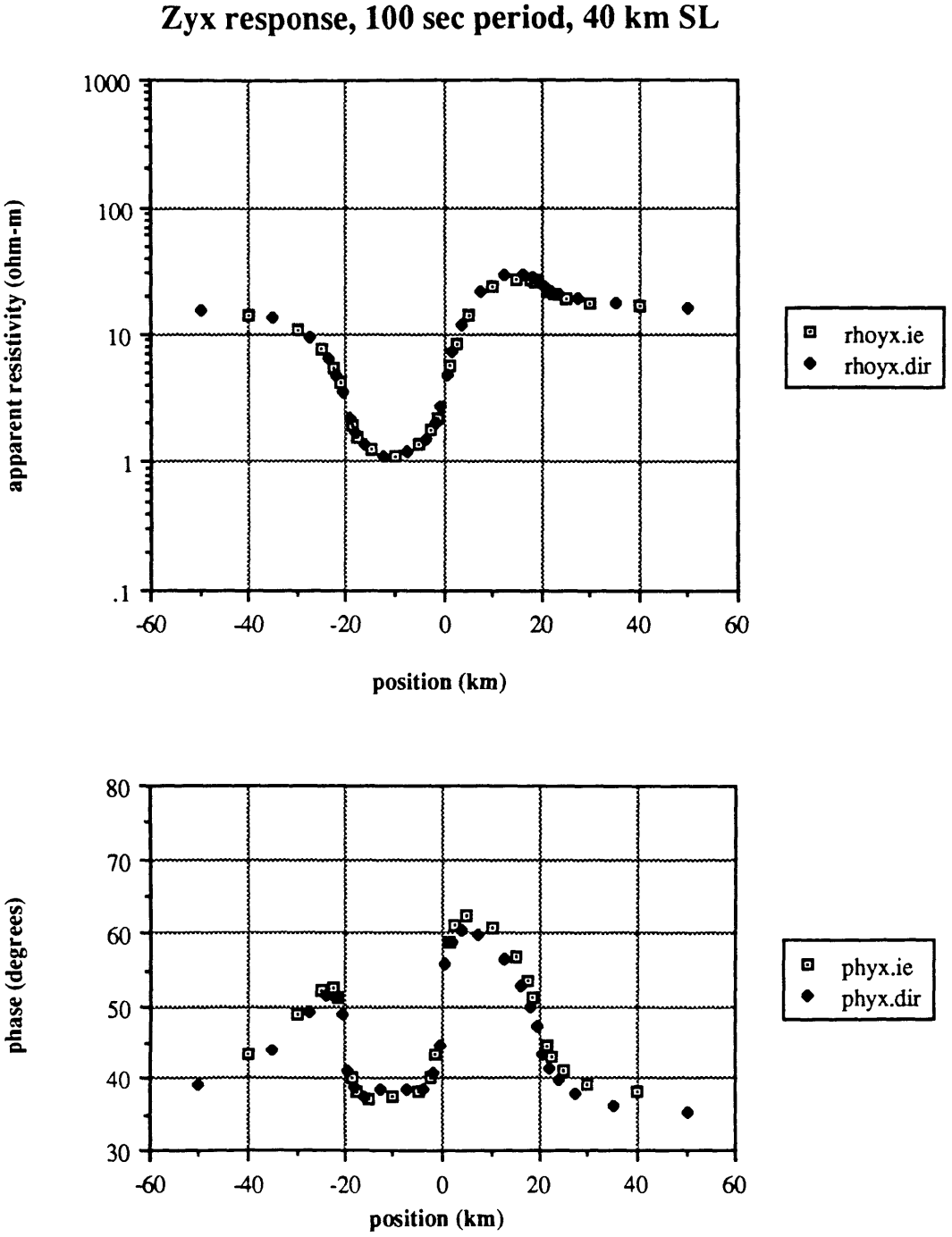


**Figure 2-10**. The $Z_{yx}$ response along a profile across the center of the bodies at a period of 100 seconds comparing the integral equation solutions with the direct difference equation solutions.

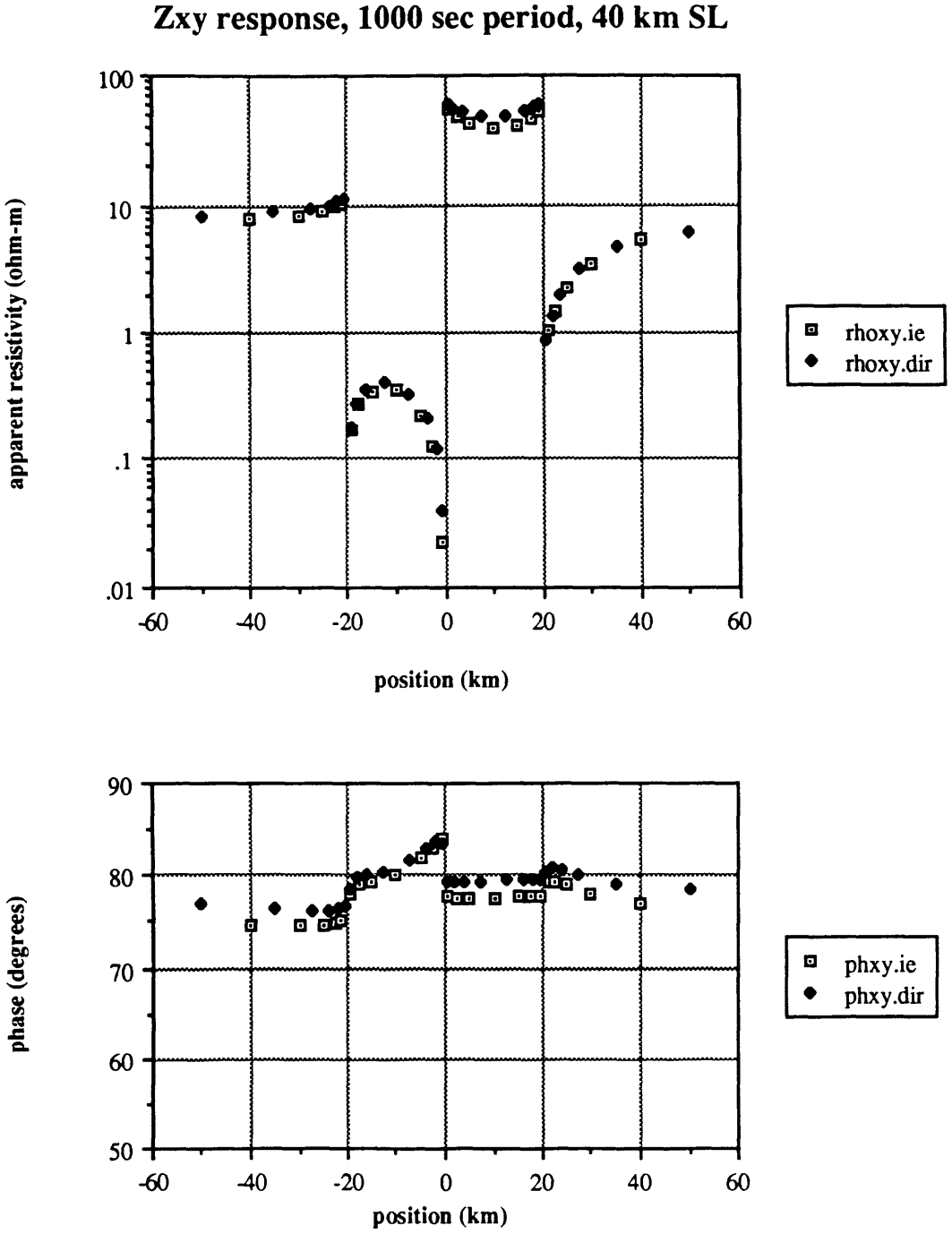


**Figure 2-11.** The $Z_{xy}$ response along a profile across the center of the bodies at a period of 1000 seconds comparing the integral equation solutions with the direct difference equation solutions.

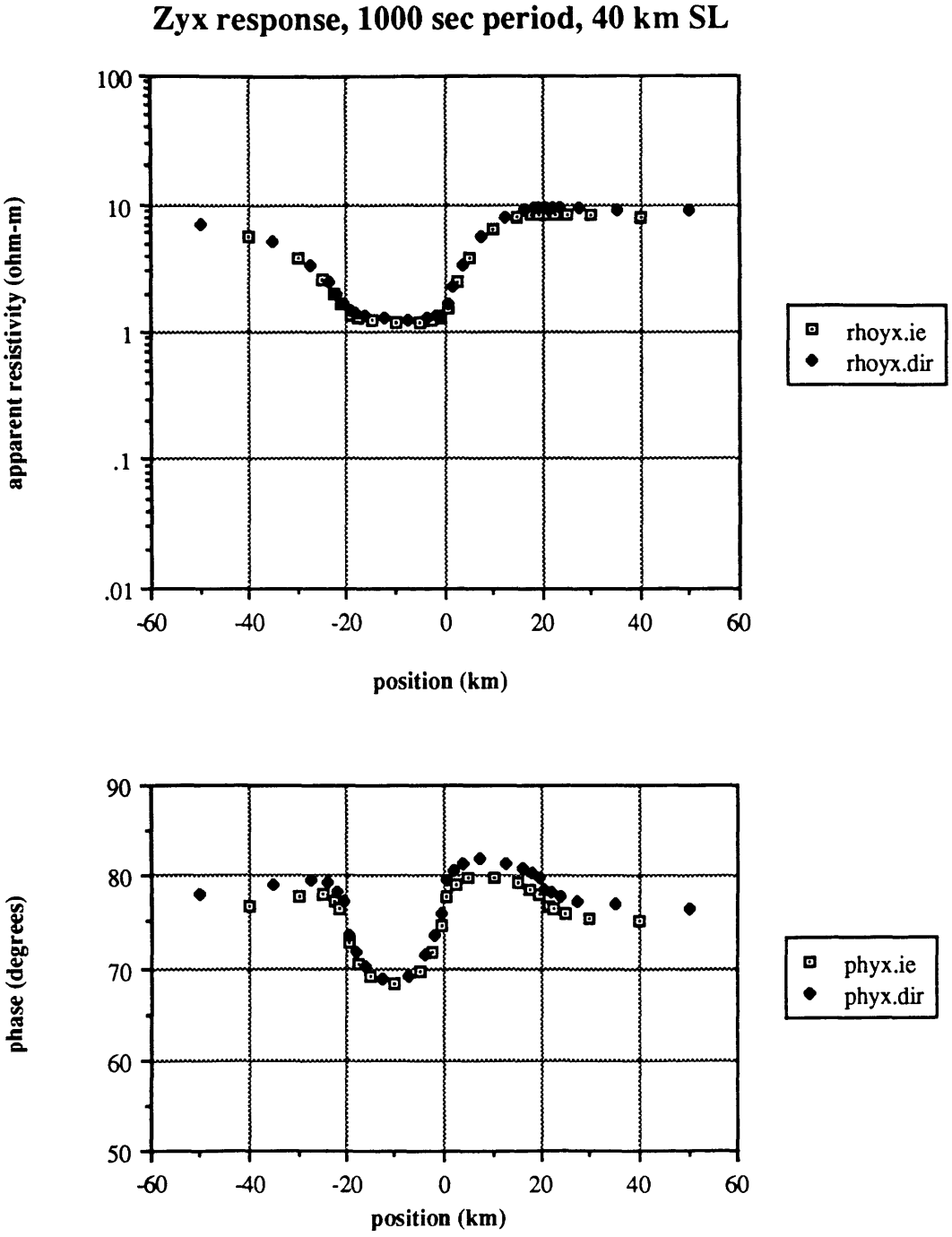


**Figure 2-12.** The $Z_{yx}$ response along a profile across the center of the bodies at a period of 1000 seconds comparing the integral equation solutions with the direct difference equation solutions.

responses, especially in the amplitudes. Discrepencies in phase are usually no more than 1°-2° and occur primarily near conductivity contacts and over the resistive body, as before.

We have made additional comparisons at a period of 10s, but for profiles along the strike direction of the bodies (the *y-direction* as shown in Figure 2-3). Figures 2-13 and 2-14 show the $Z_{xy}$ and $Z_{yx}$ mode responses respectively as a function of position along the y-axis at a strike position of x=-10km (this is down the strike of the conductive body). Likewise, Figures 2-15 and 2-16 show the $Z_{xy}$ and $Z_{yx}$ mode responses respectively as a function of position along the y-axis but at a strike position of x=+10km (this is down the strike of the resistive body). As before, there is excellent overall agreement between the integral equation responses and the difference equation responses. Minor phase differences can be found near conductivity contrasts and over the resistive body, and most likely result for the same reasons as stated earlier.

In conclusion of this section, we have shown that for the simple 3D model of Figure 2-3, there is good overall agreement between Wannamaker's integral equation solution and our difference equation solution. Minor differences in the phases were usually found near conductivity contrasts and over the resistive body. The phase differences near the conductivity contrasts were presumably due to differences in the **E** field geometry between the two solution algorithms. The phase differences over the resistive body most likely resulted from an inherent difficulty in the integral equation algorithm to accurately compute the fields over resistive bodies.

### Relaxation results

Having established the validity and accuracy of our direct solution difference equation algorithm, we will now compare the relaxation solutions to the direct solution both in terms of accuracy and robustness. Again, we will use the model shown in Figure 2-3 for the comparisons, and all comparisons will be for a period of 100 seconds.

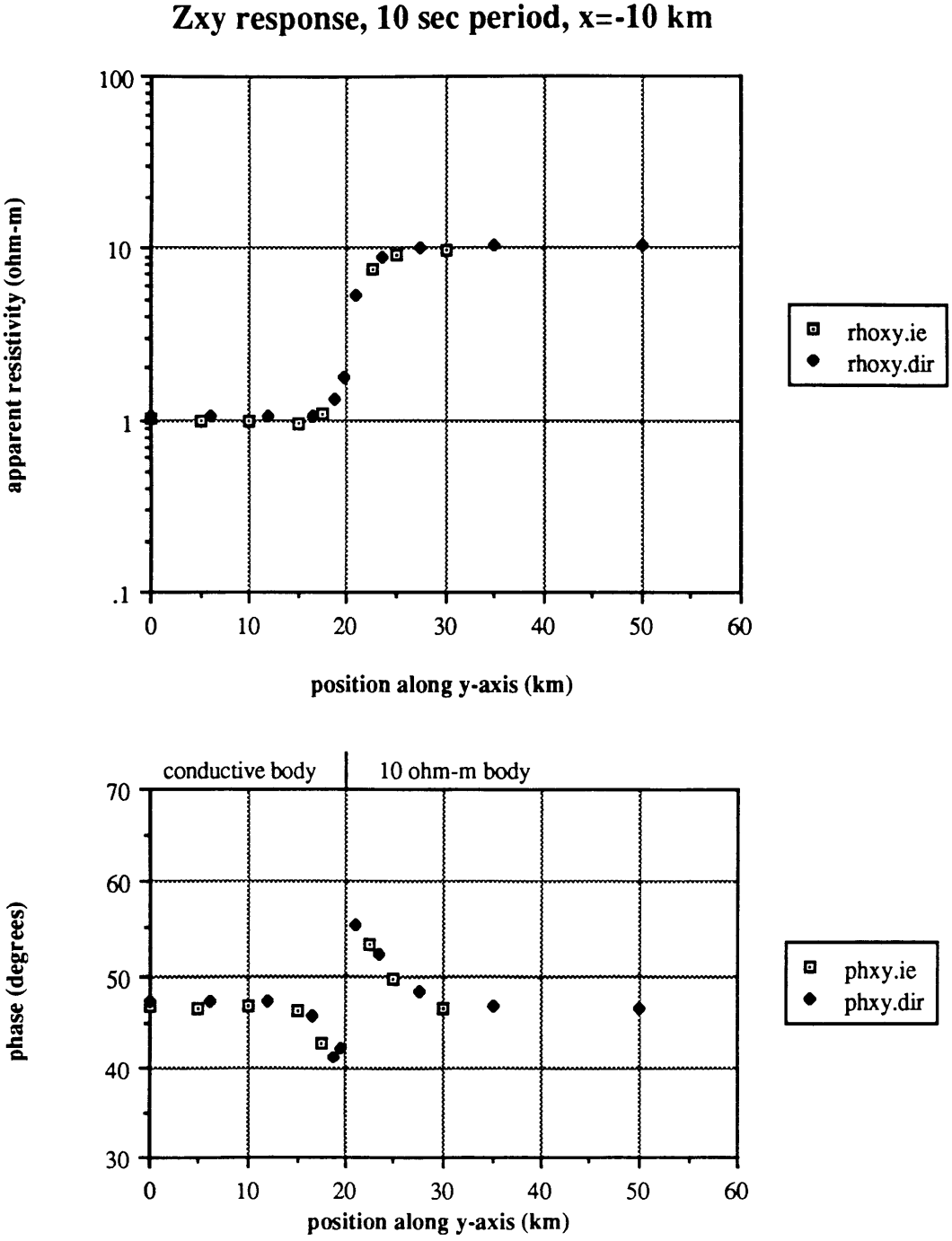


**Figure 2-13.** The $Z_{xy}$ response for a profile in the direction of the y-axis at the position x=-10km (this is down the strike of the conductive body) and a period of 10 seconds comparing the integral equation solutions with the direct difference equation solutions.

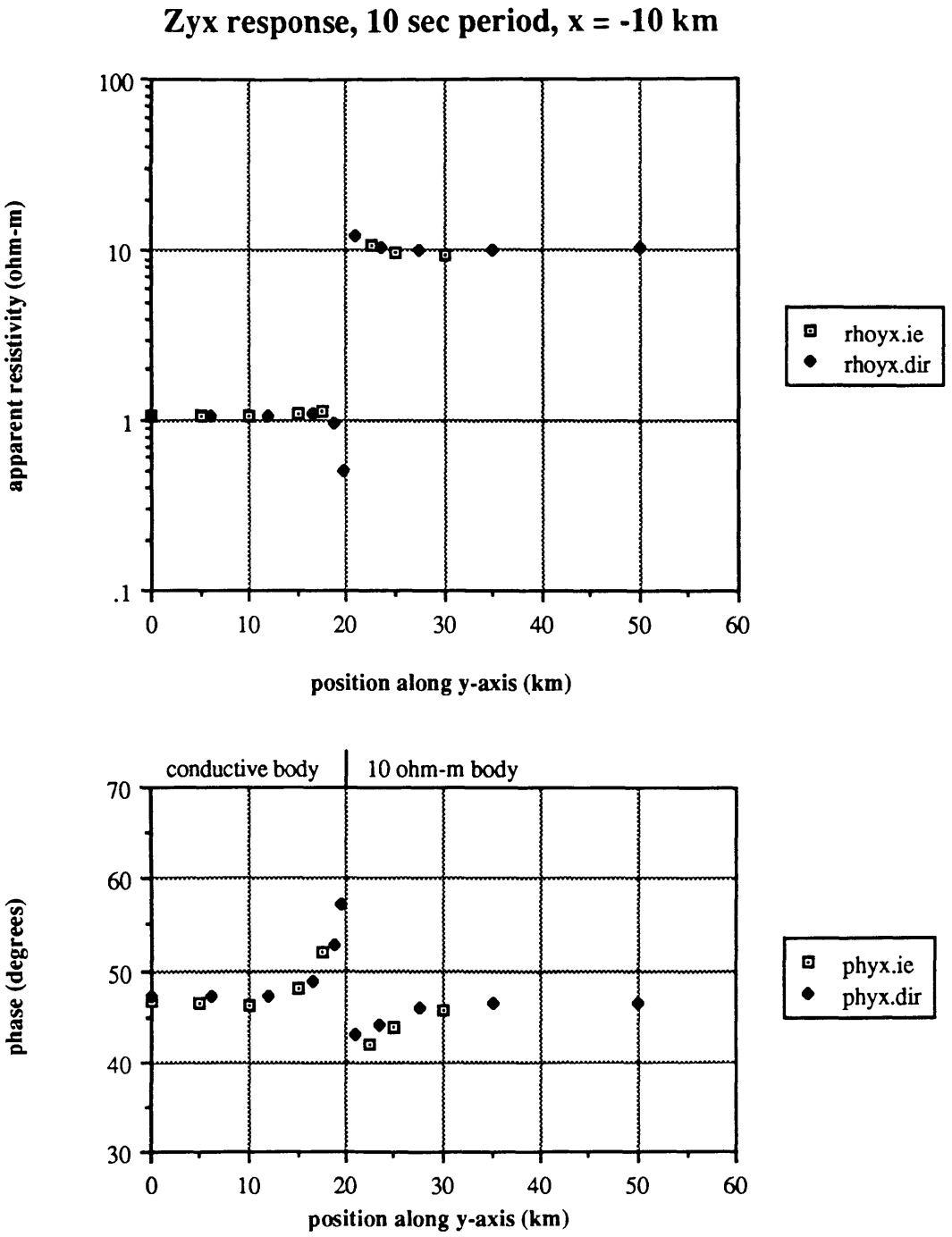


**Figure 2-14**. The $Z_{yx}$ response for a profile in the direction of the y-axis at the position x=-10km (this is down the strike of the conductive body) and a period of 10 seconds comparing the integral equation solutions with the direct difference equation solutions.

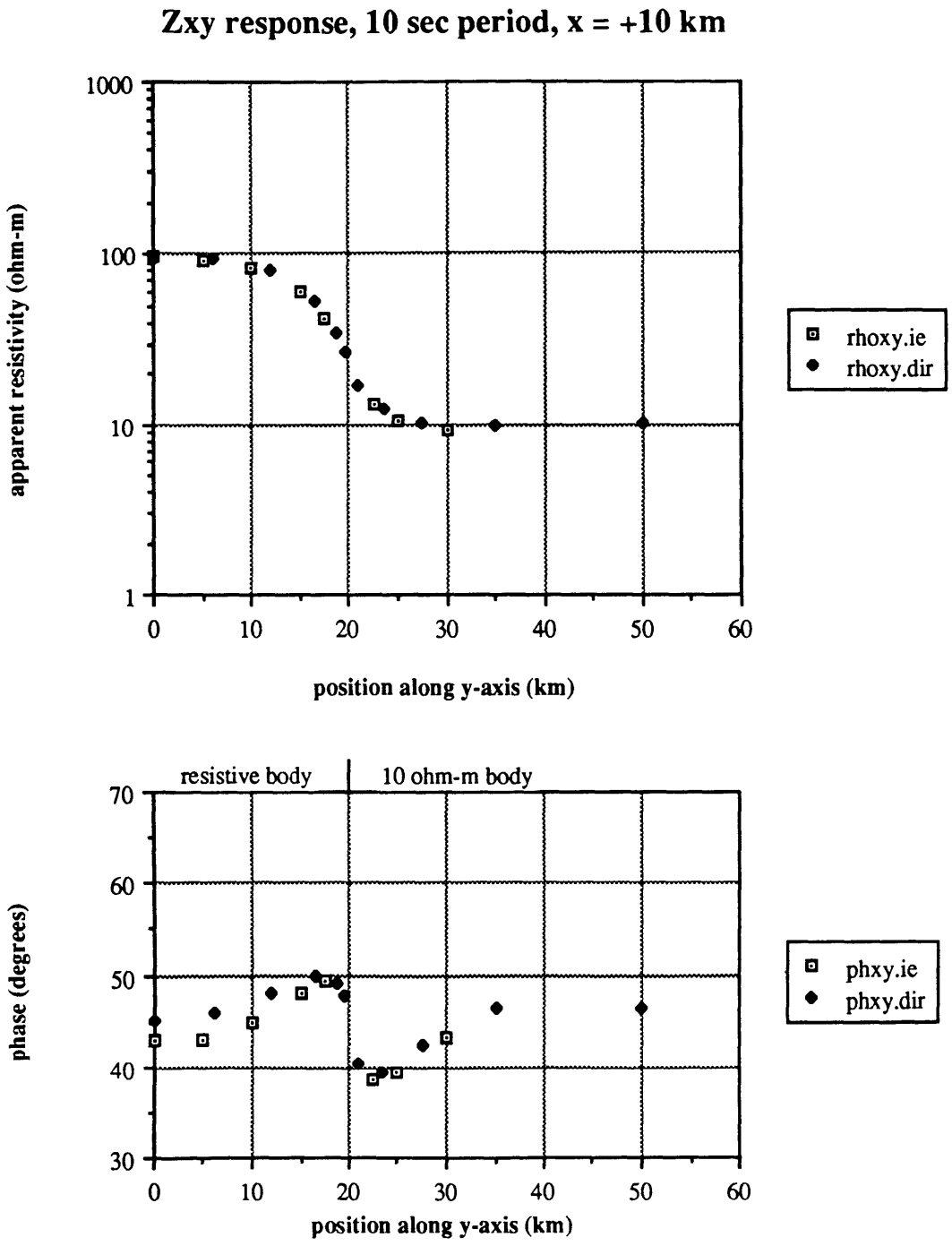


**Figure 2-15.** The $Z_{xy}$ response for a profile in the direction of the y-axis at the position x=+10km (this is down the strike of the resistive body) and a period of 10 seconds comparing the integral equation solutions with the direct difference equation solutions.

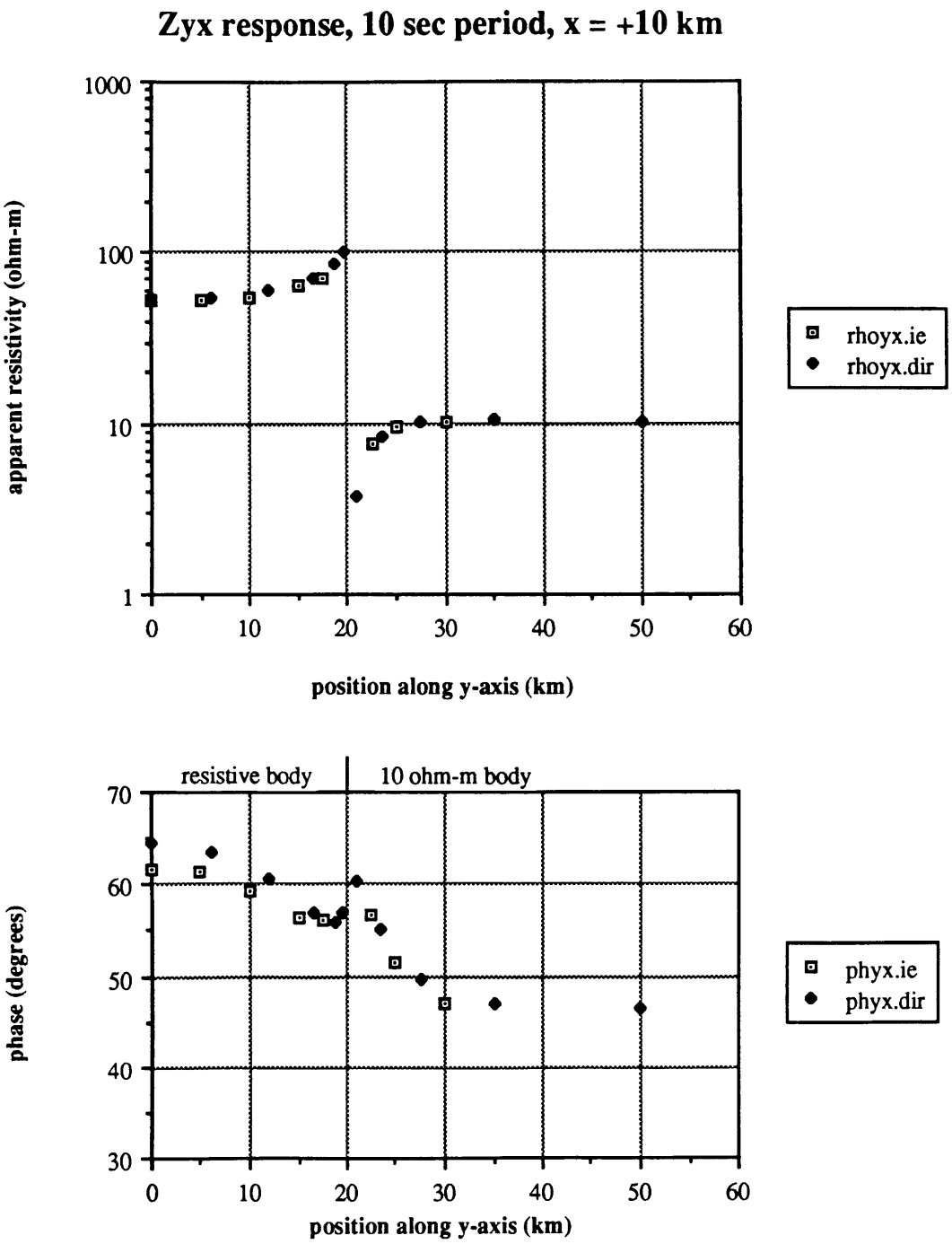


**Figure 2-16.** The $Z_{yx}$ response for a profile in the direction of the y-axis at the position x=+10km (this is down the strike of the resistive body) and a period of 10 seconds comparing the integral equation solutions with the direct difference equation solutions.

We computed the responses for the model using the MINRTRACC algorithm (recall this uses inverses of the 2D TM operators as accelerators), with one run stopping after 50 iterations per polarization, and then another run stopping after 150 iterations. A plot of the normalized error as a function of the iteration is shown in Figure 2-17. The normalized residual plotted here is $\boldsymbol{r}^T\boldsymbol{M}^{-1}\boldsymbol{r}$, where $\boldsymbol{M}$ is the diagonal matrix whose elements are the absolute value of the complex diagonal elements of the 3D operator. Also plotted in this figure is the normalized error for the MINRTR algorithm, but this will be discussed shortly. Notice that after approximately 50 iterations, the error has been reduced by about two orders of magnitude, and after an additional 100 iterations, the error has only been reduced by about another order of magnitude. Figures 2-18 and 2-19 show the $Z_{xy}$ and $Z_{yx}$ mode responses for the direct solution and for the relaxation solutions for a profile across the center of the 3D bodies (along the x-axis). There is generally good agreement in the $Z_{xy}$ mode amplitude and phase, except for a minor shift in the amplitude over the resistive body. Also notice that there is practically no difference between the relaxation responses for 50 and 150 iterations - it seems as if the extra 100 iterations have not visibly improved the results. There is much less agreement in the $Z_{yx}$ mode amplitude and phase, especially the phase over the conductive body. This is probably so because with this particular model, the $Z_{yx}$ mode response is more sensitive than the $Z_{xy}$ mode to the current gathering effects of a conductive body, and we mentioned earlier that these relaxation solutions have difficulty in modifying the **H** field because of such effects. Notice again that there is little difference between the responses for 50 and 150 iterations except near the resistive-conductive boundary where the 150 iteration response is somewhat more accurate.

In order to ascertain the distribution of the errors between the direct solution and the relaxation solution, we have made contour plots of the RMS error between the two solution techniques for both the $Z_{xy}$ and $Z_{yx}$ mode responses. We define the RMS error as:

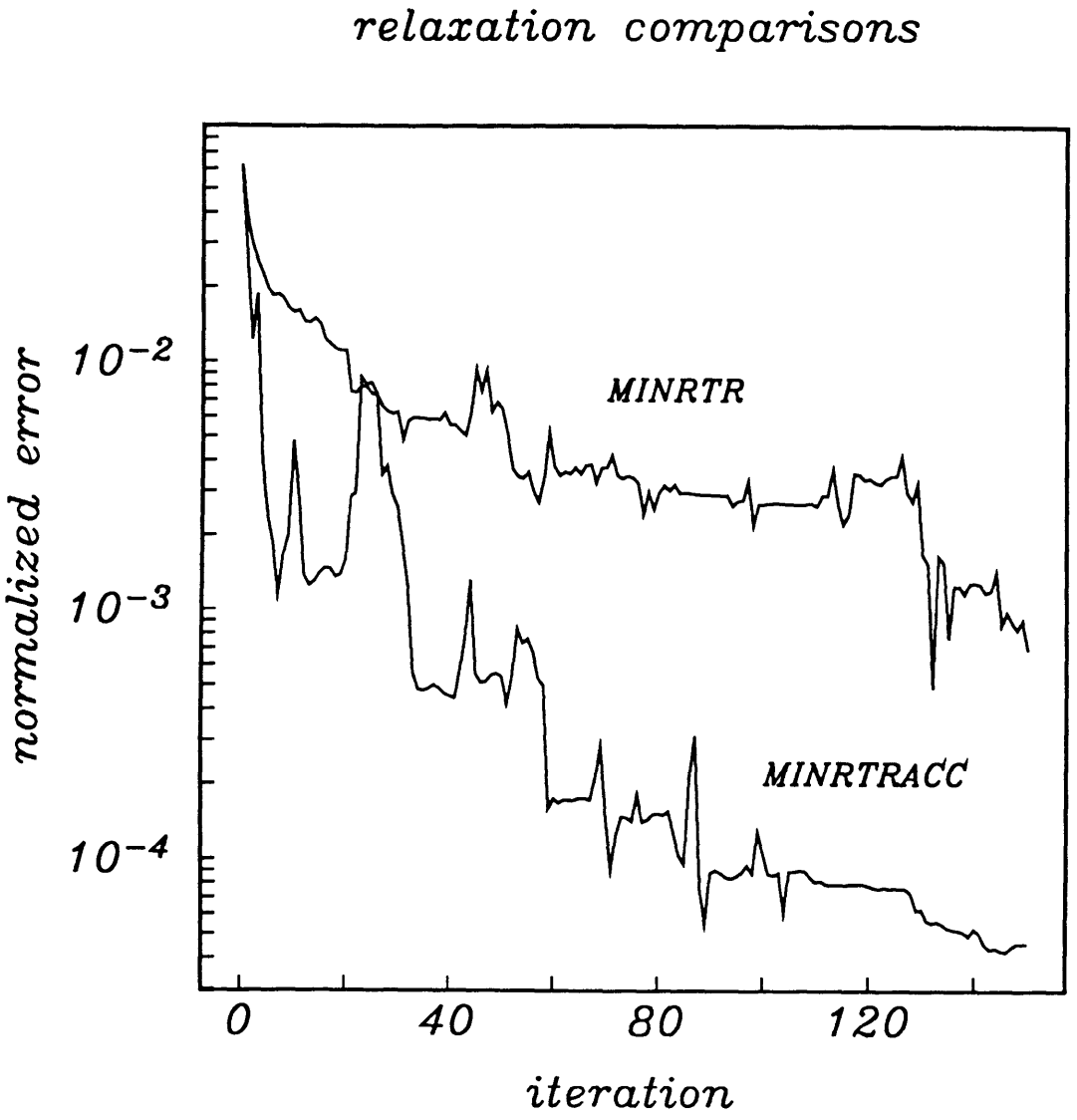


**Figure 2-17**. A plot of the normalized power in the residual vector for two runs of the model in Figure 2-3, once using the the MINRTRACC algorithm and the other using the MINRTR algorithm. The error plotted is $\mathbf{r}^T\mathbf{M}^{-1}\mathbf{r}$ where $\mathbf{M}^{-1}$ is the diagonal matrix whose elements are the absolute value of the complex diagonal elements of the 3D operator.

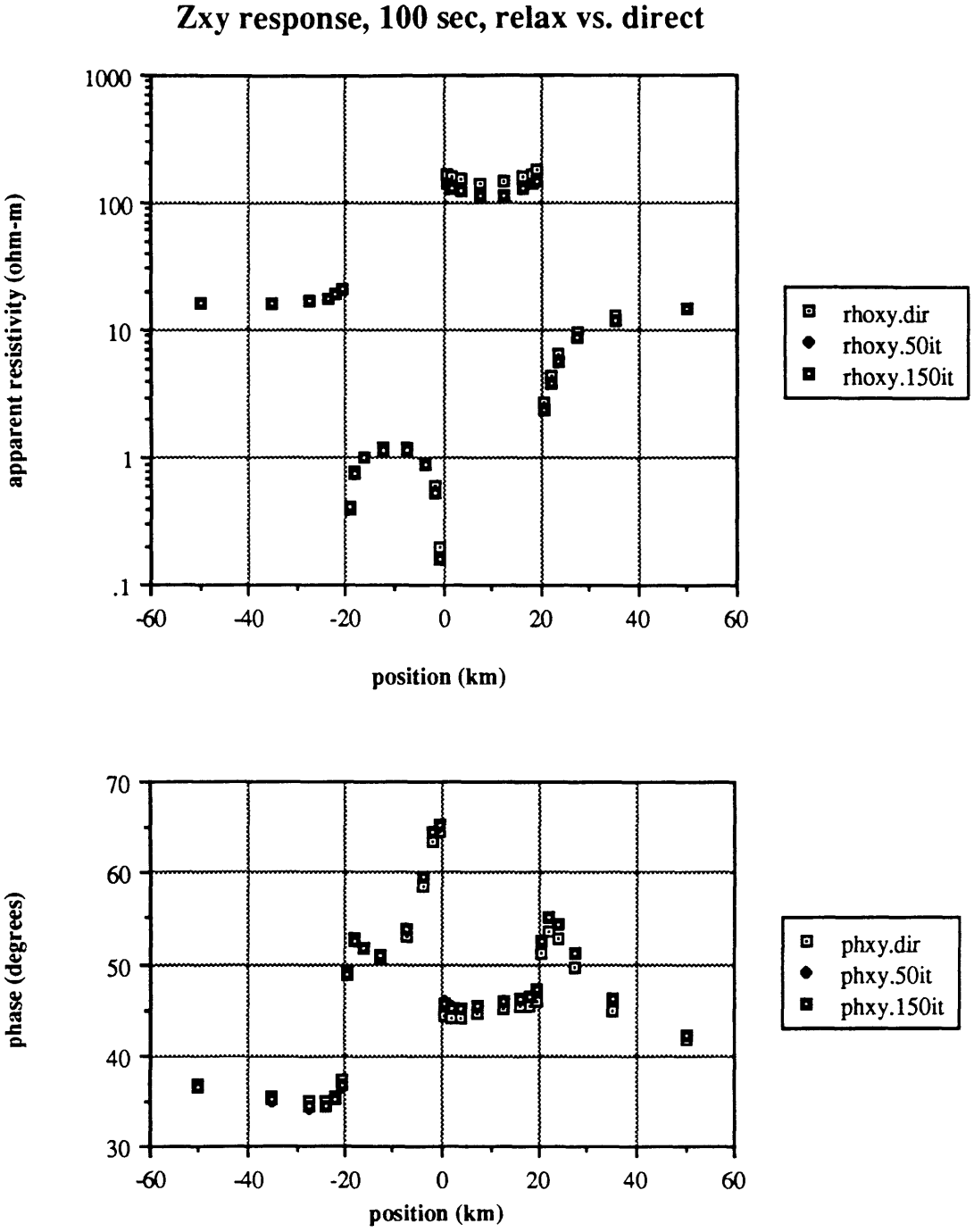


**Figure 2-18.** The $Z_{xy}$ response along a profile across the center of the bodies for a period of 100 seconds comparing the direct solution results with the results from two separate runs of the MINRTRACC algorithm, once stopping after only 50 iterations, and the other run stopping after 150 iterations. The results labelled *rhoxy.50it, etc.* are those corresponding to the 50 iteration run, the results labelled *rhoxy.150it, etc.* are those corresponding to the 150 iteration run, and the results labelled *rhoxy.dir, etc.* are those corresponding to the direct solution.

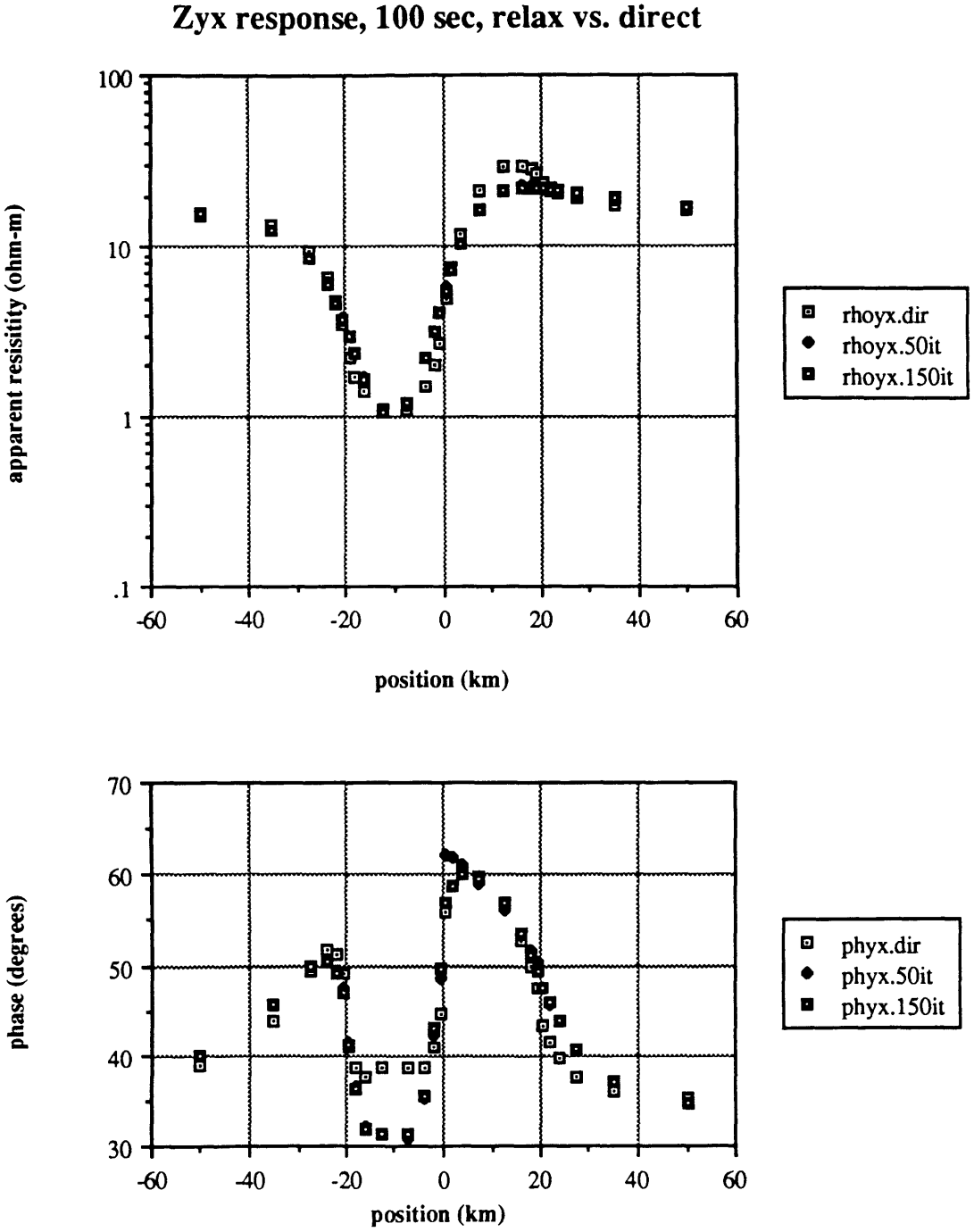


**Figure 2-19.** The $Z_{yx}$ response along a profile across the center of the bodies for a period of 100 seconds comparing the direct solution results with the results from two separate runs of the MINRTRACC algorithm, once stopping after only 50 iterations, and the other run stopping after 150 iterations.

$$\text{RMS error} = \sqrt{\frac{\left[\ln\frac{\rho_{dir}}{\rho_{rel}}\right]^2 + \left[\theta_{dir} - \theta_{rel}\right]^2}{2}} \times 100 , \qquad (2\text{-}55)$$

where the phase values are given in radians. Figures 2-20 and 2-21 show the contour plots of the RMS error between the direct solution results and those obtained using the MINRTRACC alogrithm in the $Z_{xy}$ and $Z_{yx}$ modes respectively at a period of 100 seconds. The results obtained from the MINRTRACC algorithm are those resulting after 150 iterations. The conductive and resistive bodies are both outlined on the contour plots. Not surprisingly, the greatest errors occur near conductivity contrasts, and especially so near the ends of the contact separating the resistive and conductive bodies. The errors in the $Z_{xy}$ mode are, in general, greater over the resistive body than the conductive body, whereas in the $Z_{yx}$ mode, the errors are large over both the conductive and resistive bodies (although they are more localized near the contacts over the conductive body, but spread out more evenly over the resistive body). The errors in the $Z_{xy}$ mode over the resistive body are primarily errors in the amplitudes and occur because with the relaxation solution, the **H** fields have not been depressed over the resistive body as they should be (since current is channeled around resistive bodies). Likewise, the large errors just outside the resistive body in the $Z_{xy}$ mode occur because the relaxation solution has not increased the fields due to the extra current being channeled around the ends of the resistive body. Similarly, in the $Z_{yx}$ mode, the relaxation solution has a difficult time perturbing the **H** field over the conductive and resistive bodies due to current being gathered into the conductive body and diverted around the resistive body.

Next, we will compare the MINRTRACC algorithm with the MINRTR algorithm. Figures 2-22 and 2-23 show the $Z_{xy}$ and $Z_{yx}$ mode responses across the center of the model at a period of 100 seconds for both relaxation algorithms and the direct solution algorithm. Figure 2-17 shows the progression of the error reduction for both algorithms. Even though they start at the same error, the MINRTRACC finishes with a little over an order of magnitude less error than the MINRTR algorithm. This is presumably due to the

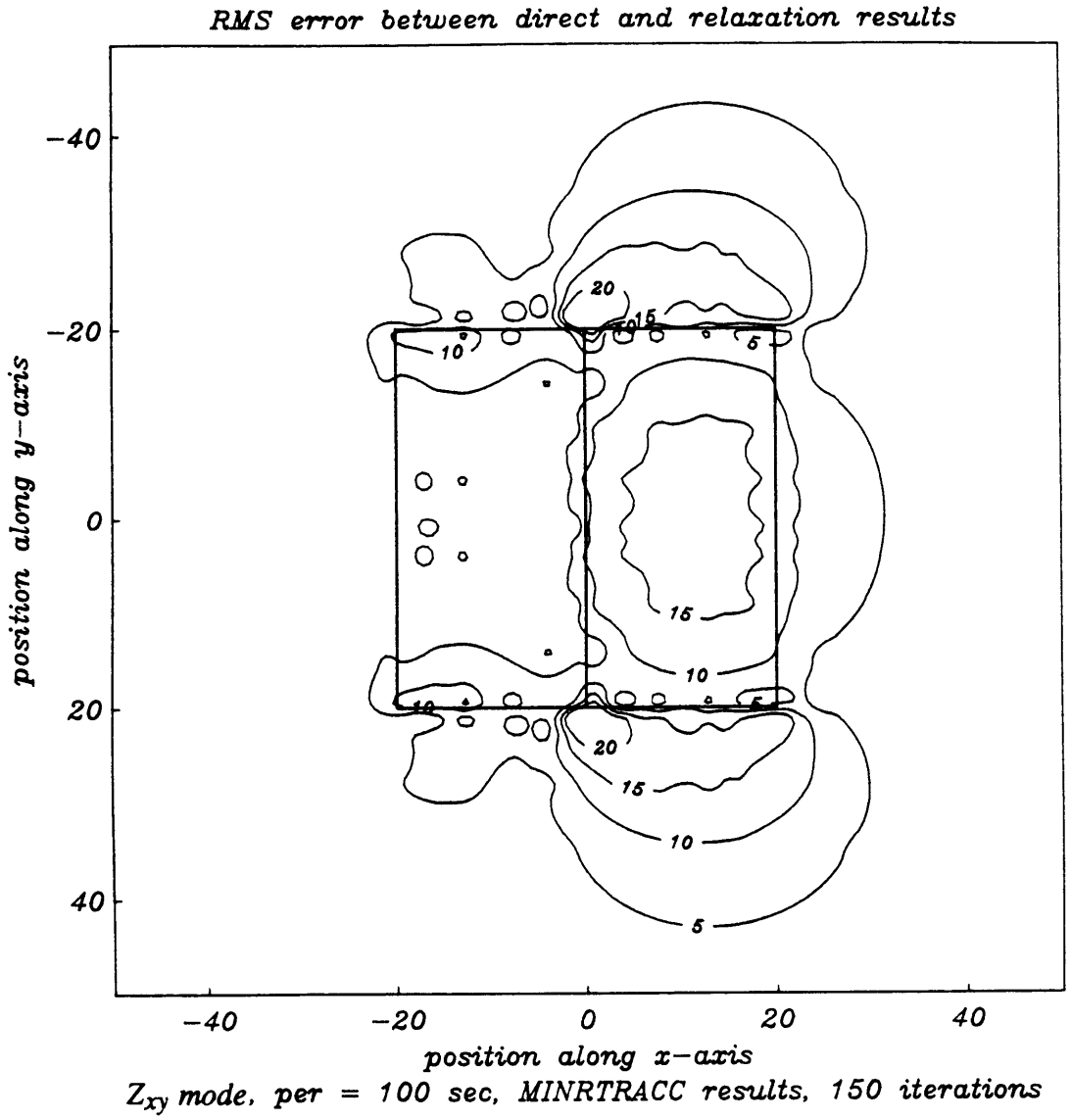


**Figure 2-20.** A contour plot of the RMS error in the $Z_{xy}$ response at a period of 100 seconds between the direct solution and the MINRTRACC relaxation solution after 150 iterations. The RMS error is defined in the text. Outlined are the positions of the conductive and resistive bodies.

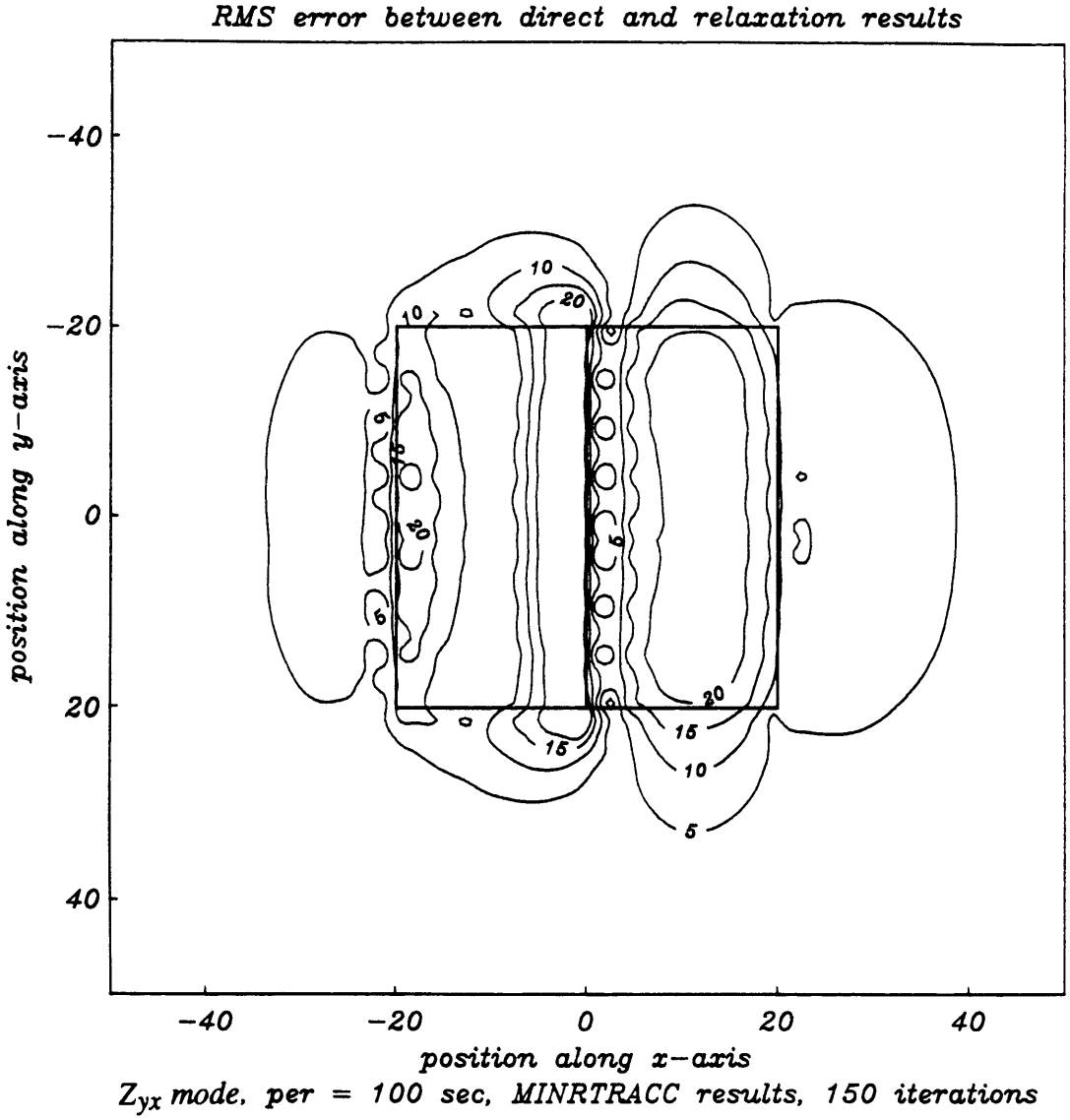


**Figure 2-21.** A contour plot of the RMS error in the Zyx response at a period of 100 seconds between the direct solution and the MINRTRACC relaxation solution after 150 iterations. The RMS error is defined in the text. Outlined are the positions of the conductive and resistive bodies.

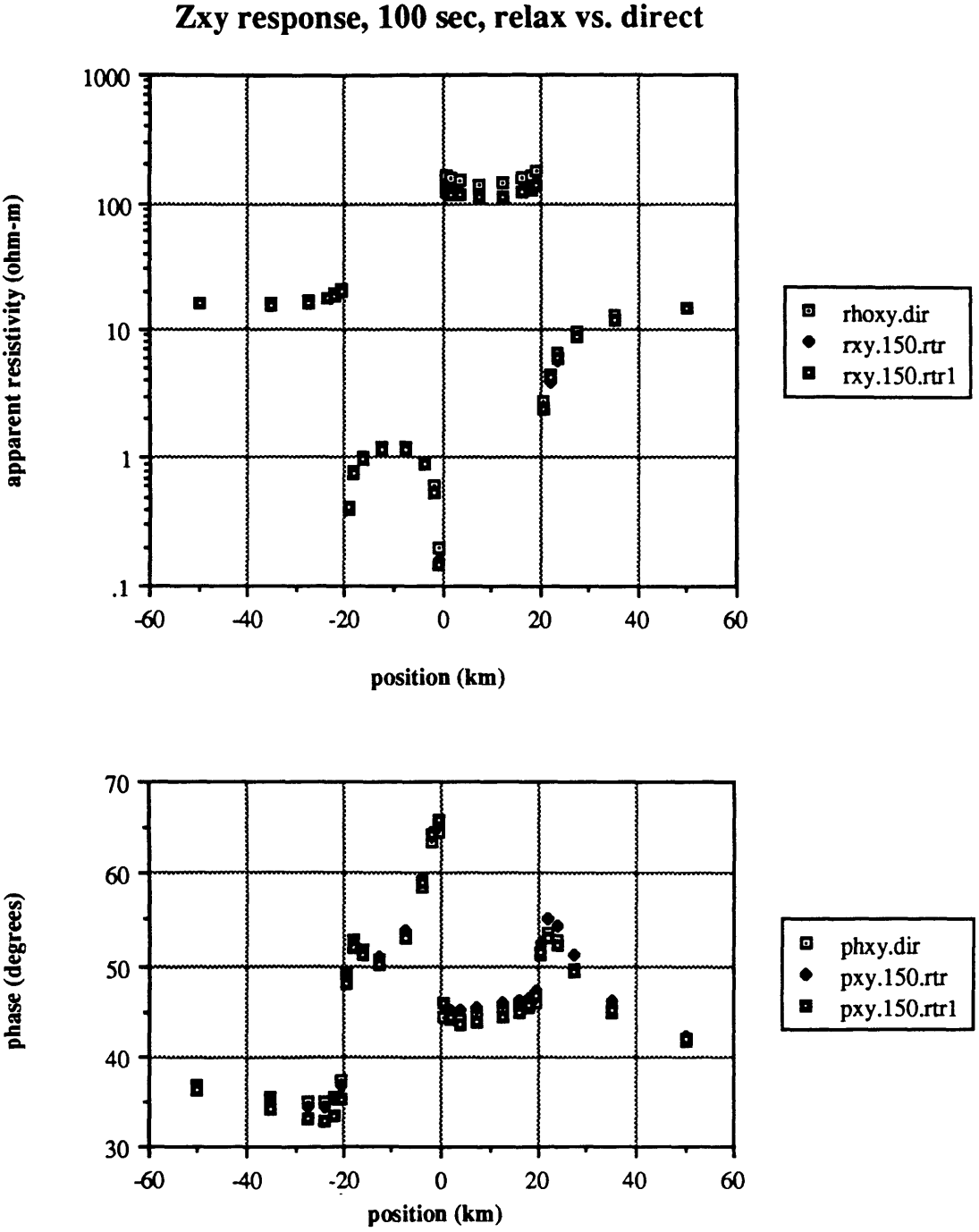


**Figure 2-22.** The $Z_{xy}$ response along a profile across the center of the bodies for a period of 100 seconds comparing the direct solution results with the results from both the MINRTRACC algorithm and the MINRTR algorithm, each time stopping after 150 iterations. The results labelled *rxy.150.rtr, etc* are those corresponding to the MINRTRACC algorithm, the results labelled *rxy.150.rtr1, etc* are those corresponding to the MINRTR algorithm, and the results labelled *rhoxy.dir, etc* are those corresponding to the direct solution.

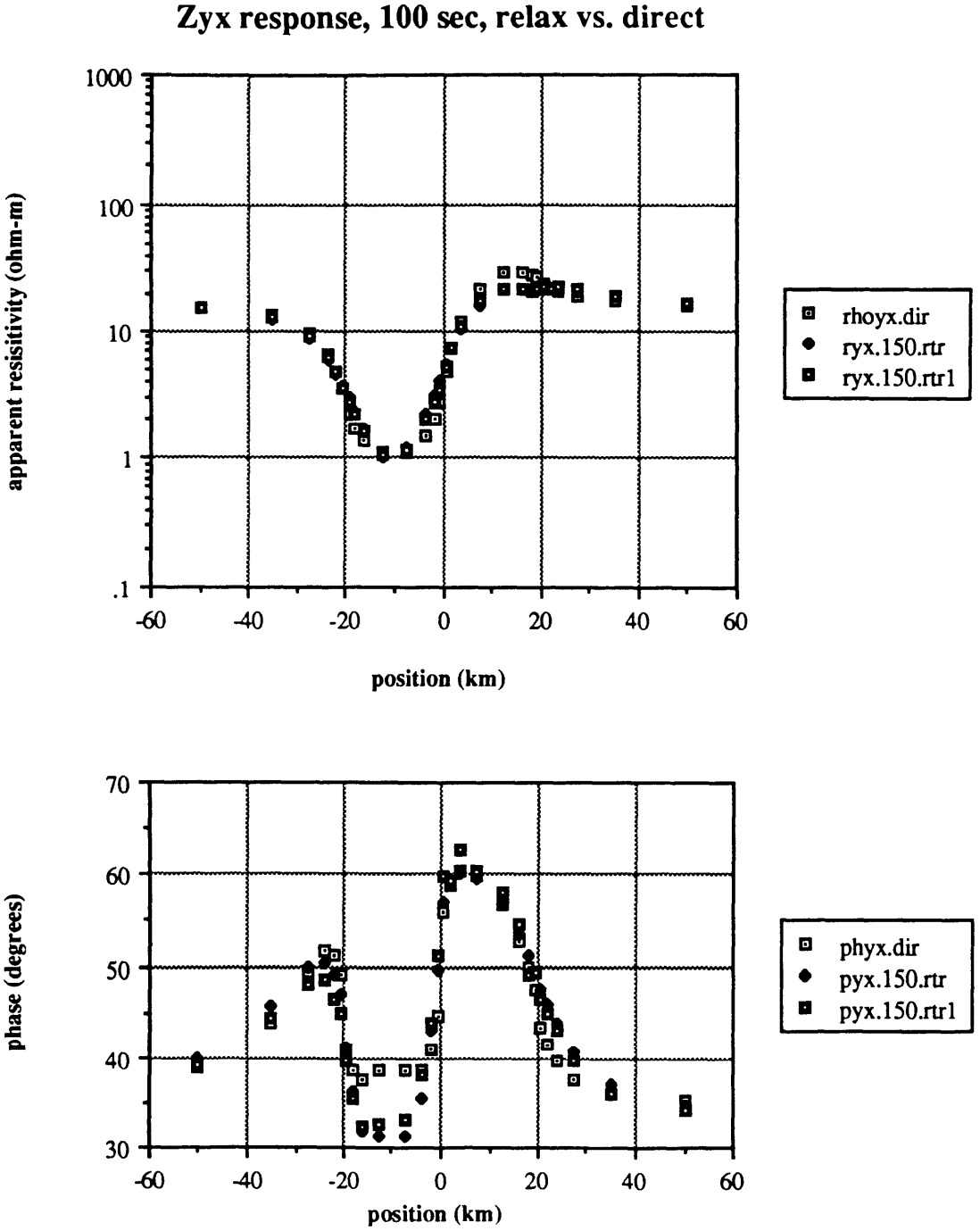


**Figure 2-23.** The $Z_{yx}$ response along a profile across the center of the bodies for a period of 100 seconds comparing the direct solution results with the results from both the MINRTRACC algorithm and the MINRTR algorithm, each time stopping after 150 iterations.

supposedly better preconditioner as discussed earlier. But, are the results really better? The $Z_{xy}$ mode responses, Figure 2-22, show fairly good agreement with the direct solution results (the results labelled *.rtr* are from the MINRTRACC algorithm and the responses labelled *.rtr1* are from the MINRTR algorithm). The responses from both algorithms are essentially equivalent except over the 10 ohm-m body near the conductive boundary (-20 km) where the MINRTRACC phases are slightly better than the MINRTR phases, and over the 10 ohm-m body near the resistive body (+20 km) where the MINRTRACC phases are slightly worse. The relaxation solutions compare less favorably to the direct solution in the $Z_{yx}$ mode responses as opposed to the $Z_{xy}$ mode responses. There is little difference between the responses from the two relaxation algorithms, although the MINRTRACC phases are somewhat better near the boundaries on either side of the conductive body. There are a few places over the conductive body, however, where the MINRTR phases are slightly better.

Figures 2-24 and 2-25 show the $Z_{xy}$ and $Z_{yx}$ mode responses for both relaxation algorithms at a strike position of 18.75 km, which is a more severe test of the algorithms' capabilities. Agreement between the relaxation algorithms and the direct solution is generally poorer than for the profile across the center of the body, and again, the responses from both relaxation algorithms are similar, except for a few locations where one is better than the other.

All of these results from the relaxation algorithms are somewhat discouraging, however, because they suggest that many more iterations are needed to obtain accurate solutions. Even doubling the number of iterations to 300 does not improve the results that much, as seen in Figure 2-26. One must bear in mind that this model, which is 28 blocks by 19 blocks by 18 blocks (including the air layers), represents a 3D operator with dimension of approximately 28,700. The original appeal of relaxation techniques, besides the fact that they require little computer storage and are relatively quick, was the possibility that reasonable answers could be obtained with only a modest number of iterations. If one

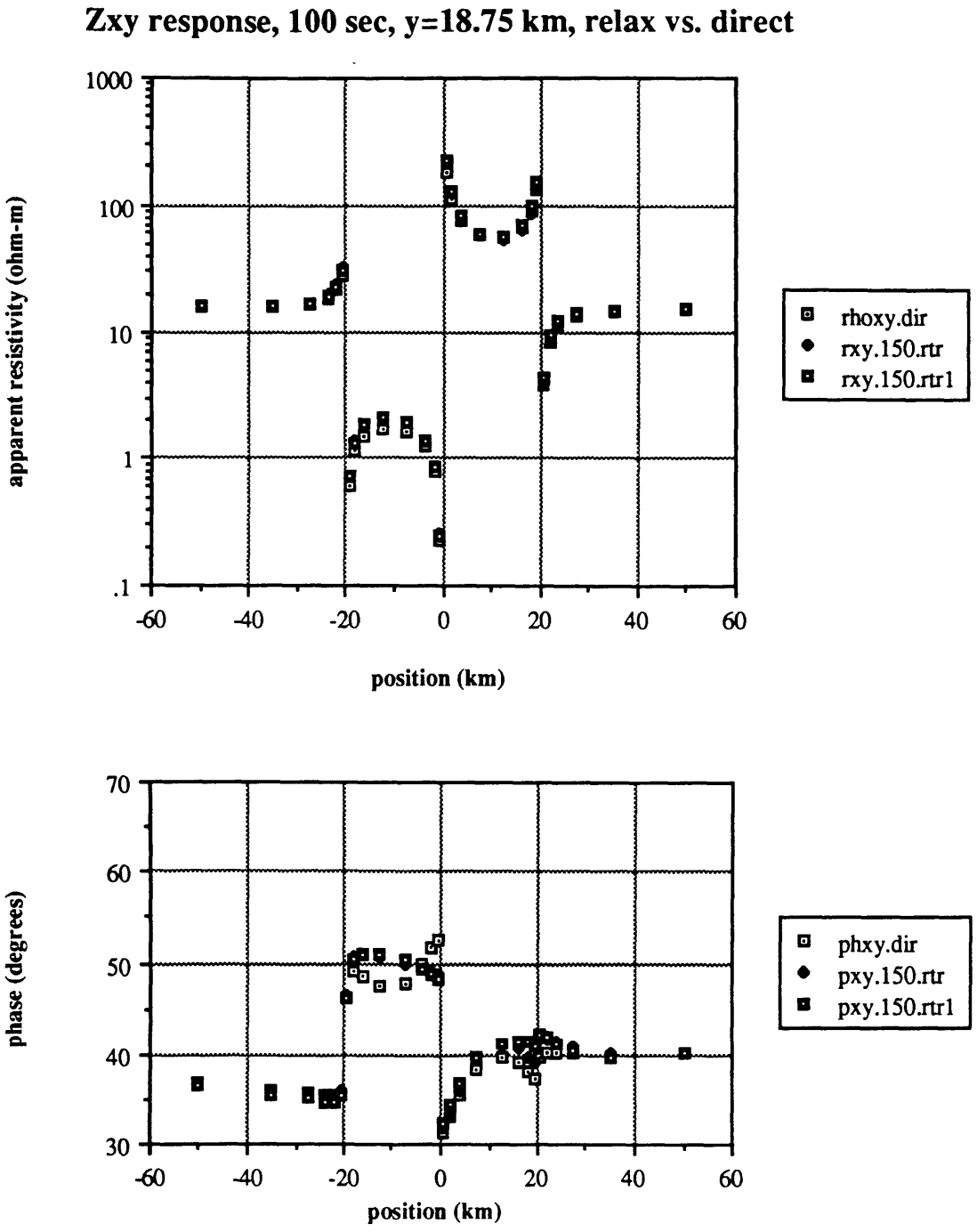


**Figure 2-24.** The $Z_{xy}$ response along a profile at a strike position of y=18.75 km for a period of 100 seconds comparing the direct solution results with the results from both the MINRTRACC algorithm and the MINRTR algorithm, each time stopping after 150 iterations.

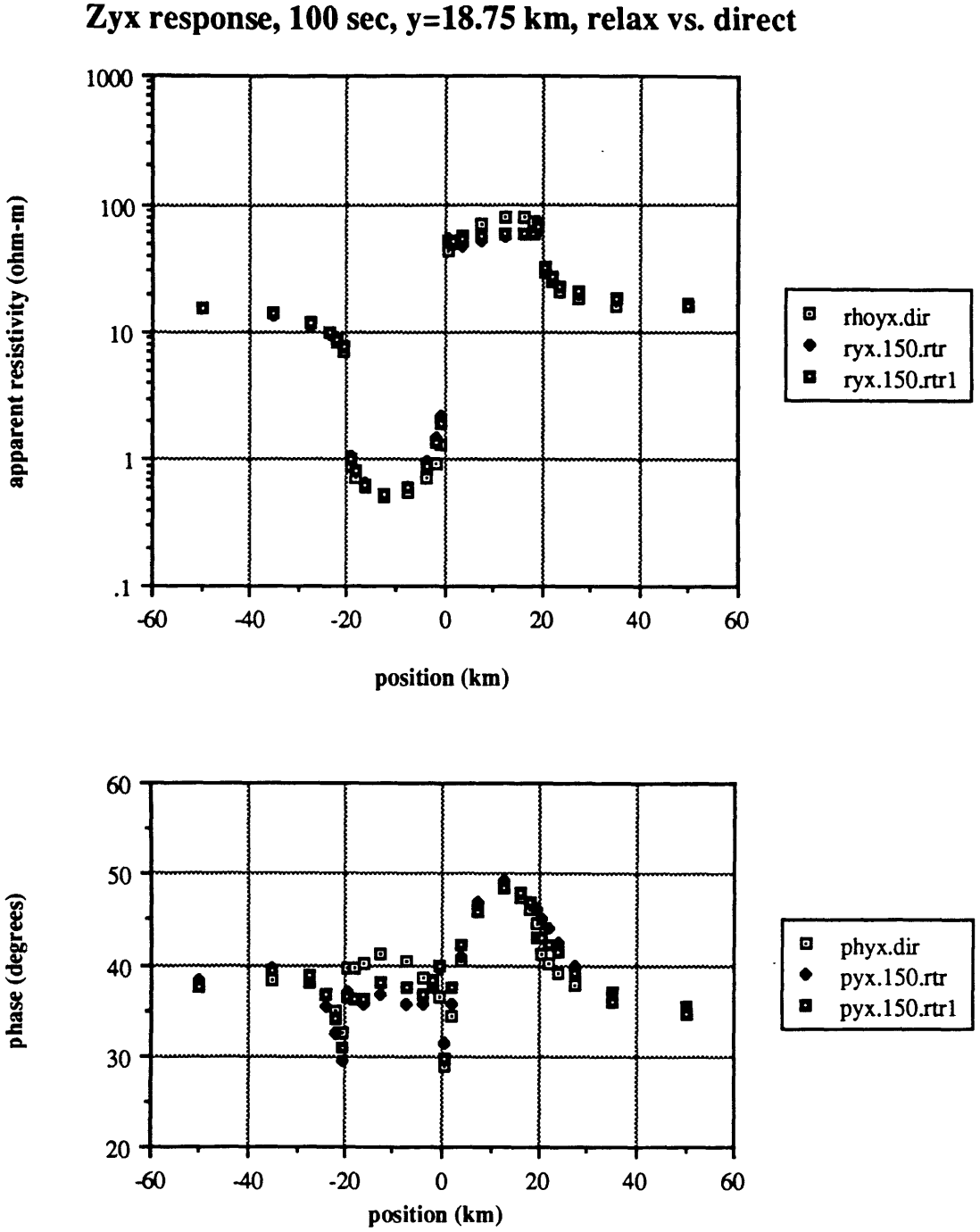


**Figure 2-25.** The $Z_{yx}$ response along a profile at a strike position of y=18.75 km for a period of 100 seconds comparing the direct solution results with the results from both the MINRTRACC algorithm and the MINRTR algorithm, each time stopping after 150 iterations.

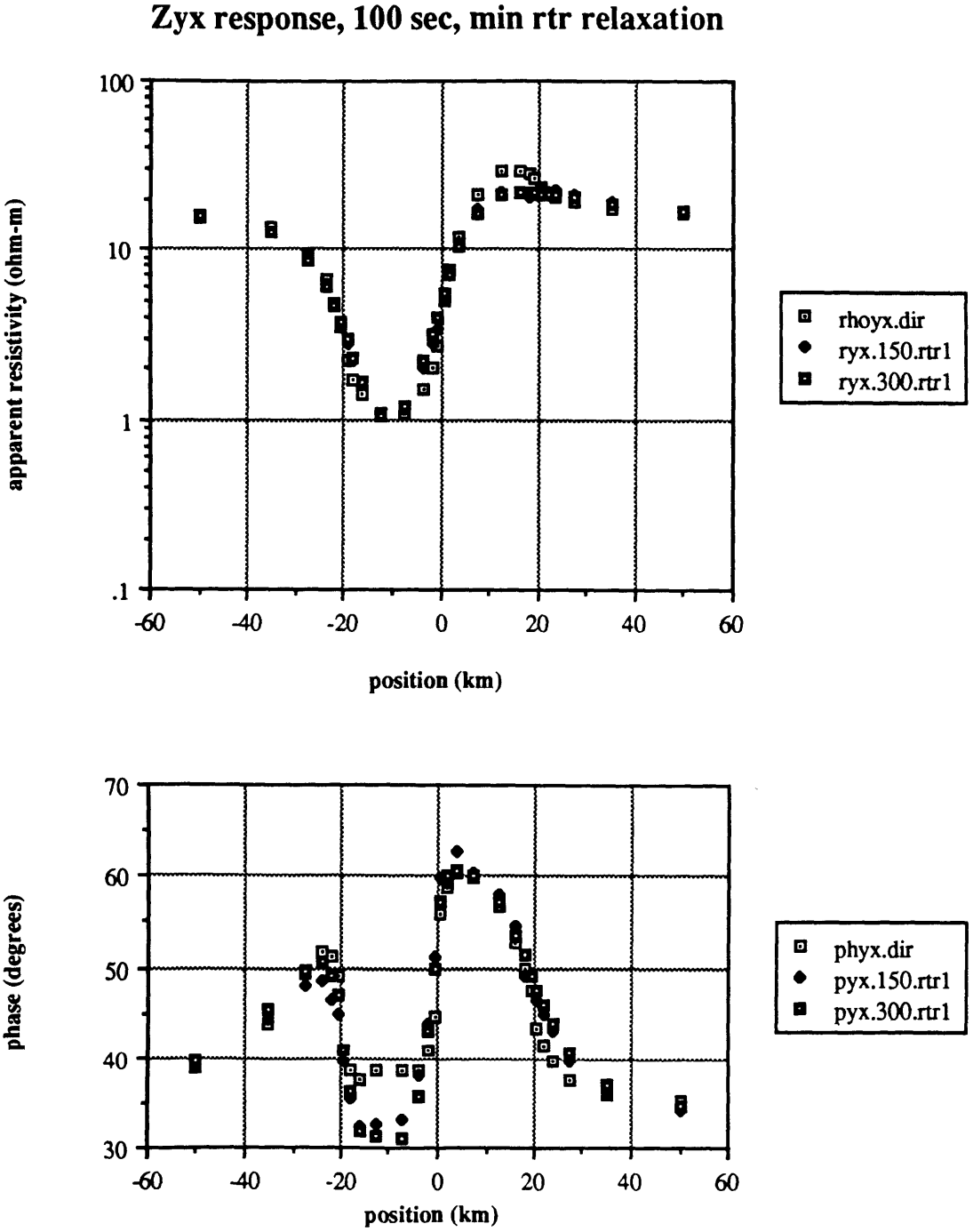


**Figure 2-26.** The $Z_{yx}$ response along a profile across the center of the bodies for a period of 100 seconds comparing the direct solution results with the results from two separate runs of the MINRTR algorithm, once stopping after only 150 iterations, and the other run stopping after 300 iterations.

had to do several thousand iterations to obtain a solution, then any time advantage over the direct solution would be lost. To be practical for people without access to supercomputers, however, the relaxation solutions would have to be improved over these first two attempts.

We turned to a multiple scaling scheme in hopes of improving the results from the relaxation techniques. The algorithm, described earlier, is designated as the MINRTRMS (minimum $\boldsymbol{r}^T\boldsymbol{r}$ multiple scaling algorithm). The model under consideration went through three scales of calculation. The first scale, eight by eight, was solved exactly, and the fields interpolated onto a 16 by 16 model. This intermediate scale model was relaxed using the MINRTR algorithm with instructions to stop and go to the next scale after either the error had been reduced four orders of magnitude or 300 iterations had been reached. At this scale, the error reduction criteria was reached in under 300 iterations. The field values were then interpolated onto the final scale model, which was the original model. At this final scale, the error dropped approximately 3.5 orders of magnitude in 300 iterations, see Figure 2-27. Also shown for comparison in this figure is the error reduction for the model running the straight MINRTR algorithm. The starting error for the MINRTRMS algorithm, though higher than that for the MINRTR algorithm, comes down quickly and ends up at about the same level as that from the MINRTR algorithm. The starting error for the MINRTRMS algorithm is higher than that for the MINRTR algorithm because of errors incurred in the interpolation to the larger scale. What this plot does not show, however, is that even though the error is approximately the same as with the straight MINRTR, the field values are more representative of the true field values. The interpolating-averaging scheme used in the multiple scaling gives errors in the field values, but these values have preserved the regional structure of the **H** field through the scaling process, and this results in much improved 3D responses. Figures 2-28 and 2-29 show the $Z_{xy}$ and $Z_{yx}$ mode responses for the multiple scaling algorithm versus the direct solution algorithm. Notice that although there are a few places where there are minor discrepencies, the multiple scaling solution matches the direct solution quite well. Even at a strike distance of 18.75 km, the multiple

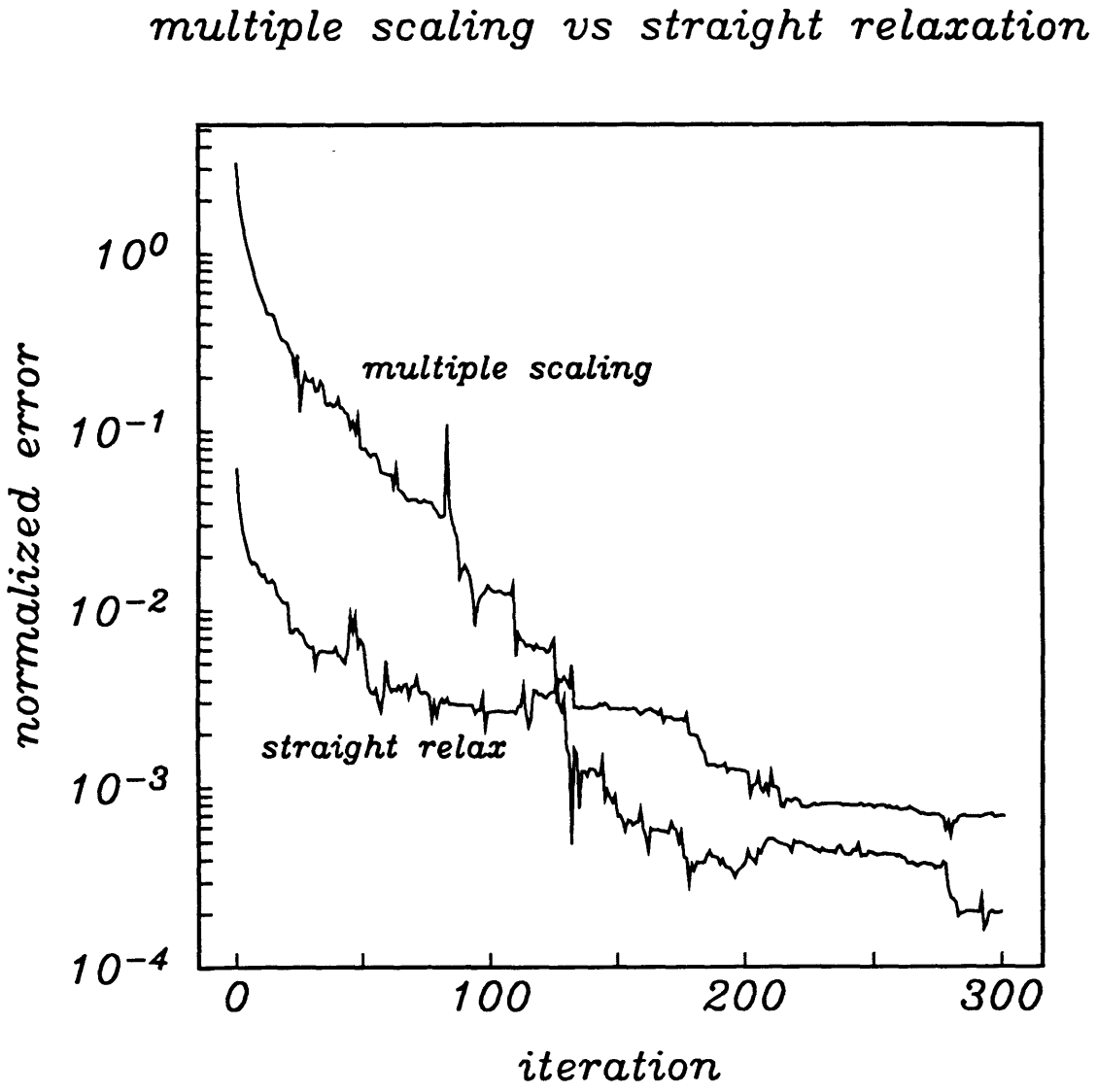


**Figure 2-27.** A plot of the normalized power in the residual vector for two runs of the model in Figure 2-3, once using the the multiple scaling algorithm (at the final scale and for the $Z_{xy}$ mode) and the other using the MINRTR algorithm. The error plotted is $\mathbf{r}^T\mathbf{M}^{-1}\mathbf{r}$ where $\mathbf{M}^{-1}$ is the diagonal matrix whose elements are the absolute value of the complex diagonal elements of the 3D operator.

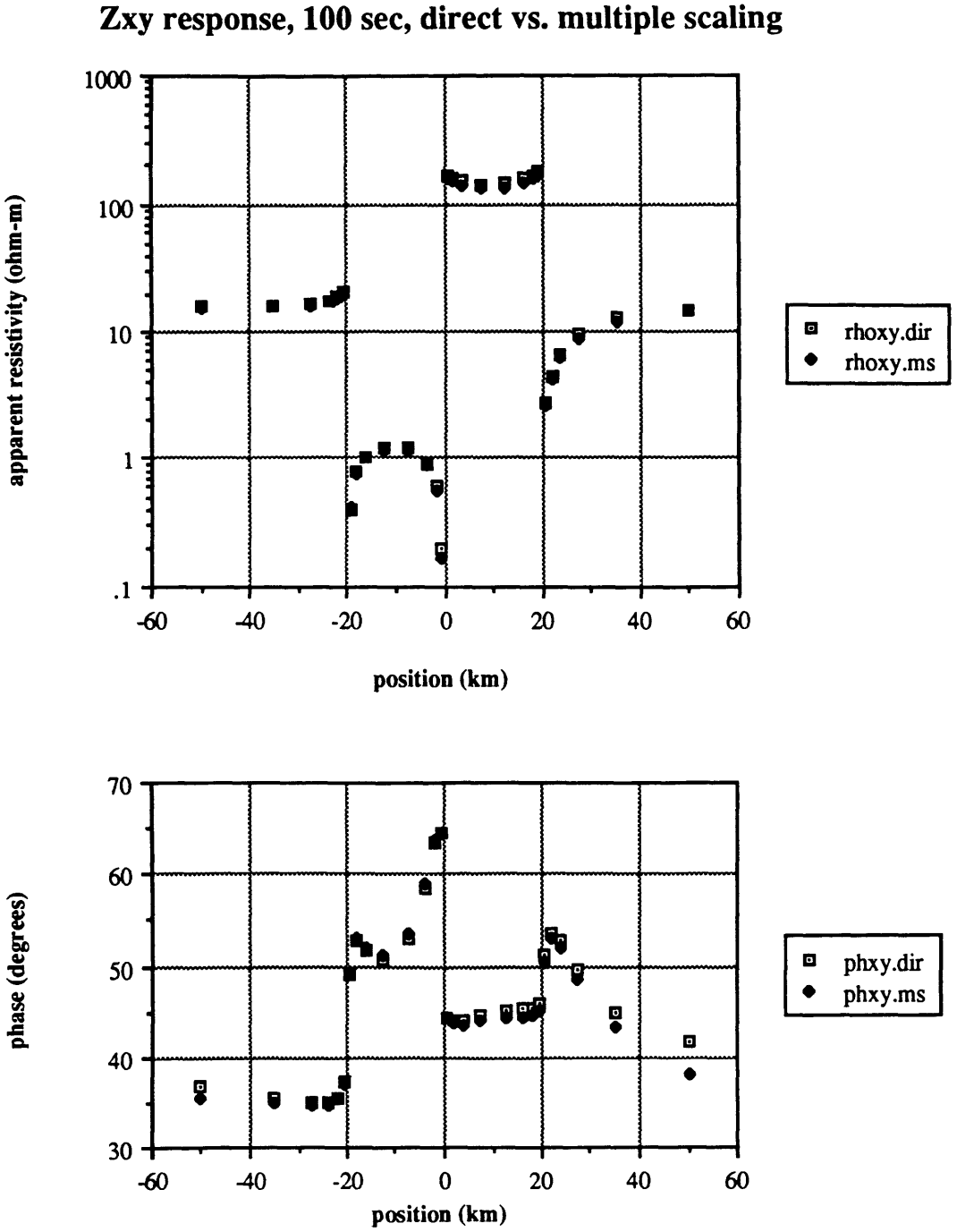


**Figure 2-28.** The $Z_{xy}$ response along a profile across the center of the bodies for a period of 100 seconds comparing the direct solution results with the multiple scaling relaxation results. The results labelled *rhoxy.ms, etc* are those corresponding to the multiple scaling algorithm, and those labelled *rhoxy.dir, etc* are those corresponding to the direct solution algorithm.

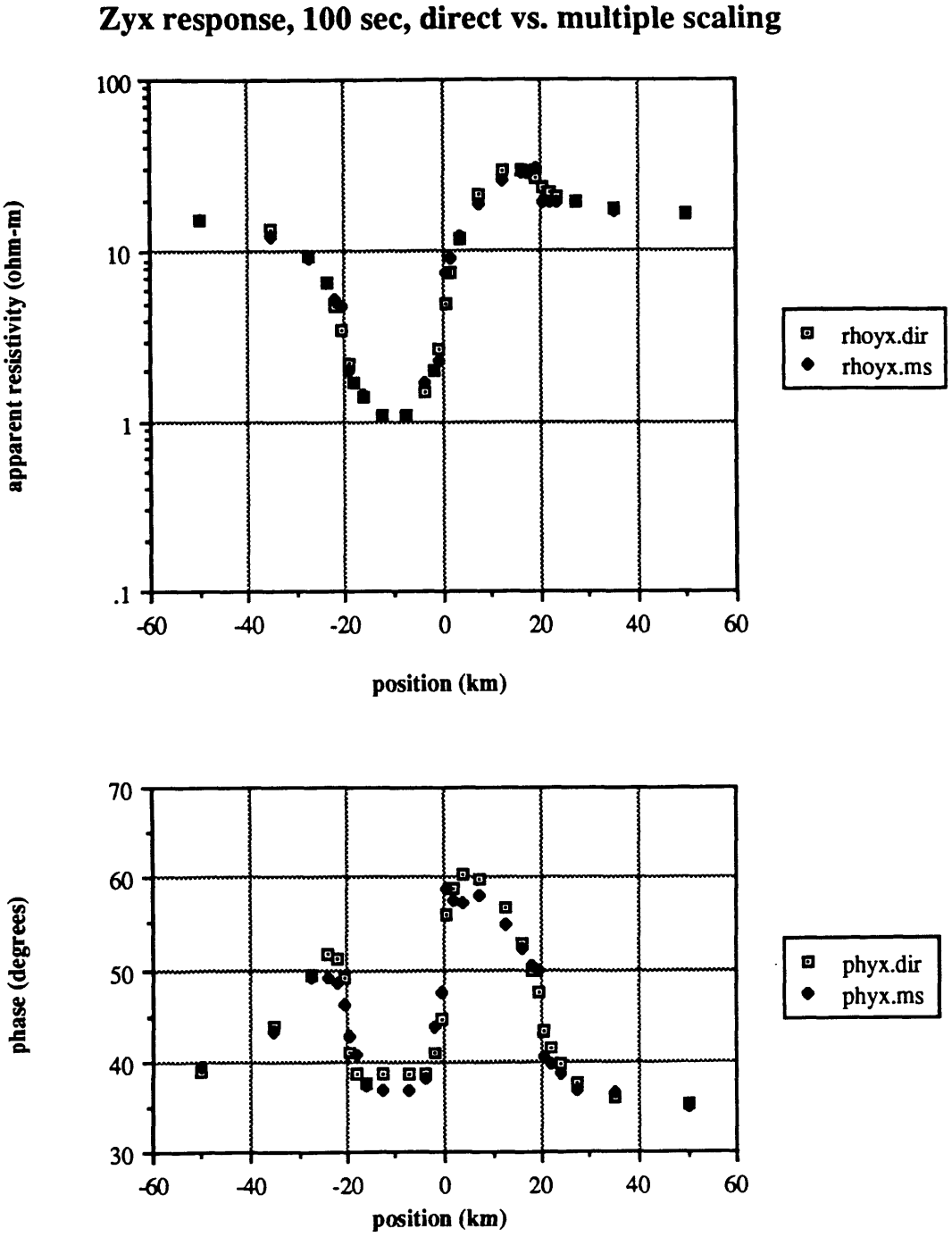


**Figure 2-29.** The $Z_{yx}$ response along a profile across the center of the bodies for a period of 100 seconds comparing the direct solution results with the multiple scaling relaxation results.

scale responses, shown in Figures 2-30 and 2-31 are far superior to the responses computed by straight relaxation. Contour plots of the RMS error between the direct solution and the multiple scaling solution are shown in Figures 2-32 and 2-33 for the $Z_{xy}$ mode and $Z_{yx}$ mode respectively. These plots, when compared to those shown in Figures 2-20 and 2-21, confirm that the multiple scaling relaxation algorithm gives superior error reduction over the MINRTRACC algorithm. Therefore, although additional testing needs to be done, it appears that multiple scaling is a viable way to use relaxation methods and obtain improved responses as compared to the traditional relaxation algorithms.

### Computational considerations

As mentioned previously, it is in our best interest to develop a reliable relaxation algorithm to solve the 3D magnetotelluric problem. Since realistic 3D finite difference Earth models invariably lead to large systems of equations to be solved, relaxation methods are needed to make 3D modeling available to those users without access to supercomputers. The relaxation algorithms take less storage space than the direct solution, but are less accurate, as was demonstrated in this chapter. The direct solutions, though accurate, require large amounts of computer memory and can be too time-consuming without a supercomputer.

All of the modeling in this chapter was done on the CRAY-2 / 4-256 computer maintained by the MIT Supercomputer Facility. The *Lanczos* (1961) method for inverting complex matrices was used in conjunction with CRAY-optimized real matrix inversion routines to invert the complex operators. Additional time-savings were obtained by using the *Lanczos* (1961) matrix partitioning method for inverting matrices, and by using CRAY-optimized routines for multiplying matrices. It took approximately 25 minutes of CPU time per frequency (two polarizations per frequency) for the direct calculations and 30 MWords of memory (1 word = 8 bytes). The MINRTRACC routine took 14.4 minutes of CPU time per frequency at 150 iterations per polarization, the MINRTR routine took 2.7 minutes of

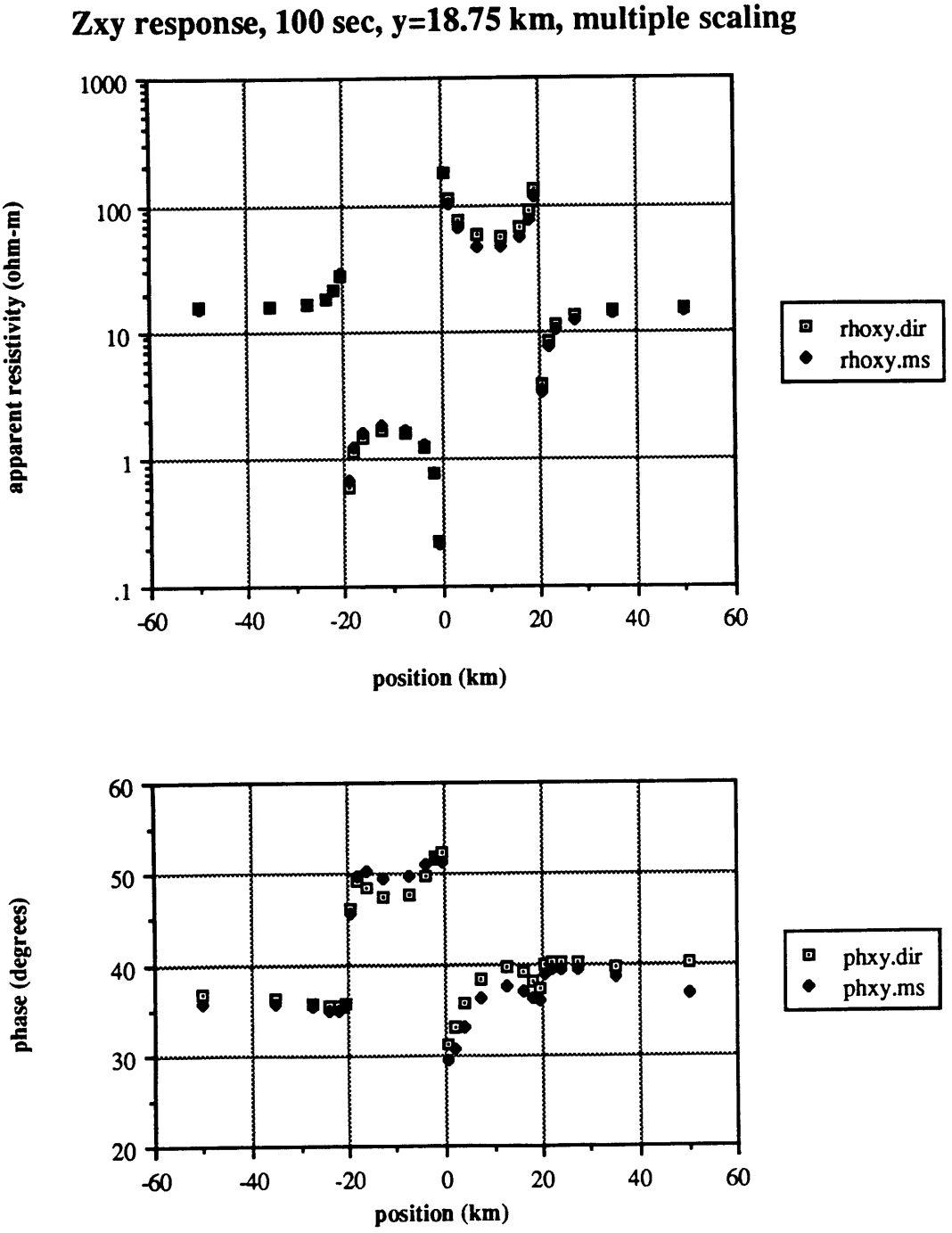


**Figure 2-30.** The $Z_{xy}$ response along a profile at a strike position of y=18.75 km for a period of 100 seconds comparing the direct solution results with the multiple scaling relaxation results.

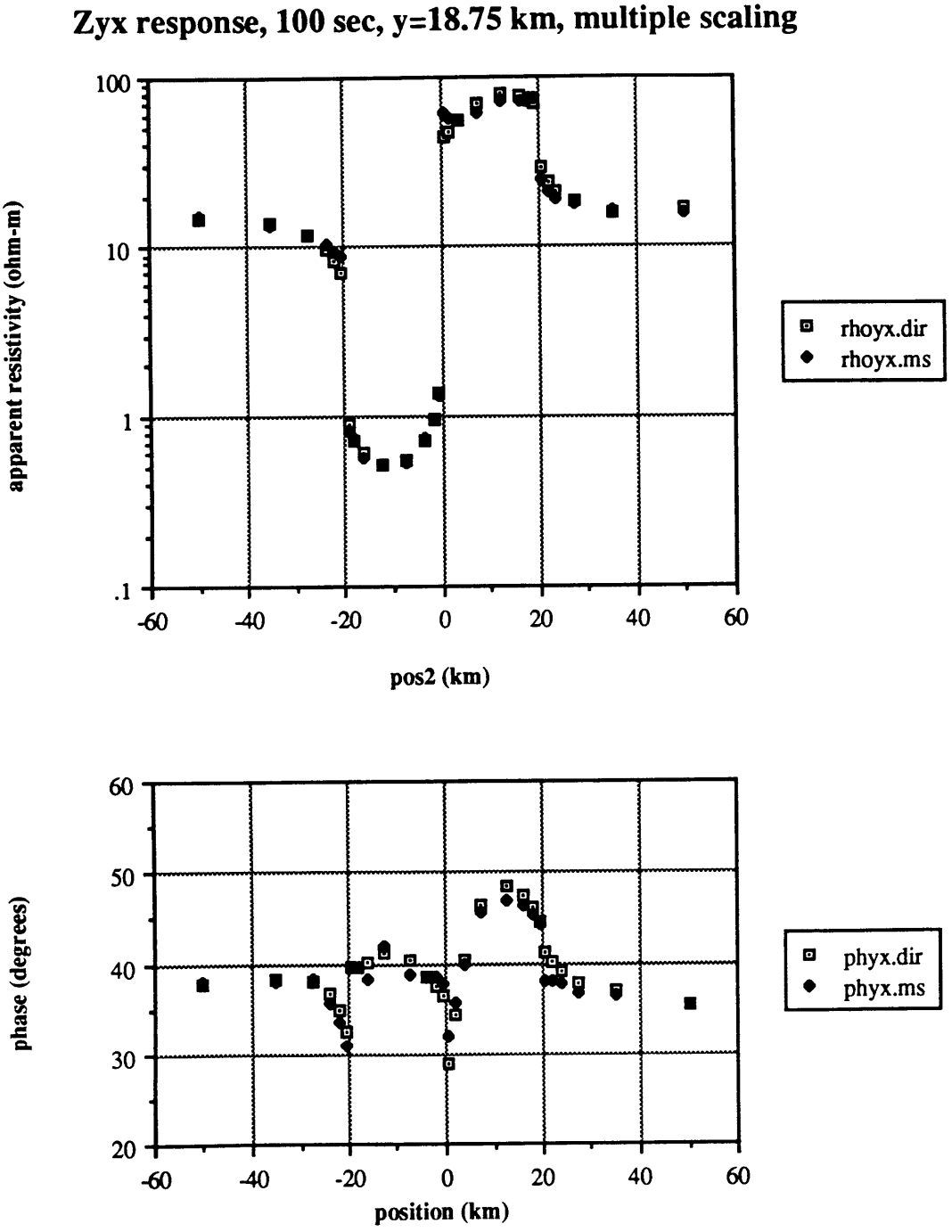


**Figure 2-31**. The $Z_{yx}$ response along a profile at a strike position of y=18.75 km for a period of 100 seconds comparing the direct solution results with the multiple scaling relaxation results.

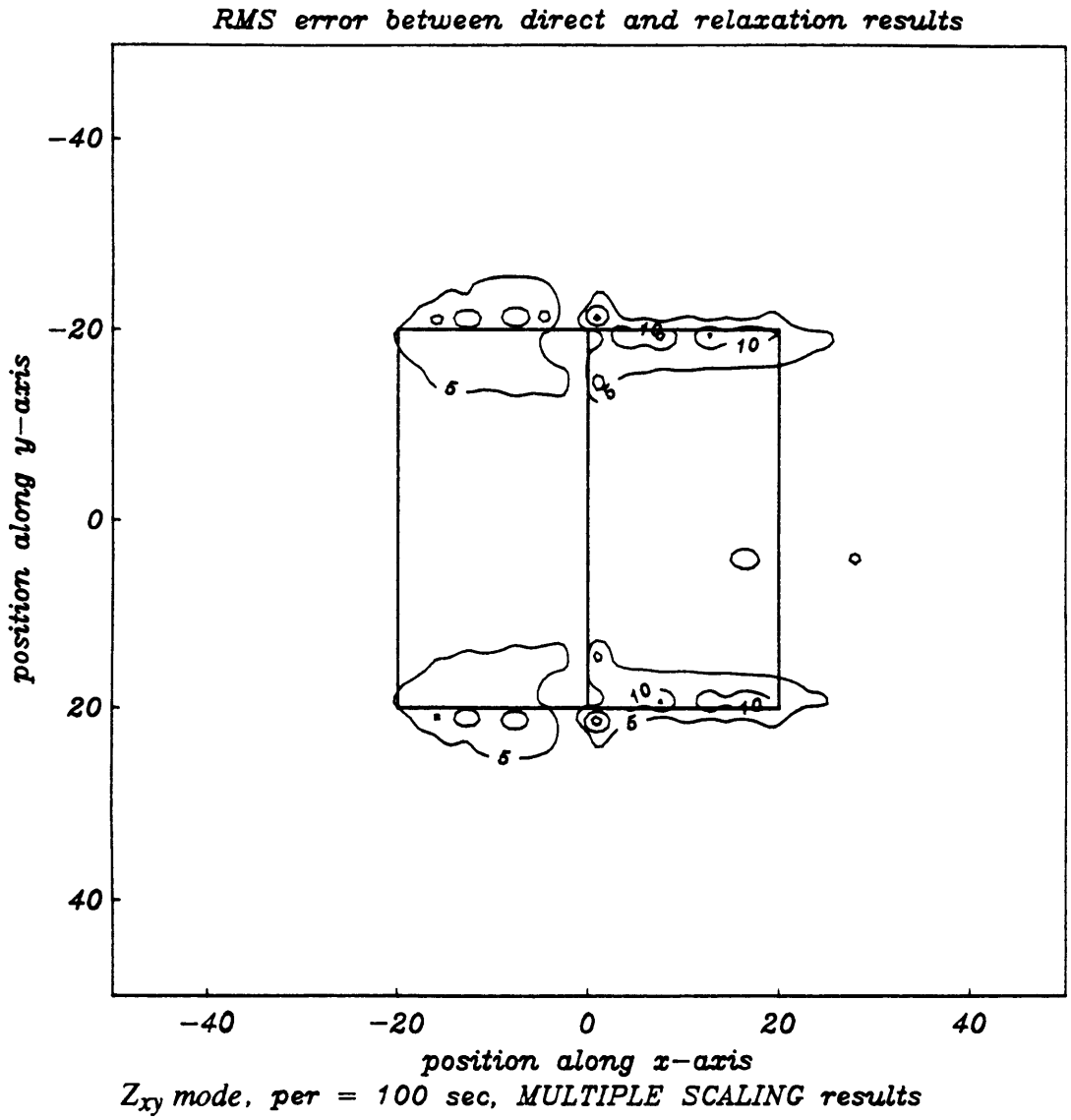


**Figure 2-32.** A contour plot of the RMS error in the $Z_{xy}$ response at a period of 100 seconds between the direct solution and the multiple scaling relaxation solution. The RMS error is defined in the text. Outlined are the positions of the conductive and resistive bodies.

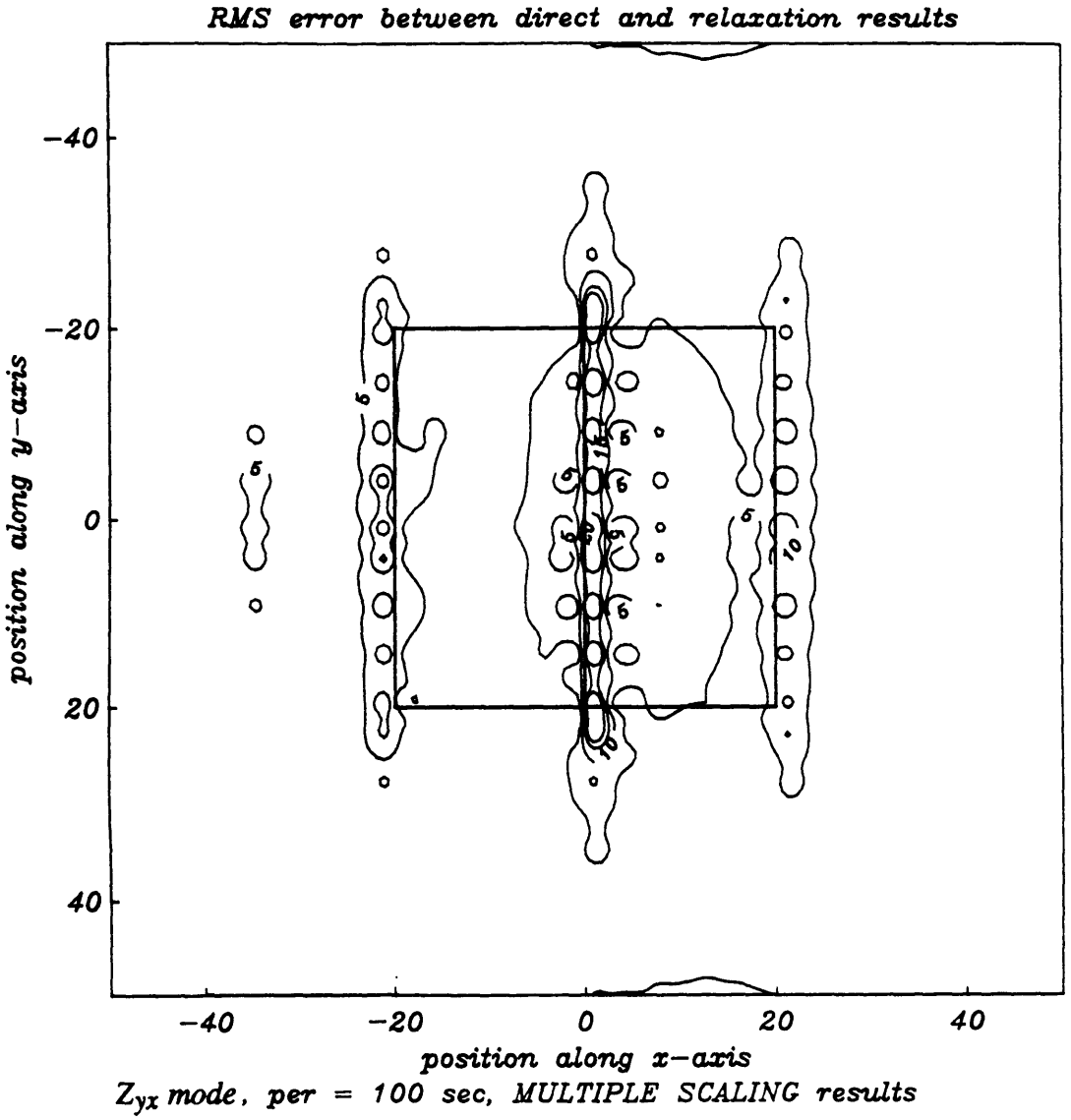


**Figure 2-33.** A contour plot of the RMS error in the $Z_{yx}$ response at a period of 100 seconds between the direct solution and the multiple scaling relaxation solution. The RMS error is defined in the text. Outlined are the positions of the conductive and resistive bodies.

CPU time per frequency at 150 iterations per polarization, and the MINRTRMS took 7 minutes of CPU time per frequency at 300 iterations per scale (two scales per polarization).

### *Conclusions*

We have developed several numerical schemes to solve for the magnetotelluric response of a 3D Earth model using finite differences on a staggered grid. The finite difference equations are based on the integral forms of Maxwell's equations, so the main issue is that of taking averages rather than in approximating derivatives. Our direct solution method is shown to compare favorably with *Wannamaker's* (1990) integral equation solutions for the same model. The relaxation solutions, though attractive because of their speed and minimal memory requirements, have difficulties in modifying the **H** field due to 3D conductivity contrasts. A multiple scaling approach has shown a dramatic improvement over the straight relaxation scheme, but more work needs to be carried out to determine the robustness of the multiple scaling method.

***References***

Adhidjaja, J.I., and Hohmann, G.W., 1989. A finite-difference algorithm for the transient electromagnetic response of a three-dimensional body, *Geophys. J. Int.*, **98**, 233-242.

Axelsson, O., 1980. Conjugate gradient type methods for unsymmetric and inconsistent systems of linear equations, *Lin. Alg. & its Applic.*, **29**, 1-16.

Concus, P., Golub, G.H., and O'Leary, D.P., 1976. A generalized conjugate gradient method for the numerical solution of elliptic partial differential equations, in *Sparse Matrix Computations*, edited by J.R. Bunch and D.J. Rose, Academic Press.

Fletcher, R., 1975. Conjugate gradient methods for indefinite systems, in *Proceedings of Dundee Conference on Numerical Analysis-1975*, edited by G.A. Watson, Springer-Verlag, Berlin.

Golub, G.H., and Van Loan, C.F., 1983. *Matrix Computations*, The John Hopkins University Press.

Greenfield, R.J., 1965. Two-dimensional calculations of magnetic micropulsation resonances, *PhD dissertation*, MIT.

Hestenes, M.R., and Stiefel, E., 1952. Methods of conjugate gradients for solving linear systems, *J. Res. Natl. Bureau Stand.*, **49**, 409-436.

Jacobs, D.A.H., 1981. The exploitation of sparsity by iterative methods, in *Sparse Matrices and their uses (Proc. Conf. Univ. Reading, Reading, 1980)*, Academic Press.

Jacobs, D.A.H., 1986. A generalization of the conjugate-gradient method to solve complex systems, *IMA J. Num. Anal.*, **6**, 447-452.

Jennings, A., 1977. Influence of the eigenvalue spectrum on the convergence rate of the conjugate gradient method, *J. Inst. Maths. Applics.*, **20**, 61-72.

Jiracek, G.R., Reddig, R.P., and Kojima, R.K., 1989. Application of the Rayleigh-FFT technique to magnetotelluric modeling and correction, *Phys. Earth planet. Int.*, **53**, 365-375.

Kershaw, D.S., 1978. The incomplete Cholesky-conjugate gradient method for the iterative solution of systems of linear equations, *J. Comp. Phys.*, **26**, 43-65.

Lanczos, C., 1961. *Linear Differential Operators*, D.Van Nostrand Co. Ltd.

Lockner, D.A., 1990. Modeling of brittle failure and comparisons to laboratory experiments, *PhD dissertation*, MIT.

Madden, T.R., 1976. Random networks and mixing laws, *Geophysics*, **41**, 1104-1125.

Madden, T.R., 1983. Microcrack connectivity in rocks: a renormalization group approach to the critical phenomena of conduction and failure in crystalline rocks, *J. Geophys. Res.*, **88**, 585-592.

Madden, T.R., and Mackie, R.L., 1989. Three-dimensional magnetotelluric modeling and inversion, *Proc. IEEE*, **77**, 318-333.

Meijerink, J.A., and Van der Vorst, H.A., 1977. An iterative solution method for linear systems of which the coefficient matrix is a symmetric M-matrix, *Math. Comp.*, **31**, 148-162.

Park, S.K., 1983. Three-dimensional magnetotelluric modeling and inversion, *PhD dissertation*, MIT, 185 p.

Park, S.K., Orange, A.S., and Madden, T.R., 1983. Effects of three-dimensional structure on magnetotelluric sounding curves, *Geophysics*, **48**, 1402-1405.

Ranganayaki, R.P., 1978. Generalized thin sheet approximation for magnetotelluric modeling, *PhD dissertation*, MIT.

Ranganayaki, R.P., and Madden, T.R., 1980. Generalized thin sheet analysis in magnetotellurics, an extension of Price's analysis, *Geophys. J. R. astr. Soc.*, **60**, 445-457.

Reid, J.K., 1971. On the method of conjugate gradients for the solution of large sparse systems of linear equations, in *Large Sparse Sets of Linear Equations*, Academic Press, 231-254.

San Filipo, W.A., and Hohmann, G.W., 1985. Integral equation solution for the transient electromagnetic response of a three-dimensional body in a conductive half-space, *Geophysics*, **50**, 798-809.

Southwell, R.V., 1946. *Relaxation Methods in Theoretical Physics*, Oxford University Press, London.

Stiefel, E., 1958. Kernal Polynomials in linear algebra and their numerical applications, *Nat. Bur. Stand. Appl. Math. Series*, **49**, 1-22.

Stratton, J.A., 1941. *Electromagnetic Theory*, McGraw-Hill Book Co.

Swift, C.M., 1967. A magnetotelluric investigation of an electrical conductivity anomaly in the southwestern United States, *PhD disseratation*, MIT.

Wannamaker, P.E., Hohmann, G.W., and San Filipo, W.A., 1984a. Electromagnetic modeling of three-dimensional bodies in layered earths using integral equations, *Geophysics*, **49**, 60-74.

Wannamaker, P.E. Hohmann, G.W., and Ward, S.H., 1984b. Magnetotelluric responses of three-dimensional bodies in layered earths, *Geophysics*, **49**, 1517-1533.

Wannamaker, P.E., 1990. Modeling three-dimensional magnetotelluric responses using integral equations, *Geophysics*, **in review**.

# Chapter 3
# Three-dimensional magnetotelluric inversion

"If there is no struggle, there is no progress."
- Frederick Douglas, 1857

## *Introduction*

Inversion algorithms operate on observed data to produce a model that predicts the observed data, perhaps subject to certain constraints. Linearized inversion schemes provide one method for dealing with non-linear inversion problems (those problems where the data are non-linearly related to the model parameters). They involve expanding the model predictions in a Taylor series around some point in the model space, and then solving for the model changes that minimize the error between the observed and predicted data. Many such schemes exist, such as the non-linear least squares method, but we prefer to use the maximum likelihood inversion procedure (*Mackie et al.*, 1988). The maximum likelihood solution is the solution that maximizes the joint probability of fitting the observed data (subject to the data covariance) and adhering to an *a priori* model (subject to the model covariance). This solution is obtained with the help of the sensitivity matrix, which is the matrix that relates small changes in the model parameters to changes in the observed data.

For the three-dimensional magnetotelluric inversion problem, we apply conjugate gradient relaxation methods to solve the maximum likelihood system of equations instead of solving that system directly using matrix inversion algorithms. In doing so, we avoid having to explicitly construct the sensitivity matrix; indeed, we only need to know the effect of the sensitivity matrix, or its transpose, multiplying an arbitrary vector. We will show that each of these operations can be done as one problem with sources distributed either in the volume, for the sensitivity matrix multiplying a vector, or sources distributed on the surface, for its transpose multiplying a matrix. This implementation greatly reduces the computational enormity of three-dimensional inversion, making practical three-dimensional inversions a possibility rather than an impossibility. Although we have not yet perfected the

algorithm described herein to the point where it is ready for practical use, we have progressed far enough to demonstrate that the method does indeed work as intended. A few details remain to be sorted out, and these will be discussed later.

### *Maximum Likelihood Inverse*

The maximum likelihood inverse is but one method to obtain a solution to a non-unique inverse problem. There are many procedures for obtaining such solutions, and each one is biased, but the maximum likelihood inverse clearly exposes its biases. The maximum likelihood inverse is an example of a linearized inversion scheme. Our derivation of the maximum likelihood inverse closely follows the work of *Tarantola and Valette* (1982) and *Tarantola* (1987). The maximum likelihood inverse, also called the stochastic inverse by *Franklin* (1970), gives the solution that minimizes a weighted sum of the variance of the difference between the data and model parameters and the difference between the model parameters and an *a priori* model (*Mackie et al.*, 1988).

To derive the maximum likelihood solution, we first assume that the errors between the observed data and the model predictions have Gaussian statistics. The data errors, therefore, are proportional to

$$\exp - \left[ (\mathbf{d} - \mathbf{g}(\mathbf{m}))^H \mathbf{R}_{\bar{dd}}^{-1} (\mathbf{d} - \mathbf{g}(\mathbf{m})) \right] \qquad (3\text{-}1)$$

where $\mathbf{d}$ are the observed data, $\mathbf{g}$ is the operator that maps a model $\mathbf{m}$ to the data space, $\mathbf{R}_{dd}$ is the data covariance matrix, and the superscript $H$ stands for Hermitian, or complex conjugate transpose. The data covariance matrix is a measure of the experimental uncertainties in the data and can be defined as $E[(\mathbf{d}-\mu)(\mathbf{d}-\mu)^H]$ where $\mu$ represents the data mean values and $E$ represents the expectation operator. If the data errors are uncorrelated, then the data covariance matrix is a diagonal matrix with each diagonal term representing the variance in that particular data parameter. We likewise assume that the errors between

the model parameters and the *a priori* information also have Gaussian statistics, and therefore are proportional to

$$\exp - \left[ (\mathbf{m} - \mathbf{m}_o)^H \mathbf{R}_{mm}^{-1} (\mathbf{m} - \mathbf{m}_o) \right] \qquad (3\text{-}2)$$

where $\mathbf{m}_o$ is the *a priori* model and $\mathbf{R}_{mm}$ is the model covariance matrix. The model covariance matrix is a measure of the uncertainties in the *a priori* information. Since it is difficult to put numerical values on the variances of the model parameters, the model covariance matrix usually specifies only relative bounds on the model parameters. That is, the entries describe the variance of each model parameter relative to the other model parameters, and the magnitude is related to how much more the data is trusted than the *a priori* information. Usually, a much larger variance is assigned to the *a priori* information than to the data. An exception to this is when a particular model parameter is well established by some other means, for example, the conductivity of sea water. In this case, a very small variance would be assigned to those parameters whose values were well known. If some parameters were known absolutely, they could alternatively be taken out of the inversion scheme altogether. If the data errors are uncorrelated with the model errors, then their joint probability distribution also has Gaussian statistics and is proportional to

$$\exp - \left[ (\mathbf{d} - \mathbf{g}(\mathbf{m}))^H \mathbf{R}_{dd}^{-1} (\mathbf{d} - \mathbf{g}(\mathbf{m})) + (\mathbf{m} - \mathbf{m}_o)^H \mathbf{R}_{mm}^{-1} (\mathbf{m} - \mathbf{m}_o) \right] . \qquad (3\text{-}3)$$

The maximum likelihood solution is that solution which maximizes the joint probability function, or equivalently minimizes the exponent in equation 3-3.

Most geophysical inverse problems, including the magnetotelluric case, are non-linear, and we can deal with them by using linearized inversion schemes. If we expand the model predictions in a Taylor Series around some model $\mathbf{m}'$, we can write:

$$\mathbf{g}(\mathbf{m}) \approx \mathbf{g}(\mathbf{m}') + \frac{\partial \mathbf{d}}{\partial \mathbf{m}} \Delta \mathbf{m} . \qquad (3\text{-}4)$$

This assumes of course that **m** and **m'** are close enough that a linear approximation is valid. The derivative terms are collected into a matrix that is called the 'sensitivity' matrix **A**. It is called the sensitivity matrix because its entries describe the perturbations in the data (or sensitivity of the data) due to perturbations in the model parameters. The sensitivity matrix takes the form $A_{ij} = \partial d_i / \partial m_j$. For non-linear problems, $\Delta\mathbf{m}$ describes only local changes, so the inversion must be iterated, each time updating the model. For simplicity, rewrite equation 3-4 as $\mathbf{g}(\mathbf{m}_{k+1}) = \mathbf{g}(\mathbf{m}_k) + \mathbf{A}\Delta\mathbf{m}_k$ where $\mathbf{m}_{k+1} = \mathbf{m}_k + \Delta\mathbf{m}_k$. We take these two expressions and substitute them into equation 3-3, take the derivative with respect to $\Delta\mathbf{m}_k^H$, and set the derivative to zero. The maximum likelihood solution for non-linear problems is then given by

$$(\mathbf{A}_k^H \mathbf{R}_{dd}^{-1} \mathbf{A}_k + \mathbf{R}_{mm}^{-1})^{-1} \Delta\mathbf{m}_k = \mathbf{A}_k^H \mathbf{R}_{dd}^{-1} (\mathbf{d} - \mathbf{g}(\mathbf{m}_k)) + \mathbf{R}_{mm}^{-1} (\mathbf{m}_o - \mathbf{m}_k) . \tag{3-5}$$

This equation has a straightforward interpretation. The model changes calculated at each step represent a compromise between fitting the data and adhering to an *a priori* model. The compromise is weighted by the inverses of the data and model covariance matrices. We usually do not explicitly know **g**, but we can calculate the model predictions **g(m)** by use of a forward modeling code.

In our implementation of the maximum likelihood inverse, we have used logarithmic parameterization of the data and model parameters. This is useful for several reasons. First, it removes any bias associated with using either conductivity or resistivity as model parameters. Furthermore, it guarantees the positiveness of the model parameters (i.e., no negative resistivities or conductivities are allowed). In addition, it is the natural way of dealing with complex-valued data that are separated into log amplitude and phase ($ln\ Z = ln\,|Z| + i\theta$). Finally, logarithmic parameterization allows for larger changes in the model parameters as the inversion is iterated For the electrical problem, where the resistivity can vary by several orders of magnitude in the Earth, this reduces the total

number of iterations needed to reach an acceptable solution. For logarithmic parameterization, the sensitivity terms become

$$A_{ij} = \frac{\partial \ln d_i}{\partial \ln m_j} = \frac{m_j}{d_i} \frac{\partial d_i}{\partial m_j} . \qquad (3\text{-}6)$$

Since the model parameters are real, $\mathbf{m_0} - \mathbf{m_k}$ becomes $\ln (\mathbf{m_0}/\mathbf{m_k})$. The data are complex-valued so that $\mathbf{d} - \mathbf{g}(\mathbf{m_k})$ becomes $\ln |\mathbf{d}/\mathbf{g}(\mathbf{m_k})| + i(\theta_d - \theta_{g(m)})$. Phase angles are already logarithmic parameters and, for the full 3D MT case, we also have to worry about directions and ellipticities, but more will be said about this later. Finally, the model changes $\mathbf{m_{k+1}} = \mathbf{m_k} + \Delta\mathbf{m_k}$ become $\mathbf{m_{k+1}} = \mathbf{m_k} \exp(\Delta\mathbf{m_k})$.

As mentioned previously, the data covariance is a measure of the uncertainties in the data and can be computed or measured directly. The model covariance, on the other hand, is much more subjective because it cannot be measured directly. The model covariance is used to apply a set of weights or constraints to the model parameters. Some simple constraints could be imposing smoothing between neighboring points, forcing certain parameters to be correlated with each other, or increasing/decreasing the freedom with which certain parameters can change. In the logarithmic parameterization scheme, the covariance matrices actually represent the covariances of the logarithms of the data and model parameters.

### A note on the use of *a priori* information

We have advocated the use of *a priori* information in our inversion schemes since it is rare that one does not have any information *a priori* concerning the geology, tectonics, or physical properties of the area being studied. Furthermore, using different *a priori* models and allowing for different model covariance constraints helps one to understand which model parameters are important, or required, in fitting the observed data. Although the obtained models represent only a few of the large number of possible models, meaningful

studies can be made testing various competing geologic hypotheses provided one interprets the results with caution.

### *Sensitivity analysis and reciprocity*

In this section we develop the sensitivity analysis for the magnetotelluric problem and then show how reciprocity can be implemented in carrying out the sensitivity analysis. Maxwell's equations can be written in matrix form as

$$\begin{bmatrix} -\sigma & \nabla x \\ \nabla x & -i\mu\omega \end{bmatrix} \begin{bmatrix} \mathbf{E} \\ \mathbf{H} \end{bmatrix} = \begin{bmatrix} \mathbf{J} \\ 0 \end{bmatrix} \tag{3-7}$$

where **J** are the media current sources, which for the MT problem are usually represented by a uniform current sheet far above the Earth's surface. If the media conductivity is perturbed by an amount $\delta\sigma$, then the **E** and **H** fields will also be perturbed by amounts $\delta E$ and $\delta H$ respectively

$$\begin{bmatrix} -(\sigma+\delta\sigma) & \nabla x \\ \nabla x & -i\mu\omega \end{bmatrix} \begin{bmatrix} \mathbf{E}+\delta\mathbf{E} \\ \mathbf{H}+\delta\mathbf{H} \end{bmatrix} = \begin{bmatrix} \mathbf{J} \\ 0 \end{bmatrix}. \tag{3-8}$$

Expanding this equation, subtracting it from equation 3-7, and dropping second-order terms, we obtain

$$\begin{bmatrix} -\sigma & \nabla x \\ \nabla x & -i\mu\omega \end{bmatrix} \begin{bmatrix} \delta\mathbf{E} \\ \delta\mathbf{H} \end{bmatrix} = \begin{bmatrix} \mathbf{E}\,\delta\sigma \\ 0 \end{bmatrix}. \tag{3-9}$$

Thus, the **E** and **H** field perturbations satisfy the original EM equations except that the current sources are equal to the media perturbations times the original **E** field. That is, the field perturbations can be solved for by doing forward problems with the proper current source distribution. In terms of Green's functions, equation 3-7 can be rewritten as (*Kong*, 1986)

$$\begin{bmatrix} \mathbf{E}(r) \\ \mathbf{H}(r) \end{bmatrix} = \iiint d^3s\, \mathbf{G}(r,s) \cdot \mathbf{J}(s) \tag{3-10}$$

where G(r,s) is the dyadic Green's function (a matrix of Green's functions). The elements of the dyadic Green's function are $G_i(r,s)_j$ where $r$ is the observation point, $s$ is the source point, $i$ represents the observed field component ($i=1,2,...,6$ corresponding to $E_x$, $E_y$,..., $H_z$ ) and $j$ represents the source component ($j=1,2,3$ corresponding to $J_x$, $J_y$, $J_z$ ). Using this notation, equation 3-9 can be expressed as

$$\begin{bmatrix} \delta\mathbf{E}(r) \\ \delta\mathbf{H}(r) \end{bmatrix} = \iiint d^3s\, \mathbf{G}(r,s) \cdot \mathbf{E}(s)\, \delta\sigma(s) \,. \tag{3-11}$$

Thus, it would appear that the dyadic Green's function needs to be computed for every point in the media where we wish to determine the electrical properties.

If reciprocity is employed, however, we find that we only need to compute Green's functions for every surface location where a measurement has been made. To derive the reciprocity relationship, we follow the work of *Lanczos* (1961) who defined the normal problem (the original system of equations) and the adjoint problem as

$$\mathbf{D}\begin{bmatrix} v_1 \\ \vdots \\ v_n \end{bmatrix} = \begin{bmatrix} b_1 \\ \vdots \\ b_m \end{bmatrix} \quad \Rightarrow \quad \mathbf{D}v_k = b_j \tag{3-12}$$

$$\mathbf{D}^H\begin{bmatrix} u_1 \\ \vdots \\ u_m \end{bmatrix} = \begin{bmatrix} a_1 \\ \vdots \\ a_n \end{bmatrix} \quad \Rightarrow \quad \mathbf{D}^H u_j = a_k \tag{3-13}$$

In these equations, the operators could represent matrices, or they could represent continuous differential operators in which case the vector products become integrations. These equations are called homogeneous if the right-hand sides are equal to zero. Notice that homogeneous differential equations do not imply that the boundary terms are also homogeneous (which means that some linear combination of the function and its derivatives are zero on the boundary). One could have homogeneous differential equations with inhomogeneous boundary conditions. An example of this is Laplace's equation with side boundary conditions. In our case, however, **D** would represent Maxwell's equations, $v_k$ would represent the **E** and **H** fields, and bj would represent the current sources. $\mathbf{D}^H$

thus represents the adjoint operator, which itself is a linear differential operator, and which is uniquely related to the normal operator by the extended Green's identity, or bilinear identity (*Lanczos,* 1961). If the boundary terms are homogeneous, then the bilinear identity for differential operators takes the form

$$\iiint \left[ \sum_{j=1}^{m} u_j^* \, \mathbf{D} \, v_k - \sum_{k=1}^{n} v_k \left( \mathbf{D}^H u_j \right)^* \right] d^3s = 0 \, . \qquad (3\text{-}14)$$

Inhomogeneous boundary terms would show up on the right-hand side as a surface integral of some bilinear function of u and v. The adjoint boundary terms are the minimum number that are required to make the right-hand side of equation 3-14 equal to zero for homogeneous boundary conditions of the normal problem.

A word is in order here concerning boundary conditions. First, it should be realized that a differential operator really has no meaning without prescribed boundary terms. The boundary conditions belong to the operator and cannot be separated from it (*Lanczos*, 1961). That is, it is not only the differential equations that determine the matrix **D**, but also the corresponding boundary conditions. The boundary conditions to the normal problem also determine the boundary conditions for the adjoint problem, and therefore, the adjoint boundary terms are also uniquely determined. In this section, we have assumed homogeneous boundary conditions. Even if the boundary conditions were inhomogeneous, it would not pose a problem because the solution to the inhomogeneous boundary value problem is obtained with the Green's function for the homogeneous boundary value problem. That is, if the problem is prescribed with inhomogeneous boundary conditions, it can be separated into two problems whose solutions are added to give the complete solution. The first problem is the homogeneous differential equation with inhomogeneous boundary values, and the second problem is the inhomogeneous differential equation with homogeneous boundary values. The solution to the first problem will be given as an integral over the surface of the volume and will involve the inhomogeneous boundary

conditions and the associated Green's function and its derivatives on the surface. The solution to the second problem will be an integral over the volume and will involve the source terms and the associated Green's function.

The solution to the inhomogeneous equation with homogeneous boundary conditions, equation 3-12, can be derived from the bilinear identity and is given by

$$v_k(\mathbf{r}) = \iiint d^3s \sum_{j=1}^{m} \underline{G}_j^*(s,\mathbf{r})_k \, b_j(s) \tag{3-15}$$

where the underscored Green's function is actually the Green's function for the adjoint problem. We will show that this can be cast into the more usual form of equation 3-10 by use of the reciprocal relationship.

The dyadic Green's function for the normal problem with homogeneous boundary conditions is given by

$$\mathbf{D}\begin{bmatrix} G_1(\xi,s)_j \\ \vdots \\ G_n(\xi,s)_j \end{bmatrix} = \begin{bmatrix} 0_1 \\ \vdots \\ \delta_j(\xi-s) \\ \vdots \\ 0_m \end{bmatrix}, \tag{3-16}$$

or $\mathbf{DG}(\xi,s)_j = \Delta_j$. Here $\Delta_j$ refers to the vector with zeros in all entries except the $j^{th}$ entry, which contains a delta function, and $\mathbf{G}(\xi,s)_j$ refers to the vector of corresponding Green's functions, which are the effect at $\xi$ due to a source at $s$, integrated over the entire space. Likewise, the Green's function for the adjoint problem is given by $\underline{\mathbf{G}}$

$$\mathbf{D}^H\begin{bmatrix} \underline{G}_1(\xi,\mathbf{r})_k \\ \vdots \\ \underline{G}_m(\xi,\mathbf{r})_k \end{bmatrix} = \begin{bmatrix} 0_1 \\ \vdots \\ \delta_k(\xi-\mathbf{r}) \\ \vdots \\ 0_n \end{bmatrix}, \tag{3-17}$$

or $\mathbf{D}^H\underline{\mathbf{G}}(\xi,r)_k = \underline{\Delta}_k$. Since the delta function is real, we could also write $\mathbf{D}^T\underline{\mathbf{G}}^*(\xi,r)_k = \underline{\Delta}_k$. Here, $\underline{\Delta}_k$ refers to the vector with all zero entries except for the $k^{th}$ entry, which contains a delta function. We denote this vector with an underbar because in the general case it may be of different length than $\Delta_j$ and is related to the adjoint operator. If these expressions for the Green's functions are substituted into the bilinear identity, we obtain, since the delta function is real,

$$\iiint \left[ \sum_{i=1}^{m} \underline{G}_i^*(\xi,r)_k \left[\Delta_j\right]_i - \sum_{i=1}^{n} G_i(\xi,s)_j \left[\underline{\Delta}_k\right]_i \right] d^3\xi = 0 . \qquad (3\text{-}18)$$

When integrated over the delta functions ( $[\Delta_j]_i = 0$ except when i=j and $\xi$=s; likewise, $[\Delta_k]_i = 0$ except when i=k and $\xi$=r), we obtain the reciprocity relation

$$\underline{G}_j^*(s,r)_k = G_k(r,s)_j . \qquad (3\text{-}19)$$

With this reciprocal relation, we can rewrite equation 3-15 in the more usual form of

$$v_k(r) = \iiint d^3s \sum_{j=1}^{m} G_k(r,s)_j \, b_j(s) . \qquad (3\text{-}20)$$

Since the curl operator and real constants are self adjoint (imaginary constants have a change in sign), the adjoint operator for Maxwell's equations is

$$\mathbf{D}^H = \begin{bmatrix} -\sigma & \nabla x \\ \nabla x & i\mu\omega \end{bmatrix} . \qquad (3\text{-}21)$$

Thus, the adjoint to Maxwell's equations is also the electromagnetic equations except with backwards time or negative frequencies. Since the adjoint in the frequency domain is simply the complex conjugated electromagnetic equations, $\underline{\mathbf{G}}^* = \mathbf{G}$, we arrive at the desired reciprocity relation,

$$G_j(s,r)_k = G_k(r,s)_j . \qquad (3\text{-}22)$$

This simple relation is of tremendous importance for all geophysical inverse problems. It says that the effect at the surface due to a source in the interior is equivalent to putting a source on the surface and solving for the effect in the interior (one must also take into account the proper interchange of vector components). In the magnetotelluric case, for example, the term $G_1(r,s)_2$ is the $E_x$ effect at $r$ (at the surface) due to a unit $J_y$ dipole source at $s$ (in the interior), which by reciprocity is equal to $G_2(s,r)_1$, which is the $E_y$ effect at $s$ (in the interior) due to a unit $J_x$ dipole source at $r$ (at the surface). Similarly, the term $G_4(r,s)_2$ is the $H_x$ effect at $r$ (at the surface) due to a unit $J_y$ dipole source at $s$ (in the interior), which by reciprocity is equal to $G_2(s,r)_4$, which is the $E_y$ effect at $s$ (in the interior) due to a unit $H_x$ magnetic source at $r$ (at the surface). Thus, if one were actually constructing the sensitivity matrix for the 3D MT problem, one would only need to do forward modeling runs with sources at each surface measurement site instead of doing forward modeling runs with sources at each model block, which results in a tremendous time savings. As we will point out, however, our inversion algorithm does not actually require computing the sensitivity matrix, but the reciprocity relationship will still play an important role.

### *Relaxation solution of the inverse problem*

To carry out a linearized inversion using the maximum-likelihood inverse, one must determine the sensitivity matrix $\mathbf{A}$, compute $\mathbf{A}^H\mathbf{A}$, and then invert $\mathbf{A}^H\mathbf{A}$ (for the moment we are neglecting the data covariance weighting). In the 3D case, computing $\mathbf{A}$ is a computationally enormous task even when using reciprocity. This is because the total number of forward problems needed to construct the sensitivity matrix is on the order of (no. measurement sites) x (no. frequencies). For a nominal 3D problem, there might be 20 measurement sites and eight frequencies, thereby requiring on the order of 160 forward problems simply to set up the sensitivity matrix for one iteration of the inversion (of course one must also take into account source polarization and vector components of the fields so

this estimate is just a lower bound). In addition, for this modest 3D problem, there might be on the order of several thousand model parameters (20x20x10 model = 4000 model parameters). Inverting the matrix $\mathbf{A}^H\mathbf{A}$, which has the dimension of the number of model parameters, is also a big computational task. To make 3D inversions computationally tractable, another way must be found which circumvents these problems.

One obvious way to reduce the computational complexity and magnitude of the 3D inverse problem is to use conjugate gradient relaxation techniques to solve the maximum likelihood equations. At each iteration of the inversion, we will use conjugate gradient relaxation to obtain an approximate solution $\Delta\mathbf{m}$ to the maximum likelihood equations. This bypasses the need to do a large matrix inversion at each iteration of the inversion procedure. We can use the standard conjugate gradient techniques because the system is positive definite and hermitian. It should be made clear that when using relaxation methods to solve the non-linear inversion, there will be two levels of iteration involved. The outer loop is the iteration of the non-linear maximum likelihood equations. The inner loop is the iteration of the conjugate gradient relaxation procedure that is used to solve for the approximate $\Delta\mathbf{m}_k$ at each iteration of the inversion. It is our contention that only a few relaxation iterations are necessary at each inversion iteration since the model must be updated and the whole process begun again. Furthermore, when using relaxation techniques, we never need to explicitly know $\mathbf{A}$, the sensitivity matrix. We only need to know the effect of $\mathbf{A}$ or $\mathbf{A}^H$ on a vector. We will show that these operations can be done without actually constructing the sensitivity matrix. These features will make the 3D inverse problem computationally manageable.

We will first summarize our 3D inversion scheme, then we will discuss the details of the algorithm:

| | |
|---|---|
| For k = 1 to max # inversion iterations | NON-LINEAR INVERSION |
| $\mathbf{g(m_k)}$ | response of current model |
| $\mathbf{d - g(m_k)}$ | data residuals |
| $\mathbf{m_o - m_k}$ | model residuals |
| $\mathbf{b = A^H R_{dd}^{-1} (d - g(m_k)) + R_{mm}^{-1} (m_o - m_k)}$ | one forward problem with surface sources per frequency |
| $\Delta\sigma_o = 0 \; ; \; \mathbf{r_o = b}$ | initialize conjugate gradient algorithm |
| For i = 1 to max # relaxation iterations | RELAXATION SOLUTION |
| $\beta_i = \mathbf{r}_{i-1}^T \mathbf{r}_{i-1} / \mathbf{r}_{i-2}^T \mathbf{r}_{i-2}$ | $(\beta_o = 0)$ |
| $\mathbf{p_i = r_{i-1} + \beta_i p_{i-1}}$ | $(\mathbf{p_1 = r_o})$ update search direction |
| $\mathbf{B p_i = \left[A^H R_{dd}^{-1} A + R_{mm}^{-1}\right] p_i}$ | two forward problems per frequency |
| $\alpha_i = \mathbf{r}_{i-1}^T \mathbf{r}_{i-1} / \mathbf{p}_i^T \mathbf{B} \, \mathbf{p}_i$ | step length along search direction |
| $\Delta\sigma_i = \Delta\sigma_{i-1} + \alpha_i \mathbf{p}_i$ | update model perturbations |
| $\mathbf{r_i = r_{i-1} - \alpha_i B p_i}$ | update residuals |
| end loop on relaxation iterations | |
| $\sigma_{k+1} = \sigma_k + \Delta\sigma$ | update model parameters |
| end loop on inversion iterations | |

A similar scheme has been developed by *Mora* (1987) who used the conjugate gradient method of nonlinear least squares to invert seismic reflection data for P-wave and S-wave velocities and density in two dimensions. He correctly ascertained that the operation of $\mathbf{A^H y}$ was equivalent to doing one forward modeling problem with sources

distributed on the surface, which he showed was actually a propagation in backwards time of the surface residual error fields. What he did not recognize, however, is that the operation **Ax** is equivalent to doing one forward problem, except that in this case, sources are distributed throughout the media and not on the surface. Consequently, he had approximated the term $\left[\mathbf{A}^H \mathbf{R}_{dd}^{-1} \mathbf{A} + \mathbf{R}_{mm}^{-1}\right]$ in his stochastic inversion procedure by $\eta \mathbf{R}_{mm}^{-1}$, where the model covariance matrix was assumed a diagonal matrix and $\eta$ was a step length that ensured his error functional was minimized. Although *Mora* (1987) obtained good results with his algorithm for the inversion of seismic reflection data, he stated that for highly non-linear problems, the method probably would not work well. Electrical properties are very non-linear and can vary over several orders of magnitude, so we feel that it is important to treat the $\mathbf{A}^H\mathbf{A}$ term more rigorously. Furthermore, since the $\mathbf{A}^H\mathbf{A}$ effect on a vector can be computed with just two forward modeling runs, as we will show, it is obviously worthwhile to proceed in this manner.

The maximum likelihood equation 3-5 can be written as $\mathbf{Bu} = \mathbf{b}$ where $\mathbf{B} = (\mathbf{A}^H\mathbf{R}_{dd}^{-1}\mathbf{A} + \mathbf{R}_{mm}^{-1})$, $\mathbf{u} = \Delta\mathbf{m}$, and $\mathbf{b} = [\mathbf{A}^H\mathbf{R}_{dd}^{-1}(\mathbf{d} - \mathbf{g}(\mathbf{m})) + \mathbf{R}_{mm}^{-1}(\mathbf{m} - \mathbf{m}_o)]$. In the standard conjugate gradient procedure (*Hestenes and Stiefel,* 1952), we need to know the initial residual, $\mathbf{r}_o = \mathbf{b} - \mathbf{Bu}_o$, and we need to be able to compute what **B** times some vector yields at each iteration. In this case, we set $\mathbf{u}_o = \Delta\mathbf{m} = 0$ since, unlike the 3D forward problem, we have no way of knowing what a good starting value for $\Delta\mathbf{m}$ would be. Therefore, in terms of the maximum likelihood equation, we need to be able to compute the initial residual $\mathbf{r}_o = [\mathbf{A}^H\mathbf{R}_{dd}^{-1}(\mathbf{d} - \mathbf{g}(\mathbf{m}))+ \mathbf{R}_{mm}^{-1}(\mathbf{m} - \mathbf{m}_o)]$, and at each relaxation step the effect of $(\mathbf{A}^H\mathbf{R}_{dd}^{-1}\mathbf{A} + \mathbf{R}_{mm}^{-1})$ on some vector. Since $\mathbf{R}_{dd}^{-1}$ and $\mathbf{R}_{mm}^{-1}$ are known , we only need to be able to compute quantities like $\mathbf{p} = \mathbf{Ax}$ and $\mathbf{q} = \mathbf{A}^H\mathbf{y}$. We can compute these quantities using one forward modeling run each without ever constructing the actual sensitivity matrix.

The sensitivity matrix, given in equation 3-6, describes the effect of a surface measurement to a small perturbation in a physical property of the media. Although we have

not stated explicitly which surface measurement we will be inverting for, it will naturally involve derivatives of the surface **E** and **H** fields, and will be made up of terms like $\partial E_x/\partial\sigma$, $\partial E_y/\partial\sigma$, $\partial H_x/\partial\sigma$, $\partial H_y/\partial\sigma$. The row space of the sensitivity matrix corresponds to the model parameter space. That is, each element in a particular row represents the perturbation in one of the surface fields at one site, one frequency, and one polarization due to a perturbation in one particular model parameter. If one were actually constructing the sensitivity matrix, one would put a unit current source at each surface measurement site for each frequency, and then compute the fields in the interior due to that current source (of course, this uses the reciprocal relationships derived in the previous section). These fields multiplying the original **E** fields, equation 3-9, would represent the values $\partial\mathbf{E}/\partial\sigma$ and $\partial\mathbf{H}/\partial\sigma$, and we could then compute the desired sensitivity terms.

For the relaxation solution, however, we do not need to construct the sensitivity matrix. Notice that by the definition of the sensitivity matrix, the sensitivity matrix multiplying a vector is simply a sum over all model parameters of the sensitivity term multiplying the vector component for that model block :

$$\mathbf{p} = \mathbf{A}\mathbf{x} \sim \sum_{\substack{\text{model} \\ \text{parameters}}} \frac{\partial(\mathbf{E},\mathbf{H})}{\partial\sigma}\mathbf{x} \,. \tag{3-23}$$

Each component of the vector **p** is defined at a particular surface measurement site and a particular frequency. We can use the principle of linear superposition to compute the vector **p** without ever computing the sensitivity matrix **A**. The superposition principle states that if **T** is the linear system transformation, then for any two inputs $x_1$ and $x_2$ and any scalar constant c,

$$\begin{aligned} \mathbf{T}[x_1 + x_2] &= \mathbf{T}[x_1] + \mathbf{T}[x_2] \text{ , and} \\ \mathbf{T}[cx_1] &= c\mathbf{T}[x_1] \,. \end{aligned} \tag{3-24}$$

If this is true for two inputs, then it can be shown to be true for any number of inputs. In our case, the linear system **T** is represented by Maxwell's equations, and the inputs

correspond to the media current sources, as shown in equation 3-1. We have seen that the sensitivity in the surface fields is the response due to a unit current source in the media multiplying the original **E** field at that location. Therefore, the vector **p** goes like

$$\mathbf{T}[E_o(1)]\, x(1) + \mathbf{T}[E_o(2)]\, x(2) + \cdots + \mathbf{T}[E_o(n)]\, x(n) \qquad (3\text{-}25)$$

where $E_o(i)$ represents a current source distribution in the media that has a current dipole at the $i^{th}$ model parameter and no other sources in the media (the current source is a unit source multiplied by the original **E** field at that location). Employing the superposition principle allows us, however, to alternatively express the vector **p** as

$$\mathbf{T}[E_o(1)\, x(1) + E_o(2)\, x(2) + \cdots + E_o(n)\, x(n)]\,. \qquad (3\text{-}26)$$

We see that this is equivalent to putting all the sources in the media at the same time and computing one forward problem to determine the effect at the surface. The surface fields give the desired result of the sensitivity matrix multiplying a vector for every surface measurement site for one frequency, and this is done without ever actually computing the sensitivity matrix. We have defined one forward problem as corresponding to two polarizations at one frequency. We see that we have gained tremendously in terms of computation time by using this approach. Computing the sensitivity matrix by the traditional, 'non-reciprocal' method required doing one forward problem for each model parameter for each frequency. Utilizing the reciprocity relationships reduces the number of forward problems to the number of surface measurement sites for each frequency. However, our approach for computing **Ax** requires only one forward problem for each frequency.

Likewise, we can employ a similar procedure for the $\mathbf{A}^H$ operation. We can express the vector $\mathbf{q}=\mathbf{A}^H\mathbf{y}$ in terms of another vector **Q** where $\mathbf{Q} = \mathbf{A}^T\mathbf{y}^*$ and $\mathbf{q} = \mathbf{Q}^* = (\mathbf{A}^T\mathbf{y}^*)^* = \mathbf{A}^H\mathbf{y}$. The column space of the sensitivity matrix corresponds to the data space, and each element in a particular column corresponds to a perturbation in one of the surface fields at

one of the measurement sites and one frequency for one particular model parameter. The vector **Q** therefore goes as,

$$\mathbf{Q} \sim \sum_{\text{freq}} \sum_{\text{surf}} \frac{\partial (E,H)_{\text{surf}}}{\partial \sigma} y^*_{\text{surf}}, \tag{3-27}$$

which is a sum over all frequencies and all surface measurements of the sensitivity term multiplying the vector component for that particular frequency and surface measurement, the result being given at an interior model block. As before, we can use the principle of linear superposition to compute the vector **Q**. Using reciprocity, we have seen that the sensitivity in the surface fields is the response due to unit current or magnetic sources on the surface, depending on whether one was solving for the perturbed **E** fields or **H** fields. We can therefore express the vector **Q** as

$$\left[\mathbf{T}\left[S(1)\right] y^*(1) + \mathbf{T}\left[S(2)\right] y^*(2) + \cdots + \mathbf{T}\left[S(k)\right] y^*(k)\right] E_o(i) \tag{3-28}$$

where S(j) represents a unit surface source, either electric or magnetic, and $E_o(i)$ is the original **E** field at the $i^{th}$ model block. The principle of linear superposition, however, allows us to rewrite the vector **Q** as

$$\left[\mathbf{T}\left[S(1)\, y^*(1) + S(1)\, y^*(1) + \cdots + S(k)\, y^*(k)\right]\right] E_o(i) \tag{3-29}$$

which corresponds to one forward modeling run with all the sources distributed at the surface simultaneously. This computation is similar to a downwards propagation of surface fields, but is actually a downwards propagation in *backwards* time. Since we are really computing $\mathbf{A}^H\mathbf{y}$, and since by reciprocity $G_j(\mathbf{s},\mathbf{r})_i = G_i(\mathbf{r},\mathbf{s})_j$, the $\mathbf{A}^H\mathbf{y}$ operation is actually a sum of the complex conjugate of the Green's function responses to the surface sources, and the complex conjugate of the Green's function involves negative frequencies, or equivalently, backwards time.

Therefore, we can carry out one iteration of the conjugate gradient procedure without ever explicitly computing the sensitivity matrix. We merely need to compute two forward problems per frequency with sources distributed throughout the volume and across

the surface (at the initial iteration one additional forward problem is required to compute the initial residual). The surface sources in the calculation of the initial residual are simply $\mathbf{R}_{dd}^{-1}(\mathbf{d} - \mathbf{g}(\mathbf{m}_k))$, which are given at each surface measurement location and frequency. For each iteration of the conjugate gradient procedure, one must first compute $\mathbf{A}\mathbf{p}_i$ where $\mathbf{p}_i$ is the search direction at the $i^{th}$ iteration. The sources for this calculation are therefore the vector $\mathbf{p}_i$, which has a value at each interior model block. One must then compute $\mathbf{A}^H \mathbf{R}_{dd}^{-1} \mathbf{A}\, \mathbf{p}_i$. The sources for this calculation therefore are $\mathbf{R}_{dd}^{-1} \mathbf{A}\, \mathbf{p}_i$, which is a vector with values given at each surface measurement location and frequency. The relaxation inversion procedure, therefore, is seen to be a tremendous time savings when compared to constructing and storing the sensitivity matrix for a 3D model.

Our motivation for this procedure came from our experiences in implementing it in 1D and 2D geometries (*Madden and Mackie*, 1989). In 1D and 2D geometries, there is no time savings involved in using relaxation methods because the models are not too large, and by using networks, one can compute the sensitivity terms quickly and accurately. However, we found that in 1D and 2D, the relaxation technique gave results comparable to the direct results. Here, direct results refer to explicitly computing the sensitivity matrix and solving the maximum likelihood equations by matrix inversion whereas relaxation results refer to the relaxation solution outlined above. The results of the 1D and 2D comparisons are found in *Madden and Mackie* (1989) but we will summarize them here.

For 1D inversions, a one relaxation step solution for $\Delta\mathbf{m}$ was practically indistinguishable from the direct inversion for $\Delta\mathbf{m}$. When extended to 2D geometries, we found that we could not get away with one relaxation step per inversion iteration. With only one relaxation step, the RMS data error (error between the observed data and that predicted by the model) was reduced to approximately 20% and did not decrease any further. This is because the relaxation procedure filters out eigenvectors in the solution that are associated with small eigenvalues. Presumably, the finer details of the 2D models, which are necessary to reduce the data error, are associated with small eigenvalue eigenvectors.

Increasing the number of relaxation steps helps to some degree, but does not help as much as we would like. Implementing a preconditioning scheme improves the convergence properties of the inversion. We used inverses of the 1D sensitivity analyses ($\mathbf{A}^T\mathbf{A}$) for each vertical strip of model blocks as preconditioners. With this preconditioning and five relaxation steps per inversion iteration, the relaxation inversion is able to compete with the direct solution. That is, error levels are routinely reduced to below 1% for noise-free theoretical data.

For 3D data and Earth models, we had no idea what type of behavior to expect. As a first step, we implemented the standard conjugate gradient procedure without any form of preconditioning. As we will show later, this routinely decreases the error levels to around 2% for theoretical noise-free data. Indeed, we found that the simple preconditioning used in the 2D procedures was numerically unstable in 3D geometries. We will discuss this behavior more extensively later.

### *Details of the 3D inversion procedure*

The first step in the inversion procedure is deciding which parameters to invert for (e.g., phase, apparent resistivities, etc.). In magnetotellurics, we typically measure the impedance tensor over a range of frequencies at each measurement site. The impedance tensor, which relates the horizontal **E** fields to the horizontal **H** fields, is given by

$$\begin{bmatrix} E_x(\omega) \\ E_y(\omega) \end{bmatrix} = \begin{bmatrix} Z_{xx} & Z_{xy} \\ Z_{yx} & Z_{yy} \end{bmatrix} \begin{bmatrix} H_x(\omega) \\ H_y(\omega) \end{bmatrix}. \tag{3-30}$$

Assuming that there are two linearly independent source polarizations, the impedance tensor is given by

$$\mathbf{Z} = \frac{\begin{bmatrix} (E_{x1}H_{y2} - E_{x2}H_{y1}) & (E_{x2}H_{x1} - E_{x1}H_{x2}) \\ (E_{y1}H_{y2} - E_{y2}H_{y1}) & (E_{y2}H_{x1} - E_{y1}H_{x2}) \end{bmatrix}}{H_{x1}H_{y2} - H_{x2}H_{y1}} \tag{3-31}$$

where the subscripts 1 and 2 refer to the fields from the two different source polarizations. At first glance, it might seem logical to just invert for the four complex impedance elements. The difficulty with this, however, is that in many situations, $Z_{xx}$ and $Z_{yy}$ can be zero or close to zero. This is a problem when using logarithmic parameterization. Since $\partial \ln Z / \partial \ln \sigma = \sigma/Z \, (\partial Z/\partial \sigma)$, we see the possibility for a division by zero if any of the impedance elements are zero.

Instead, we take an approach similar to *Eggers* (1982) and *LaTorraca et al.* (1986), both of whom looked at eigenstate formulations for the impedance tensor. They were mainly concerned with extracting physically meaningful scalar parameters from the complex impedance tensor, especially where three-dimensional geometries were concerned. We use a somewhat simpler approach, however, and decompose the impedance tensor in terms of two complex vector fields (cf. *Jackson*, 1975). We consider the **E** field due to a unit $H_x$ field, which is $\mathbf{E} = [\hat{\mathbf{x}}\, Z_{xx} + \hat{\mathbf{y}}\, Z_{yx}]$, and the **E** field due to a unit $H_y$ field, which is $\mathbf{E} = [\hat{\mathbf{x}}\, Z_{xy} + \hat{\mathbf{y}}\, Z_{yy}]$. These two vectors serve as the basis set for the impedance tensor. Every complex vector can be described in terms of four scalar quantities: amplitude, phase, direction, and ellipticity. These quantities for the **E** vectors given above are closely related to the apparent resistivity, phase, and direction measurements usually measured from field data since, in many situations, the **H** field predominately induces a perpendicular **E** field.

Any complex vector in the frequency domain, $\mathbf{E}(\omega) = \mathbf{a} + j\mathbf{b}$, can be expressed in the time domain, assuming an $e^{-i\omega t}$ dependancy, as $\mathbf{e}(t) = \mathrm{Re}[\, \mathbf{E}(\omega)\, e^{-i\omega t}] = \mathbf{a} \cos\omega t + \mathbf{b} \sin\omega t$. The magnitude of the complex vector is simply $[\mathbf{E}^*\mathbf{E}]^{1/2}$. In the time domain, the vector traces out an ellipse, which in some cases degenerates to a circle or a line depending upon the vector's polarization. One uses the major axis of the ellipse to define the direction corresponding to that vector field, and defines the phase as the phase along that axis. The ellipticity is the ratio of the major axis to the minor axis. Ellipticities are difficult to measure accurately from field data, but magnitudes, phases, and directions are more robust in comparison. Consequently, we obtained all the inversion results in this chapter inverting

only for amplitudes, phases, and directions. Following *Eggers* (1982), we can write down the expressions for the magnitudes, phases ($\phi$), and directions ($\psi$) in terms of our vector basis set:

$$|E_{Hx}| = \left[ Z_{xx}Z^{*}_{xx} + Z_{yx}Z^{*}_{yx} \right]^{1/2}$$

$$|E_{Hy}| = \left[ Z_{xy}Z^{*}_{xy} + Z_{yy}Z^{*}_{yy} \right]^{1/2}$$

$$\phi_{Hx} = \frac{1}{2}\tan^{-1}\frac{2(Z^{R}_{xx}Z^{I}_{xx} + Z^{R}_{yx}Z^{I}_{yx})}{(Z^{R}_{xx})^2 + (Z^{R}_{yx})^2 - (Z^{I}_{xx})^2 - (Z^{I}_{yx})^2}$$

$$\phi_{Hy} = \frac{1}{2}\tan^{-1}\frac{2(Z^{R}_{xy}Z^{I}_{xy} + Z^{R}_{yy}Z^{I}_{yy})}{(Z^{R}_{xy})^2 + (Z^{R}_{yy})^2 - (Z^{I}_{xy})^2 - (Z^{I}_{yy})^2} \qquad (3\text{-}32)$$

$$\psi_{Hx} = \frac{1}{2}\tan^{-1}\frac{2(Z^{R}_{xx}Z^{R}_{yx} + Z^{I}_{xx}Z^{I}_{yx})}{(Z^{R}_{xx})^2 + (Z^{I}_{xx})^2 - (Z^{R}_{yx})^2 - (Z^{I}_{yx})^2}$$

$$\psi_{Hy} = \frac{1}{2}\tan^{-1}\frac{2(Z^{R}_{xy}Z^{R}_{yy} + Z^{I}_{xy}Z^{I}_{yy})}{(Z^{R}_{xy})^2 + (Z^{I}_{xy})^2 - (Z^{R}_{yy})^2 - (Z^{I}_{yy})^2}$$

where the terms like $Z^{R}_{xx}$ stand for the real part of $Z_{xx}$, and so on. The sensitivity terms are derived by algebraically taking the derivatives of the above expressions. We first need the partial derivatives of the components of the impedance tensor, which are given by

$$\frac{\partial Z_{xx}}{\partial \sigma} = \frac{1}{\text{detHH}}\left[E_{x1}\frac{\partial H_{y2}}{\partial \sigma} + H_{y2}\frac{\partial E_{x1}}{\partial \sigma} - E_{x2}\frac{\partial H_{y1}}{\partial \sigma} - H_{y1}\frac{\partial E_{x2}}{\partial \sigma} - Z_{xx}\,\partial\text{HH}\right]$$

$$\frac{\partial Z_{xy}}{\partial \sigma} = \frac{1}{\text{detHH}}\left[E_{x2}\frac{\partial H_{x1}}{\partial \sigma} + H_{x1}\frac{\partial E_{x2}}{\partial \sigma} - E_{x1}\frac{\partial H_{x2}}{\partial \sigma} - H_{x2}\frac{\partial E_{x1}}{\partial \sigma} - Z_{xy}\,\partial\text{HH}\right]$$

$$\frac{\partial Z_{yx}}{\partial \sigma} = \frac{1}{\text{detHH}}\left[E_{y1}\frac{\partial H_{y2}}{\partial \sigma} + H_{y2}\frac{\partial E_{y1}}{\partial \sigma} - E_{y2}\frac{\partial H_{y1}}{\partial \sigma} - H_{y1}\frac{\partial E_{y2}}{\partial \sigma} - Z_{yx}\,\partial\text{HH}\right] \qquad (3\text{-}33)$$

$$\frac{\partial Z_{yy}}{\partial \sigma} = \frac{1}{\text{detHH}}\left[E_{y2}\frac{\partial H_{x1}}{\partial \sigma} + H_{x1}\frac{\partial E_{y2}}{\partial \sigma} - E_{y1}\frac{\partial H_{x2}}{\partial \sigma} - H_{x2}\frac{\partial E_{y1}}{\partial \sigma} - Z_{yy}\,\partial\text{HH}\right]$$

where we have made the following definitions:

$$\text{detHH} = H_{x1}H_{y2} - H_{x2}H_{y1}$$

$$\partial HH = H_{x1}\frac{\partial H_{y2}}{\partial \sigma} + H_{y2}\frac{\partial H_{x1}}{\partial \sigma} - H_{x2}\frac{\partial H_{y1}}{\partial \sigma} - H_{y1}\frac{\partial H_{x2}}{\partial \sigma}\,. \tag{3-34}$$

With these definitions, the sensitivity terms for the magnitudes are given by

$$\begin{aligned}\frac{\partial |E_{Hx}|}{\partial \sigma} &= \frac{1}{|E_{Hx}|}\left[\,\mathrm{Re}\left(Z_{xx}^{*}\frac{\partial Z_{xx}}{\partial \sigma}\right) + \mathrm{Re}\left(Z_{yx}^{*}\frac{\partial Z_{yx}}{\partial \sigma}\right)\right] \\ \frac{\partial |E_{Hy}|}{\partial \sigma} &= \frac{1}{|E_{Hy}|}\left[\,\mathrm{Re}\left(Z_{xy}^{*}\frac{\partial Z_{xy}}{\partial \sigma}\right) + \mathrm{Re}\left(Z_{yy}^{*}\frac{\partial Z_{yy}}{\partial \sigma}\right)\right]\end{aligned} \tag{3-35}$$

where we have used relationships such as

$$Z_{xx}\frac{\partial Z_{xx}^{*}}{\partial \sigma} + Z_{xx}^{*}\frac{\partial Z_{xx}}{\partial \sigma} = 2\,\mathrm{Re}\left[Z_{xx}^{*}\frac{\partial Z_{xx}}{\partial \sigma}\right] \tag{3-36}$$

in simplifying the expressions for the derivatives. The expressions for the derivatives of the phase terms are a bit more complicated, and are given by

$$\begin{aligned}\frac{\partial \phi_{Hx}}{\partial \sigma} = \frac{1}{1+u^2}\Bigg[&\left(\frac{Z_{xx}^{I}}{u_d} - \frac{2\,Z_{xx}^{R}\,u_n}{u_d^2}\right)\frac{\partial Z_{xx}^{R}}{\partial \sigma} + \left(\frac{Z_{yx}^{I}}{u_d} - \frac{2\,Z_{yx}^{R}\,u_n}{u_d^2}\right)\frac{\partial Z_{yx}^{R}}{\partial \sigma} \\ &+ \left(\frac{Z_{xx}^{R}}{u_d} - \frac{2\,Z_{xx}^{I}\,u_n}{u_d^2}\right)\frac{\partial Z_{xx}^{I}}{\partial \sigma} + \left(\frac{Z_{yx}^{R}}{u_d} - \frac{2\,Z_{yx}^{I}\,u_n}{u_d^2}\right)\frac{\partial Z_{yx}^{I}}{\partial \sigma}\Bigg] \\ \frac{\partial \phi_{Hy}}{\partial \sigma} = \frac{1}{1+v^2}\Bigg[&\left(\frac{Z_{xy}^{I}}{v_d} - \frac{2\,Z_{xy}^{R}\,v_n}{v_d^2}\right)\frac{\partial Z_{xy}^{R}}{\partial \sigma} + \left(\frac{Z_{yy}^{I}}{v_d} - \frac{2\,Z_{yy}^{R}\,v_n}{v_d^2}\right)\frac{\partial Z_{yy}^{R}}{\partial \sigma} \\ &+ \left(\frac{Z_{xy}^{R}}{v_d} - \frac{2\,Z_{xy}^{I}\,v_n}{v_d^2}\right)\frac{\partial Z_{xy}^{I}}{\partial \sigma} + \left(\frac{Z_{yy}^{R}}{v_d} - \frac{2\,Z_{yy}^{I}\,v_n}{v_d^2}\right)\frac{\partial Z_{yy}^{I}}{\partial \sigma}\Bigg]\end{aligned} \tag{3-37}$$

where we have made the following definitions

$$\begin{aligned}u &= \frac{2\left(Z_{xx}^{R}Z_{xx}^{I} + Z_{yx}^{R}Z_{yx}^{I}\right)}{\left(Z_{xx}^{R}\right)^2 + \left(Z_{yx}^{R}\right)^2 - \left(Z_{xx}^{I}\right)^2 - \left(Z_{yx}^{I}\right)^2} \\ v &= \frac{2\left(Z_{xy}^{R}Z_{xy}^{I} + Z_{yy}^{R}Z_{yy}^{I}\right)}{\left(Z_{xy}^{R}\right)^2 + \left(Z_{yy}^{R}\right)^2 - \left(Z_{xy}^{I}\right)^2 - \left(Z_{yy}^{I}\right)^2}\,,\end{aligned} \tag{3-38}$$

with $u_d$ and $u_n$ representing the denominator and numerator respectively of the expression given above for u, and $v_d$ and $v_n$ likewise representing the denominator and numerator of the expression given above for v. The sensitivity terms for the directions of the major axes are given by

$$\frac{\partial \psi_{Hx}}{\partial \sigma} = \frac{1}{1+s^2}\left[\left(\frac{Z^R_{xx}}{s_d} + \frac{2\,Z^R_{yx}\,s_n}{s_d^2}\right)\frac{\partial Z^R_{yx}}{\partial \sigma} + \left(\frac{Z^R_{yx}}{s_d} - \frac{2\,Z^R_{xx}\,s_n}{s_d^2}\right)\frac{\partial Z^R_{xx}}{\partial \sigma}\right.$$
$$\left. + \left(\frac{Z^I_{xx}}{s_d} + \frac{2\,Z^I_{yx}\,s_n}{s_d^2}\right)\frac{\partial Z^I_{yx}}{\partial \sigma} + \left(\frac{Z^I_{yx}}{s_d} - \frac{2\,Z^I_{xx}\,s_n}{s_d^2}\right)\frac{\partial Z^I_{xx}}{\partial \sigma}\right]$$

$$\frac{\partial \psi_{Hy}}{\partial \sigma} = \frac{1}{1+t^2}\left[\left(\frac{Z^R_{xy}}{t_d} + \frac{2\,Z^R_{yy}\,t_n}{t_d^2}\right)\frac{\partial Z^R_{yy}}{\partial \sigma} + \left(\frac{Z^R_{yy}}{t_d} - \frac{2\,Z^R_{xy}\,t_n}{t_d^2}\right)\frac{\partial Z^R_{xy}}{\partial \sigma}\right.$$
$$\left. + \left(\frac{Z^I_{xy}}{t_d} + \frac{2\,Z^I_{yy}\,t_n}{t_d^2}\right)\frac{\partial Z^I_{yy}}{\partial \sigma} + \left(\frac{Z^I_{yy}}{t_d} - \frac{2\,Z^I_{xy}\,t_n}{t_d^2}\right)\frac{\partial Z^I_{xy}}{\partial \sigma}\right] \qquad (3\text{-}39)$$

where we have made the following definitions

$$s = \frac{2\left(Z^R_{xx}Z^R_{yx} + Z^I_{xx}Z^I_{yx}\right)}{\left(Z^R_{xx}\right)^2 + \left(Z^I_{xx}\right)^2 - \left(Z^R_{yx}\right)^2 - \left(Z^I_{yx}\right)^2}$$
$$t = \frac{2\left(Z^R_{xy}Z^R_{yy} + Z^I_{xy}Z^I_{yy}\right)}{\left(Z^R_{xy}\right)^2 + \left(Z^I_{xy}\right)^2 - \left(Z^R_{yy}\right)^2 - \left(Z^I_{yy}\right)^2}, \qquad (3\text{-}40)$$

with $s_d$ and $s_n$ representing the denominator and numerator respectively of the above expression for s and $t_d$ and $t_n$ representing the denominator and numerator of the above expression for t.

### *Source distributions*

As mentioned previously, computing the effect of the sensitivity matrix multiplying a vector requires one forward problem with sources distributed throughout the volume, and computing the effect of the transpose of the sensitivity matrix multiplying a vector requires

one forward problem with sources distributed across the surface. Because we are using logarithmic parameterization, the vector $\mathbf{p} = \mathbf{Ax}$, from equation 3-6, is of the form

$$\mathbf{p} = \mathbf{Ax} \sim \sum_{\substack{\text{model} \\ \text{parameters}}} \frac{\sigma}{(E,H)} \frac{\partial(E,H)}{\partial\sigma} \mathbf{x} \,. \tag{3-41}$$

By virtue of equation 3-11, and since each component of the vector **x** corresponds to a particular model parameter in the volume, we see that the volume sources for the problem $\mathbf{p} = \mathbf{Ax}$ are equal to

$$\left.\begin{aligned} J_x(k) &= \sigma(k)\, E_x(k)\, x(k) \\ J_y(k) &= \sigma(k)\, E_y(k)\, x(k) \\ J_z(k) &= \sigma(k)\, E_z(k)\, x(k) \end{aligned}\right\} \; k = 1,\ldots,n \tag{3-42}$$

where n is the number of model parameters, and the $\sigma(k)$ are included because of the logarithmic parameterization. There are actually two sets of sources involved here, one for the $H_x$ polarization and one for the $H_y$ polarization. The **E** fields are those that we compute from the original forward problem at one particular frequency and polarization of inducing field. These sources are distributed throughout the volume and the resulting **E** and **H** fields, by dint of equation 3-11, actually correspond to the derivatives of these fields, $\partial\mathbf{E}/\partial\sigma$ and $\partial\mathbf{H}/\partial\sigma$, summed over all model perturbations. One can then use these values to compute the required sensitivity terms given in equations 3-33, 3-35, 3-37, and 3-39.

The sources for the $\mathbf{A}^T$ problem are a bit more difficult to set up, but we can use reciprocity to obtain the desired results. Recall that the perturbed fields went like the Green's function times the original **E** field. For example, the effect in the $E_x$ field due to a conductivity perturbation at depth, equation 3-11, is given by $\partial E_x/\partial\sigma = G_1(r,s)_1\, E_x(s) + G_1(r,s)_2\, E_y(s) + G_1(r,s)_3\, E_z(s)$ where $G_1(r,s)_1$ is the $E_x$ effect at *r* due to a $J_x$ source at *s*, $G_1(r,s)_2$ is the $E_x$ effect at *r* due to a $J_y$ source at *s*, and $G_1(r,s)_3$ is the $E_x$ effect at *r* due to a $J_z$ source at *s*. Integration over the volume is implicitly assumed in this expression. By using the reciprocal relation, equation 3-22, we can also express this as $\partial E_x/\partial\sigma = G_1(s,r)_1\, E_x(s) + G_2(s,r)_1\, E_y(s) + G_3(s,r)_1\, E_z(s)$ where $G_1(s,r)_1$ is the $E_x$ effect at *s* due to a $J_x$

source at $r$, $G_2(s,r)_1$ is the $E_y$ effect at $s$ due to a $J_x$ source at $r$, and $G_3(s,r)_1$ is the $E_z$ effect at $s$ due to a $J_x$ source at $r$. Similarly, the effect in the $H_x$ field due to a conductivity perturbation at depth is given by $\partial H_x/\partial\sigma = G_4(r,s)_1\, E_x(s) + G_4(r,s)_2\, E_y(s) + G_4(r,s)_3\, E_z(s)$ where $G_4(r,s)_i$ represented the $H_x$ effect at $r$ due to current sources $i$ at $s$. Likewise, we can turn this around using reciprocity and express it equivalently as $\partial H_x/\partial\sigma = G_1(s,r)_4\, E_x(s) + G_2(s,r)_4\, E_y(s) + G_3(s,r)_4\, E_z(s)$ where now, $G_i(s,r)_4$ represents the electric fields at $s$ in the media due to $H_x$ sources at the surface position $r$. So, for example, if one of the sensitivity terms was, from equation 3-33, $H_{y2}\,(\partial E_{x1}/\partial\sigma)$, then the $\mathbf{A}^T$ operation would be carried out by putting a $J_x$ current source proportional to $H_{y2}$ at the surface location, calculating the forward problem with this source, computing the **E** fields in the interior location, multiplying the computed **E** fields by the original **E** fields, and summing as indicated above. Since the problem is linear in sources, we can compute the effect of $\mathbf{A}^T$ on a vector by putting all sources at the surface simultaneously and solving for the interior **E** fields everywhere. If one denotes the fields due to the surface sources as **E'** and the original **E** fields as **E**, then the $\mathbf{A}^T$ operation is

$$\mathbf{A}^T\mathbf{Q}(k) = \sum_{\text{freq}} \sigma(k)\Big[E_{x1}(k)E'_{x1}(k) + E_{y1}(k)E'_{y1}(k) + E_{z1}(k)E'_{z1}(k) + E_{x2}(k)E'_{x2}(k) + E_{y2}(k)E'_{y2}(k) + E_{z2}(k)E'_{z2}(k)\Big] \tag{3-43}$$

where the results are summed over frequencies for both polarizations of inducing field.

Some care must be taken in setting up the sources for the $\mathbf{A}^T$ problem, however, because the sensitivity analysis involves terms like Re $(\partial Z_{xx}/\partial\sigma)$ and Im $(\partial Z_{xx}/\partial\sigma)$. Notice that this was not a difficulty for the **A** problem because one simply took the real or imaginary part of the resulting surface field values. To see how to deal with the $\mathbf{A}^T$ problem, let us first look at two complex vectors **a** and **b**. The complex quantity **ab** is equal to $(a_R b_R - a_I b_I) + i\,(a_R b_I + a_I b_R)$. However, the complex quantity Re(**a**)**b** is equal to $a_R b_R + i\, a_R b_I$, and the complex quantity Im(**a**)**b** is equal to $a_I b_R + i\, a_I b_I$. Therefore, the quantity Re(**a**)**b** can be expressed as Re(**a** $b_R$) + i Im(**a** $b_I$) and Im(**a**)**b** can be expressed as

$\mathrm{Im}(\mathbf{a}\, b_R) - i\, \mathrm{Re}(\mathbf{a}\, b_I)$. Consequently, to compute the sensitivity effects like $\mathrm{Re}(\,)\mathbf{Q}$ in the $A^T$ problem, two forward problems must be done, one with $Q_R$ as sources, and one with $Q_I$ as sources, and likewise for the $\mathrm{Im}(\,)\mathbf{Q}$ terms.

***Boundary Conditions and other practical matters***

Up to this point, we have not dealt specifically with the issues of the boundary conditions. We mentioned earlier that the boundary conditions are tied to the differential operator and cannot be separated from it, and that they also determine the boundary conditions for the adjoint boundary value problem. The 3D forward modeling algorithm we described in the previous chapter assigned tangential **H** field values on the boundaries of the 3D model. In this chapter, we avoid having to deal with the boundary values and their effect on the sensitivity terms by assuming the model is repeated in the horizontal directions; that is, there are no side boundary terms assigned. With this assignment, one can simply compute the adjoint problem by putting sources on the surface and solving for the fields in the interior, also assuming horizontal model repetition. We made this assignment to simplify the programming and to test our concepts about relaxation inversion. In the future, however, we will include the boundaries and their effect on the sensitivity terms in order to deal with realistic Earth models.

We made one additional modification in the inversion algorithm because of the geometry of the 3D forward solution. With our geometry there can be no curl of the **E** fields within an individual model cell; hence, we broke the top Earth layer into two sections, the top one being 1% of the original thickness of the top layer and the other section being 99% of the original thickness. Otherwise, we could not correctly compute the response to a current dipole in the top Earth layer because the current fields would not be able to properly turn around above the dipole. The addition of this thin layer allows for the correct computation of the response to a current source in the second layer, and the resistivity of the thin layer is tied to the resistivity of the second layer. Additionally, we did

this for the bottom layer where we had the same problem because of the bottom impedance condition. We split the bottom layer up into two sections, the top one being 90% of the original thickness and the bottom one being 10% of the original thickness.

***Results for theoretical data***

In this section, we present results using the relaxation inversion routine for inverting numerically-computed, noise-free 3D magnetotelluric data. We have not extensively tested the algorithm on a wide variety of models, but nonetheless, we wish to demonstrate that, even at this stage in the development of the algorithm, it does work as intended.

The model used to generate the data is shown in Figure 3-1 and consists of a conductive, three-dimensional inhomogeneity embedded at a shallow depth in an otherwise layered media. The model was made up laterally of five blocks in the x-direction and five blocks in the y-direction. Vertically, there were eight layers and a halfspace. The impedance for a 30 ohm-m halfspace was used at the bottom of the layers in the 3D model, and it was held fixed throughout all the inversions. Data were output for eight frequencies equally-spaced in the logarithm of period from 0.01 seconds to 30 seconds. The *a priori* model used for all inversions had the same dimensions as the one used to generate the 'observed data', but with a uniform resistivity of 100 ohm-m, except for the 30 ohm-m halfspace.

Shown in Figures 3-2, 3-3, and 3-4 are the observed and *a priori* model responses for three different locations on the surface of the 3D model. These three sites were chosen because it would be too voluminous to show the responses at all the sites, and the sites at xb=2, yb=2 and xb=4, yb=4 represent sites where 3D effects are the severest. Figure 3-5 shows the error progression versus inversion iteration for an inversion with five relaxation steps per inversion iteration. We define the data error as

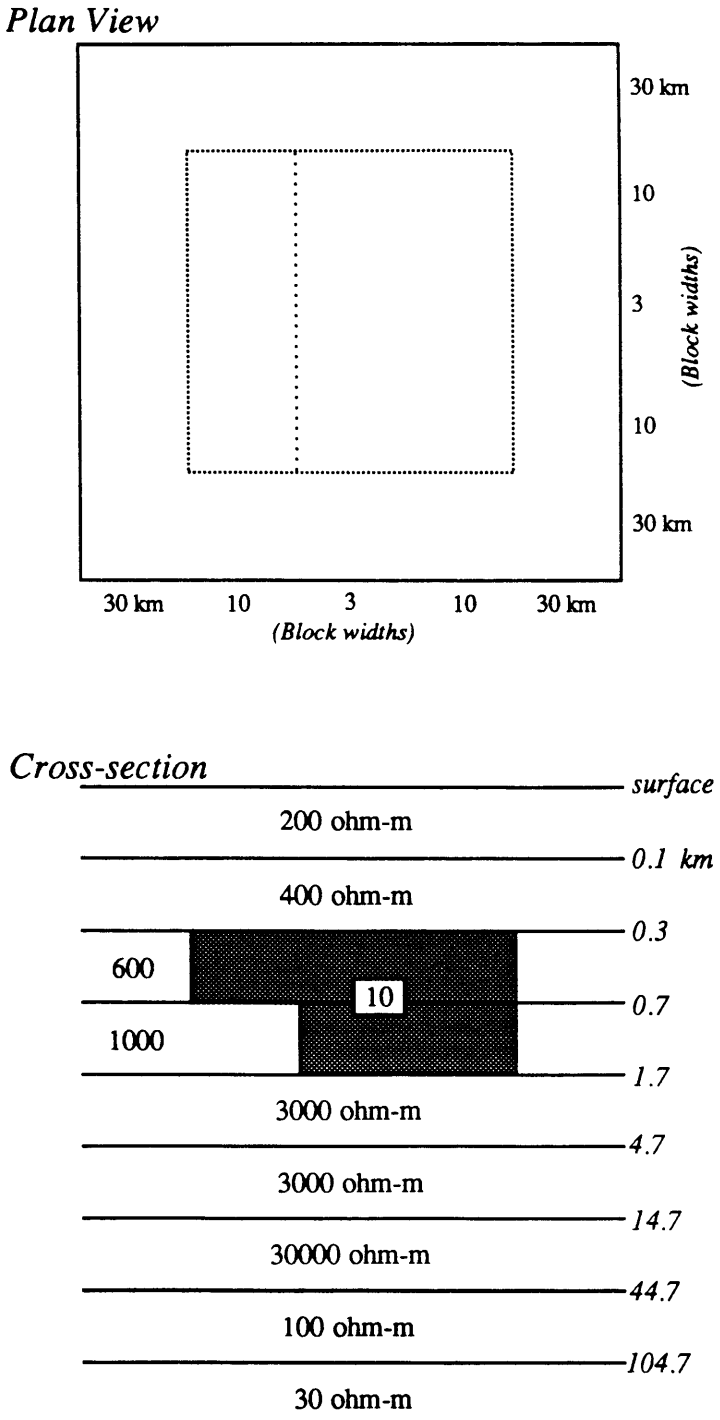


**Figure 3-1.** The 3D model used to generate synthetic MT data. This data was used to test the 3D MT inversion algorithm. The model was 5 blocks by 5 blocks by 9 layers. A 10 ohm-m inhomogeneity was buried in an otherwise layered earth.

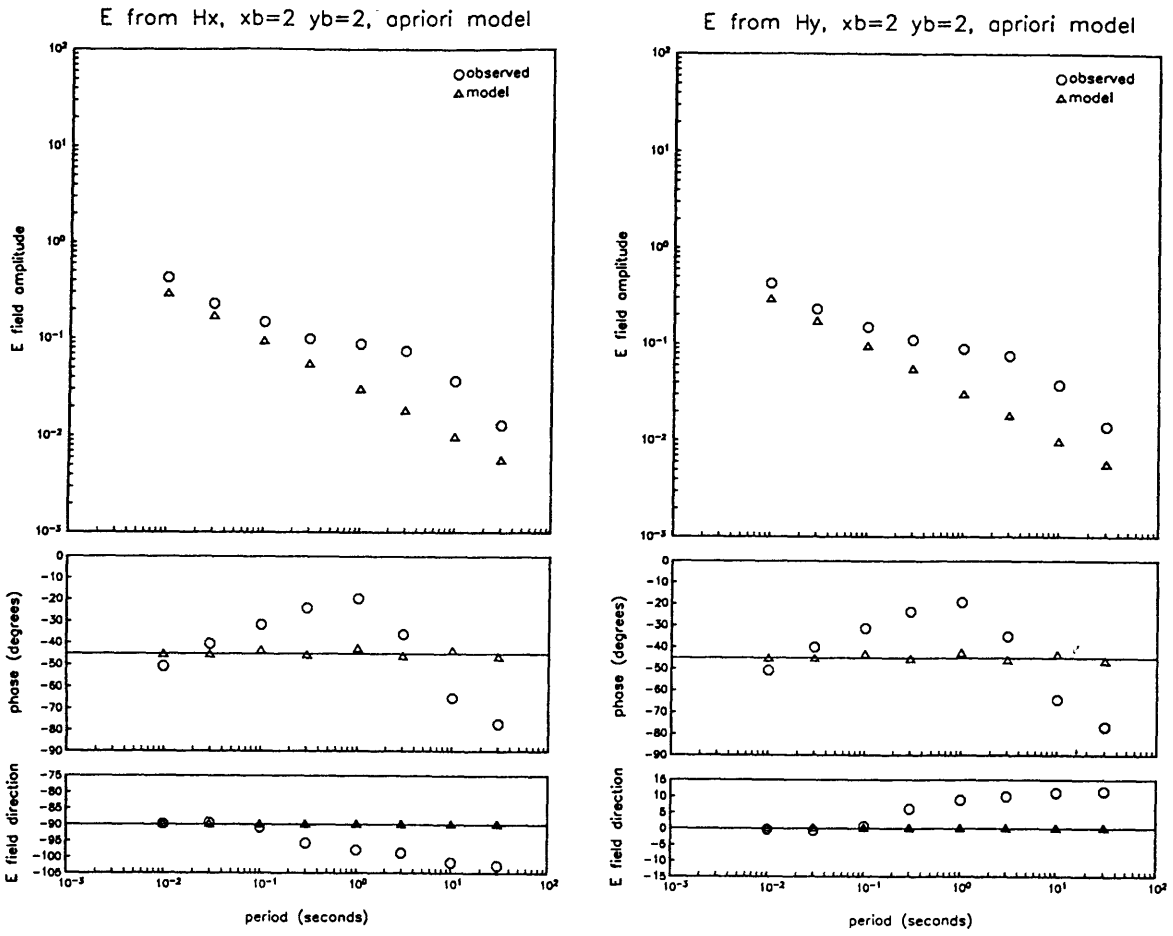


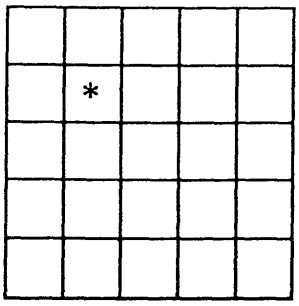

**Figure 3-2.** The observed and *a priori* model responses for the surface location xb=2, yb=2. Shown are the amplitudes, phases (in degrees), and directions (in degrees clockwise from the positive x-axis, which runs to the right) versus period. These values are defined in the text, see equation 3-32.

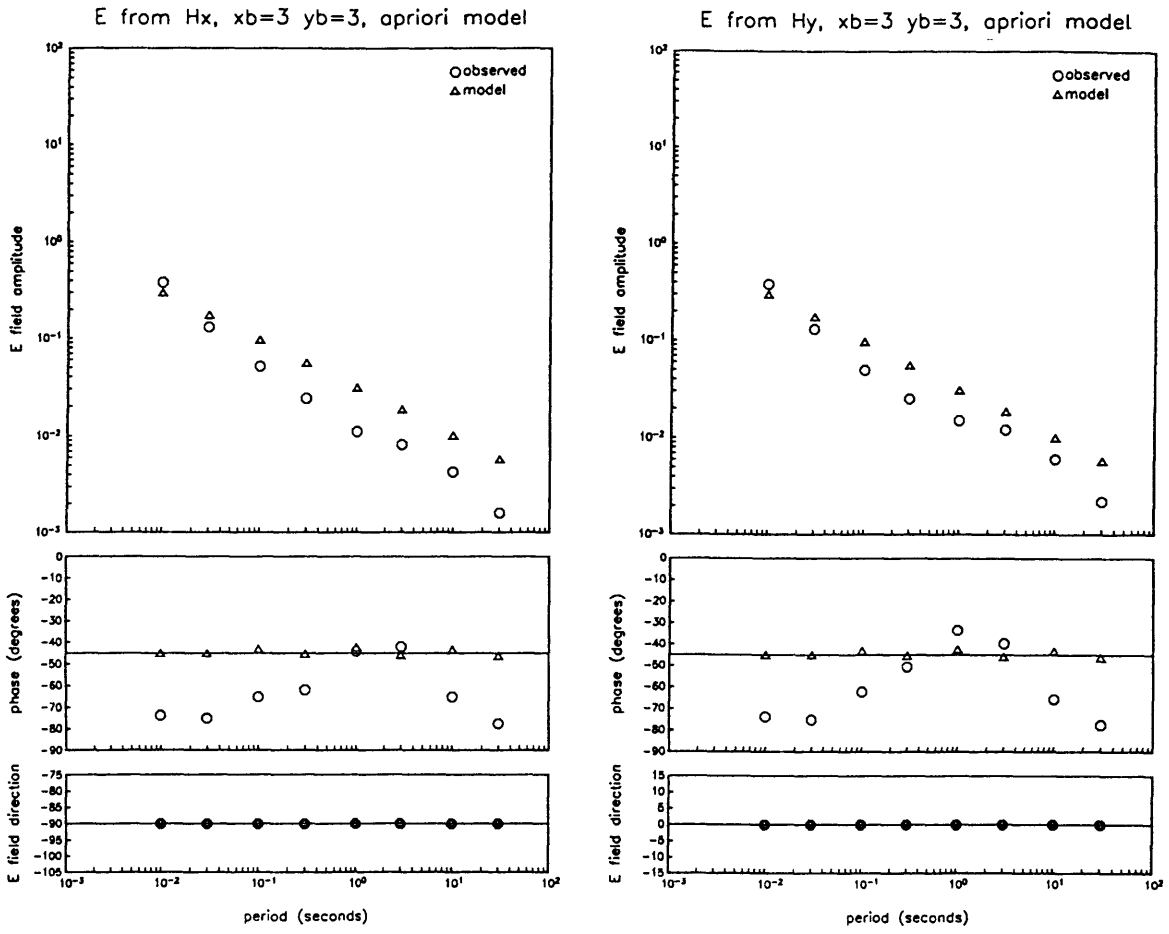


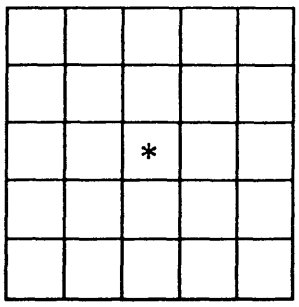

**Figure 3-3.** The observed and *a priori* model responses for the surface location xb=3, yb=3. Shown are the amplitudes, phases (in degrees), and directions (in degrees clockwise from the positive x-axis, which runs to the right) versus period. These values are defined in the text, see equation 3-32.

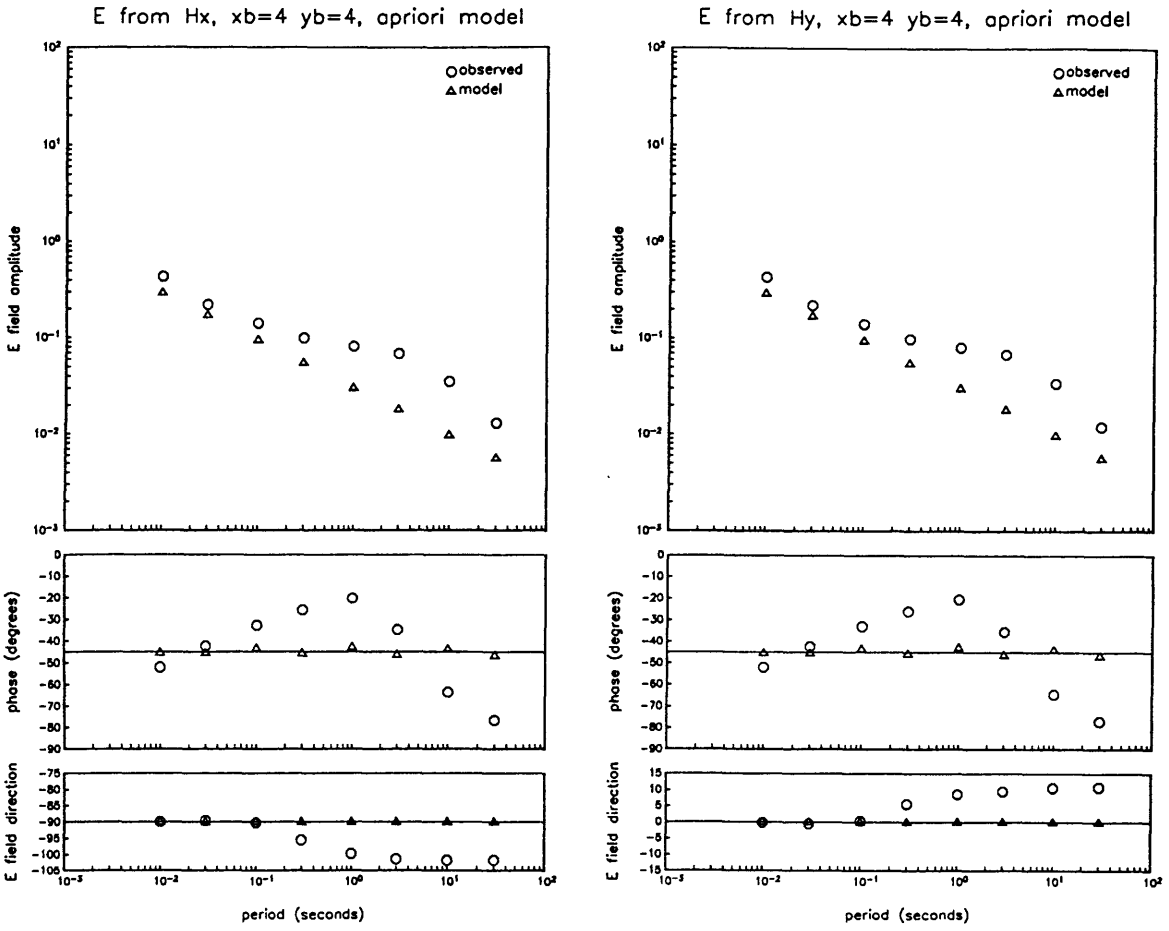


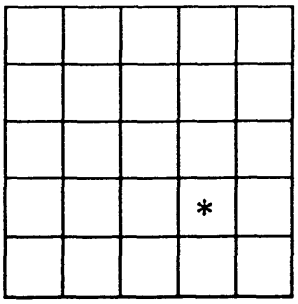

**Figure 3-4.** The observed and *a priori* model responses for the surface location xb=4, yb=4. Shown are the amplitudes, phases (in degrees), and directions (in degrees clockwise from the positive x-axis, which runs to the right) versus period. These values are defined in the text, see equation 3-32.

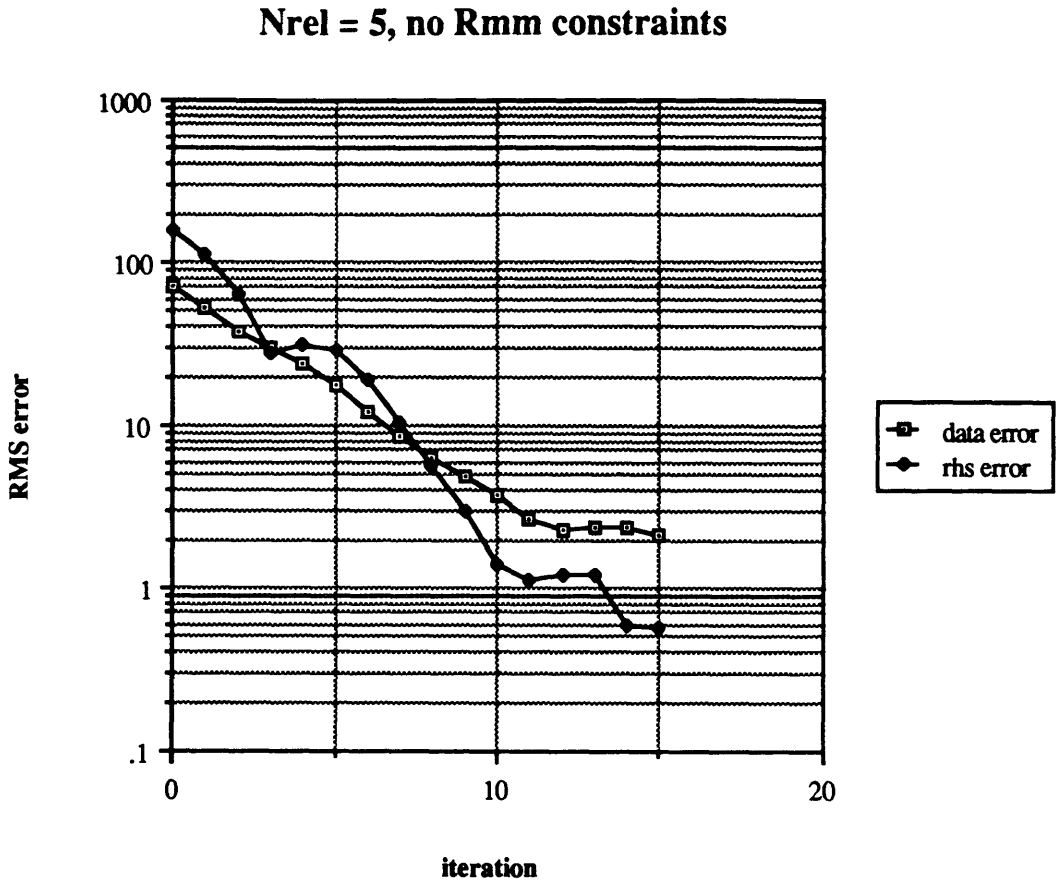


**Figure 3-5**. The RMS error progression as a function of the inversion iteration step. This particular run used 5 conjugate gradient relaxation steps per inversion iteration. The ratio of $\sigma_d^2 / \sigma_m^2$ was equal to $3 \times 10^{-5}$. The data error is defined in equation 3-44, and the right-hand-side error (*rhs error*) is defined in equation 3-45. The right-hand-side error should go to zero when the solution to the maximum likelihood equations is obtained.

$$\sqrt{\frac{\sum_{ndat}\sum_{nfreq}\sum_{npol}\left[\left(\ln\frac{|E_o|}{|E_m|}\right)^2+(\theta_o-\theta_m)^2+(\psi_o-\psi_m)^2\right]}{ndat \times nfreq \times 2}} \times 100 \qquad (3\text{-}44)$$

where $\theta$ and $\psi$ are given in radians, the subscripts *o* and *m* refer to observed and model respectively, *ndat* is the number of data locations, *nfreq* is the number of frequencies, and *npol* is the number of polarizations (npol=2). The right-hand-side error is the error in the right-hand-side of the maximum likelihood equations, equation 3-5. When the maximum likelihood equations are exactly satisfied, the right-hand-side goes to zero. This does not necessarily correspond to the solution in which the data are exactly predicted because the fit is actually a compromise between fitting the data and adhering to the *a priori* model, weighted by the inverses of the data and model covariances. The right-hand-side error plotted in Figure 3-5 was computed by the following equation, where *r(k)* represents the element of the right-hand-side corresponding to the $k^{th}$ model block:

$$\sqrt{\frac{\sum_{k=1}^{nmod} r(k)\,r(k)}{nmod}} \times 100 \qquad (3\text{-}45)$$

For this example, we used five relaxation steps per inversion iteration, and we assumed that both the model covariance and the data covariance matrices were of the form $\sigma^2\mathbf{I}$. That is, we set $\mathbf{R}_{dd} = \sigma_d^2\,\mathbf{I}$ and $\mathbf{R}_{mm} = \sigma_m^2\,\mathbf{I}$, where the ratio $\sigma_d^2 / \sigma_m^2 = 3\text{x}10^{-5}$. This simply means that the variance of the fit to the *a priori* model was assumed greater than the variance of the data errors. In other words, the data were trusted much more than the *a priori* model, and the fit to the observed data was more important in the inversion than was the fit to the *a priori* model. An additional damping term was added to stabilize the inversions and was tied to the error in the right-hand-side so that as the error decreased, so did the added damping. The damping term was equal to $(1.0)*(1/\sigma_d^2)*$(RHS error). Damping terms reduce the influence of the small eigenvalues in the early stages of the

inversion, then allow them to become more influential at the latter stages. Damping terms should depend on the magnitudes of the eigenvalues, but the damping term added in these 3D inversions came about largely from our experience with 2D inversions and experimenting with the damping factor for 3D inversions. This damping is somewhat larger than what we are use to dealing with in 2D inversions, but this is probably due to the increased degrees of freedom in 3D inversions as compared to 2D inversions.

For this particular example, fifteen iterations reduced the error in the fit to the data to approximately 2% and the right-hand-side error to 0.6%. The resulting model and the actual model for this inversion are both shown in Figure 3-6, where the numbers are the resistivity values in ohm-meters. Note that the resistivity structure of the top four layers is fairly-well resolved, but that the image of the conductive feature is smeared into the lower layers. This is a common byproduct of many inversion schemes where one only has data coverage on one side of the feature one is trying to image. The inherent difficulty magnetotellurics has of resolving resistive bodies, especially if they are underneath more conductive layers or bodies, enhances this phenomenon. Figures 3-7, 3-8, and 3-9 show the data predictions for the model of Figure 3-6 for the three surface locations shown earlier. We see excellent agreement in both polarizations for amplitudes, phases, and directions. We find similarly good fits to the observed data at all other locations, but we do not show them here.

As a further example, we inverted the same data starting from the same *a priori* model, except this time, we included $\mathbf{R}_{mm}$ constraints to keep the bottom four layers 1D (that is, in each layer, all the resistivity values in that layer are tied together). We ran this inversion for different numbers of relaxation iterations per inversion iteration. Figure 3-10 shows the resulting model after fifteen inversion iterations using only one relaxation step per inversion iteration. Figure 3-11 shows the resulting model after fifteen inversion iterations using three relaxation steps per inversion iteration, and Figure 3-12 shows the resulting model after fifteen inversion iterations using ten relaxation steps per inversion

Number of relaxation steps = 5
Number of inversion iterations = 15
No Rmm constraints

Rmmfac=3.0e-5
Damping=1.0

RESULTS FROM INVERSION PROGRAM

| | | | | |
|---|---|---|---|---|
| layer1 | | | | |
| 239 | 237 | 242 | 240 | 235 |
| 245 | 263 | 266 | 267 | 234 |
| 231 | 260 | 254 | 250 | 240 |
| 246 | 263 | 266 | 269 | 235 |
| 236 | 235 | 240 | 240 | 240 |
| layer2 | | | | |
| 344 | 347 | 353 | 353 | 343 |
| 333 | 194 | 248 | 198 | 367 |
| 306 | 249 | 253 | 267 | 397 |
| 333 | 193 | 248 | 199 | 369 |
| 340 | 344 | 351 | 353 | 350 |
| layer3 | | | | |
| 531 | 537 | 491 | 510 | 545 |
| 578 | 11 | 11 | 10 | 485 |
| 586 | 10 | 13 | 13 | 458 |
| 578 | 11 | 11 | 10 | 486 |
| 527 | 536 | 488 | 509 | 553 |
| layer4 | | | | |
| 1196 | 1281 | 1218 | 1155 | 1278 |
| 1280 | 154 | 9 | 9 | 1139 |
| 1302 | 121 | 14 | 13 | 1228 |
| 1281 | 154 | 9 | 9 | 1139 |
| 1193 | 1290 | 1213 | 1149 | 1275 |
| layer5 | | | | |
| 2346 | 2651 | 2681 | 2725 | 2444 |
| 2792 | 490 | 99 | 126 | 2637 |
| 2833 | 231 | 99 | 82 | 2630 |
| 2801 | 491 | 99 | 125 | 2625 |
| 2366 | 2676 | 2686 | 2710 | 2418 |
| layer6 | | | | |
| 3041 | 4717 | 4813 | 4938 | 3033 |
| 4811 | 829 | 356 | 1021 | 4787 |
| 4980 | 192 | 154 | 111 | 4462 |
| 4826 | 828 | 355 | 1016 | 4804 |
| 3074 | 4713 | 4823 | 4919 | 3001 |
| layer7 | | | | |
| 19461 | 14747 | 9627 | 14495 | 22294 |
| 18683 | 373 | 173 | 365 | 12812 |
| 17577 | 149 | 94 | 131 | 5318 |
| 18702 | 368 | 172 | 361 | 12847 |
| 19390 | 14820 | 10843 | 14680 | 22130 |
| layer8 | | | | |
| 90 | 86 | 85 | 85 | 88 |
| 87 | 114 | 102 | 102 | 86 |
| 86 | 107 | 99 | 99 | 86 |
| 87 | 114 | 102 | 102 | 86 |
| 90 | 86 | 85 | 86 | 89 |

ACTUAL MODEL

| | | | | |
|---|---|---|---|---|
| layer 1 | | | | |
| 200 | 200 | 200 | 200 | 200 |
| 200 | 200 | 200 | 200 | 200 |
| 200 | 200 | 200 | 200 | 200 |
| 200 | 200 | 200 | 200 | 200 |
| 200 | 200 | 200 | 200 | 200 |
| layer 2 | | | | |
| 400 | 400 | 400 | 400 | 400 |
| 400 | 400 | 400 | 400 | 400 |
| 400 | 400 | 400 | 400 | 400 |
| 400 | 400 | 400 | 400 | 400 |
| 400 | 400 | 400 | 400 | 400 |
| layer 3 | | | | |
| 600 | 600 | 600 | 600 | 600 |
| 600 | 10 | 10 | 10 | 600 |
| 600 | 10 | 10 | 10 | 600 |
| 600 | 10 | 10 | 10 | 600 |
| 600 | 600 | 600 | 600 | 600 |
| layer 4 | | | | |
| 1000 | 1000 | 1000 | 1000 | 1000 |
| 1000 | 1000 | 10 | 10 | 1000 |
| 1000 | 1000 | 10 | 10 | 1000 |
| 1000 | 1000 | 10 | 10 | 1000 |
| 1000 | 1000 | 1000 | 1000 | 1000 |
| layer 5 | | | | |
| 3000 | 3000 | 3000 | 3000 | 3000 |
| 3000 | 3000 | 3000 | 3000 | 3000 |
| 3000 | 3000 | 3000 | 3000 | 3000 |
| 3000 | 3000 | 3000 | 3000 | 3000 |
| 3000 | 3000 | 3000 | 3000 | 3000 |
| layer 6 | | | | |
| 3000 | 3000 | 3000 | 3000 | 3000 |
| 3000 | 3000 | 3000 | 3000 | 3000 |
| 3000 | 3000 | 3000 | 3000 | 3000 |
| 3000 | 3000 | 3000 | 3000 | 3000 |
| 3000 | 3000 | 3000 | 3000 | 3000 |
| layer 7 | | | | |
| 30000 | 30000 | 30000 | 30000 | 30000 |
| 30000 | 30000 | 30000 | 30000 | 30000 |
| 30000 | 30000 | 30000 | 30000 | 30000 |
| 30000 | 30000 | 30000 | 30000 | 30000 |
| 30000 | 30000 | 30000 | 30000 | 30000 |
| layer 8 | | | | |
| 100 | 100 | 100 | 100 | 100 |
| 100 | 100 | 100 | 100 | 100 |
| 100 | 100 | 100 | 100 | 100 |
| 100 | 100 | 100 | 100 | 100 |
| 100 | 100 | 100 | 100 | 100 |

**Figure 3-6.** The resulting model after 15 iterations of the inversion procedure. The actual model is shown on the right for comparison. The resistivity values for each block are given in ohm-m. The 30 ohm-m bottom halfspace was held fixed during the inversion, and is not shown here.

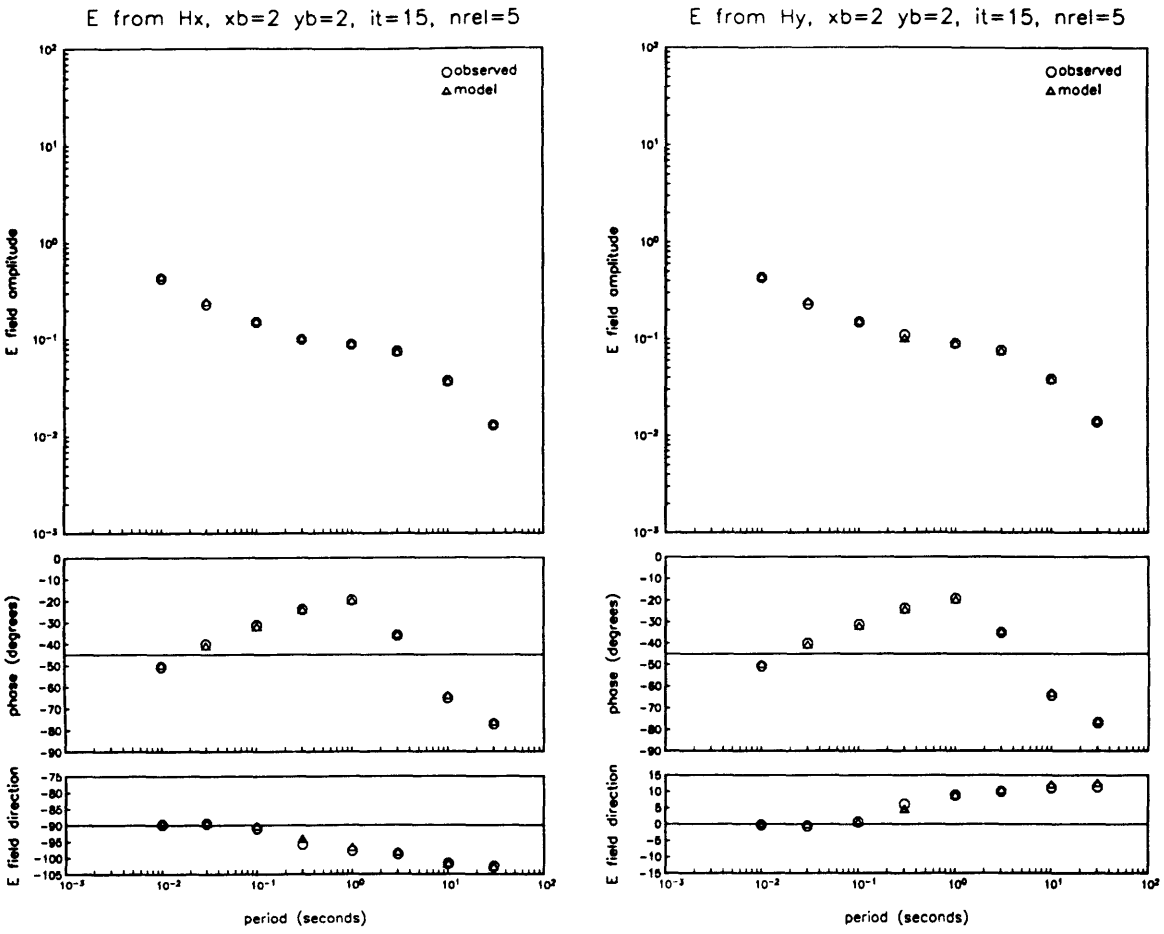


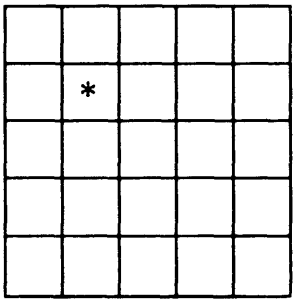


**Figure 3-7**. The data predictions for the model of Figure 3-6 for the surface location xb=2, yb=2. Also shown are the observed data responses. Shown are the amplitudes, phases, and directions versus period. These values are defined in the text, see equation 3-32.

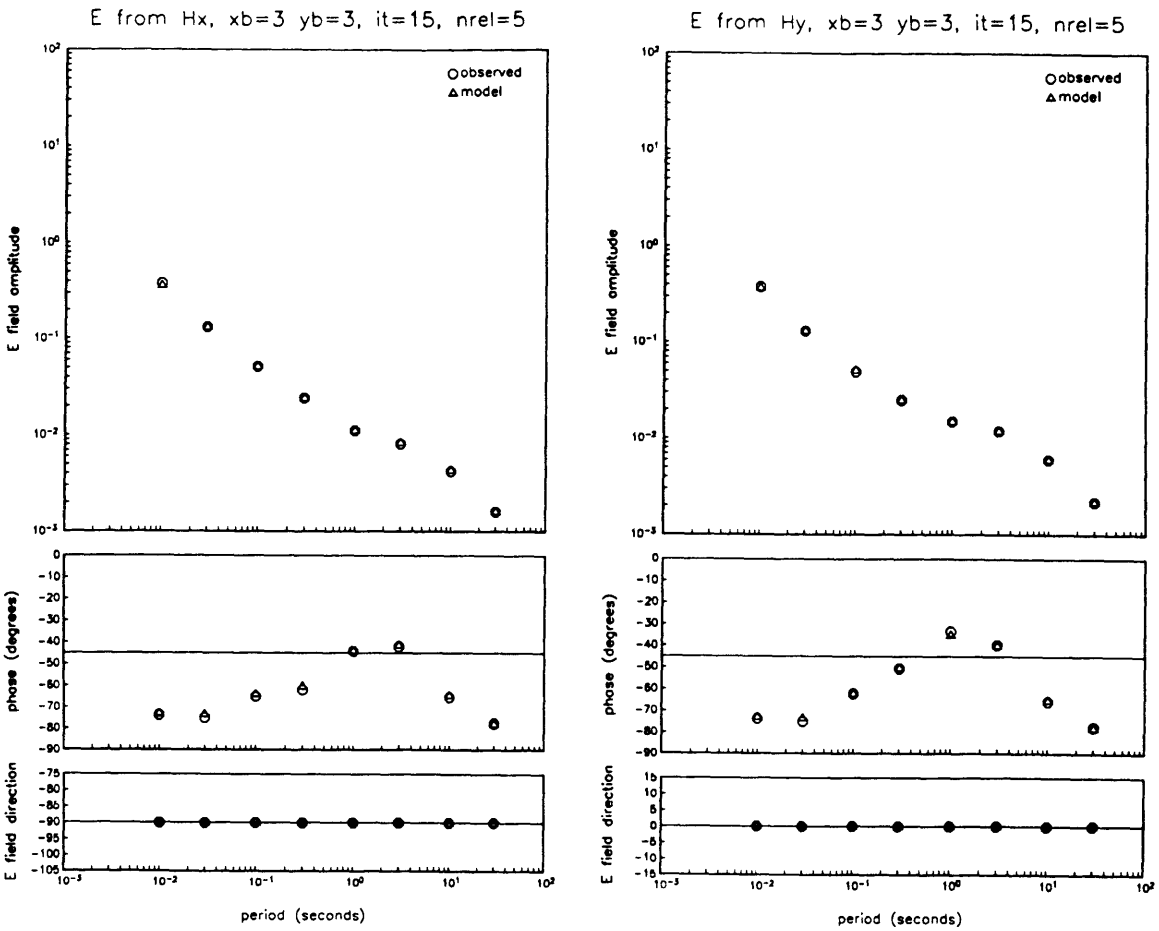


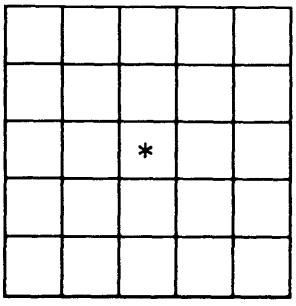

**Figure 3-8**. The data predictions for the model of Figure 3-6 for the surface location xb=3, yb=3. Also shown are the observed data responses. Shown are the amplitudes, phases, and directions versus period. These values are defined in the text, see equation 3-32.

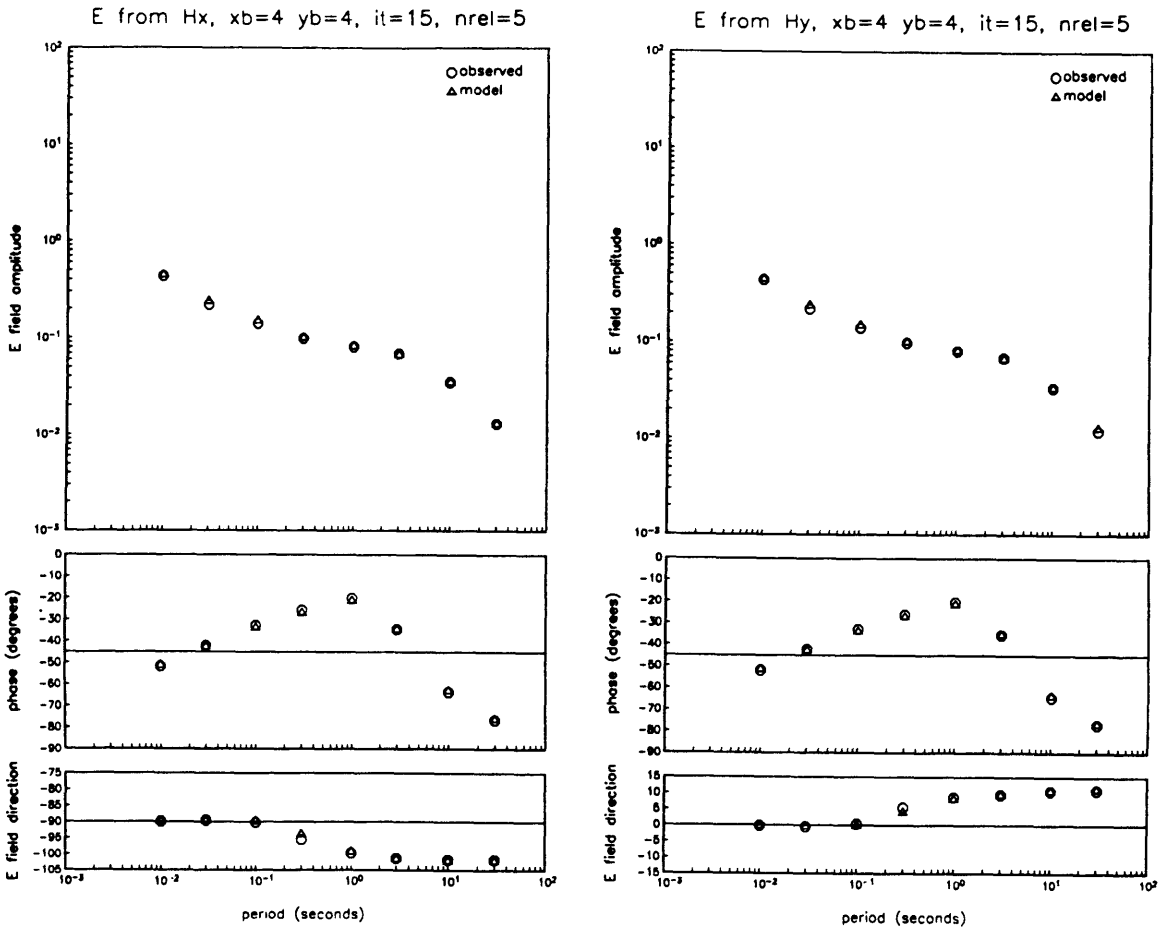


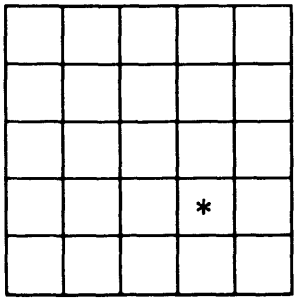

**Figure 3-9**. The data predictions for the model of Figure 3-6 for the surface location xb=4, yb=4. Also shown are the observed data responses. Shown are the amplitudes, phases, and directions versus period. These values are defined in the text, see equation 3-32.

Number of relaxation steps = 1
Number of inversion iterations = 15
Rmm constraints to keep layers 5,6,7,8 1D

Rmmfac=3.0e-5
Damping=1.0

RESULTS FROM INVERSION PROGRAM

| | | | | |
|---|---|---|---|---|
| layer1 | | | | |
| 204 | 218 | 218 | 220 | 194 |
| 213 | 253 | 282 | 258 | 223 |
| 205 | 270 | 207 | 267 | 219 |
| 213 | 253 | 282 | 258 | 223 |
| 204 | 218 | 218 | 220 | 194 |
| layer2 | | | | |
| 381 | 357 | 339 | 345 | 362 |
| 345 | 196 | 249 | 198 | 356 |
| 330 | 244 | 194 | 240 | 349 |
| 345 | 196 | 249 | 198 | 356 |
| 381 | 357 | 339 | 345 | 362 |
| layer3 | | | | |
| 690 | 565 | 508 | 497 | 662 |
| 553 | 11 | 16 | 8 | 514 |
| 543 | 16 | 24 | 14 | 533 |
| 553 | 11 | 16 | 8 | 514 |
| 690 | 565 | 508 | 497 | 662 |
| layer4 | | | | |
| 1291 | 1223 | 1113 | 1078 | 1268 |
| 1186 | 68 | 16 | 9 | 1108 |
| 1206 | 64 | 22 | 13 | 1128 |
| 1186 | 68 | 16 | 9 | 1108 |
| 1291 | 1223 | 1113 | 1078 | 1268 |
| layer5 | | | | |
| 1795 | 2493 | 2179 | 2536 | 1753 |
| 2411 | 450 | 244 | 263 | 2400 |
| 2220 | 333 | 216 | 209 | 2112 |
| 2411 | 450 | 244 | 263 | 2400 |
| 1795 | 2493 | 2179 | 2536 | 1753 |
| layer6 | | | | |
| 4626 | 6279 | 4062 | 5827 | 4559 |
| 6293 | 866 | 570 | 936 | 5873 |
| 4600 | 465 | 360 | 368 | 3722 |
| 6293 | 866 | 570 | 936 | 5873 |
| 4626 | 6279 | 4062 | 5827 | 4559 |
| layer7 | | | | |
| 15301 | 7318 | 2739 | 7194 | 14479 |
| 8984 | 617 | 339 | 604 | 6277 |
| 3604 | 325 | 222 | 297 | 2295 |
| 8984 | 617 | 339 | 604 | 6277 |
| 15301 | 7318 | 2739 | 7194 | 14479 |
| layer8 | | | | |
| 63 | 74 | 83 | 74 | 63 |
| 74 | 88 | 92 | 88 | 74 |
| 83 | 92 | 93 | 92 | 83 |
| 74 | 88 | 92 | 88 | 74 |
| 63 | 74 | 83 | 74 | 63 |

ACTUAL MODEL

| | | | | |
|---|---|---|---|---|
| layer 1 | | | | |
| 200 | 200 | 200 | 200 | 200 |
| 200 | 200 | 200 | 200 | 200 |
| 200 | 200 | 200 | 200 | 200 |
| 200 | 200 | 200 | 200 | 200 |
| 200 | 200 | 200 | 200 | 200 |
| layer 2 | | | | |
| 400 | 400 | 400 | 400 | 400 |
| 400 | 400 | 400 | 400 | 400 |
| 400 | 400 | 400 | 400 | 400 |
| 400 | 400 | 400 | 400 | 400 |
| 400 | 400 | 400 | 400 | 400 |
| layer 3 | | | | |
| 600 | 600 | 600 | 600 | 600 |
| 600 | 10 | 10 | 10 | 600 |
| 600 | 10 | 10 | 10 | 600 |
| 600 | 10 | 10 | 10 | 600 |
| 600 | 600 | 600 | 600 | 600 |
| layer 4 | | | | |
| 1000 | 1000 | 1000 | 1000 | 1000 |
| 1000 | 1000 | 10 | 10 | 1000 |
| 1000 | 1000 | 10 | 10 | 1000 |
| 1000 | 1000 | 10 | 10 | 1000 |
| 1000 | 1000 | 1000 | 1000 | 1000 |
| layer 5 | | | | |
| 3000 | 3000 | 3000 | 3000 | 3000 |
| 3000 | 3000 | 3000 | 3000 | 3000 |
| 3000 | 3000 | 3000 | 3000 | 3000 |
| 3000 | 3000 | 3000 | 3000 | 3000 |
| 3000 | 3000 | 3000 | 3000 | 3000 |
| layer 6 | | | | |
| 3000 | 3000 | 3000 | 3000 | 3000 |
| 3000 | 3000 | 3000 | 3000 | 3000 |
| 3000 | 3000 | 3000 | 3000 | 3000 |
| 3000 | 3000 | 3000 | 3000 | 3000 |
| 3000 | 3000 | 3000 | 3000 | 3000 |
| layer 7 | | | | |
| 30000 | 30000 | 30000 | 30000 | 30000 |
| 30000 | 30000 | 30000 | 30000 | 30000 |
| 30000 | 30000 | 30000 | 30000 | 30000 |
| 30000 | 30000 | 30000 | 30000 | 30000 |
| 30000 | 30000 | 30000 | 30000 | 30000 |
| layer 8 | | | | |
| 100 | 100 | 100 | 100 | 100 |
| 100 | 100 | 100 | 100 | 100 |
| 100 | 100 | 100 | 100 | 100 |
| 100 | 100 | 100 | 100 | 100 |
| 100 | 100 | 100 | 100 | 100 |

**Figure 3-10.** The resulting model after 15 iterations of the inversion procedure when the bottom 4 layers, excluding the bottom 30 ohm-m halfspace, have been constrained to be 1D. For this run, 1 relaxation step per inversion iteration was used. The actual model is shown on the right for comparison. The resistivity values for each block are given in ohm-m. The 30 ohm-m bottom halfspace was held fixed during the inversion, and is not shown here.

Number of relaxation steps = 3
Number of inversion iterations = 15
Rmm constraints to keep layers 5,6,7,8 1D

Rmmfac=3.0e-5
Damping=1.0

RESULTS FROM INVERSION PROGRAM

| | | | | |
|---|---|---|---|---|
| layer1 | | | | |
| 241 | 247 | 244 | 235 | 234 |
| 247 | 262 | 276 | 260 | 231 |
| 231 | 268 | 255 | 261 | 247 |
| 247 | 256 | 278 | 267 | 250 |
| 235 | 231 | 245 | 253 | 235 |
| layer2 | | | | |
| 342 | 366 | 356 | 339 | 342 |
| 357 | 178 | 255 | 178 | 338 |
| 327 | 255 | 255 | 262 | 383 |
| 346 | 175 | 256 | 182 | 373 |
| 334 | 334 | 357 | 374 | 343 |
| layer3 | | | | |
| 507 | 559 | 464 | 479 | 528 |
| 577 | 10 | 11 | 8 | 467 |
| 535 | 10 | 15 | 13 | 450 |
| 538 | 11 | 11 | 8 | 517 |
| 505 | 503 | 465 | 532 | 524 |
| layer4 | | | | |
| 1193 | 1410 | 1263 | 1247 | 1321 |
| 1441 | 145 | 10 | 10 | 1221 |
| 1438 | 102 | 14 | 13 | 1217 |
| 1382 | 148 | 10 | 10 | 1242 |
| 1222 | 1349 | 1260 | 1291 | 1259 |
| layer5 | | | | |
| 2116 | 2347 | 2301 | 2346 | 2394 |
| 2459 | 1564 | 1070 | 1209 | 2301 |
| 2346 | 1076 | 1072 | 968 | 2351 |
| 2467 | 1538 | 1073 | 1213 | 2238 |
| 2262 | 2336 | 2303 | 2373 | 2144 |
| layer6 | | | | |
| 3335 | 4135 | 4601 | 4251 | 3794 |
| 4211 | 3090 | 2503 | 2881 | 4119 |
| 4662 | 2168 | 2239 | 2035 | 4415 |
| 4285 | 3067 | 2517 | 2932 | 3984 |
| 3630 | 4202 | 4625 | 4281 | 3305 |
| layer7 | | | | |
| 14505 | 11338 | 9014 | 11118 | 15182 |
| 12526 | 3787 | 3138 | 3708 | 10802 |
| 10454 | 3081 | 2800 | 3009 | 7924 |
| 12516 | 3791 | 3141 | 3718 | 10860 |
| 14621 | 11379 | 9166 | 11250 | 14952 |
| layer8 | | | | |
| 87 | 84 | 82 | 83 | 86 |
| 84 | 85 | 84 | 84 | 83 |
| 82 | 84 | 84 | 84 | 82 |
| 84 | 85 | 84 | 84 | 83 |
| 87 | 84 | 82 | 83 | 86 |

ACTUAL MODEL

| | | | | |
|---|---|---|---|---|
| layer 1 | | | | |
| 200 | 200 | 200 | 200 | 200 |
| 200 | 200 | 200 | 200 | 200 |
| 200 | 200 | 200 | 200 | 200 |
| 200 | 200 | 200 | 200 | 200 |
| 200 | 200 | 200 | 200 | 200 |
| layer 2 | | | | |
| 400 | 400 | 400 | 400 | 400 |
| 400 | 400 | 400 | 400 | 400 |
| 400 | 400 | 400 | 400 | 400 |
| 400 | 400 | 400 | 400 | 400 |
| 400 | 400 | 400 | 400 | 400 |
| layer 3 | | | | |
| 600 | 600 | 600 | 600 | 600 |
| 600 | 10 | 10 | 10 | 600 |
| 600 | 10 | 10 | 10 | 600 |
| 600 | 10 | 10 | 10 | 600 |
| 600 | 600 | 600 | 600 | 600 |
| layer 4 | | | | |
| 1000 | 1000 | 1000 | 1000 | 1000 |
| 1000 | 1000 | 10 | 10 | 1000 |
| 1000 | 1000 | 10 | 10 | 1000 |
| 1000 | 1000 | 10 | 10 | 1000 |
| 1000 | 1000 | 1000 | 1000 | 1000 |
| layer 5 | | | | |
| 3000 | 3000 | 3000 | 3000 | 3000 |
| 3000 | 3000 | 3000 | 3000 | 3000 |
| 3000 | 3000 | 3000 | 3000 | 3000 |
| 3000 | 3000 | 3000 | 3000 | 3000 |
| 3000 | 3000 | 3000 | 3000 | 3000 |
| layer 6 | | | | |
| 3000 | 3000 | 3000 | 3000 | 3000 |
| 3000 | 3000 | 3000 | 3000 | 3000 |
| 3000 | 3000 | 3000 | 3000 | 3000 |
| 3000 | 3000 | 3000 | 3000 | 3000 |
| 3000 | 3000 | 3000 | 3000 | 3000 |
| layer 7 | | | | |
| 30000 | 30000 | 30000 | 30000 | 30000 |
| 30000 | 30000 | 30000 | 30000 | 30000 |
| 30000 | 30000 | 30000 | 30000 | 30000 |
| 30000 | 30000 | 30000 | 30000 | 30000 |
| 30000 | 30000 | 30000 | 30000 | 30000 |
| layer 8 | | | | |
| 100 | 100 | 100 | 100 | 100 |
| 100 | 100 | 100 | 100 | 100 |
| 100 | 100 | 100 | 100 | 100 |
| 100 | 100 | 100 | 100 | 100 |
| 100 | 100 | 100 | 100 | 100 |

**Figure 3-11.** The resulting model after 15 iterations of the inversion procedure when the bottom 4 layers, excluding the bottom 30 ohm-m halfspace, have been constrained to be 1D. For this run, 3 relaxation steps per inversion iteration were used. The actual model is shown on the right for comparison. The resistivity values for each block are given in ohm-m. The 30 ohm-m bottom halfspace was held fixed during the inversion, and is not shown here.

```
Number of relaxation steps = 10                    Rmmfac=3.0e-5
Number of inversion iterations = 15                Damping=1.0
Rmm constraints to keep layers 5,6,7,8 1D

RESULTS FROM INVERSION PROGRAM                     ACTUAL MODEL
==============================                     ============================

 layer1                                            layer 1
   240   233   236   235   224                       200   200   200   200   200
   239   269   258   266   226                       200   200   200   200   200
   239   250   240   243   226                       200   200   200   200   200
   244   267   255   264   225                       200   200   200   200   200
   235   229   234   232   233                       200   200   200   200   200
 layer2                                            layer 2
   340   335   352   344   344                       400   400   400   400   400
   295   228   255   221   386                       400   400   400   400   400
   306   258   241   286   400                       400   400   400   400   400
   312   228   257   228   367                       400   400   400   400   400
   337   332   353   343   349                       400   400   400   400   400
 layer3                                            layer 3
   541   559   514   517   565                       600   600   600   600   600
   577    12    12    11   527                       600    10    10    10   600
   591    11    13    12   481                       600    10    10    10   600
   587    12    11    13   505                       600    10    10    10   600
   538   551   507   519   559                       600   600   600   600   600
 layer4                                            layer 4
  1123  1272  1144  1117  1186                      1000  1000  1000  1000  1000
  1328   164    10    10  1067                      1000  1000    10    10  1000
  1295   140    13    12  1181                      1000  1000    10    10  1000
  1333   168     9    10  1043                      1000  1000    10    10  1000
  1109  1299  1164  1139  1181                      1000  1000  1000  1000  1000
 layer5                                            layer 5
  2407  2561  2536  2619  2480                      3000  3000  3000  3000  3000
  2625  2385  2223  1962  2551                      3000  3000  3000  3000  3000
  2574  2204  2162  2074  2624                      3000  3000  3000  3000  3000
  2672  2297  2219  1880  2611                      3000  3000  3000  3000  3000
  2373  2611  2614  2565  2468                      3000  3000  3000  3000  3000
 layer6                                            layer 6
  3276  3506  3693  3731  3276                      3000  3000  3000  3000  3000
  3585  3534  3475  3099  3480                      3000  3000  3000  3000  3000
  3625  3328  3356  3197  3688                      3000  3000  3000  3000  3000
  3561  3429  3467  2968  3664                      3000  3000  3000  3000  3000
  3266  3574  3756  3644  3367                      3000  3000  3000  3000  3000
 layer7                                            layer 7
 17528 14841 13532 14859 17793                     30000 30000 30000 30000 30000
 14980 12371 11607 12237 14863                     30000 30000 30000 30000 30000
 13575 11586 11351 11538 13395                     30000 30000 30000 30000 30000
 15017 12317 11592 12173 14874                     30000 30000 30000 30000 30000
 17501 14822 13523 14787 17896                     30000 30000 30000 30000 30000
 layer8                                            layer 8
    96    94    94    94    97                       100   100   100   100   100
    94    93    93    93    95                       100   100   100   100   100
    94    93    93    93    94                       100   100   100   100   100
    94    93    93    93    95                       100   100   100   100   100
    97    94    94    94    97                       100   100   100   100   100
```

**Figure 3-12.** The resulting model after 15 iterations of the inversion procedure when the bottom 4 layers, excluding the bottom 30 ohm-m halfspace, have been constrained to be 1D. For this run, 10 relaxation steps per inversion iteration were used. The actual model is shown on the right for comparison. The resistivity values for each block are given in ohm-m. The 30 ohm-m bottom halfspace was held fixed during the inversion, and is not shown here.

iteration. We started each of these inversions from an *a priori* model that had a uniform resistivity of 100 ohm-m except for the 30 ohm-m halfspace which we held fixed. The results using only one relaxation step per iteration are surprisingly good, although the results using ten relaxation steps per iteration are clearly the best. Tying together the resistivities within each of the bottom four layers has removed the smearing caused by the shallow conductive body and improved the estimates of the resistivities for these layers. Of course, in this example, we had the luxury of knowing beforehand that the bottom four layers should be uniform, but nonetheless, this demonstrates the usefulness of *a priori* information if it is available. Figure 3-13 shows the progression of the data errors and right-hand-side errors as a function of inversion iteration for the cases just described. Even though the inversions with three relaxation steps and ten relaxation steps per inversion iteration wound up at about the same data error level, the one with ten relaxation steps clearly did a better job at imaging the original model and adhering to the model covariance constraints.

We attempted to implement preconditioning of the relaxation scheme for the 3D inversion as we did for the 2D inversion (*Madden and Mackie*, 1989). As in that case, we tried using the inverses of the 1D sensitivity analyses for the vertical strip of blocks beneath each data site. Implementing this type of preconditioning in the 3D case caused numerical instabilities that made the inversion diverge away from the correct solution. What would generally happen is that the error would be reduced for the first few steps, then would steadily increase as the model parameters were driven to extreme values in one direction or another. We do not know exactly what causes this behavior, although we will hazard a guess. The 1D sensitivities are more closely related to the actual 2D sensitivities rather than the 3D sensitivities because in both the 1D and 2D cases, there are sensitivity terms for the phase and resistivity whereas in the 3D case, there are sensitivity terms for amplitudes, phases, and directions. Furthermore, in the 1D and 2D cases, there is only one electromagnetic mode whereas in the 3D case, there are two modes and they are coupled to

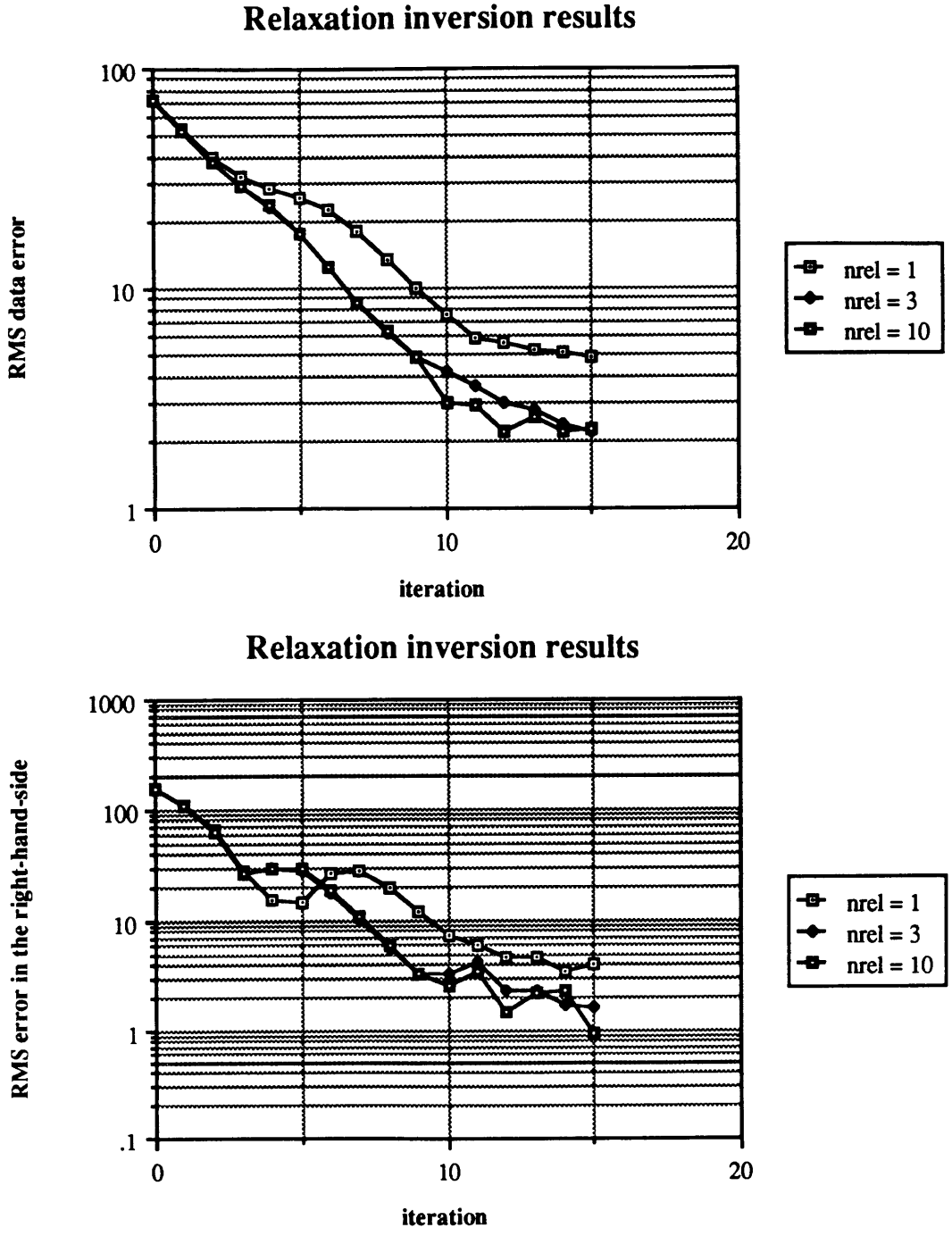


**Figure 3-13**. The RMS error progression as a function of the inversion iteration step for three different runs of the inversion algorithm. One run used 1 relaxation step per inversion iteration, one run used 3 relaxation steps per inversion iteration, and one run used 10 relaxation steps per inversion iteration. For each run, the bottom 4 layers of the model, excluding the bottom 30 ohm-m halfspace, have been constrained to be 1D. The data error and right-hand-side errors are defined in the text, equations 3-44 and 3-45.

each other. This coupling of the modes makes the 3D inversion inherently more difficult, but may also be the reason for the numerical instabilities when one uses preconditioning. This is because the preconditioning may be trying to drive the two separate electromagnetic modes in opposite directions, and this may cause the divergence we observed. Of course, the two modes increase the amount of data one has at each data site, and this fact alone should improve the convergence properties of the inversion so that the preconditioning may not be absolutely necessary for 3D data and 3D models. We saw in the examples presented earlier that we obtained extremely good fits to the data with just a few relaxation steps per inversion iteration without any sort of preconditioning. This is one point that we need to explore in more detail before we can make a definitive statement.

### *Future work*

The examples we show in this chapter are for uncomplicated, small 3D models. We have demonstrated that our relaxation inversion algorithm works fairly well for these models, implying that perhaps one day we will be able to routinely run 3D inversions. We must first learn to walk, however, before we can learn to run.

In the future, we must learn to include the effects of the boundary values in the sensitivity analysis. Then we can get away from using horizontally repeated models that we argued against in the previous chapter. Additionally, we must perform more extensive testing of the algorithm. This testing must include a wider variety of models and data coverage, it must include the effects of noise on the data, and it must include applications to real data. Lastly, we should explore alternate preconditioners that might help to improve the convergence properties of the algorithm.

### *Conclusions*

In this chapter, we introduced a method to invert magnetotelluric data for 3D Earth models. This method uses conjugate gradient relaxation to solve the maximum likelihood

inversion equations. Since at each iteration of the inversion one must update the model and begin the procedure anew, one need only use a few relaxation steps at each step of the inversion. Since we are using relaxation methods, we do not need to explicitly construct and store the sensitivity matrix, we only need to know the effect of the sensitivity matrix or its transpose multiplying an arbitrary vector. We have shown that each of these, the sensitivity matrix multiplying a vector and the transpose of the sensitivity matrix multiplying a vector, can be accomplished by one forward problem per frequency (both polarizations) each. This results in a tremendous time savings over the more traditional approach, and makes 3D inversions much more practical. We have demonstrated that the procedure works well for simple 3D models. Much work remains to be done to make the algorithm practical for realistic data and Earth models.

***References***

Eggers, D.E., 1982. An eigenstate formulation of the magnetotelluric impedance tensor, *Geophysics,* **47**, 1204-1214.

Franklin, J.N., 1970. Well-posed stochastic extensions of ill-posed linear problems, *J. math. Anal. Appl.*, **31**, 682-716.

Hestenes, M.R., and Stiefel, E., 1952. Methods of conjugate gradients for solving linear systems, *J. Res. Natl. Bureau Stand.*, **49**, 409-436.

Jackson, J.D., 1975. *Classical Electrodynamics*, John Wiley & Sons, New York.

Kong, J.A., 1986. *Electromagnetic Wave Theory*, John Wiley & Sons, New York.

Lanczos, C., 1961. *Linear Differential Operators*, D.Van Nostrand Co. Ltd.

LaTorraca, G.A., Madden, T.R., and Korringa, J., 1986. An analysis of the magnetotelluric impedance for three-dimensional conductivity structures, *Geophysics*, **51**, 1819-1829.

Mackie, R.L., Bennett, B.R., and Madden, T.R., 1988. Long-period magnetotelluric measurements near the central California coast: a land-locked view of the conductivity structure under the Pacific Ocean, *Geophys. J.*, **95**, 181-194.

Madden, T.R., and Mackie, R.L., 1989. Three-dimensional magnetotelluric modeling and inversion, *Proc. IEEE*, **77**, 318-333.

Mora, P.R., 1987, Nonlinear two-dimensional elastic inversion of multioffset seismic data, *Geophysics*, **52**, 1211-1228.

Tarantola, A. and Valette, B., 1982. Generalized nonlinear inverse problems solved using the least squares criterion, *Rev. Geophys. Space Phys.*, **20**, 219-232.

Tarantola, A., 1987. *Inverse Problem Theory: Methods for Data fitting and Model Parameter Estimation*, Elsevier, New York.

# Chapter 4
# Magnetotellurics in the California Basin and Range

"MT is a technical acronym for a sort of measurement taken by EE's in the guise of geophysicists ... MT involves many highly sophisticated instruments including shovels, picks, and little pieces of plastic and electrical tape used to cover the ends of missle-like objects ... buried in the desert for no reason at all..."
*-Carolyn Ruppel, crack MT data collector* (1989)

## *Introduction*

Over the past three years, we have collected magnetotelluric data across the California Basin and Range Province. Most of the data were acquired in the valleys where road access is good. The data are limited primarily to frequencies between 10 and 300 seconds because of equipment limitations and are generally of fair-to-good quality. We initially became interested in this area because an analysis of magnetotelluric data taken in Panamint Valley, California, at the January, 1987 MIT Geophysics Field Camp revealed several intriguing results. We expected that data at these periods would primarily experience the influence of the conductive mantle and that both modes of the impedance tensor would have decreasing apparent resistivity with increasing period and E/H phases of around 50°-70°. We were quite surprised to find that only one mode displayed this type of behavior, and that the other mode behaved as if it were being influenced by excess ocean electrical currents trapped in the upper crust. Excess ocean currents, in general, retard the impedance spectra to longer periods (*Mackie et al.*, 1988); in other words, the spectra are not influenced by the conductive mantle until longer periods. This was surprising not only because we thought we were far enough away from the ocean not to be influenced by it (approximately 300 km), but because the anomalous current system was in the *north-south* direction and not the east-west direction as one might have initially assumed.

These results were interesting enough by themselves to be followed up with additional measurements in order to determine the nature of this anomalous current system. However, there was an added incentive to expand our measurements across the California

Basin and Range Province. The nature of extension in this region and its accommodation in the lower crust are two controversial issues (cf., *Zoback et al.*, 1981; *Wernicke*, 1985; *Jones*, 1987). If, as we suspected, the current system in the California Basin and Range was anomalous because of excess ocean electrical currents trapped in the upper crust, then these currents would be very sensitive to the electrical properties of the lower crust (*Ranganayaki and Madden*, 1980). We were able to document with additional measurements and theoretical modeling (*this chapter*) that the anomalous current system is indeed caused by excess ocean electrical currents trapped in the upper crust. By modeling the responses at these locations, we are able to construct a plausible, and possible, conductivity model for the region.

### *MT response terminology*

Throughout this chapter, we use a terminology that is useful for describing certain components of the magnetotelluric response. This terminology is based on an idealized 1D Earth model, but applies to real Earth responses. Consider a hypothetical continental 1D Earth model that has a moderately conductive upper crust, a resistive lower crust, and an increasingly conductive mantle, Figure 4-1. The apparent resistivity and phase for this model are plotted in Figure 4-2. At higher frequencies, the response is sensitive to the upper crustal resistivity structure, and this part of the response we term the *upper crustal branch.* At these frequencies, all of the induced current is in the upper crust because of the skin effect of electromagnetic fields in a conductive medium. For this particular example, the upper crust has a uniform resistivity of 300 ohm-m, so the apparent resistivity is constant at 300 ohm-m and the phase is 45°. For other more complicated upper crustal structures, the corresponding resistivity and phase would also be more complicated, and would be dependent on that resistivity structure. At intermediate frequencies, the apparent resistivity rises and the absolute values of the phase drop to low values. This is due to the influence of the resistive lower crust. This part of the spectrum we term the *lower crustal*

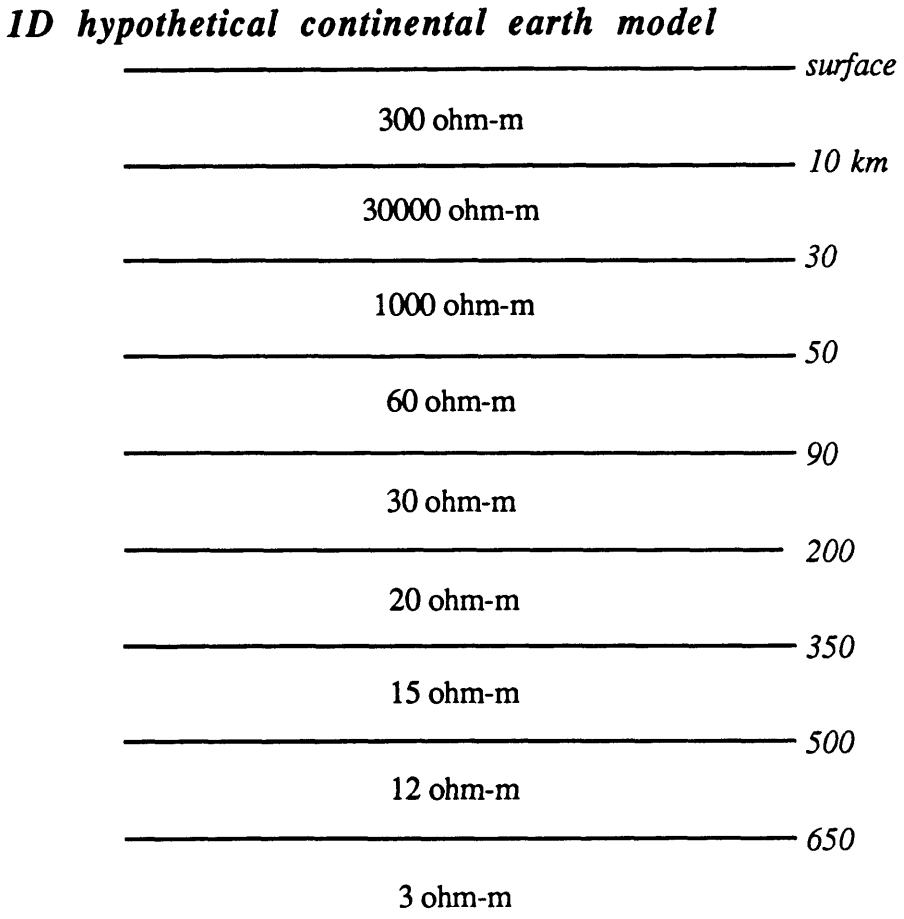


**Figure 4-1.** The 1D hypothetical continental Earth model used to generate the 1D MT soundings shown in Figure 4-2. This model has a 300 ohm-m upper crust, a 30,000 ohm-m lower crust, and an increasingly conductive mantle.

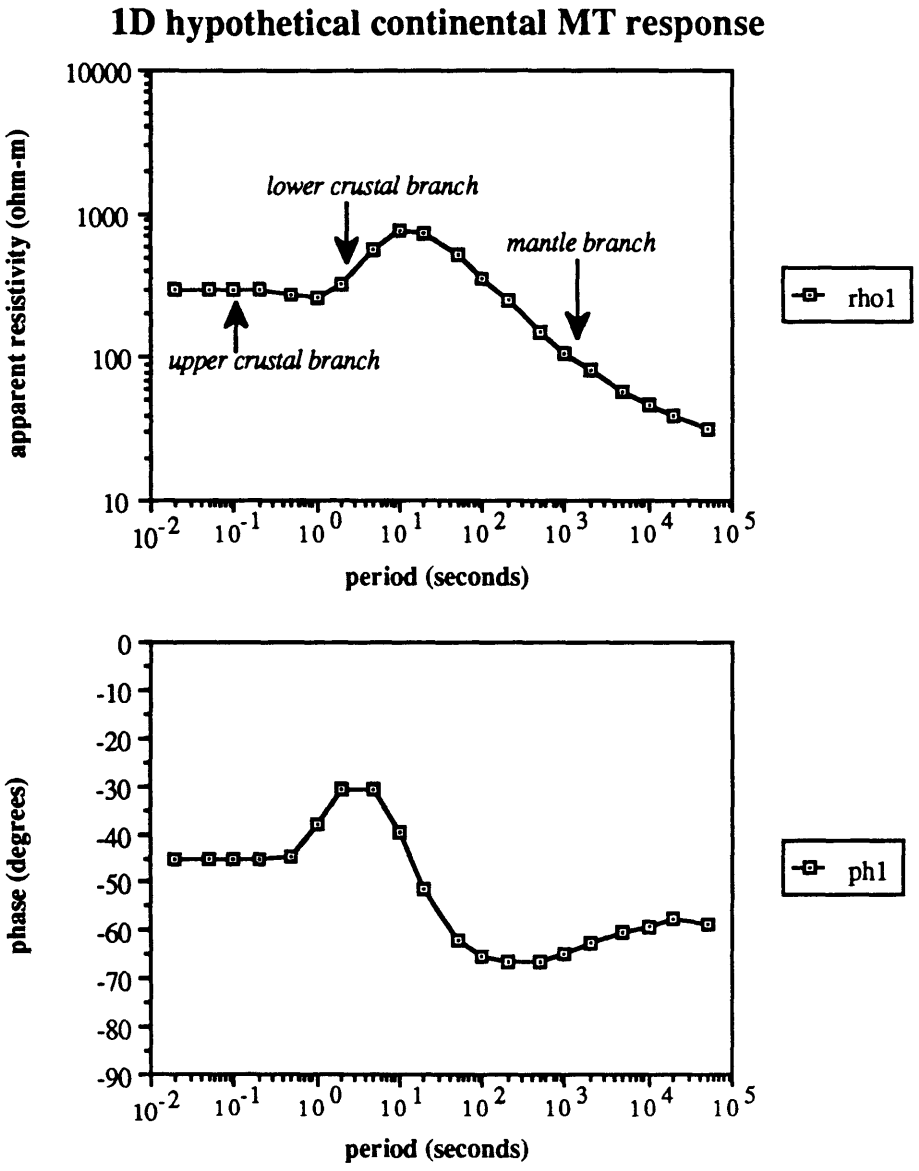


**Figure 4-2.** The MT response for the 1D hypothetical continental model of Figure 4-1. We have plotted apparent resistivity and phase versus period. The upper crustal branch, lower crustal branch, and mantle branch are indicated on the plot, and they are defined in the text.

*branch.* Since the lower crust is usually much more resistive than the upper crust, and since the periods are not yet long enough for the fields to penetrate into the conductive mantle, all the induced current gets concentrated in the more conductive upper crust. Consequently, the electric field is approximately constant within the upper crustal layer, and its amplitude is dependent primarily on the conductance of the upper crustal layer and the strength of the source field (*Kaufmann and Keller*, 1981). The impedance, therefore, is constant and frequency-independent over this frequency range. This causes the apparent resistivity, which is proportional to the period, to increase with increasing period and the phase to decrease (in the limit of an infinitely resistive and infinitely thick halfspace, the phase would go to zero). At the longest periods, most of the current is induced in the conductive mantle, and consequently, the amplitude of the impedance decreases, causing a decrease in the apparent resistivity. The phase also increases because the mantle is much more conductive than the crust (in the limit of a perfect conductor, the phase would go to 90°). At these longer periods, the surface impedance, especially the phase, is determined largely by the fields induced in the mantle even though the fields are measured on the Earth's surface. This part of the spectrum we term the *mantle branch.* In typical continental regimes, the mantle branch begins at periods of around 10-100s, depending on the conductivity structure. Near ocean-continent margins, however, the mantle branch can be retarded to much longer periods because of the influence of the ocean on the induced fields.

### *The MT coast effect*

Electromagnetic fields are affected by an ocean-continent boundary in two very distinct ways. The first, and probably most well known, is the coast effect that was first described by *Parkinson* (1962) and later by *Schmucker* (1963). They realized that anomalies in the vertical magnetic field recorded near an ocean coast were most likely due to electrical currents running *parallel* to the coast in both the ocean and the conductive upper mantle. *Menvielle et al.* (1982) suggest that the primary source of this coast effect is from

the ocean, and that the electric currents are deflected by the more resistive continental upper crust. They reached this conclusion by modeling the geomagnetic variations observed at coastal magnetic observatories. Measurements of the **E** fields in the ocean, however, seem to imply that there is not enough current in the ocean to cause all of the observed effects, and that some of the effect must be due to currents in the upper mantle (*Schmucker,* 1970, p.100). In the work herein, we are concerned with another coast effect - one that perturbs the electric fields running *perpendicular* to the coast. For this type of coastal effect, electric currents induced in the ocean remain trapped in the continental upper crust for some distance away from the coast, although they gradually leak off into the mantle as one progresses away from the coast.

Because the ocean has such a high conductance, most of the induced electrical current in oceanic regimes is concentrated in the ocean itself, even down to very long periods. This has the effect of retarding the mantle branch to very long periods (to greater than 12h even). Consider a 1D model that is the same as the model shown in Figure 4-1, except that the upper five km is replaced with an ocean of 0.3 ohm-m. The magnetotelluric response for this model is shown in Figure 4-3. Notice how the mantle branch is retarded to very long periods. In a continental regime far away from the ocean, the response is more typical of that shown in Figure 4-2. Since electrical currents are divergence-free, there is continuity in the normal component of current across the ocean-continent boundary. Consequently the currents must readjust to the change in the vertical conductivity structure in some broad zone around the ocean-continent boundary. This readjustment takes place by leaking currents out of the upper crust, across the resistive lower crust, and into the mantle. In this readjustment zone, the current system is a mix between the oceanic system and the continental system.

This readjustment depends on the conductance of the upper crust and the resistance of the lower crust (*Ranganayaki and Madden,* 1980). The distance over which two-thirds of this excess current has leaked back into the mantle is termed the *adjustment distance*, and

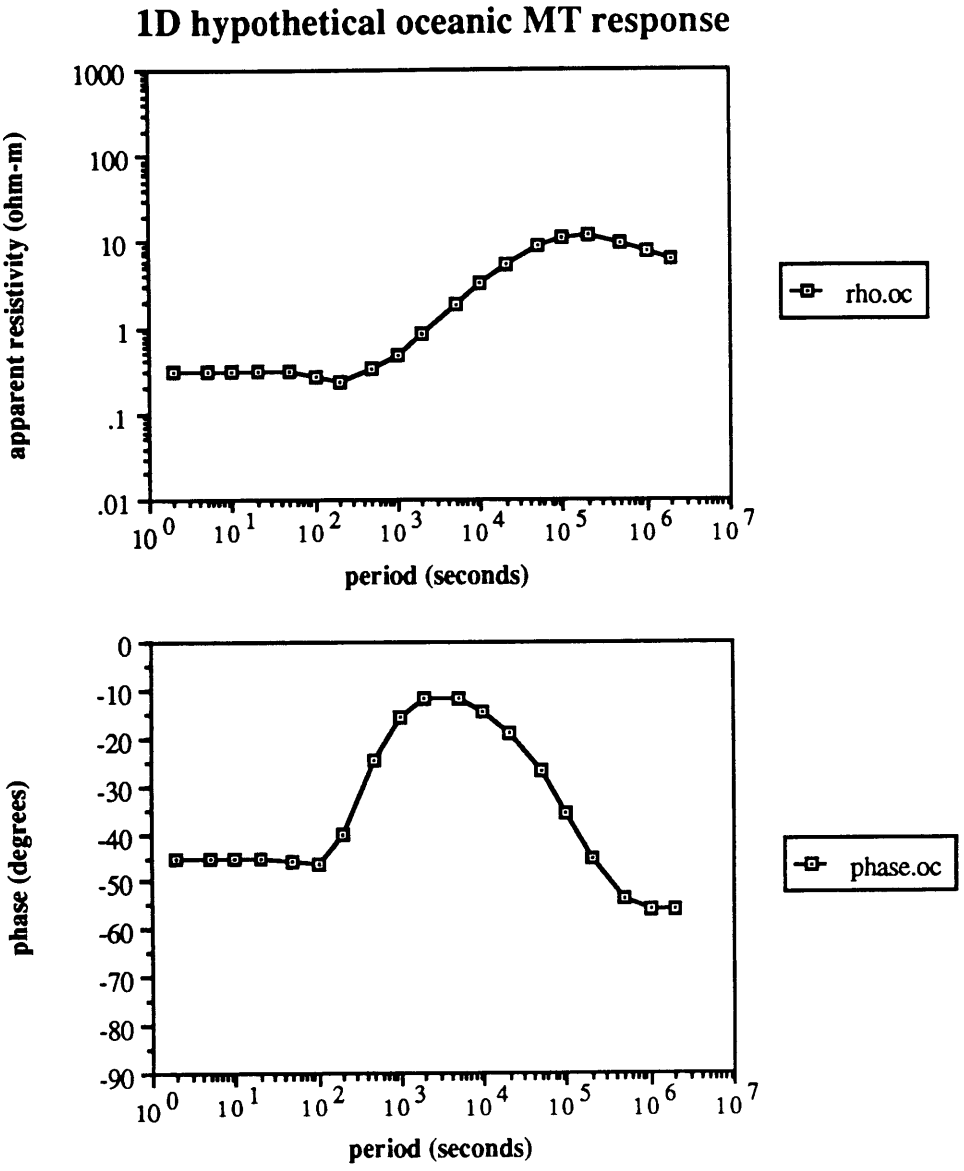


**Figure 4-3**. The MT response for the 1D model similar to that of Figure 4-1 except for the top 5 km of crust, which has been replaced by an ocean of 0.3 ohm-m. Notice how the mantle branch is retarded to long periods.

is equal to the square root of the product of the upper crustal conductivity-thickness product and the lower crustal resistivity-thickness product (*Ranganayaki*, 1978). Alternatively, one could interpret the adjustment distance as the distance over which currents are brought up from the mantle into the ocean. This distance can be 100 km or more for continental regimes, depending upon the resistivity structure. One must remember that even one adjustment distance away from the ocean, the upper crustal current system will still be contaminated by the ocean. It actually takes several adjustment distances for the current system to be returned to normal continental values.

Consider a simple 2D ocean-continental model, Figure 4-4. Figure 4-5 shows the TM mode responses at several locations on the continental side for this model. We plot the apparent resistivity and phase for six continental locations from 15 km to 550 km away from the ocean-continent boundary. In addition, we also plot the 1D response for the continental resistivity structure for comparison. The TM mode has **E** fields perpendicular to the strike of the geologic model and the **H** field parallel to the strike. Looking at Figure 4-4, we take the z-axis as vertically down, the y-axis horizontally across the page, and the x-axis (which is the strike axis) into the page. The TM mode, therefore, consists of the fields $E_y$, $E_z$, and $H_x$. The **E** fields, since they are normal to conductivity contrasts, suffer discontinuities across these contrasts. The continental adjustment distance for this model is 145 km. Notice the manner in which the apparent resistivity curves and phase curves behave as one progresses away from the ocean. Near the ocean, the mantle branch is not observed even at a period of $10^5$ seconds (about a 28 h period). It takes a distance of 200-300 km away from the ocean before the mantle branch begins to be seen at lower periods. As one progresses away from the ocean, the longer period portion of the apparent resistivity curve is shifted downwards and the phase curve is shifted down to larger phases as more of the ocean current leaks into the mantle. It is not until 550 km, or a little more than 3 adjustment distances, that the response is 1D-like.

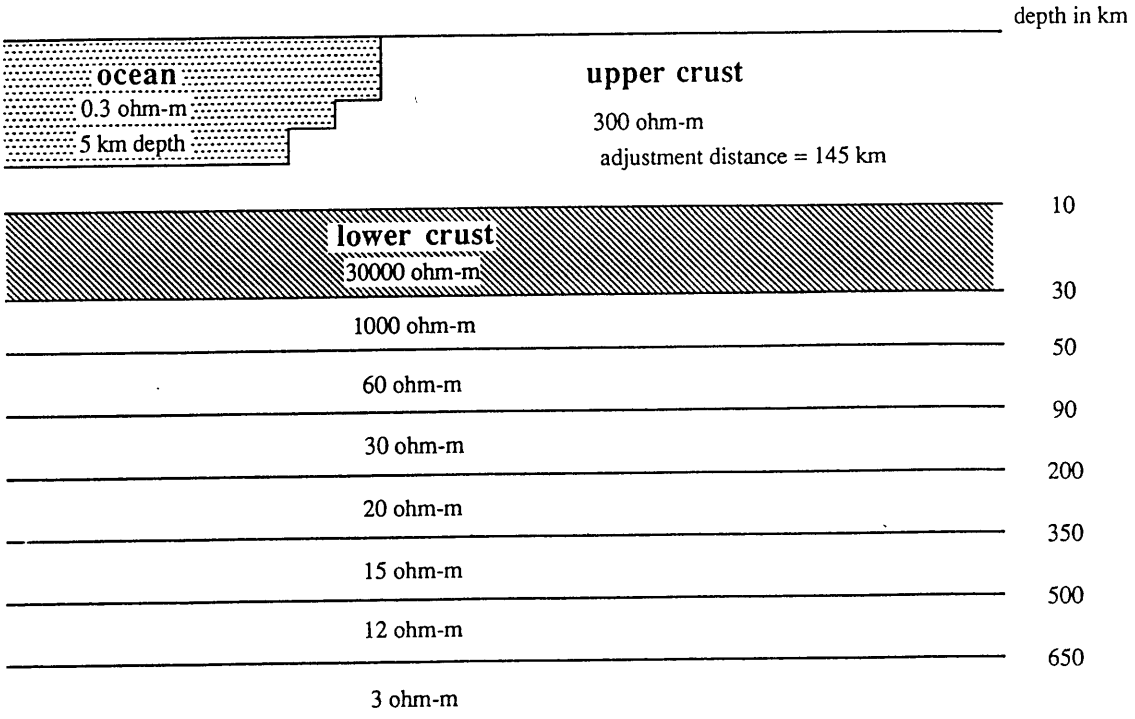


**Figure 4-4.** A simple 2D model representing an ocean-continent boundary. The continental adjustment distance for this model is 145 km.

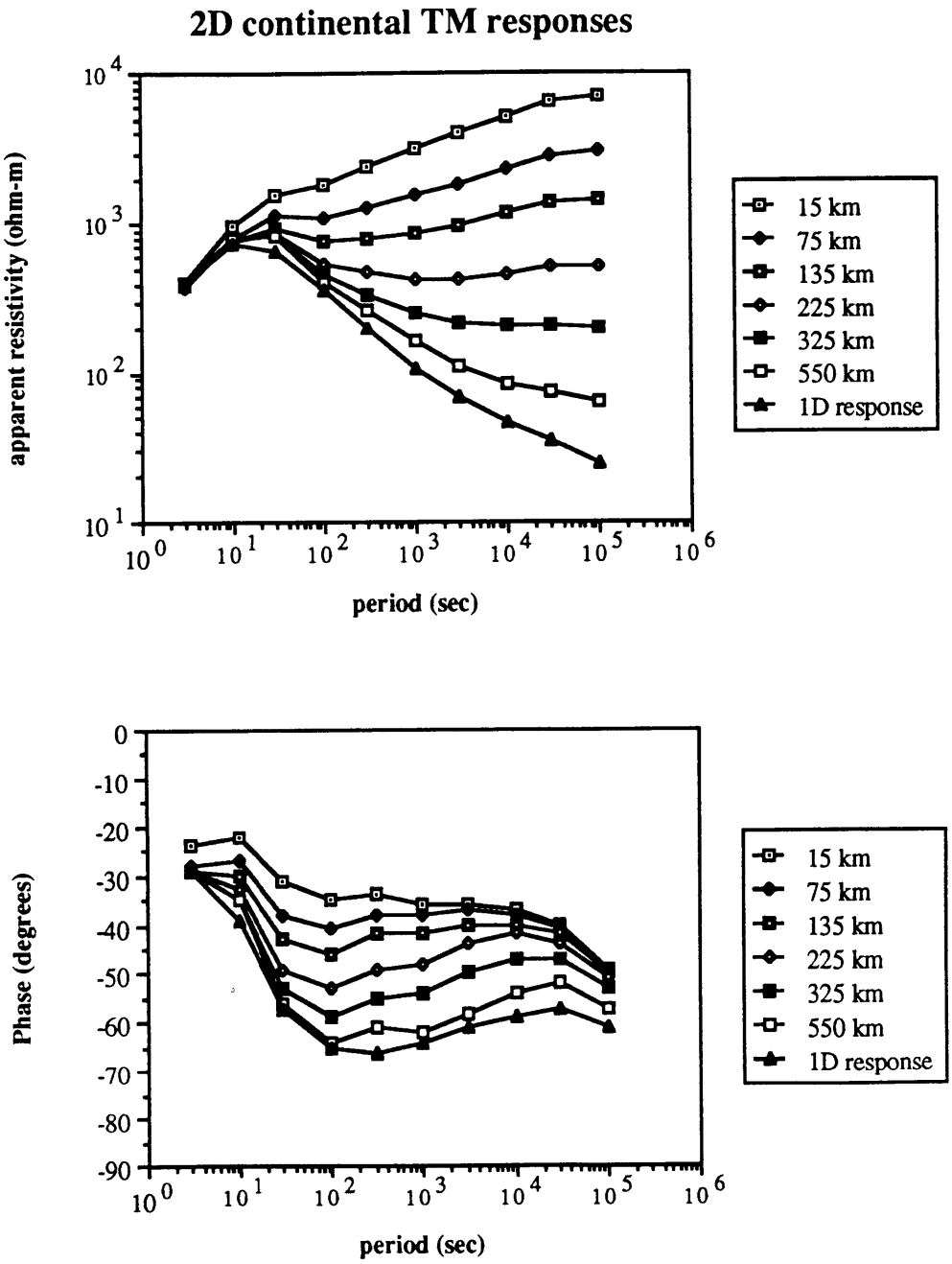


**Figure 4-5.** The 2D TM mode responses for the model shown in Figure 4-4. Plotted are the apparent resistivity and phase for 6 continental locations from 15 km to 550 km away from the ocean-continent boundary. Also plotted is the 1D continental response for comparison.

Figure 4-6 shows the 2D TE mode responses for the same locations. The TE mode has the **E** field parallel to the strike of the model and the **H** fields perpendicular to the strike ($H_y$, $H_z$, and $E_x$). The shapes and slopes of the apparent resistivity curves, and hence the phases, are about the same for all locations, except nearest to the ocean where the apparent resistivity is reduced somewhat. The TE mode responses are not influenced in a dramatic fashion, as are the TM mode responses. This is because the tangential component of the **E** field ($E_x$) is continuous across resistivity contrasts, and this **E** field is approximately constant across the entire model.

Anomalous conductive or resistive zones in the lower crust or upper crust can dramatically alter the behavior of the TM response curves. Figure 4-7 shows an example of such a situation, which is the model of Figure 4-4 except with a large conductive zone in the lower crust. Figure 4-8 shows the TM mode responses for this model as a function of period and position. Notice that the responses are basically separated into two groups, one group corresponding to the responses on the oceanic side of the anomalous conductive zone, and the other group corresponding to the responses on the continental side. Because of the conductive zone in the crust, more current from the ocean is attracted onto the continental upper crust. This causes the **E** fields on the oceanic side of the conductive zone to be larger than those for the uniform crust model of Figure 4-4. Consequently, the apparent resistivities are larger on the oceanic side of the conductive zone than those for the model with uniform crust (compare Figures 4-5 and 4-8). Additionally, the responses at 15 km and 75 km are practically equivalent. This is because the current in the upper crust would rather remain there until it has reached the conductive window instead of leaking some current across the resisitive lower crust before it reached the window (simply, current takes the path of least resistance). All of the responses for stations after the conductive zone are basically at the 1D response, although there are still some leakage effects at the longest periods. This is because, in this example, the conductive zone is so large that all of the excess ocean current went into the mantle through that zone. The response at 135 km,

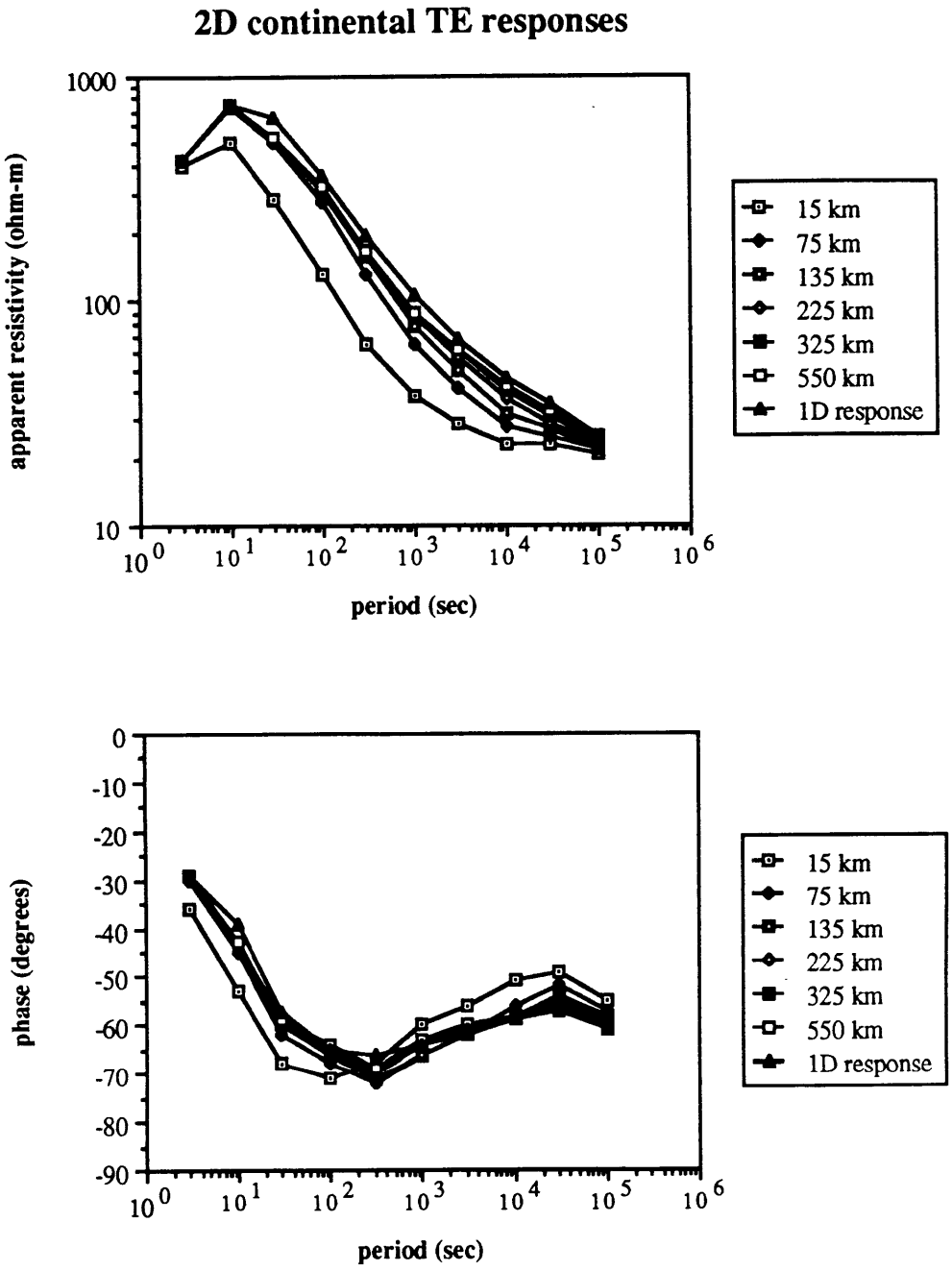


**Figure 4-6.** The 2D TE mode responses for the model shown in Figure 4-4. Plotted are the apparent resistivity and phase for 6 continental locations from 15 km to 550 km away from the ocean-continent boundary. Also plotted is the 1D continental response for comparison.

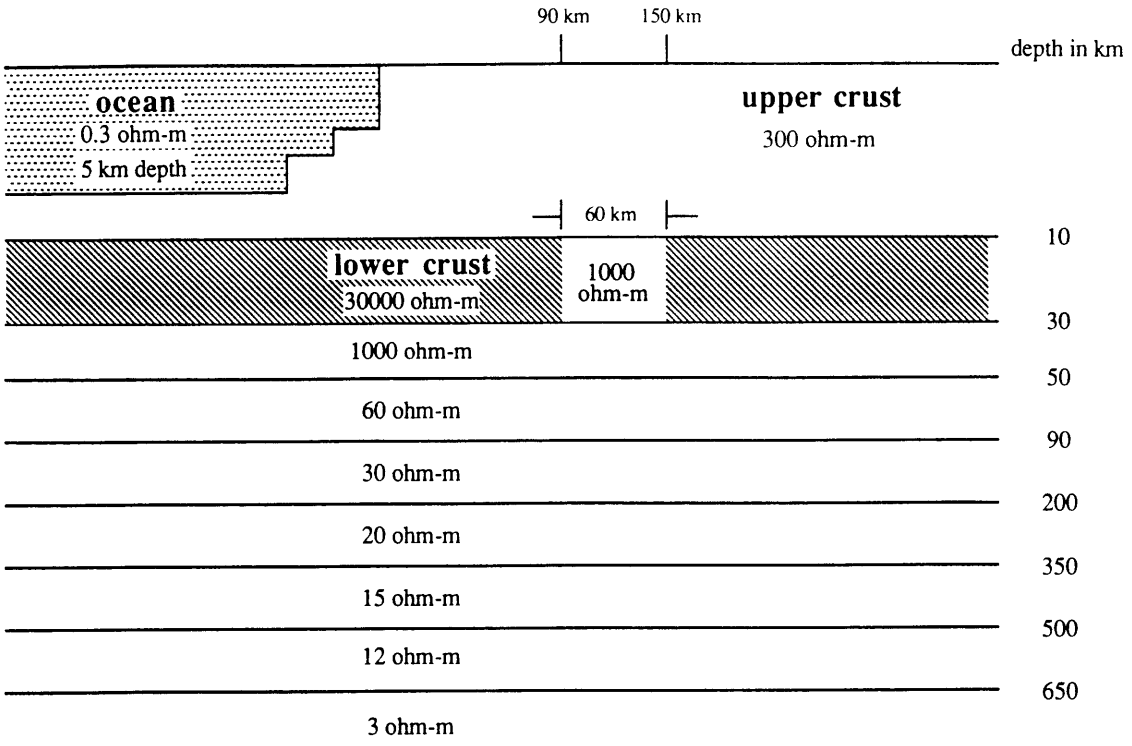


**Figure 4-7**. This 2D model is the same as that shown in Figure 4-4 except that a conductive window has been put into the lower crust.

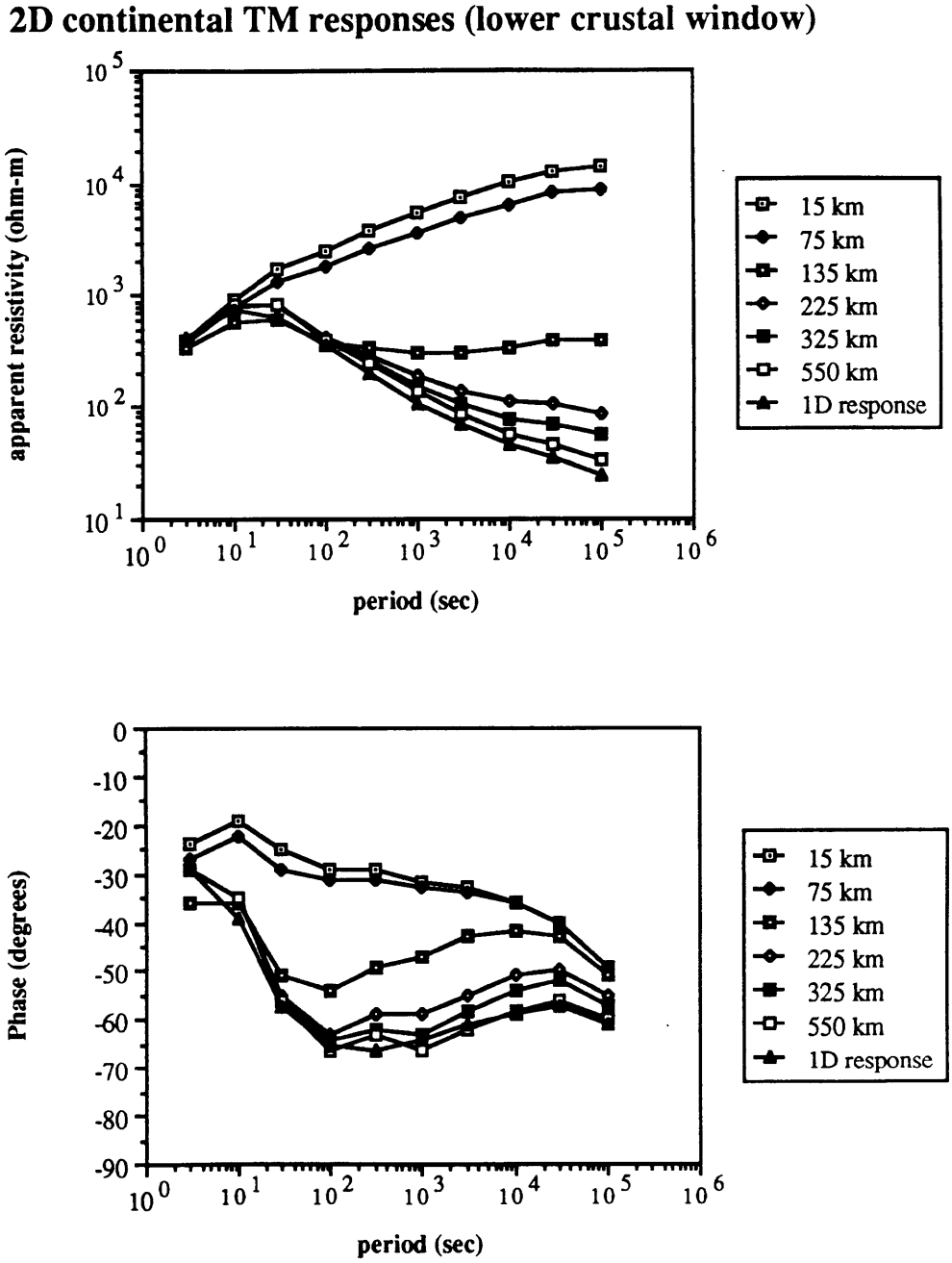


**Figure 4-8.** The 2D TM mode responses for the model shown in Figure 4-7. Plotted are the apparent resistivity and phase for 6 continental locations from 15 km to 550 km away from the ocean-continent boundary. Also plotted is the 1D continental response for comparison.

within the conductive zone, is a mix between the oceanic system and the continental system, but is more continental because much of the current has already leaked off. The TE mode responses for this model, Figure 4-9, show little effect from the anomalous conductive zone for the same reason as stated before.

From these examples, it is obvious that the TM mode response is extremely sensitive to the crustal resistivity structure near ocean margins, whereas the TE mode lends much less information regarding anomalous zones in the lower crust. By carefully following the readjustment of the TM current system, one can map out anomalous features in the lower crustal resisitivity structure.

It should be kept in mind that the readjustment across anomalous zones in the lower crust is dependent not only on the resistivity of that zone, but also on its horizontal dimensions. A conductive zone that is much narrower will not attract as much current as the broad zone, but there will still be a noticeable change in the TM response across that zone. The examples we have shown are not intended to cover all possible scenarios; indeed, they show just two simple examples one might actually encounter in field data. *Park et al.* (1990) followed the TM mode response across the central Great Valley and Sierra Nevada and found two zones of dramatic current loss - one on the west side of the Great Valley and another on the east. They interpreted these to be a suture zone between the Coast Ranges and the Great Valley and a contact between the basement of the Great Valley and the Sierra Nevada. The increased conductance of these zones was inferred to result from fluids in sedimentary rocks trapped during subduction that occurred in the Late Mesozoic and Early Cenozoic eras. In this chapter, we document examples in the California Basin and Range where we have found anomalous conductive zones in the lower crust. We interpret these zones to result from the recent extension that has caused higher than normal levels of porosity and fluids in the lower crust.

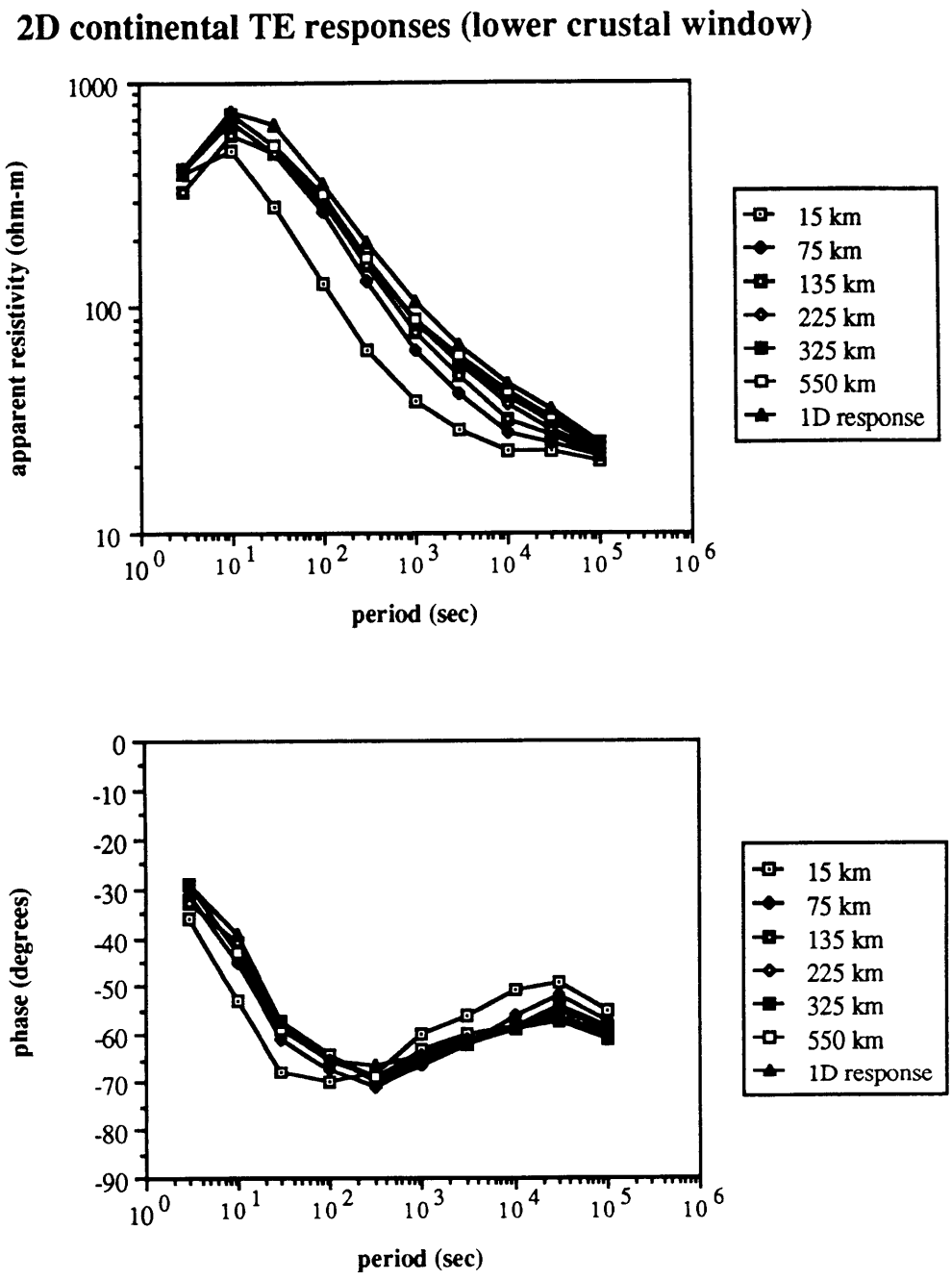


**Figure 4-9**. The 2D TE mode responses for the model shown in Figure 4-7. Plotted are the apparent resistivity and phase for 6 continental locations from 15 km to 550 km away from the ocean-continent boundary. Also plotted is the 1D continental response for comparison.

### *Geologic framework*

The Basin and Range Province of Western North America is a broad region approximately 1000 km wide that is characterized by extensive normal faulting, high heat flow, and a high regional elevation (*Eaton et al.*, 1978). The Basin and Range has experienced a multitude of tectonic events throughout its geologic history including extension, arc-related compressional orogenies, arc volcanism, and plutonism (*Burchfiel and Davis*, 1972, 1975; *Wernicke et al.*, 1987). Nevertheless, recent Cenozoic extension is largely responsible for the present physiography of the region, which is typified by elongate ranges separated by basins filled with recent alluvial sediments. The ranges and valleys are aligned approximately parallel, and they are perpendicular to the modern stress field which is roughly WNW-ESE (*Zoback et al.*, 1981).

Extension in the Basin and Range Province has not been uniform in time or areal extent. One can think of this province as a broad, diffuse zone of extension with localized zones of extreme extension mixed in with unextended or only mildly extended terranes. What has controlled the timing, magnitude, and location of the extension is still not known, nor is it known what role plate interactions and motions have played in producing the extended terrane (*Atwater*, 1970). Nevertheless, the mechanics of the crust, and especially the lower crust, are probably important in influencing the style and magnitude of extension, and this is one area where our magnetotelluric measurements can provide some information.

Several models have emerged in recent years to explain the mechanics of extensional terranes like the Basin and Range Province. One model, initially put forth some twenty years ago, is termed the pure shear model (*Stewart*, 1971) in which normal faulting in the upper crust is accommodated by penetrative ductile stretching in the middle and lower crust. In this model, the amount of extension is vertically uniform throughout the crust and upper mantle. The pure shear model contrasts with the simple shear model in which extension is accommodated along a low-angle master detachment surface that penetrates the

entire crust and perhaps the upper mantle (*Wernicke*, 1985). In this model, brittle behavior along the detachment surface in the upper crust gives way to some form of ductile deformation in the lower crust. Another possible model is that of lithospheric necking (*Froidevaux*, 1986; *Zuber et al.*, 1986) in which brittle extension in the upper crust at one location is coupled to, but separated horizontally from, the ductile thinning of the mantle lithosphere in another area. These models are only end-members whereas extension in the Basin and Range may actually involve some component of each of these models.

*Wernicke* (1985) proposed that the uplift of the Sierra Nevada is related to extension in Death Valley by simple shear extension of the crust. In his model, crustal thinning in Death Valley is accommodated by lithospheric thinning under the Sierra Nevada along a low-angle master detachment surface. *Jones* (1987) also concludes that the mantle lithosphere is thinned under the Sierra Nevada and that the crust is highly extended and thinned under Death Valley. He suggests, however, that either simple shear or lithospheric necking correctly predict the observed gravity, topography, and seismic refraction data, and that both models produce extended crust overlying unextended mantle lithosphere near Death Valley and unextended crust overlying thinned mantle lithosphere under the Sierra Nevada. Although they did not specifically model the Death Valley-Sierra Nevada transect, *Buck et al.*, (1988) suggest that based on their models for the evolution of the Red Sea Rift, simple shear extension, as proposed by *Jones* (1987) and *Wernicke* (1985), would be a viable extension mechanism along that transect. And although the extension in the Panamint-Saline system appears to be confined to the upper few kilometers of the crust (*Burchfiel et al.*, 1987), it is probably related to the larger scale extension that is occurring in the Death Valley area.

In each scenario discussed above, thinning of the upper crust by extension must be accommodated in the lower crust by some type of ductile deformation process. The models differ, however, in how the deformation in the upper crust is accommodated in the lower crust. Unlike most geophysical measurements, magnetotellurics can look at the lower crust

in this province and perhaps provide constraints to the deformation processes occurring there.

***Previous electromagnetic investigations***

*Schmucker* (1970) carried out an extensive geomagnetic variation study in California analyzing magnetic bays and disturbances at 1 cph (1 cycle per hour = 3600 s), 2 cph, and 4 cph. He found that the Parkinson vectors near the California coast were very large in magnitude and pointed uniformly towards the ocean. By definition, Parkinson vectors point toward conductive features. Near the coast, the ocean overwhelms any local conductivity anomalies. Stations on the eastern side of the Sierra Nevada (Inyokern, Lone Pine, and Bishop), however, had Parkinson vectors pointing toward the Basin and Range. This indicates that the Basin and Range is more conductive than the Sierra Nevada to the west. Furthermore, these stations had a significant out-of-phase component that was in the opposite direction as the in-phase component. This signifies that an anomalous concentration of induction current is aligned parallel to the Sierra Nevada. *Schmucker* (1970) interpreted these anomalies as due to a narrow zone of high-conductivity east of the Sierra Nevada at a depth of 40-50 km.

*Wannamaker* (1983) conducted a magnetotelluric study in southwestern Utah. Two-dimensional TM modeling of his data required a low-resistivity (approximately 20 ohm-m) layer from about 35 km to 65 km in the upper mantle. He interpreted this feature as a zone of interconnected melt that had resulted from diapiric uprising of mantle-derived melts. Although this survey was carried out on the eastern margin of the northern Basin and Range, he postulated that a similar resistivity structure might exist on the western margin of the northern Basin and Range because of the similarities in tectonic style between the two regions.

*Park and Torres-Verdin* (1988) analyzed magnetotelluric data taken around the Long Valley, California caldera complex, which is north of our survey area. They were

primarily interested in seeing whether their data justified the existence of a magmatic body at depth, and did not concentrate on the lower crustal resistivity structure. Excess ocean electrical currents, however, did not seem to be influencing their data.

*Bennett* (1986) and *Mackie et al.* (1988) analyzed long-period magnetotelluric measurements made in Palmdale, California and Hollister, California to examine the lower crustal resistivity structure near the California coast. Both studies required a resistivity-thickness product for the oceanic lower crust on the order of $10^6$ ohm-m-km to fit the observed data. This correlates well with an independent study carried out by *Cox et al.* (1986) who made controlled-source electromagnetic measurements in the Pacific ocean with the transmitter and receiver directly on the ocean floor. They were able to model their data with an oceanic lower-crustal resistivity-thickness product of $2x10^6$ ohm-m-km. *Park et al.* (1990) analyzed shorter-period magnetotelluric data taken across central California. Their data also required similar resisitivities in the lower crustal parts of their model except for two zones of dramatic current leakage on either side of the Great Valley in central California.

There have been additional magnetotelluric surveys conducted in the vicinity of the Transverse Ranges in Southern California (*Reddy et al.*, 1977; and *Lienert et al.*, 1980), but these have failed to address the interaction between the ocean and the continent. And finally, *Towle* (1980) made magnetic measurements on the eastern front of the Sierra Nevada along a transect from the Sierra Nevada across to Death Valley. The fields he measured were the DC magnetic fields that resulted from the single-pole operation of the Pacific Northwest-Southwest DC Power line that runs down Owens Valley. He suggests that high electrical conductivity along the eastern front of the Sierra Nevada would explain his data.

## *Magnetotelluric data in the California Basin and Range*

### *I. Data collection*

From January, 1988 through March, 1989, we collected narrow-band magnetotelluric data at 27 sites in the California Basin and Range, shown in Figure 4-10. The data were sampled at a rate of 2s. Because of the filters in our system, the data were limited to periods of 10-300s. We modified the electronics prior to our last field trip so that we could collect data to 1000s periods. The data from the northern Mojave Desert (Garlock, Harper Lake, Coyote Lake, and Baker) sample to 1000s. Each sounding site consisted of two dipoles and two induction coils. Vertical **H** was not collected, nor were we able to remote reference the data.

Ted Madden at the Massachusetts Institute of Technology (MIT) and Steve Park at the University of California at Riverside (UCR) designed and built the magnetotelluric field systems that we used. The **E** fields were measured on dipoles approximately 800m long, which were grounded at each end with Ag-AgCl porous-pot electrodes. The signals from the dipoles were amplified, filtered, then digitized. The **H** fields were measured on induction coils that were originally built by *Cantwell* (1960), then later modified by *Davis* (1979). The signals from the coils were fed into a preamplifier, then the output from this was amplified again, filtered, and digitized. The MIT system uses a commercial Starbuck model 1232 digitizer, and the UCR system uses a digitizer built by Steve Park. Both systems are controlled by portable Hewlett Packard computers. Data collected on the two systems are internally consistent and repeatable (*Park et al.*, 1990).

### *II. Impedance estimation*

We processed the data using traditional processing methods (e.g., *Swift*, 1967; *Sims et al.*, 1971; and *Vozoff*, 1972). This processing consists of the following steps: 1) removal of gains, 2) removal of DC shift, 3) windowing the data, 4) Fourier transforming the data, 5) removing the system response (phase shifts caused by the

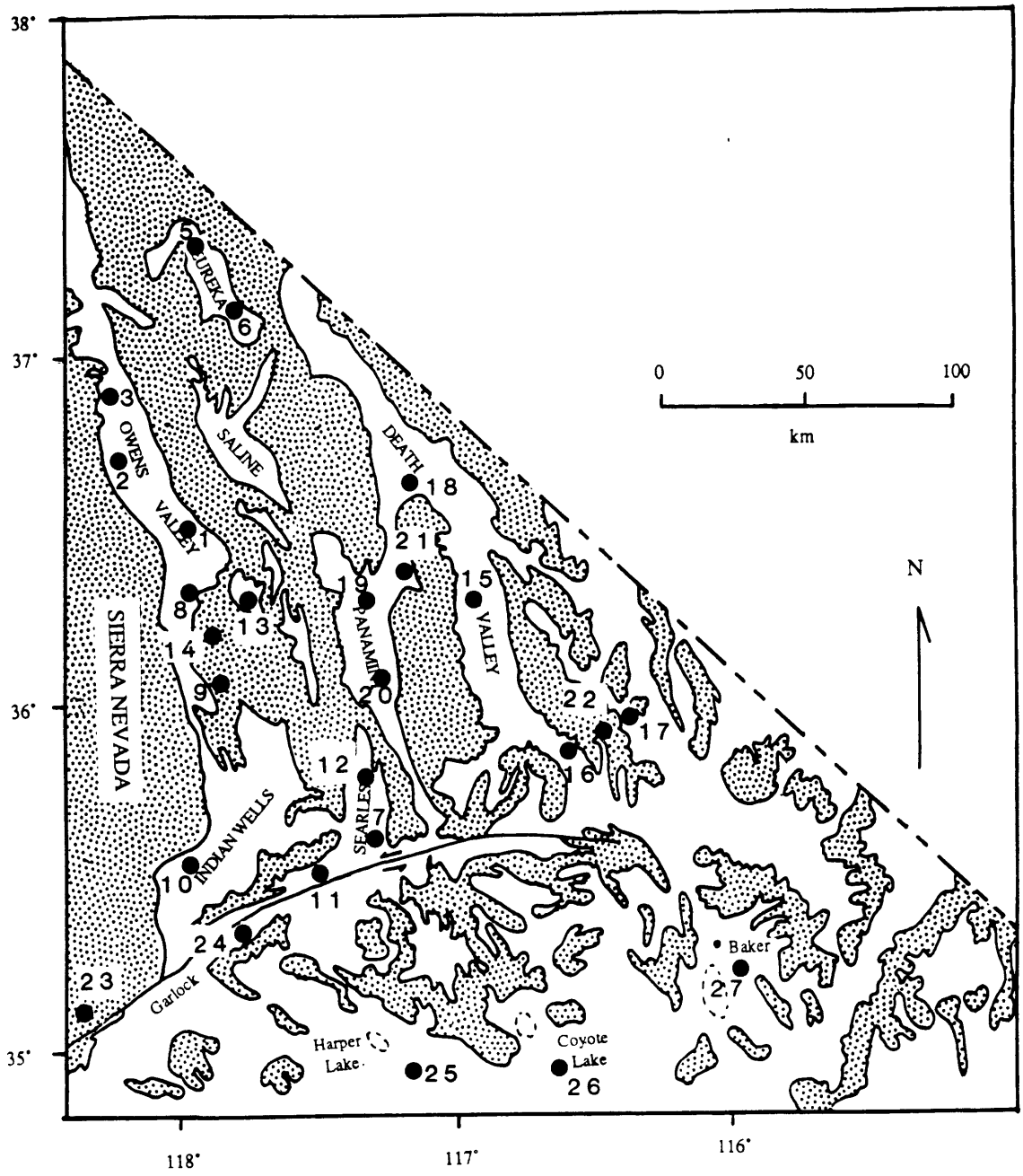


**Figure 4-10**. A simplified map of the California Basin and Range Province and the northern Mojave Desert. The mountain ranges and major outcrops are shaded. The locations of all our MT soundings are shown with black dots. The numbers next to each dot are the site numbers.

electronics and digitizer), and 6) computing the impedances as a function of frequency. We compute two estimates of the impedance tensor (see *Sims et al.*, 1971 for a detailed discussion of impedance estimates). The first estimate we term the $\mathbf{Z_h}$ estimate, which is given by

$$\begin{bmatrix} Z_{xx} & Z_{xy} \\ Z_{yx} & Z_{yy} \end{bmatrix} = \begin{bmatrix} \langle E_x H_x^* \rangle & \langle E_x H_y^* \rangle \\ \langle E_y H_x^* \rangle & \langle E_y H_y^* \rangle \end{bmatrix}^{-1} \begin{bmatrix} \langle H_x H_x^* \rangle & \langle H_x H_y^* \rangle \\ \langle H_y H_x^* \rangle & \langle H_y H_y^* \rangle \end{bmatrix}. \qquad (4\text{-}1)$$

In this equation, $\langle\ \rangle$ represents an average of values over a narrow bandwidth centered at a particular frequency. The quantities like $\langle E_x H_x^* \rangle$, etc., are the auto and cross power spectra of the observed fields. The second estimate we term the $\mathbf{Z_e}$ estimate, which is given by

$$\begin{bmatrix} Z_{xx} & Z_{xy} \\ Z_{yx} & Z_{yy} \end{bmatrix} = \begin{bmatrix} \langle E_x E_x^* \rangle & \langle E_x E_y^* \rangle \\ \langle E_y E_x^* \rangle & \langle E_y E_y^* \rangle \end{bmatrix}^{-1} \begin{bmatrix} \langle H_x E_x^* \rangle & \langle H_x E_y^* \rangle \\ \langle H_y E_x^* \rangle & \langle H_y E_y^* \rangle \end{bmatrix}. \qquad (4\text{-}2)$$

The $\mathbf{Z_h}$ estimate is biased down by noise in **H** while the $\mathbf{Z_e}$ estimate is biased up by noise in **E**. Computing both estimates gives us a good idea of the noise in the data. In our analysis, we make impedance estimates at twenty evenly-spaced logarithmic values from 10s to 300s (or 1000s for the Mojave Desert sites). Each impedance estimate averages the auto and cross power spectra over a band with a half-bandwidth of 30% of the center frequency. Before averaging, however, the **E** fields are corrected for the frequency dependence of the impedance amplitude. Since $\rho = 0.2\ T\ |Z|^2$, where T is the period in seconds and Z is the impedance, and since we are assuming that the impedance is constant over this wide band, the **E** fields are first multiplied by $\sqrt{(f_o/f_i)}$, where $f_o$ is the center frequency and $f_i$ is the frequency for the individual Fourier value. This removes the frequency bias caused by assuming a constant **Z** over the wide band. This method could be improved by allowing the impedance to have a slope across the band.

### *III. Computation of apparent resistivities, phases, and directions*

Once the impedance spectra are computed, they are rotated into an orthogonal north-east coordinate system, then decomposed using the shifted eigenvalue analysis of *LaTorraca et al.* (1986). This analysis determines the maximum and minimum apparent resistivities, the associated phases, the directions of the principal electric and magnetic eigenvectors, and the ellipticities. This analysis is superior to traditional rotation analyses because the electric and magnetic fields are not required to be perpendicular. The maximum apparent resistivity is associated with the electric and magnetic fields in the principal directions. The minimum apparent resistvity is associated with the electric field perpendicular to the principal electric field and the magnetic field perpendicular to the principal magnetic field. The **E** field eigenvector direction corresponds to the direction of current flow at that site.

The results of this analysis for each data location are shown in Figures 4-11 to 4-36. We plot the results for both the $\mathbf{Z}_h$ and the $\mathbf{Z}_e$ estimates. The maximum apparent resistivities and phases are plotted with open circles, and the minimum apparent resistivities and phases are plotted with closed triangles. The upper estimate at each frequency is the $\mathbf{Z}_e$ estimate since it is biased up by noise in **E**, while the lower estimate is the $\mathbf{Z}_h$ estimate. The principal **E** and **H** eigenvector directions are also plotted (the letter E represents the **E** principal direction and the letter H represents the **H** principal direction). The directions are plotted clockwise from geographic north. We also plot coherencies of the predicted **E** fields to the actual **E** fields in the maximum and minimum directions. These coherencies are the geometric mean of the coherencies from the $\mathbf{Z}_h$ and the $\mathbf{Z}_e$ estimates. The data from site 4, which was in Owens Valley, is not shown because the **H** field data from that site are contaminated with microseismic noise and are totally unusable.

**Figures 4-11 to 4-36.** These are the processed MT data for each site. The eigenstate analysis of *LaTorraca et al.* (1986) was used to generate the results. Plotted are the maximum and minimum apparent resistivities and phases, the principal electric and magnetic eigenvector directions, and the coherencies of the electric fields in the eigenvector directions. The upper estimate of apparent resistivity at each frequency is the $\mathbf{Z}_e$ estimate while the lower estimate is the $\mathbf{Z}_h$ estimate. The eigenvector directions are plotted as clockwise from geographic north. The coherencies are the geometric mean of coherencies from the $\mathbf{Z}_h$ and $\mathbf{Z}_e$ estimates.

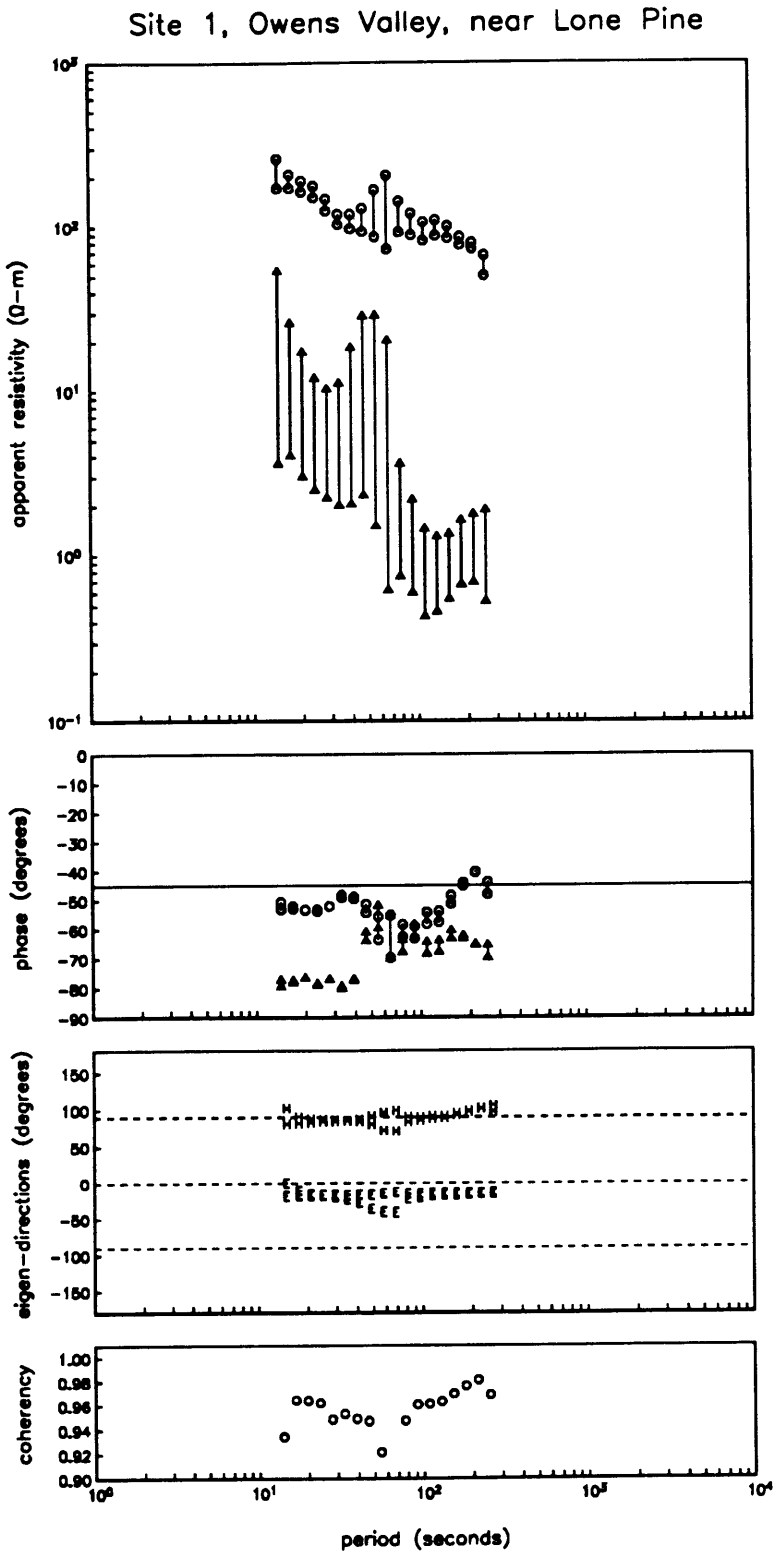
Site 1, Owens Valley, near Lone Pine
apparent resistivity (Ω-m)
phase (degrees)
eigen-directions (degrees)
coherency
period (seconds)

Figure 4-11.

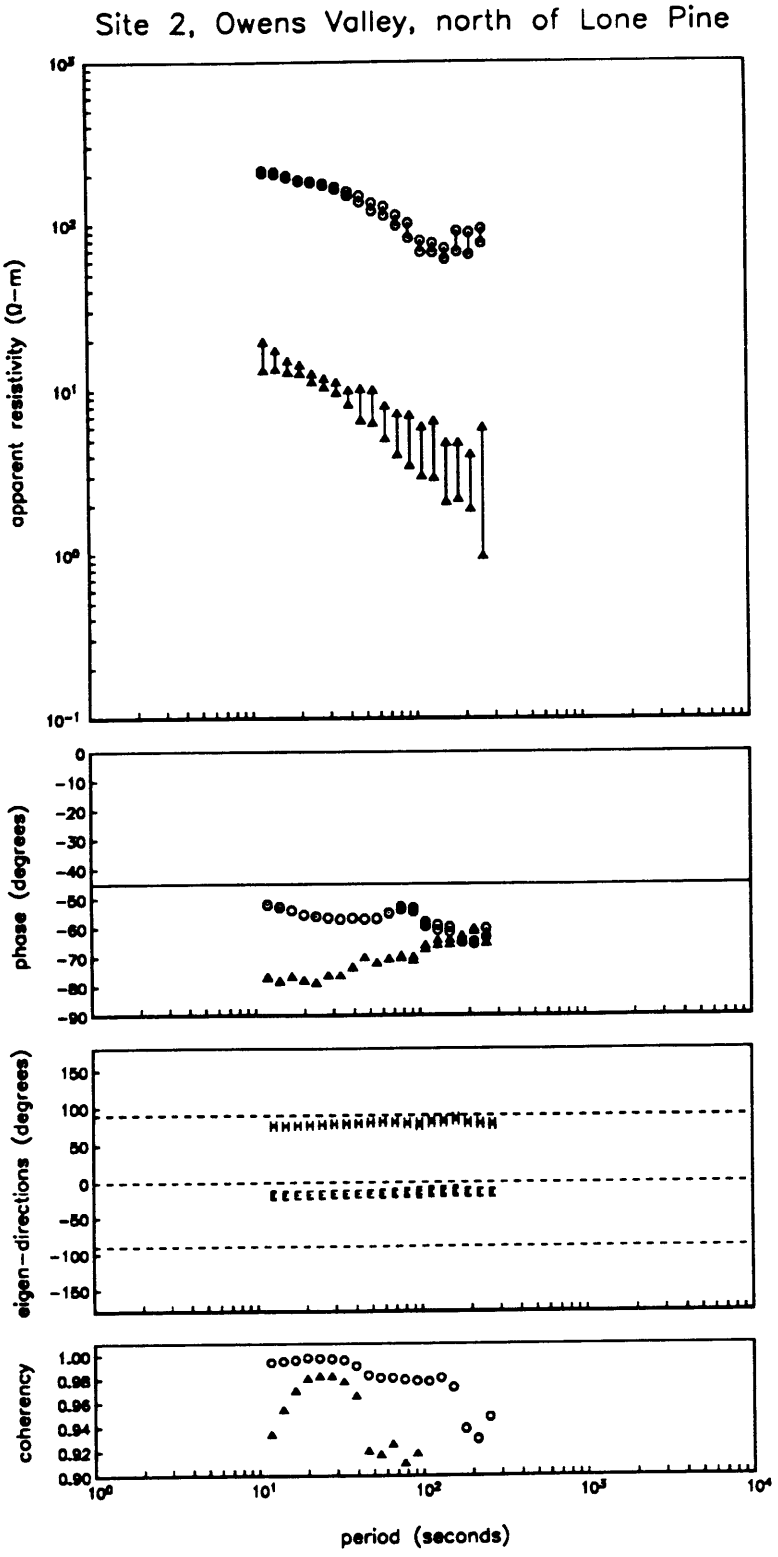
Site 2, Owens Valley, north of Lone Pine
apparent resistivity (Ω-m)
phase (degrees)
eigen-directions (degrees)
coherency
period (seconds)

**Figure 4-12.**

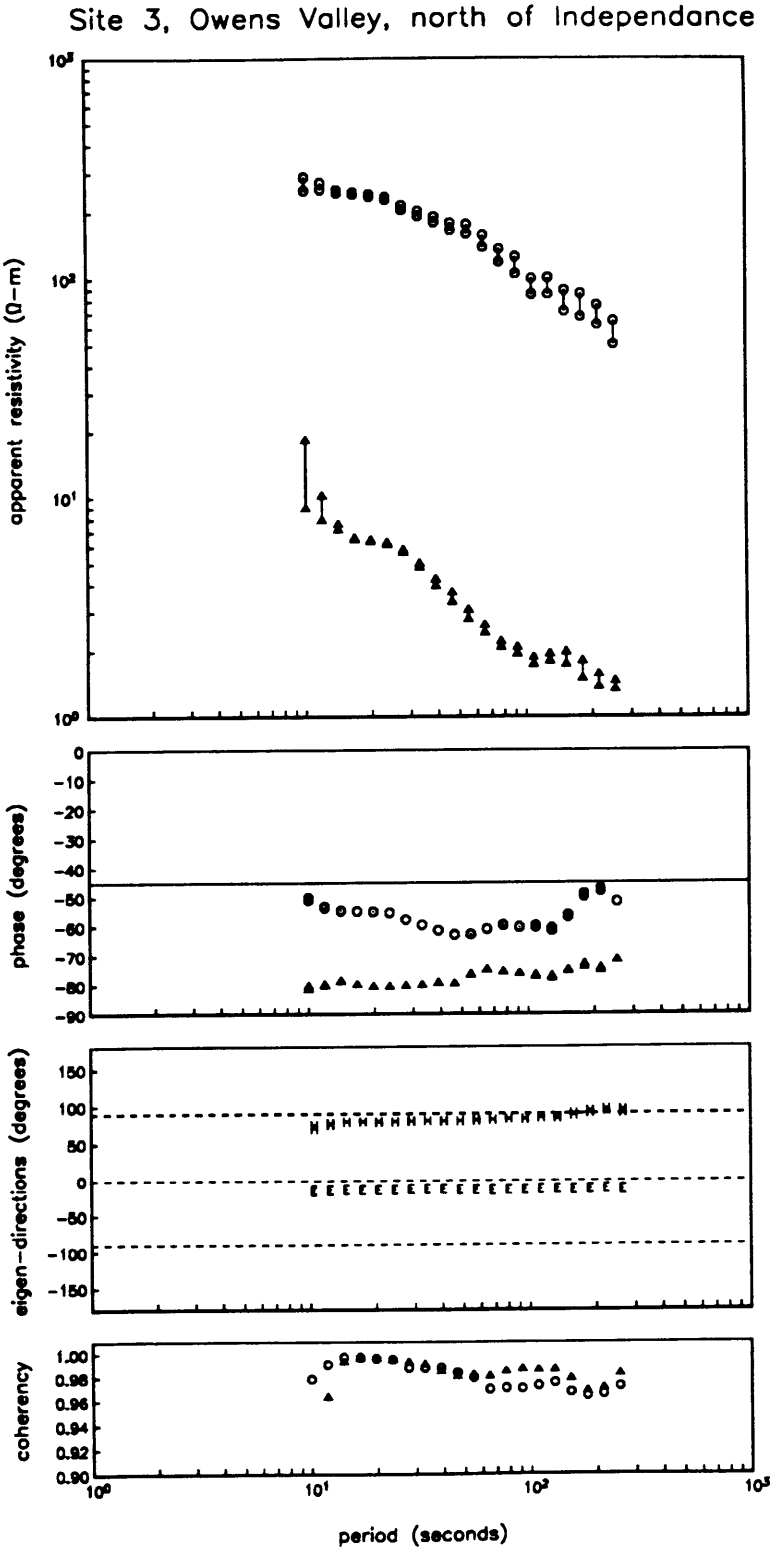
Site 3, Owens Valley, north of Independance
apparent resistivity (Ω-m)
phase (degrees)
eigen-directions (degrees)
coherency
period (seconds)

Figure 4-13.

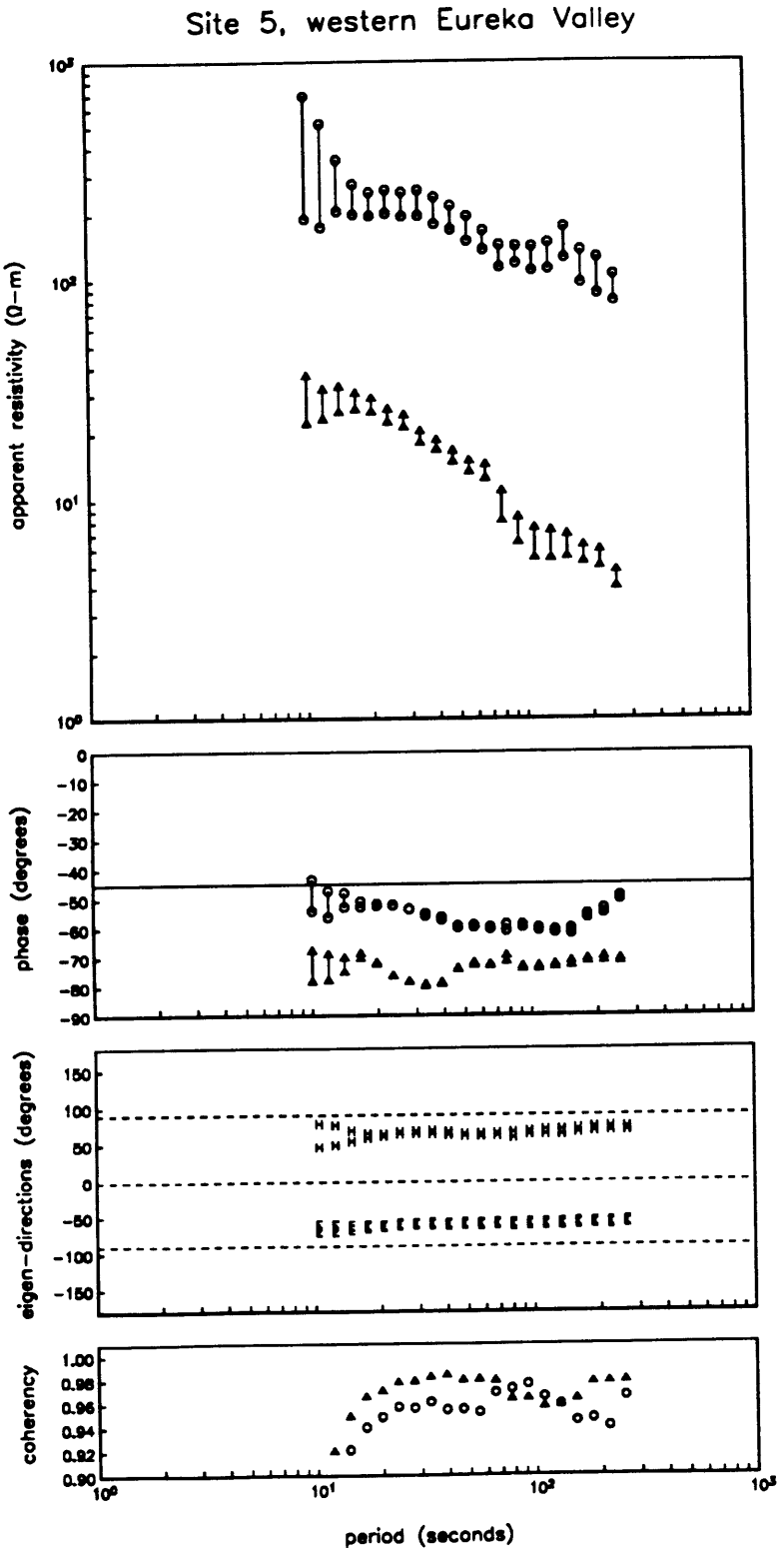
Site 5, western Eureka Valley
apparent resistivity (Ω-m)
phase (degrees)
eigen-directions (degrees)
coherency
period (seconds)

Figure 4-14.

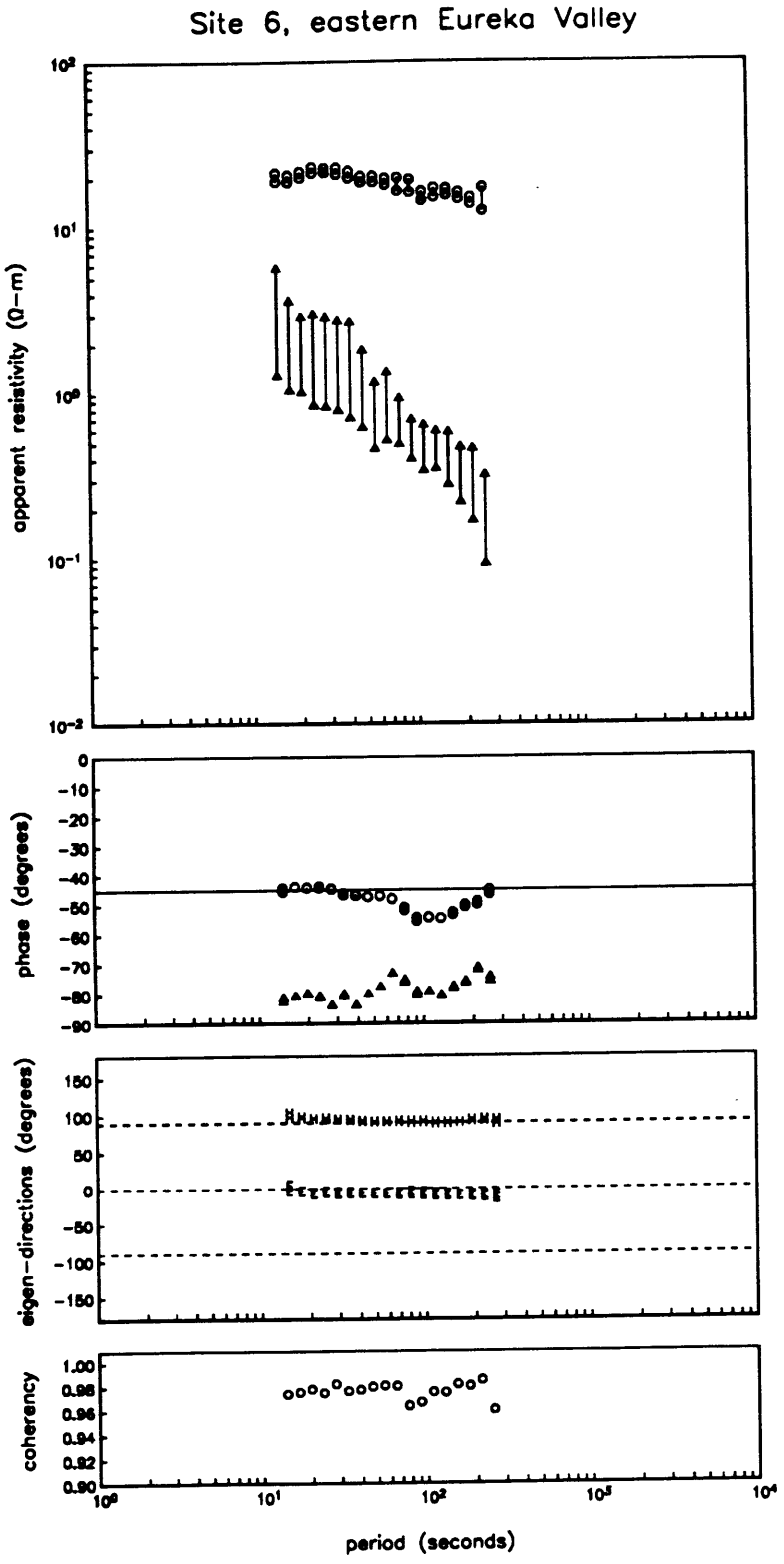
Site 6, eastern Eureka Valley
apparent resistivity (Ω-m)
phase (degrees)
eigen-directions (degrees)
coherency
period (seconds)

Figure 4-15.

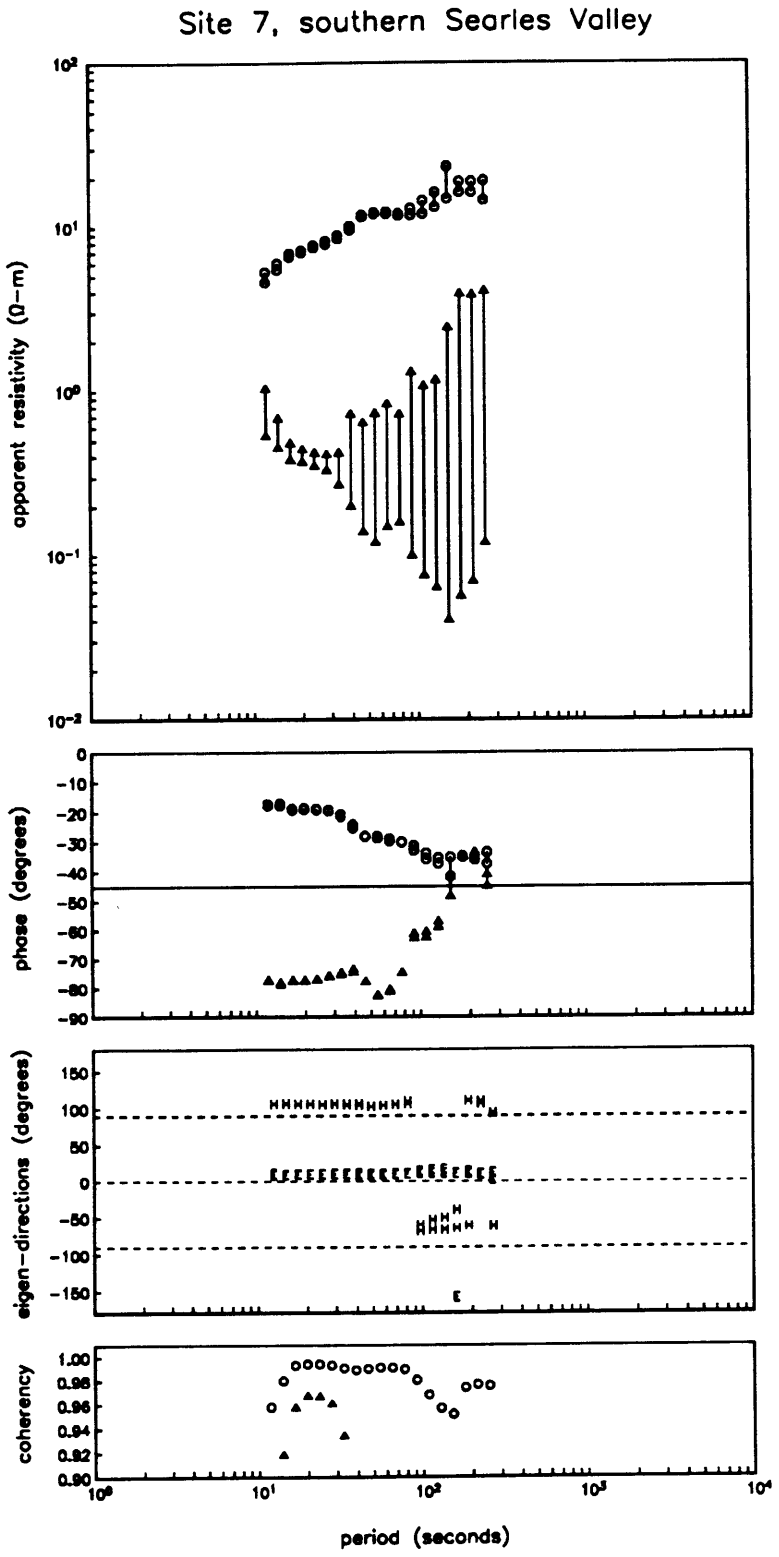
Site 7, southern Searles Valley
apparent resistivity (Ω-m)
phase (degrees)
eigen-directions (degrees)
coherency
period (seconds)

**Figure 4-16.**

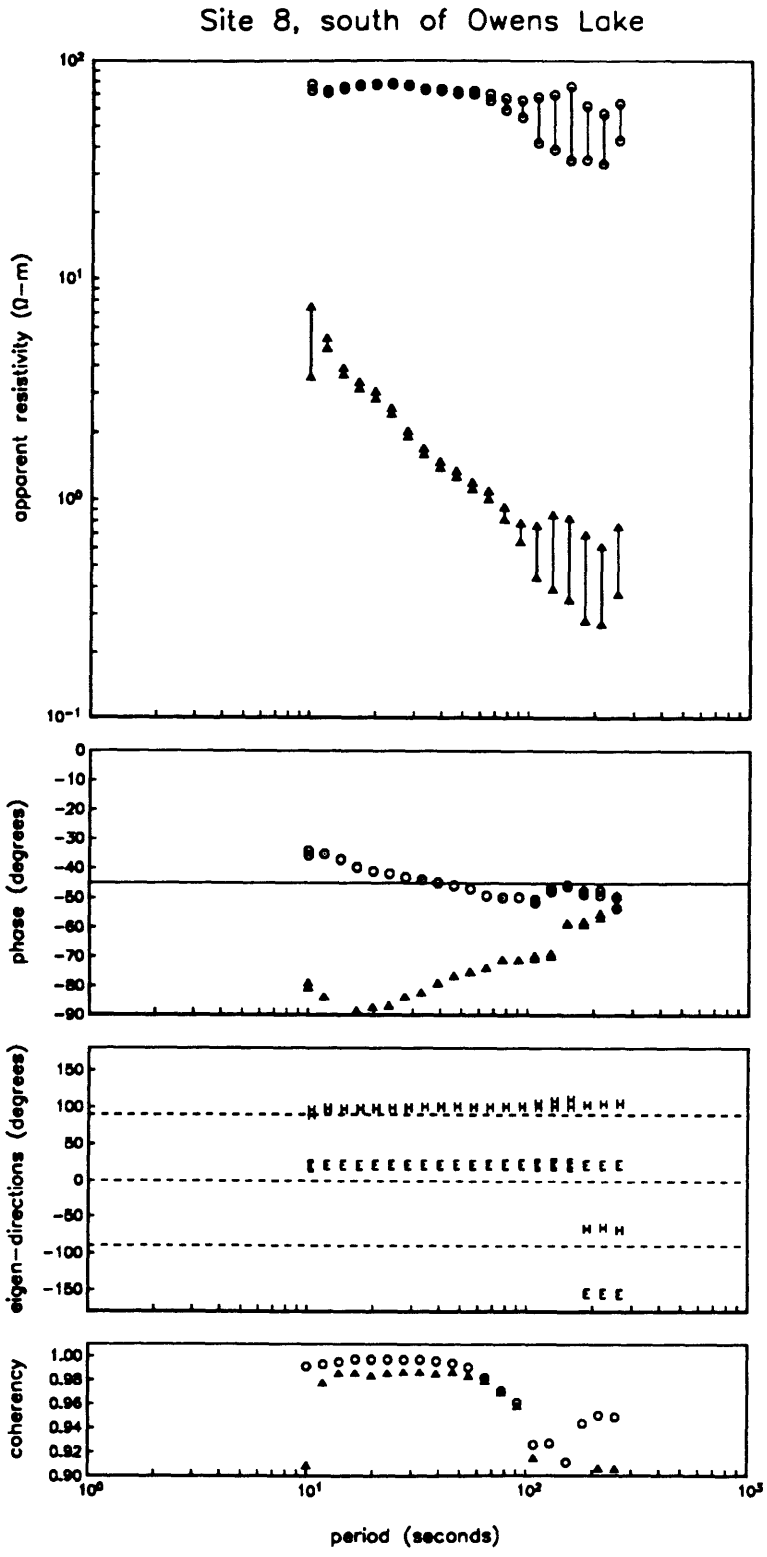
Site 8, south of Owens Lake
apparent resistivity (Ω-m)
phase (degrees)
eigen-directions (degrees)
coherency
period (seconds)

**Figure 4-17.**

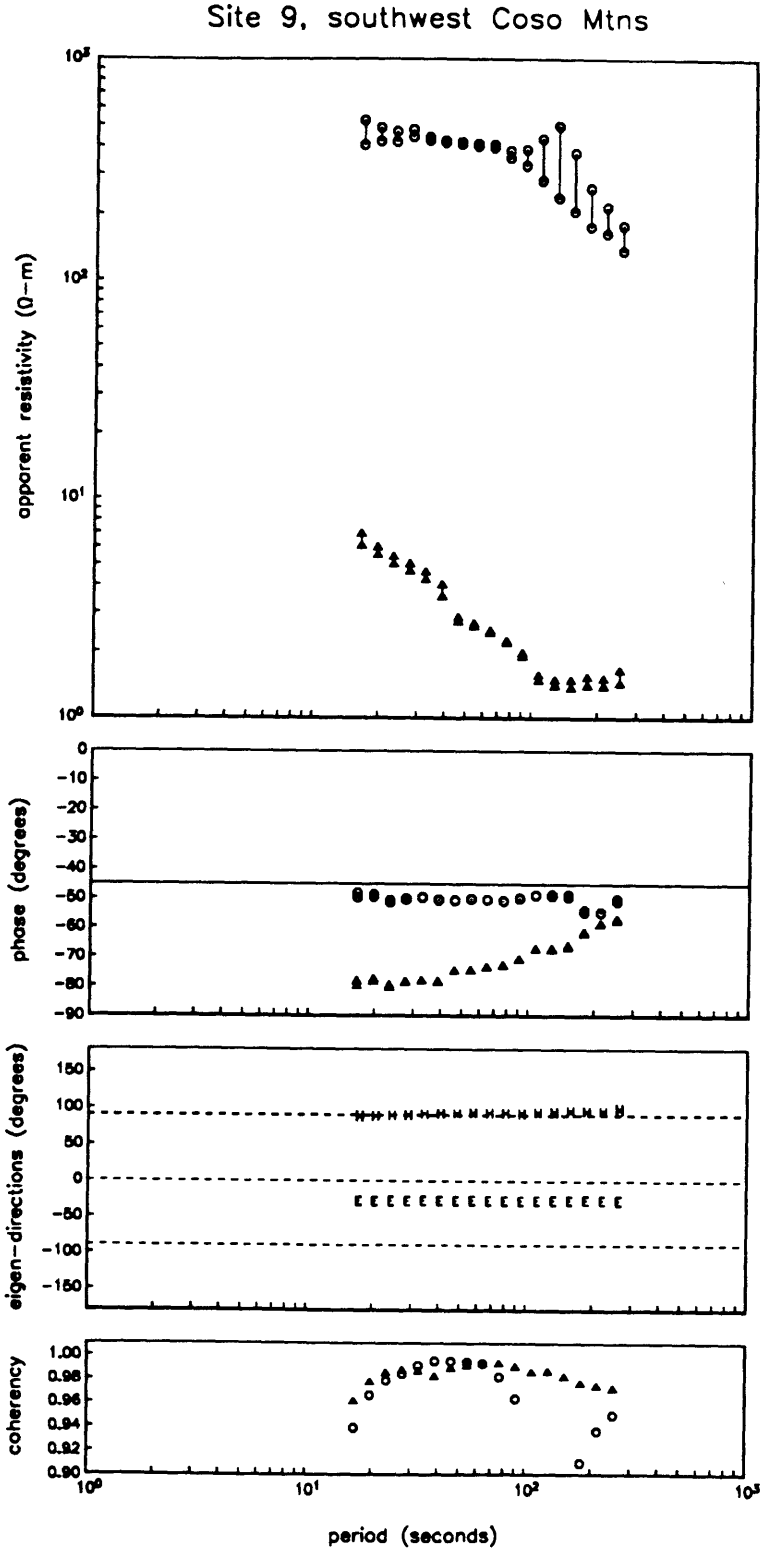
Site 9, southwest Coso Mtns
apparent resistivity (Ω-m)
phase (degrees)
eigen-directions (degrees)
coherency
period (seconds)

Figure 4-18.

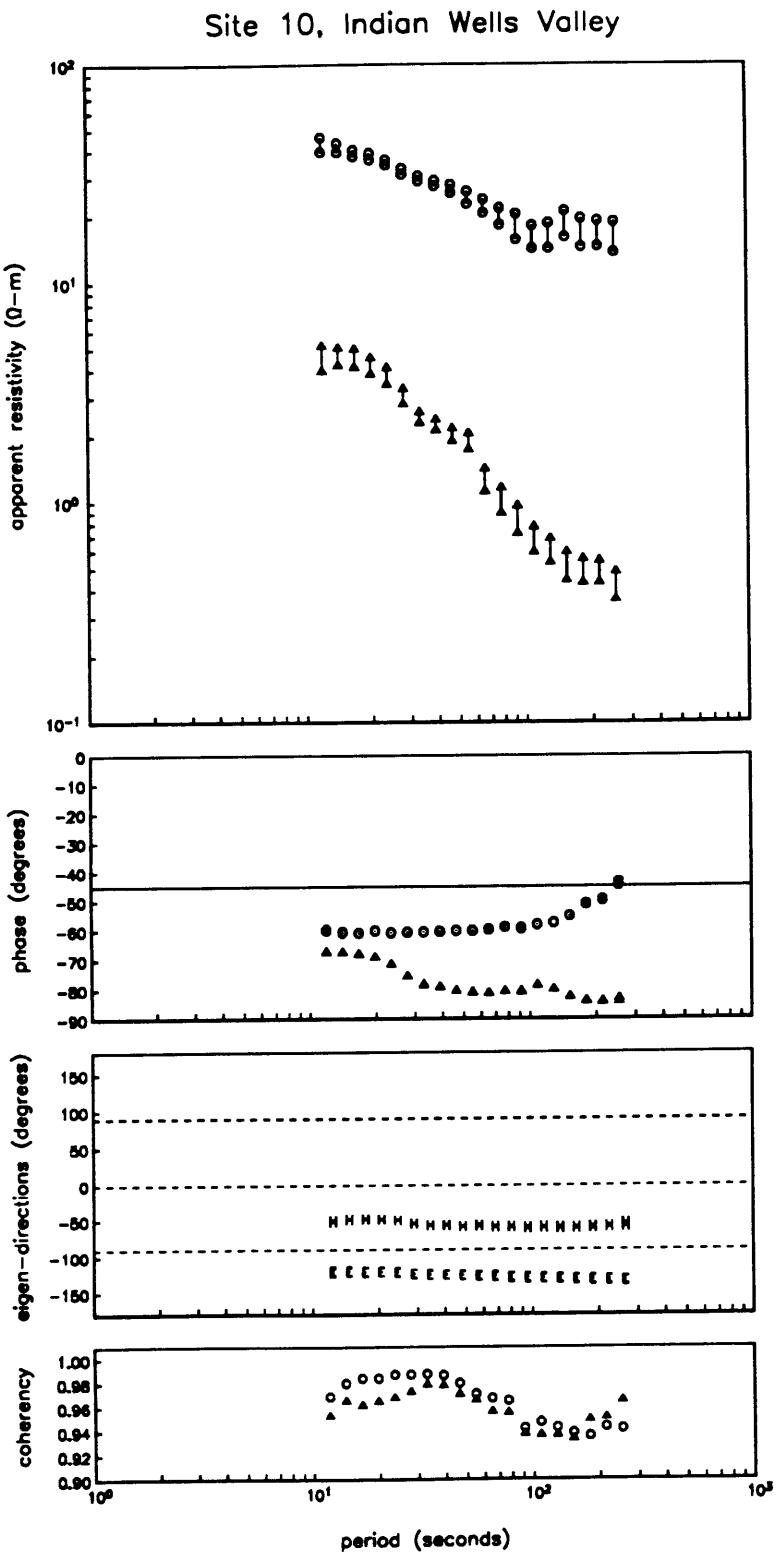
Site 10, Indian Wells Valley
apparent resistivity (Ω-m)
phase (degrees)
eigen-directions (degrees)
coherency
period (seconds)

Figure 4-19.

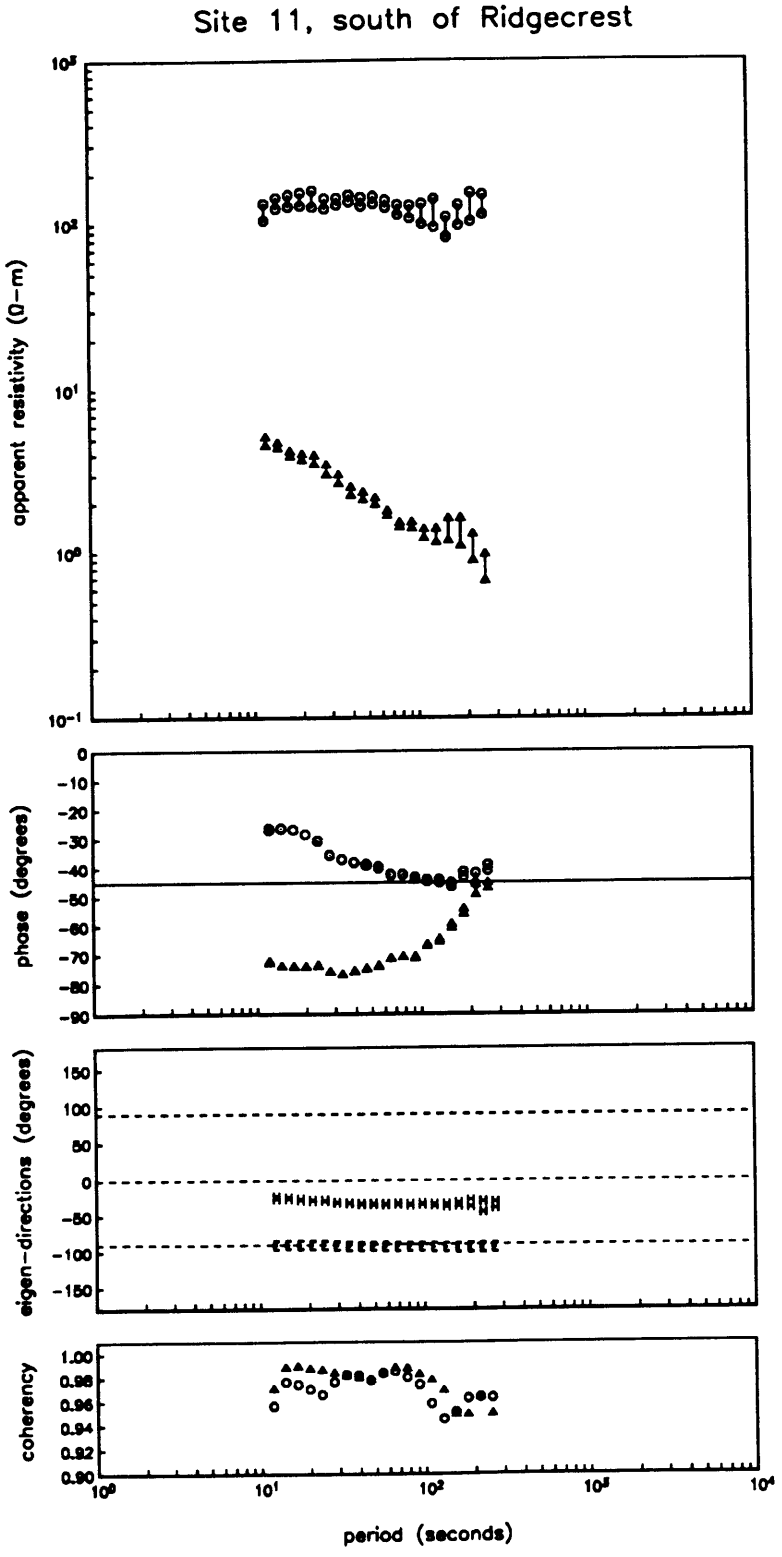
Site 11, south of Ridgecrest
apparent resistivity (Ω-m)
phase (degrees)
eigen-directions (degrees)
coherency
period (seconds)

Figure 4-20.

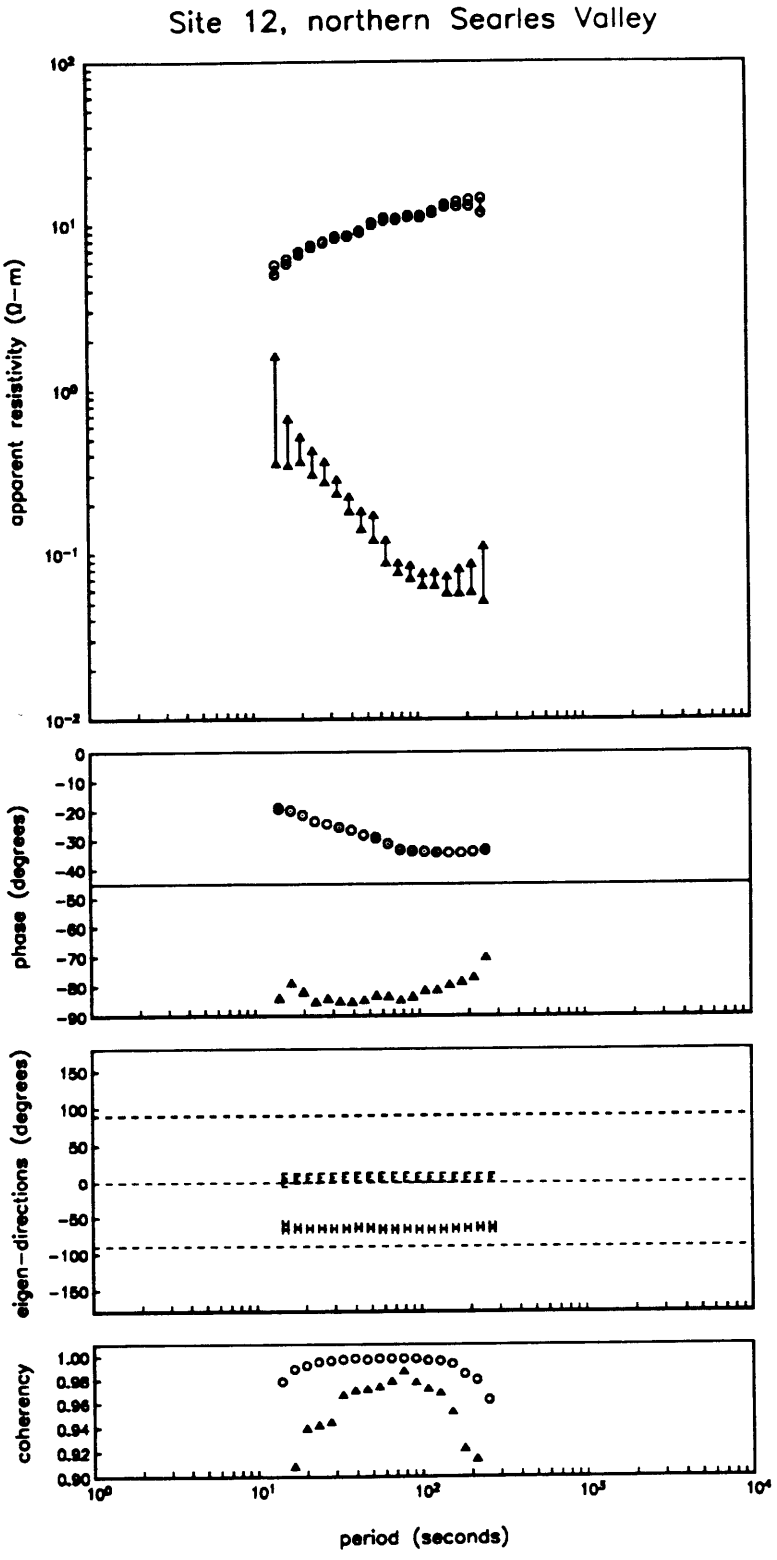
Site 12, northern Searles Valley
apparent resistivity (Ω-m)
phase (degrees)
eigen-directions (degrees)
coherency
period (seconds)

**Figure 4-21.**

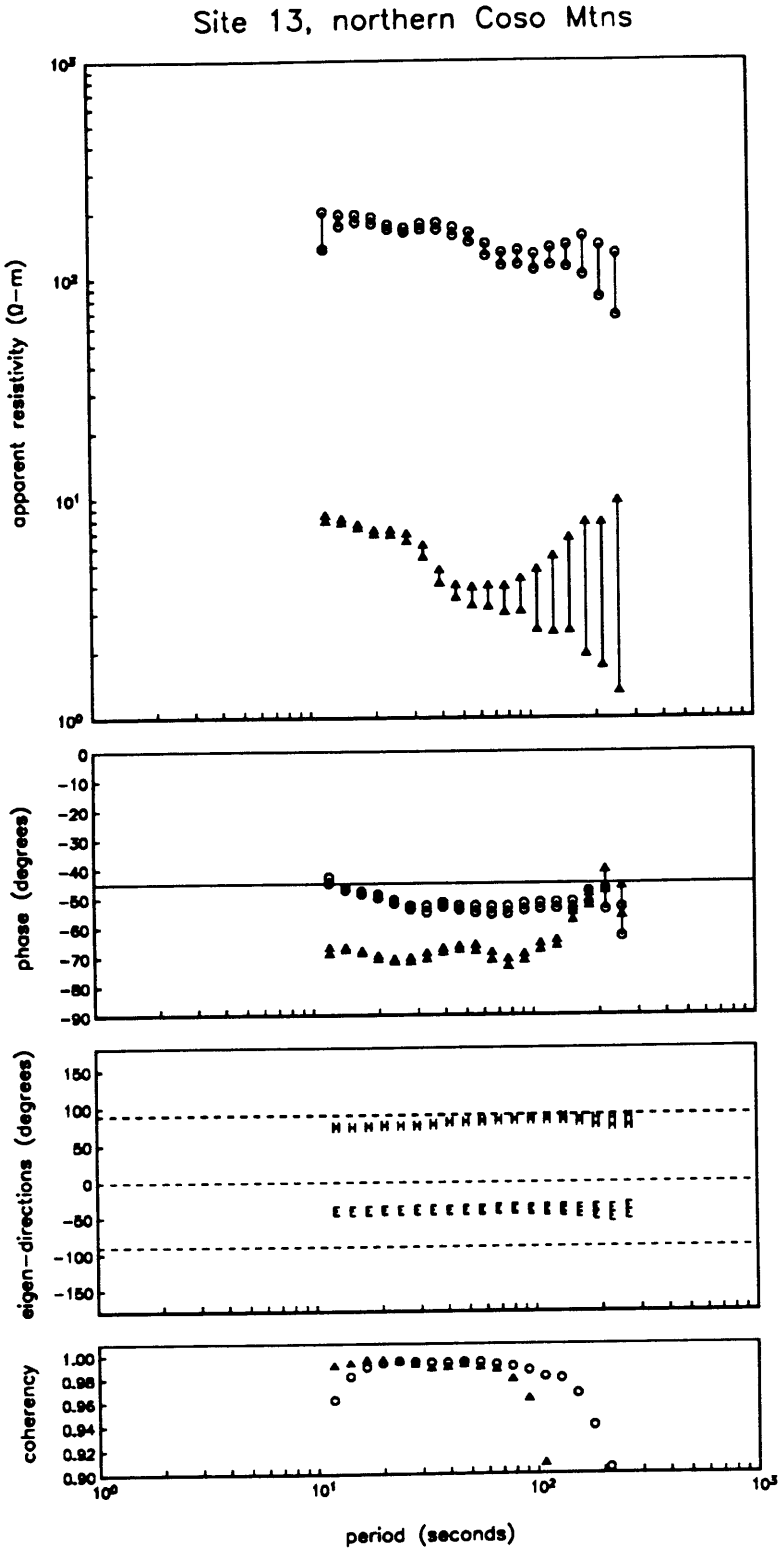
Site 13, northern Coso Mtns
apparent resistivity (Ω-m)
phase (degrees)
eigen-directions (degrees)
coherency
period (seconds)

Figure 4-22.

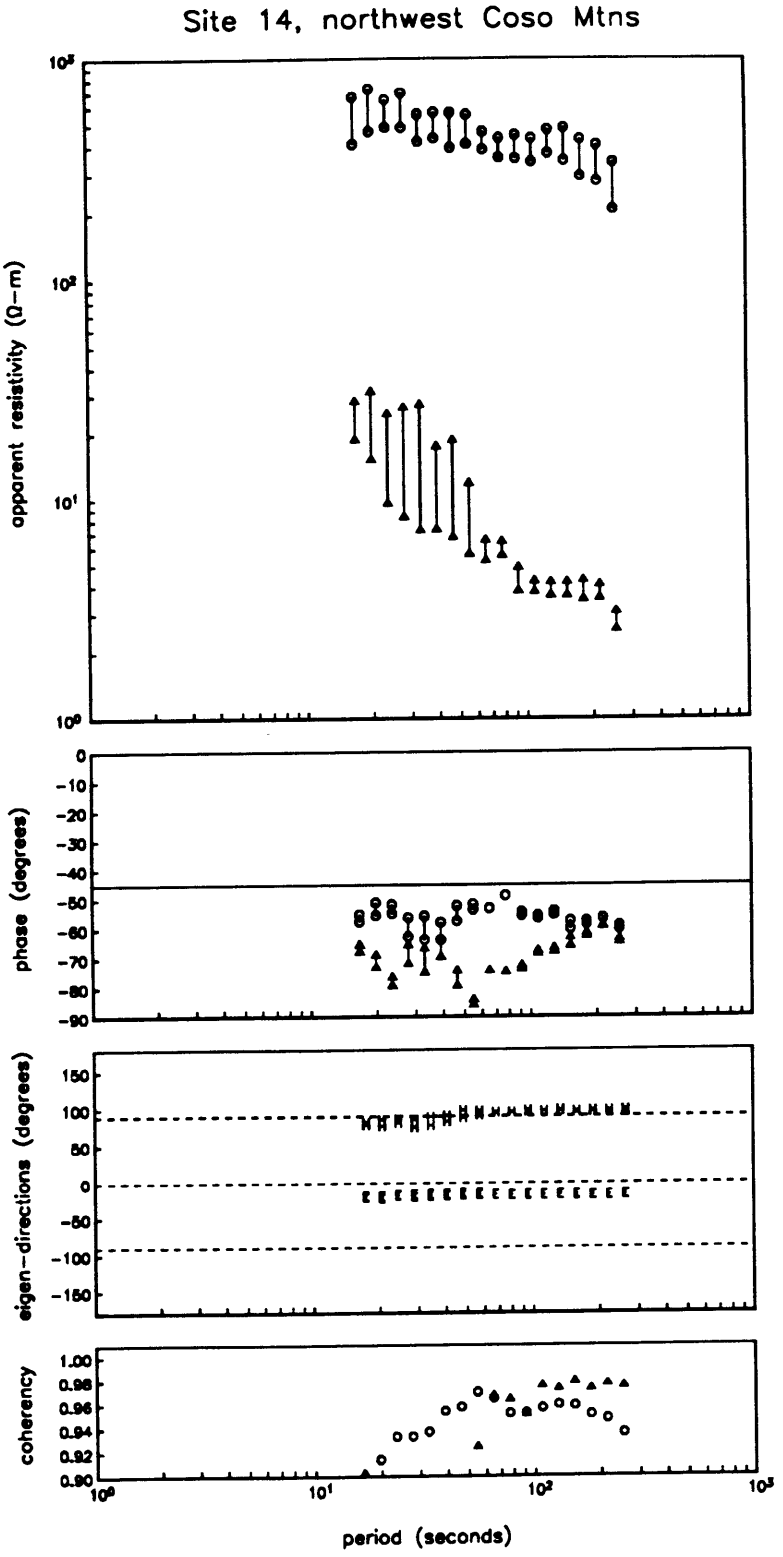
Site 14, northwest Coso Mtns
apparent resistivity (Ω-m)
phase (degrees)
eigen-directions (degrees)
coherency
period (seconds)

Figure 4-23.

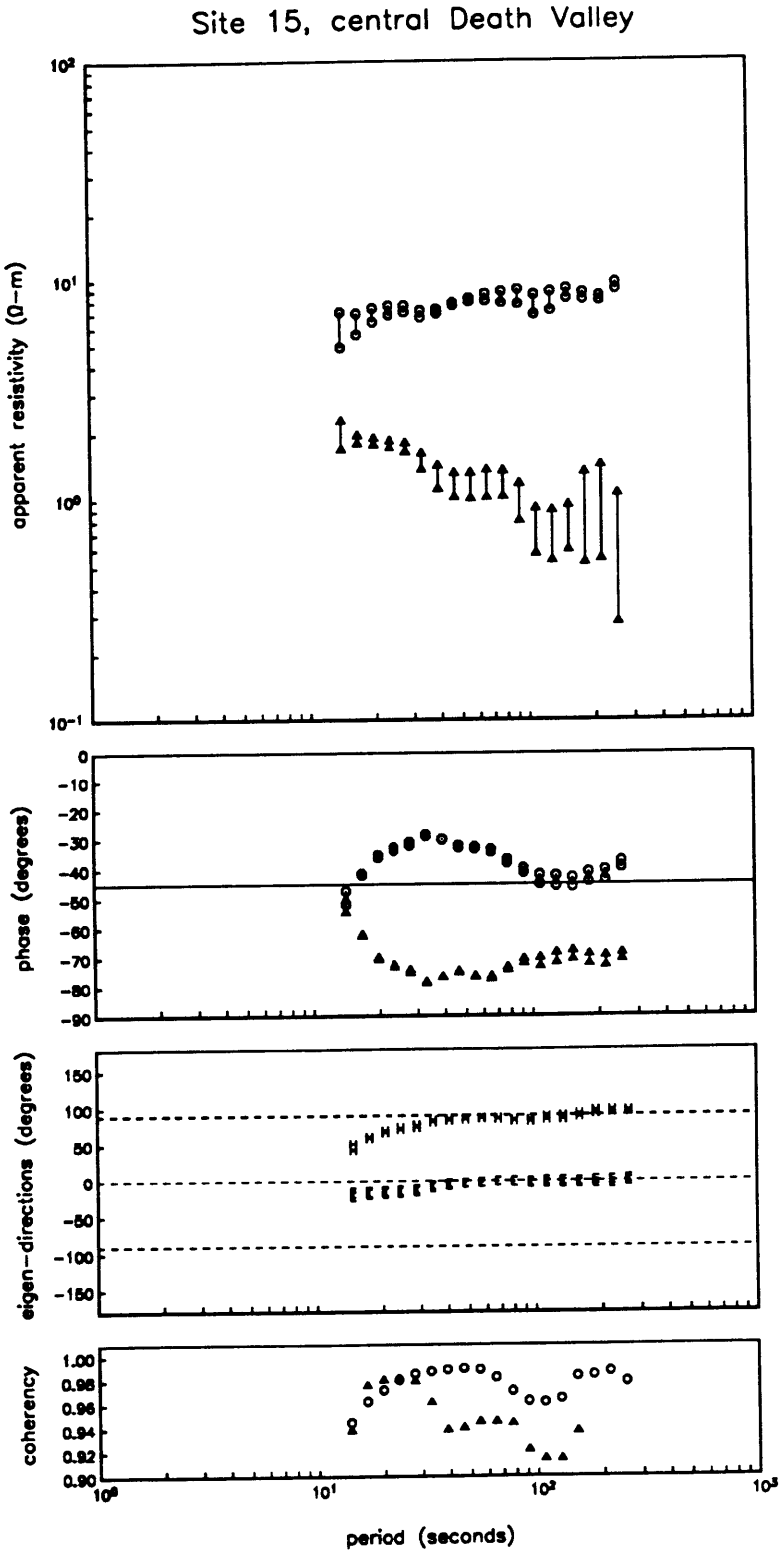
Site 15, central Death Valley
apparent resistivity (Ω-m)
phase (degrees)
eigen-directions (degrees)
coherency
period (seconds)

Figure 4-24.

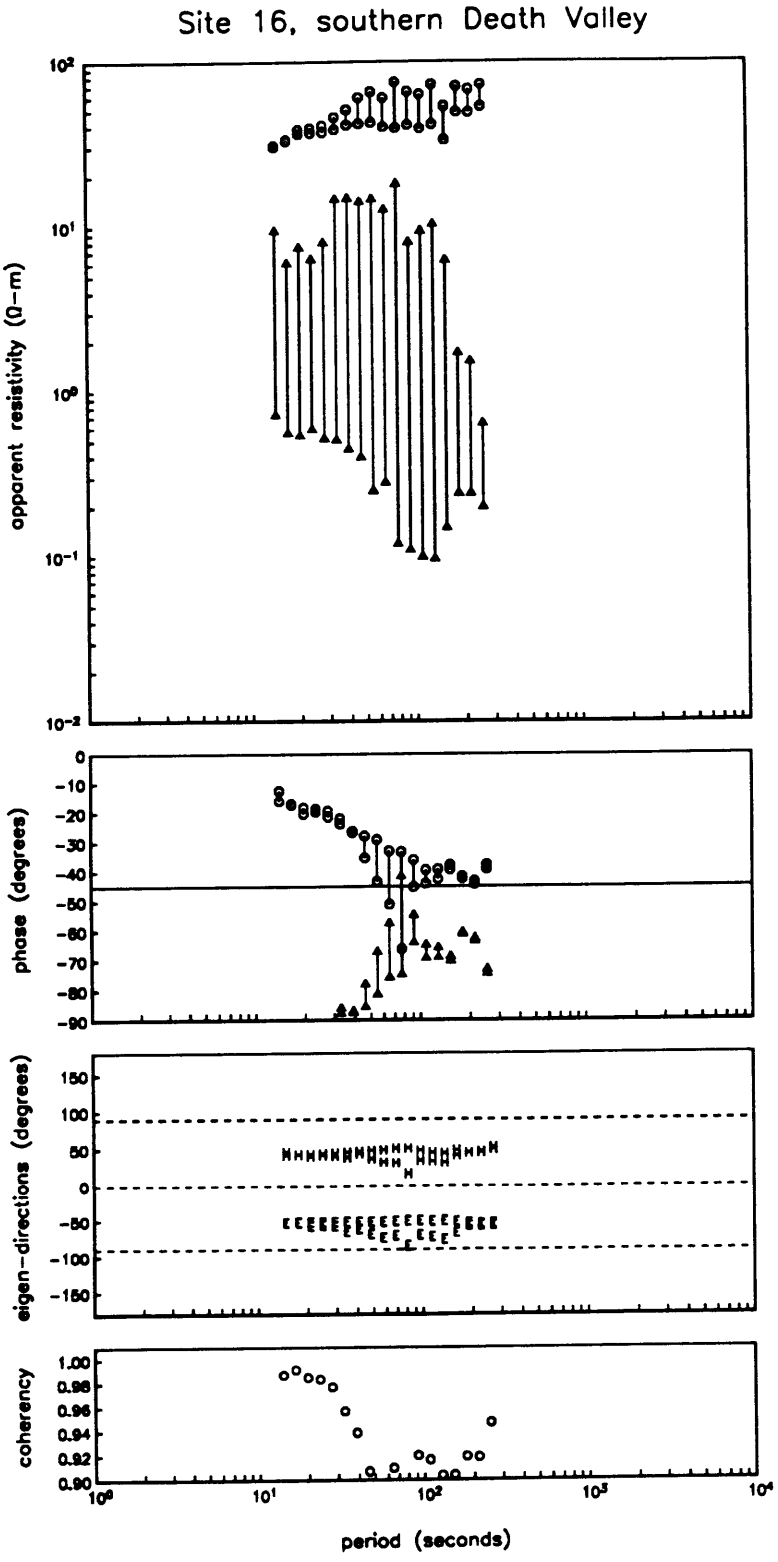
Site 16, southern Death Valley
apparent resistivity (Ω-m)
phase (degrees)
eigen-directions (degrees)
coherency
period (seconds)

Figure 4-25.

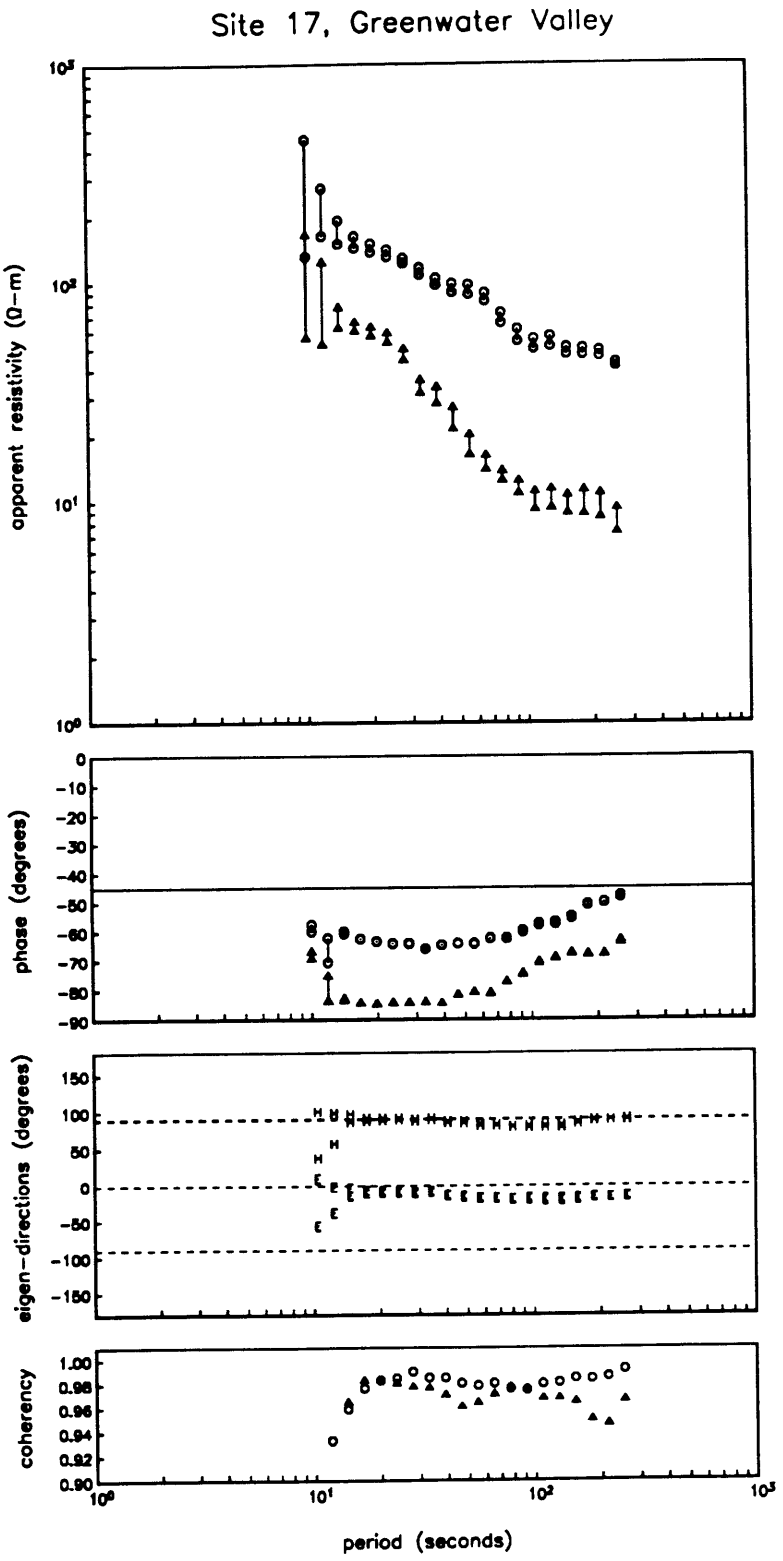
Site 17, Greenwater Valley
apparent resistivity (Ω-m)
phase (degrees)
eigen-directions (degrees)
coherency
period (seconds)

Figure 4-26.

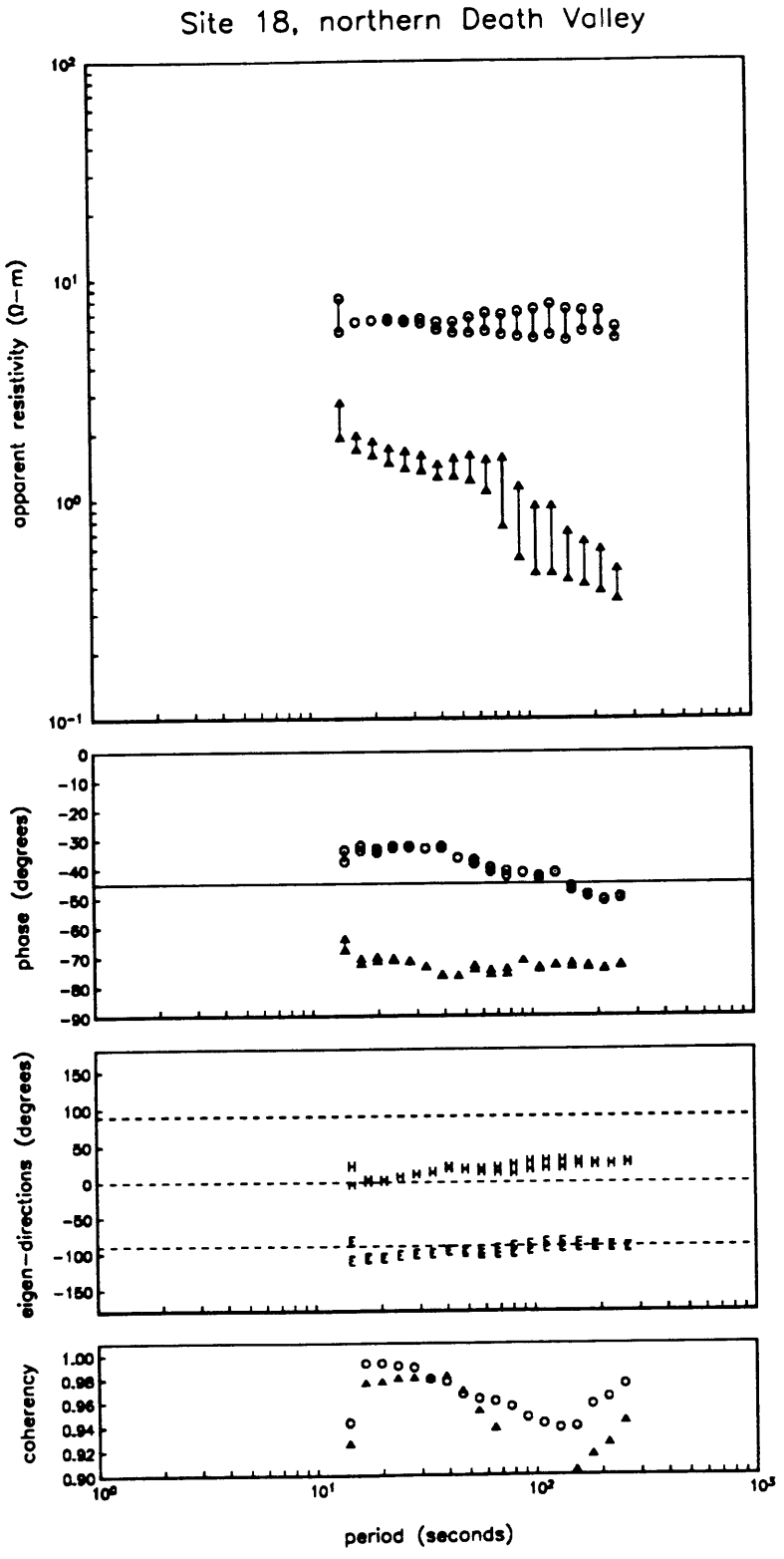
Site 18, northern Death Valley
apparent resistivity (Ω-m)
phase (degrees)
eigen-directions (degrees)
coherency
period (seconds)

Figure 4-27.

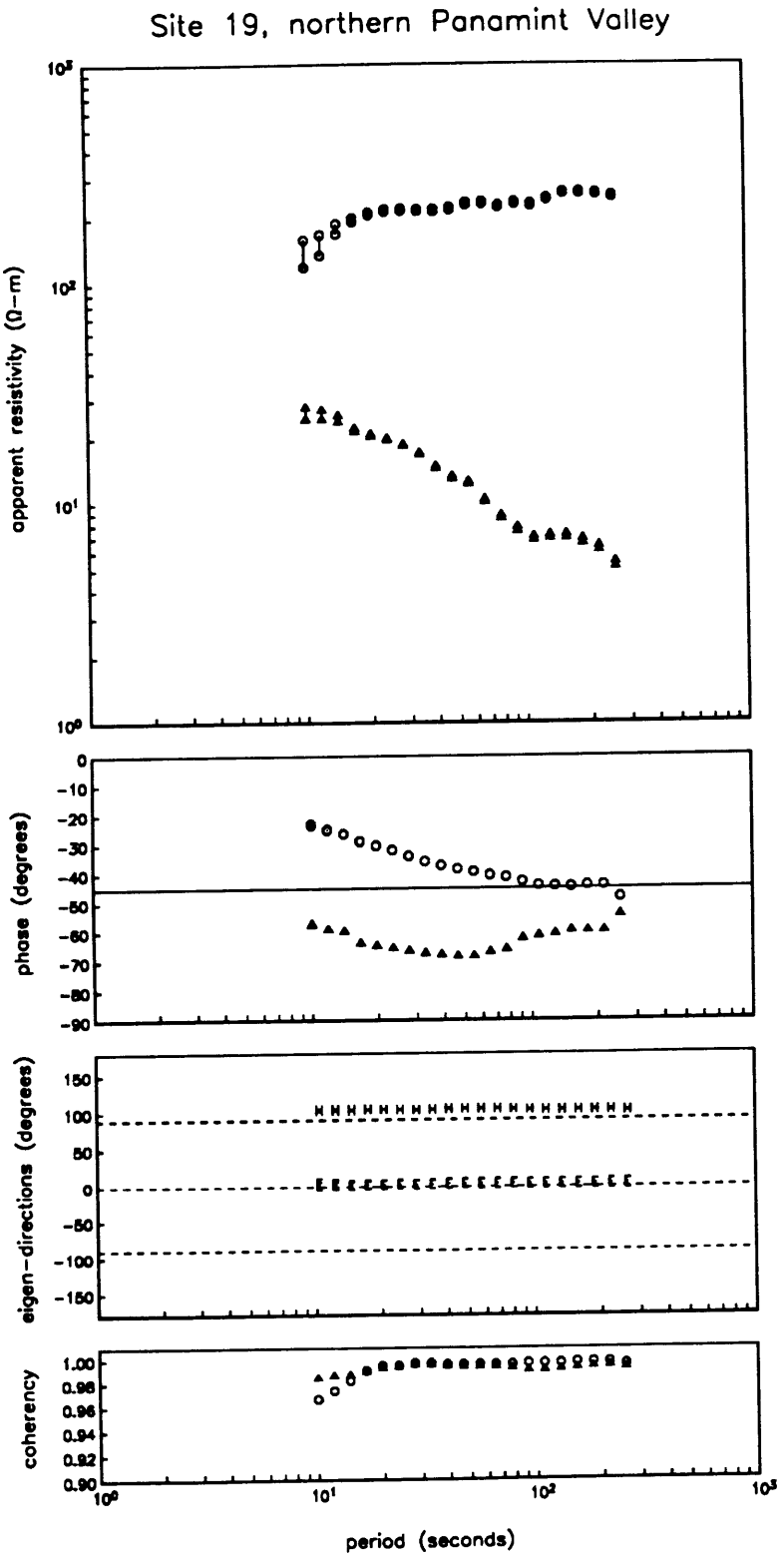
Site 19, northern Panamint Valley
apparent resistivity (Ω-m)
phase (degrees)
eigen-directions (degrees)
coherency
period (seconds)

Figure 4-28.

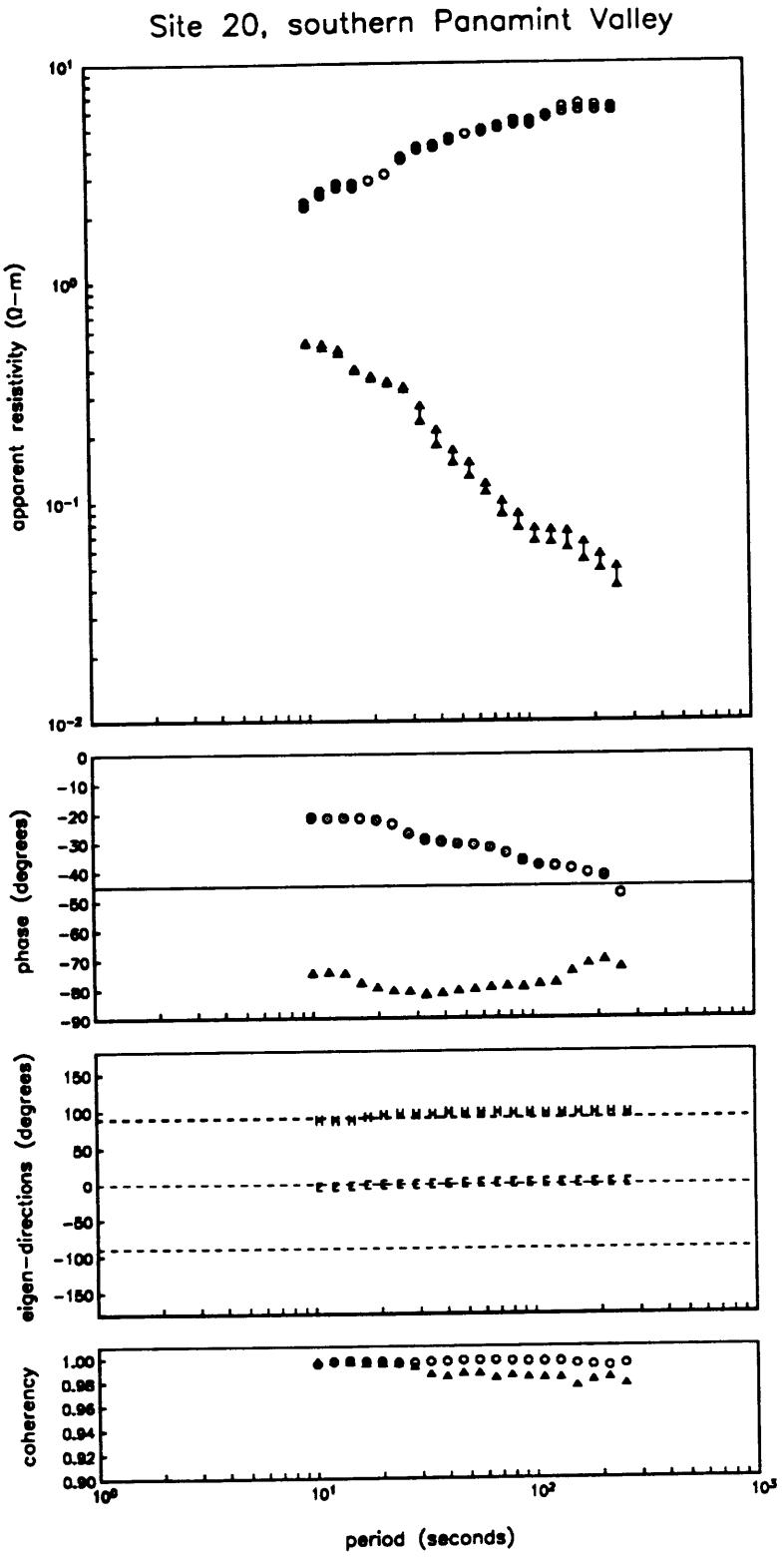
Site 20, southern Panamint Valley
apparent resistivity (Ω-m)
phase (degrees)
eigen-directions (degrees)
coherency
period (seconds)

Figure 4-29.

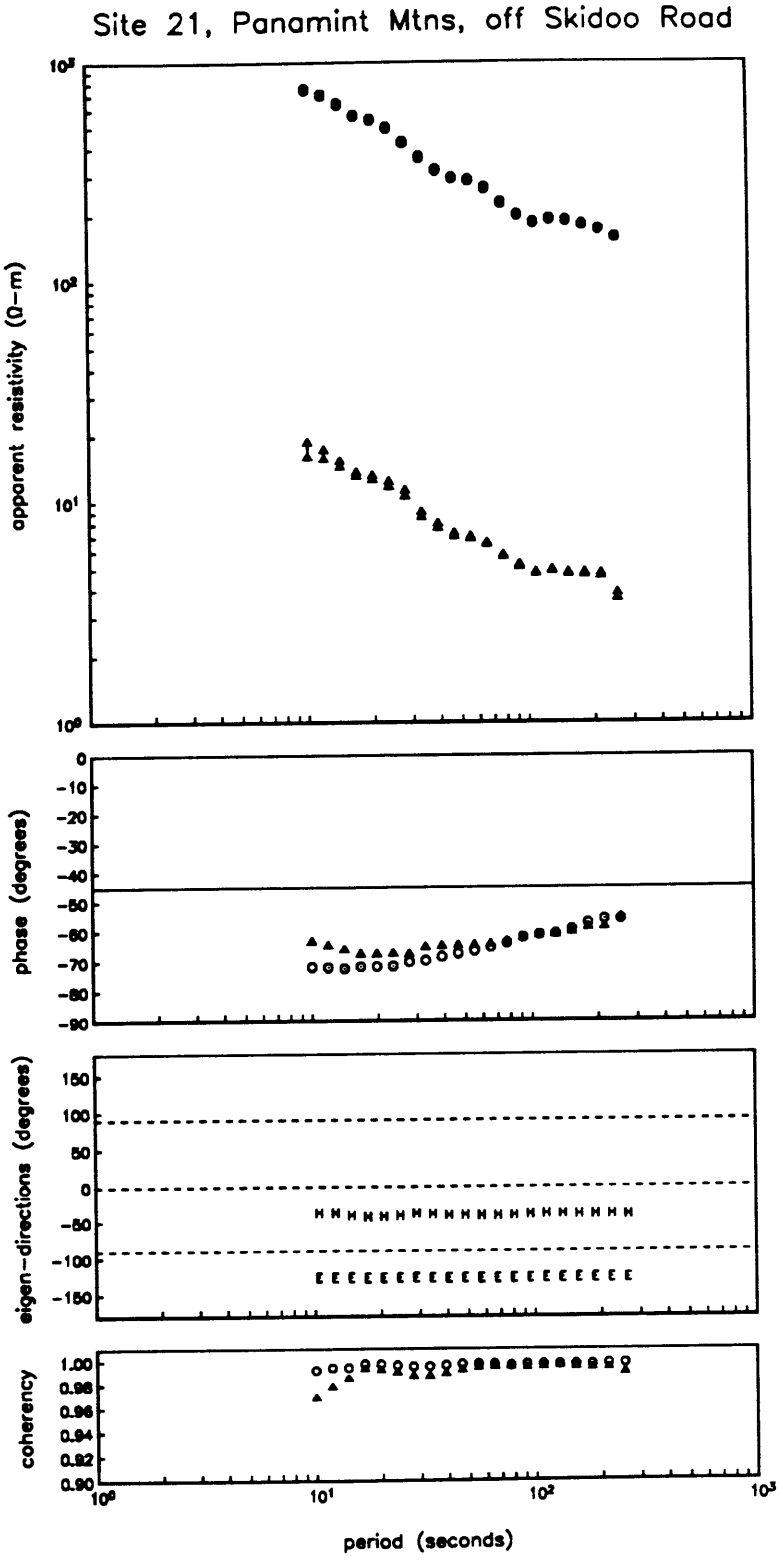
Site 21, Panamint Mtns, off Skidoo Road
apparent resistivity (Ω-m)
phase (degrees)
eigen-directions (degrees)
coherency
period (seconds)

Figure 4-30.

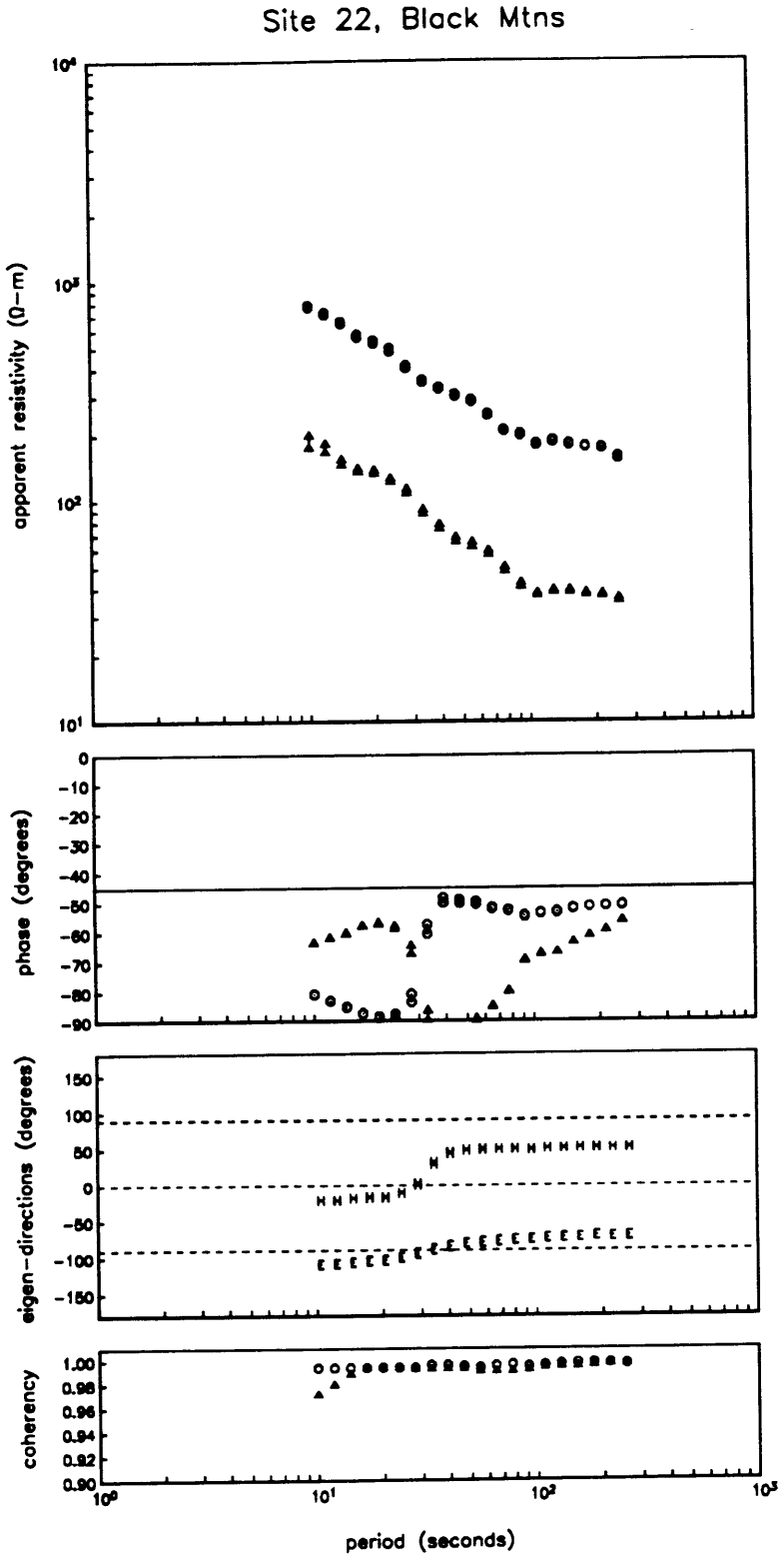
Site 22, Black Mtns
apparent resistivity (Ω-m)
phase (degrees)
eigen-directions (degrees)
coherency
period (seconds)

Figure 4-31.

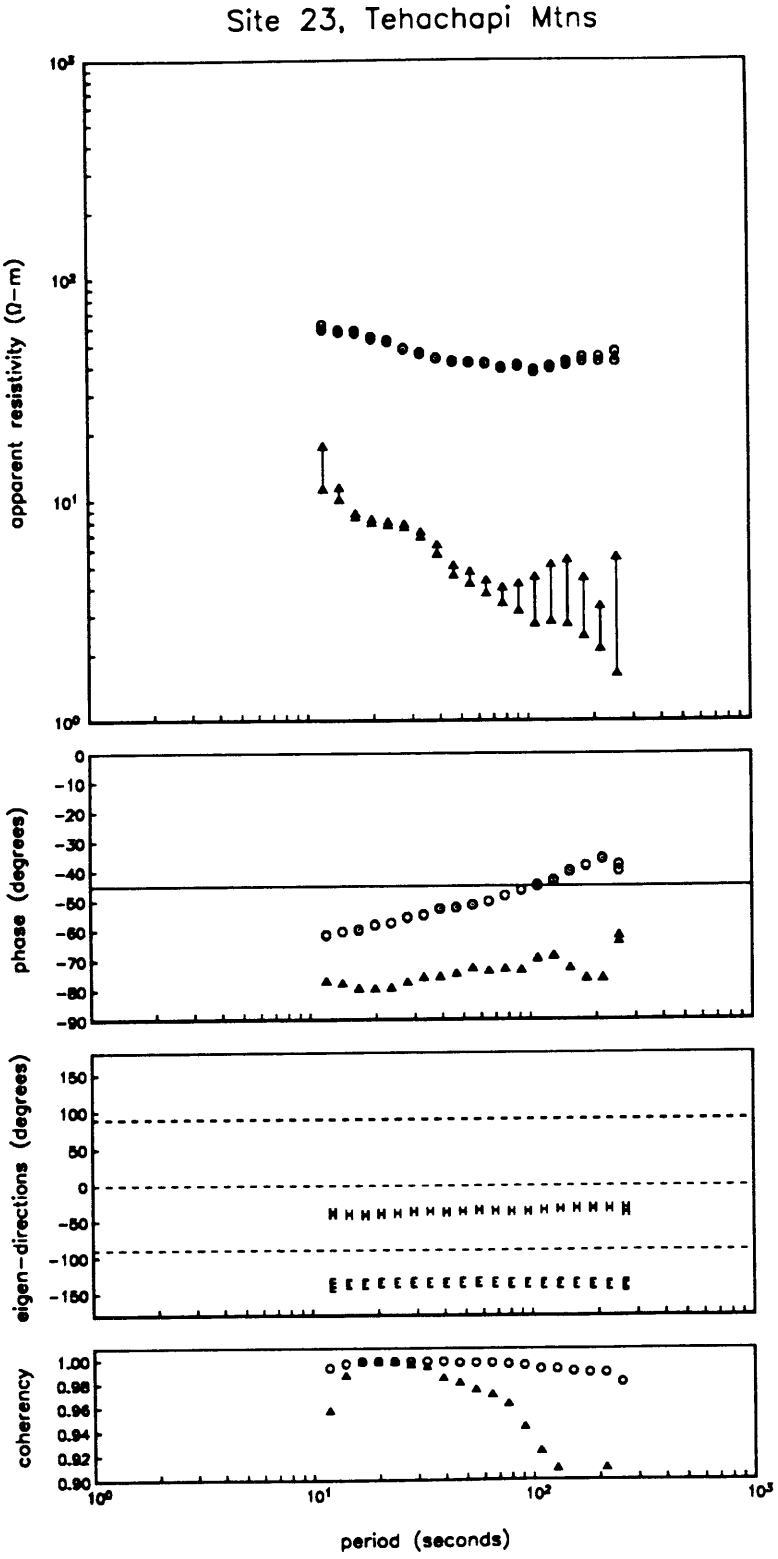
Site 23, Tehachapi Mtns
apparent resistivity (Ω-m)
phase (degrees)
eigen-directions (degrees)
coherency
period (seconds)

**Figure 4-32.**

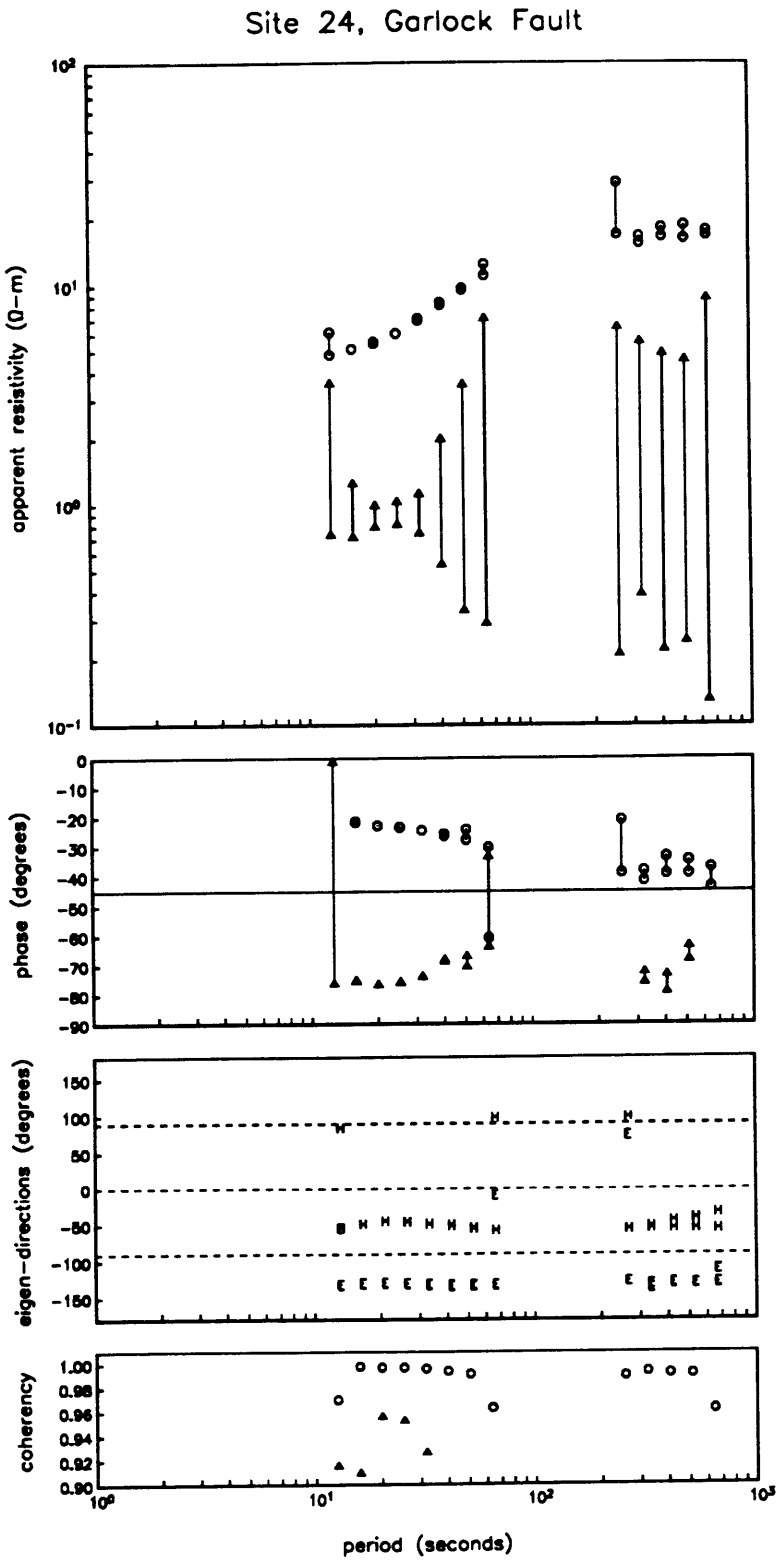
Site 24, Garlock Fault
apparent resistivity (Ω-m)
phase (degrees)
eigen-directions (degrees)
coherency
period (seconds)

Figure 4-33.

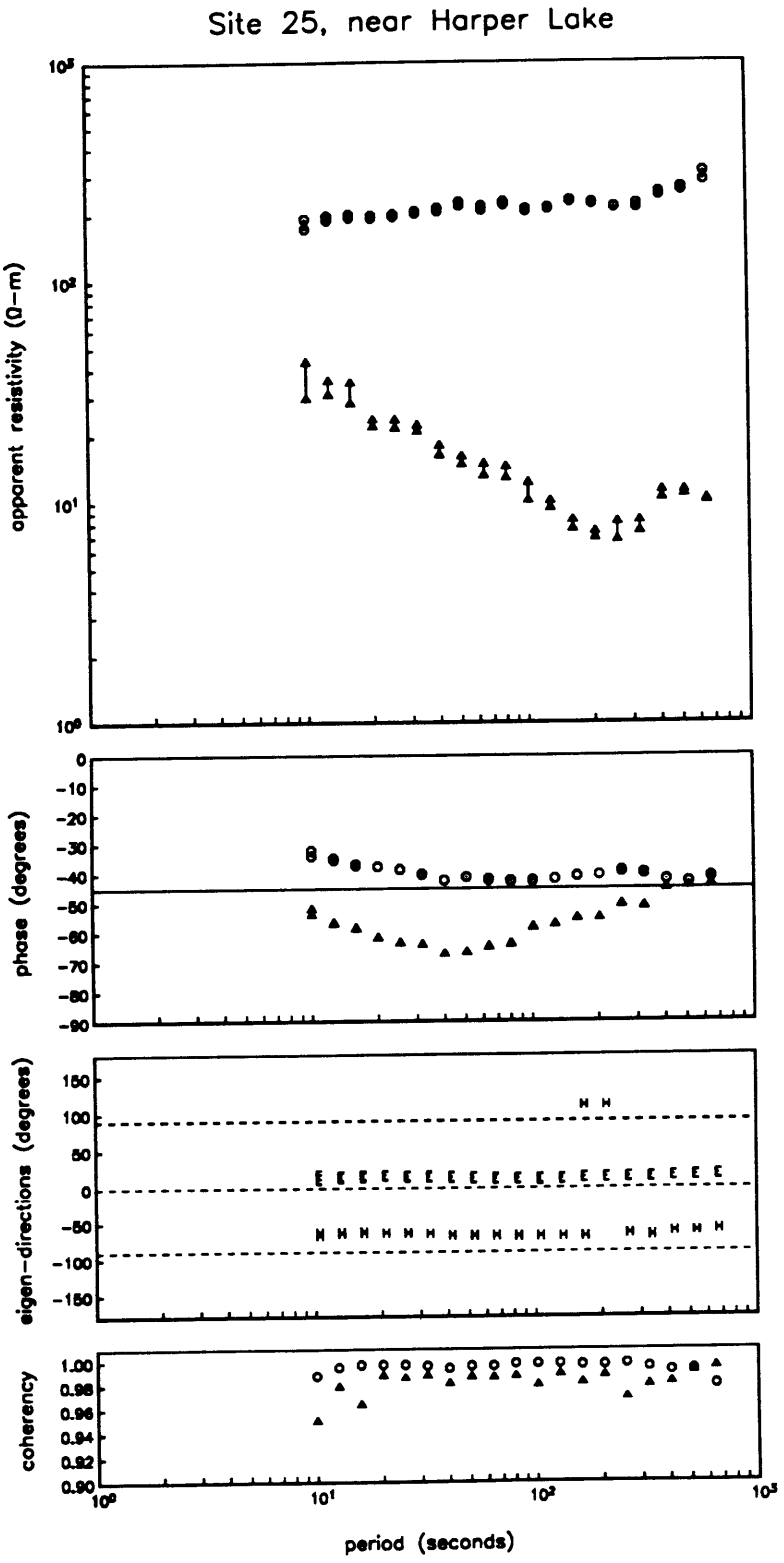
Site 25, near Harper Lake
apparent resistivity (Ω-m)
phase (degrees)
sign-directions (degrees)
coherency
period (seconds)

Figure 4-34.

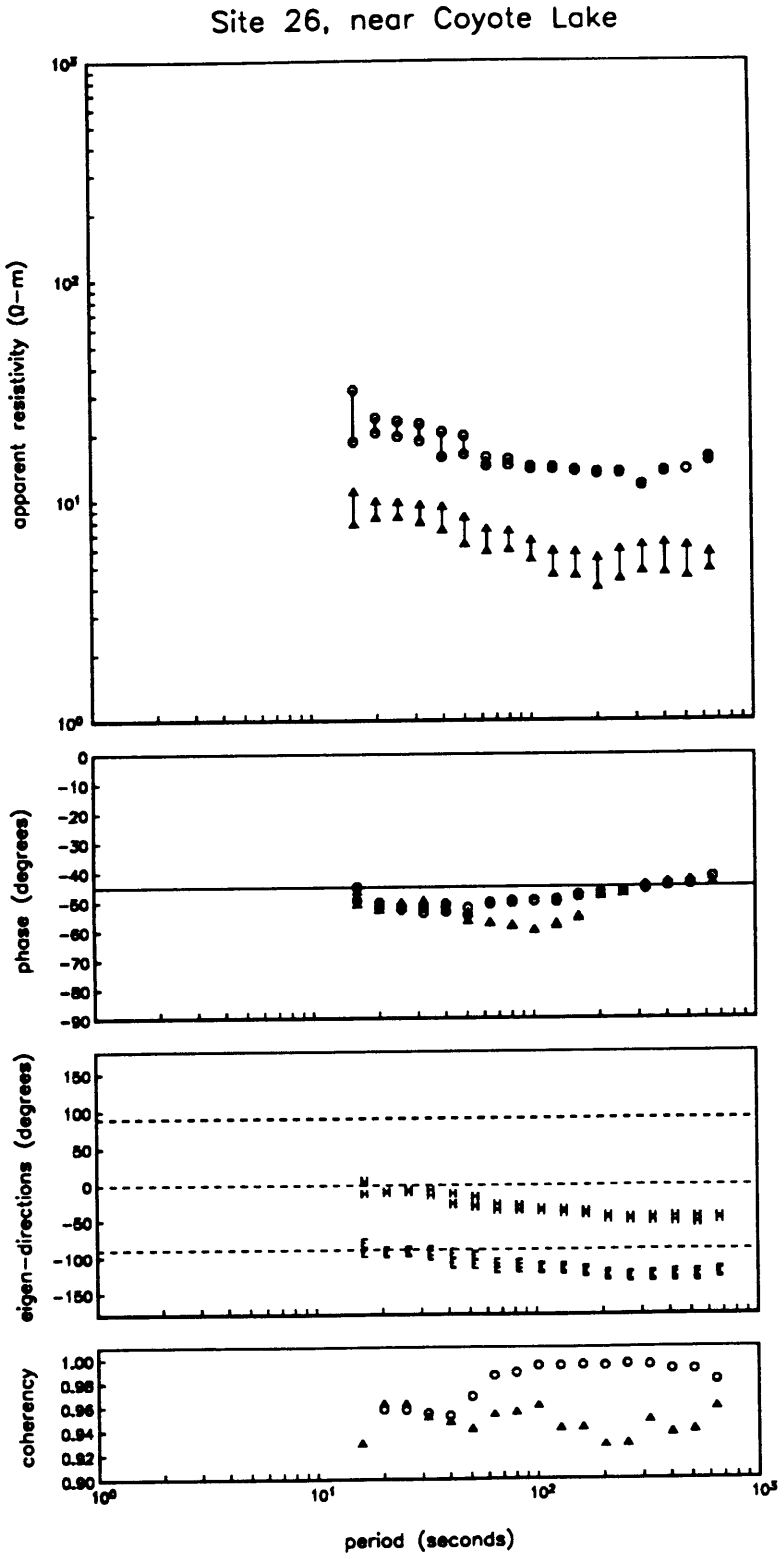
Site 26, near Coyote Lake
apparent resistivity (Ω-m)
phase (degrees)
eigen-directions (degrees)
coherency
period (seconds)

Figure 4-35.

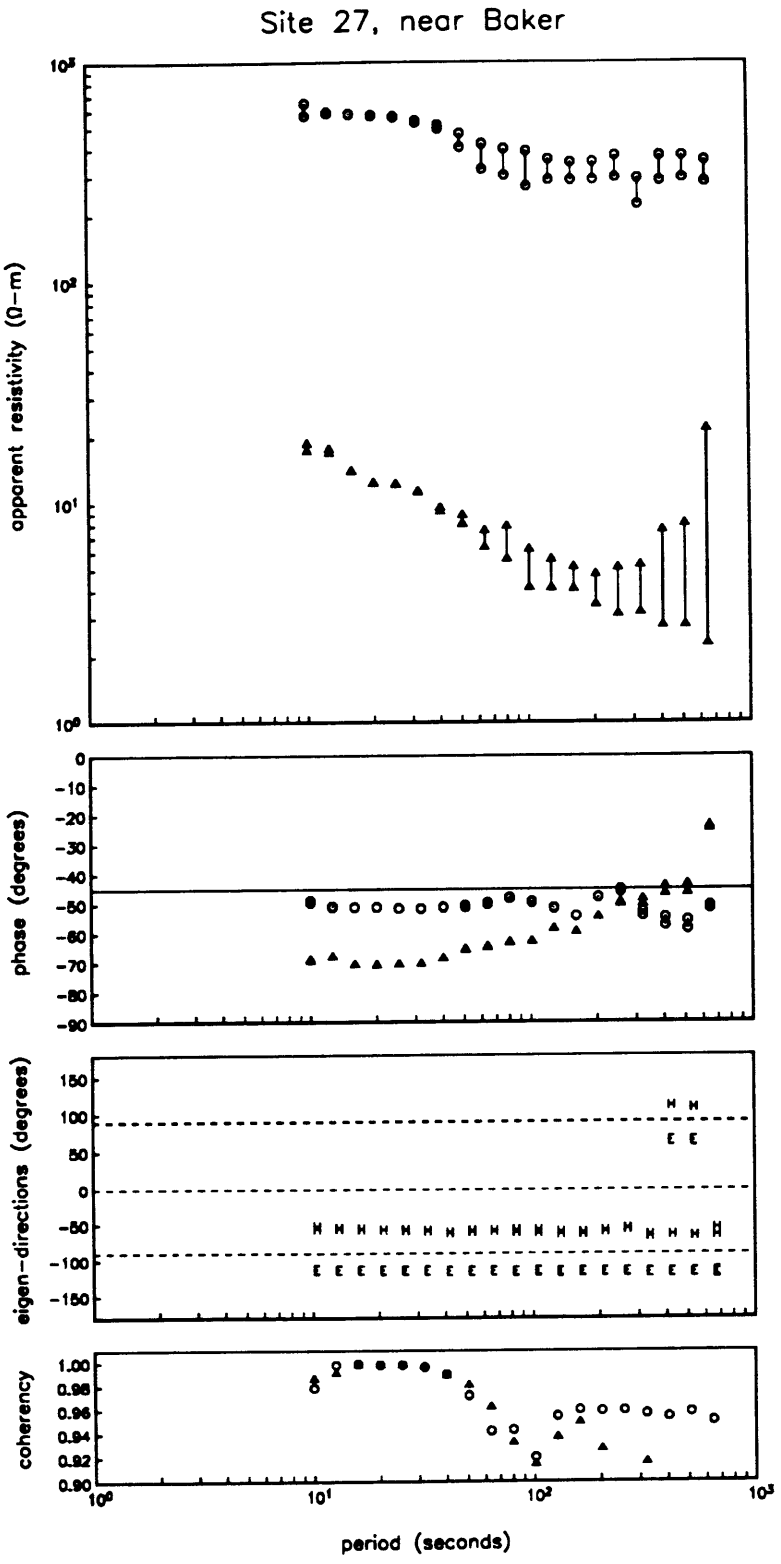
Site 27, near Baker
apparent resistivity (Ω-m)
phase (degrees)
eigen-directions (degrees)
coherency
period (seconds)

Figure 4-36.

### *IV. Editing to improve impedance estimates*

The quality of the impedance estimates is determined largely by the signal levels when the data are recorded. If there are high signal levels and a good mix of frequencies, the impedance estimates will be very coherent. On days when the signal levels are low, the estimates are much less coherent. We implemented an editing algorithm in an attempt to improve the impedance estimates when signal levels were low, or when there appeared to be a lot of noise present in the data. Our editing algorithm is similar to the coherence-based rejection algorithms described in *Jones* (1981, 1984), *Chave and Thomson* (1989), and *Jones et al.* (1989), but is actually more closely related to the editing algorithms of *Madden et al.* (1990) and *Egbert and Booker* (1986).

Our editing algorithm operates in the frequency-domain and is an iterative process that determines which points in an impedance estimate to reject in order to give the most coherent impedance estimate. The technique assumes Gaussian statistics. At each iteration, the algorithm ignores points that have errors in their predicted values greater than $2\sigma$. A new impedance is computed that is based only on the points not thrown out. The new variance is adjusted for the fact that all points with errors greater than $2\sigma$ were thrown out. We iterate the editing algorithm using the entire data set until the coherency converges to a constant value, which happens when the same points are thrown out in two successive passes.

Out of all of our data, only three stations had improved responses after editing the impedance estimates. These are sites 2, 8, and 13. At these sites, the editing improved the responses and increased the coherencies (compare Figures 4-37, 4-38, and 4-39 with Figures 4-12, 4-17, and 4-22). At all of the other stations, the editing procedure did not noticeably improve the results. This might have happened because either the noise was not describable by Gaussian statistics, or the signal-to-noise ratio was just too small for editing to make improvements.

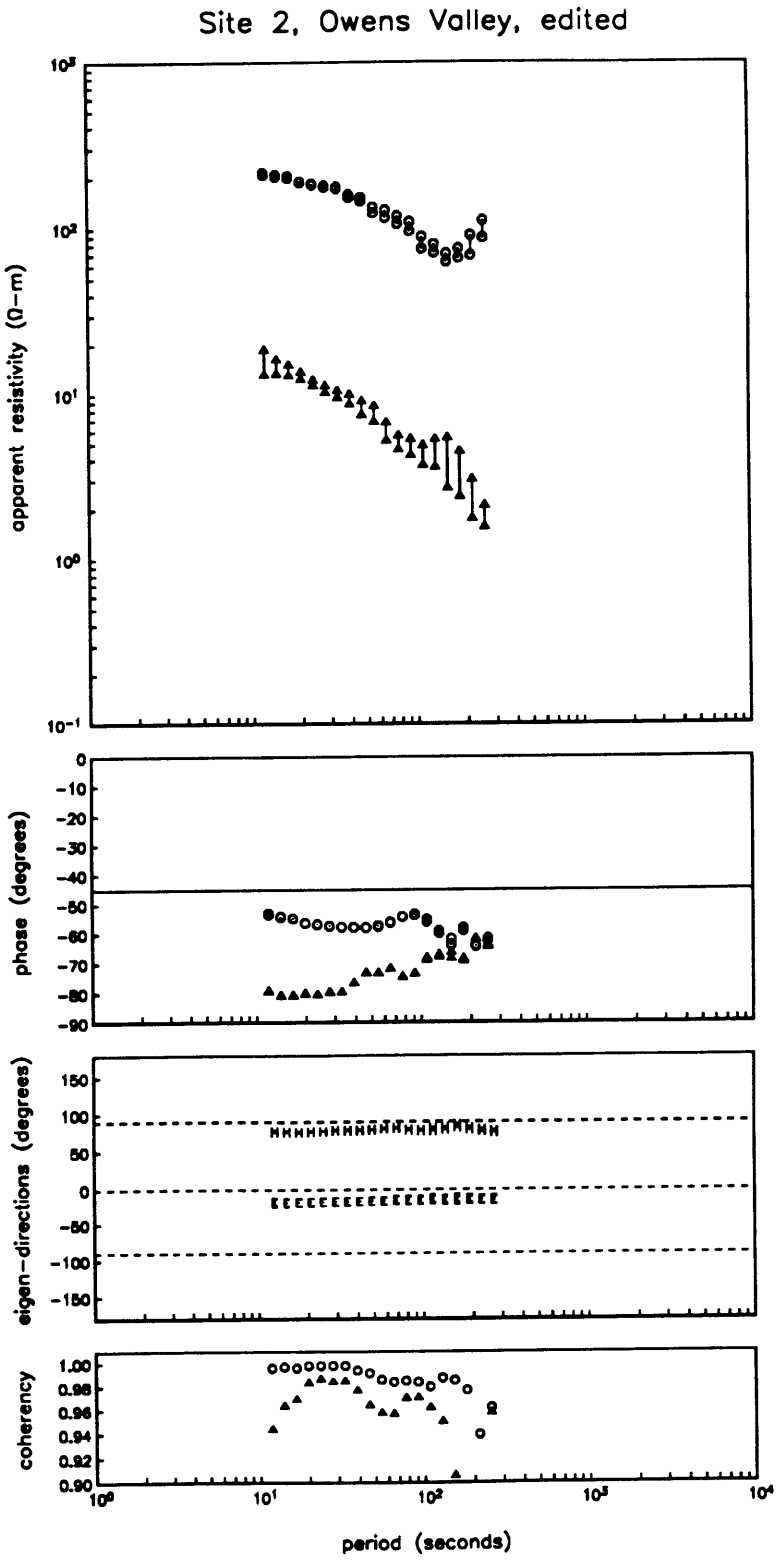


**Figure 4-37**. MT data after editing for site 2.

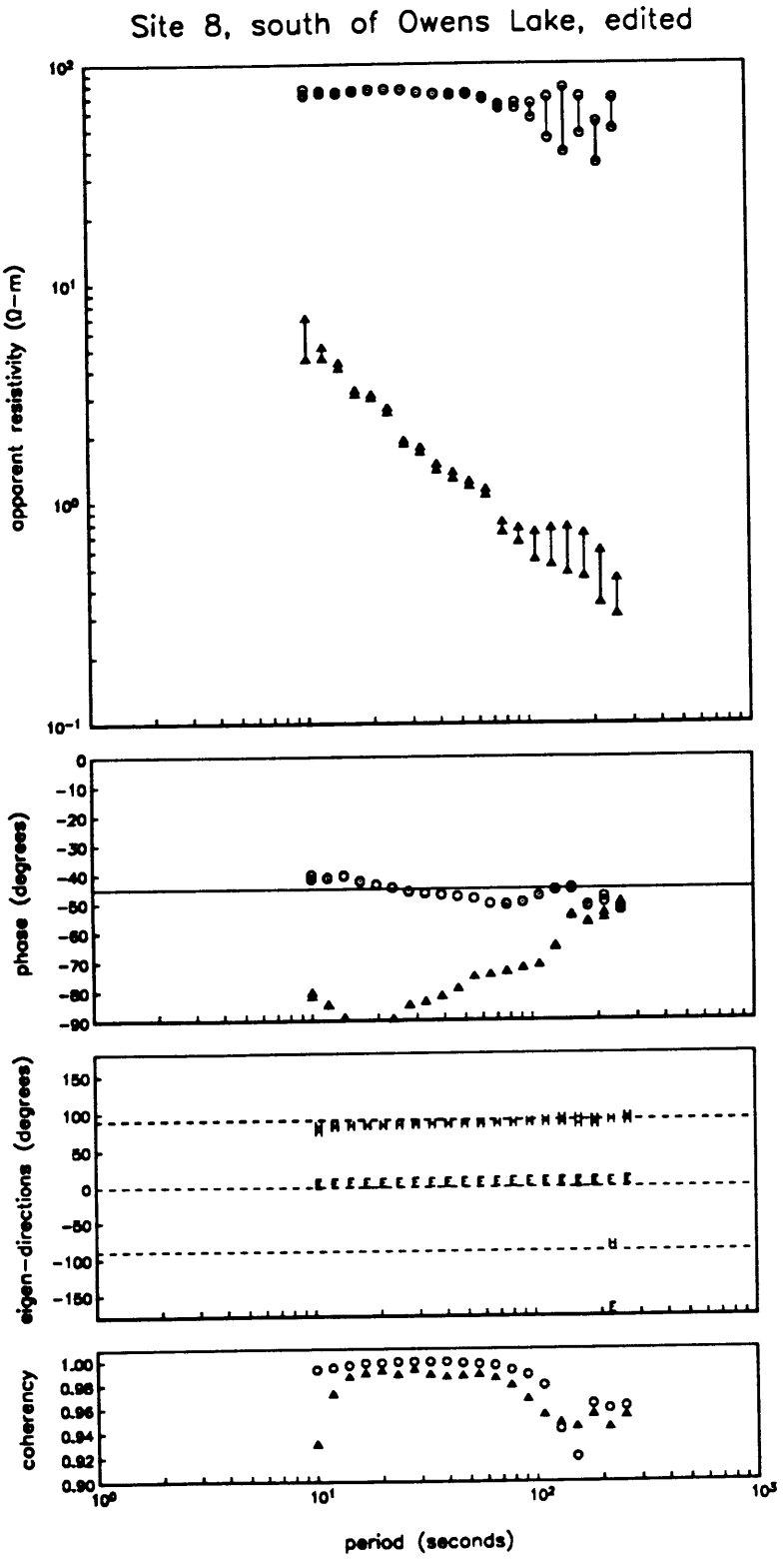


**Figure 4-38.** MT data after editing for site 8.

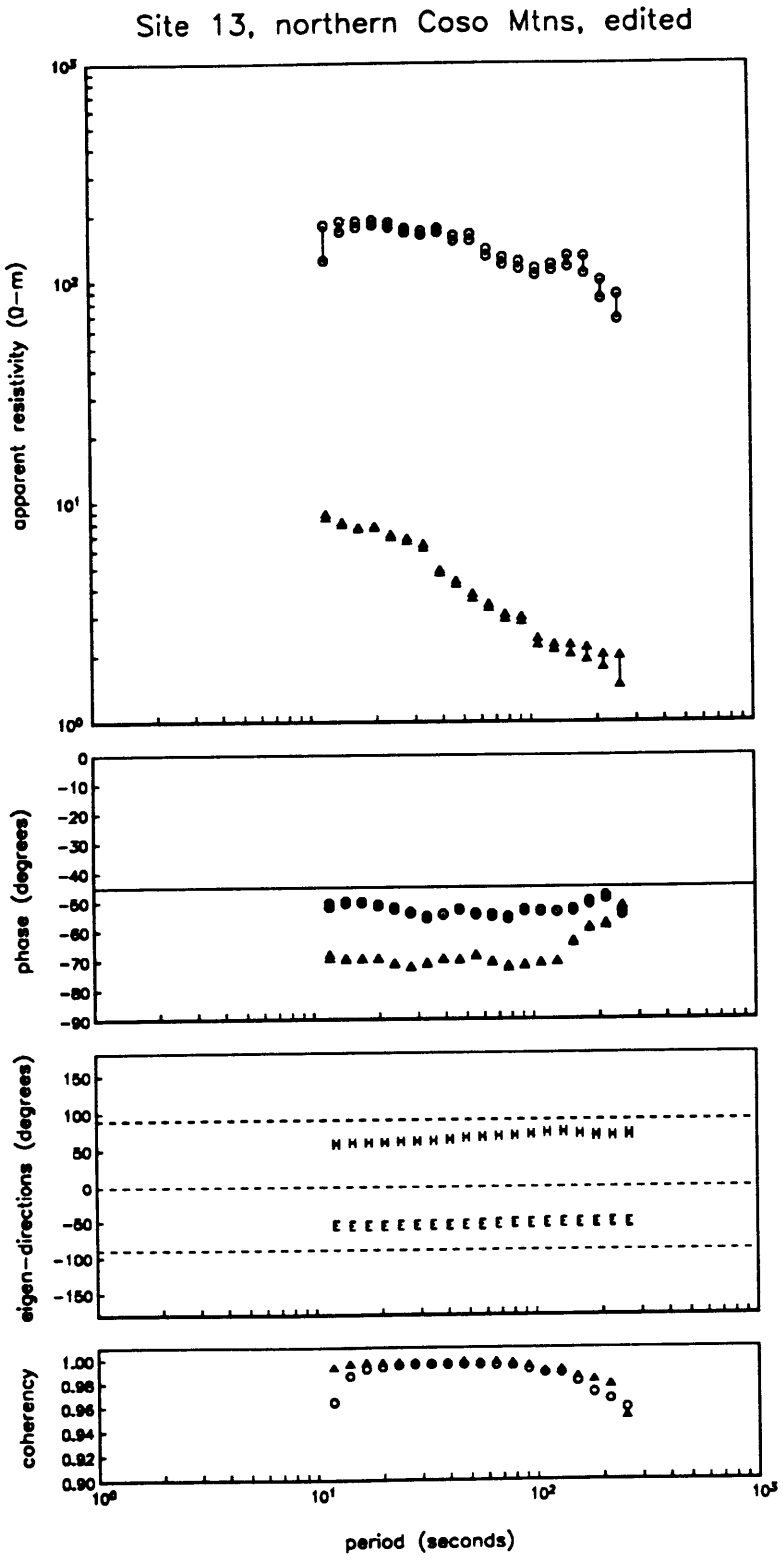


**Figure 4-39**. MT data after editing for site 13.

*A qualitative interpretation of the data*

The data plotted in Figures 4-11 to 4-36 are generally of sufficient quality to identify the behavior of the principle (maximum) mode of the impedance. It is this mode at most data locations (i.e. valleys) that we believe is contaminated by excess ocean electrical currents. Therefore, this mode will be sensitive to the resistivity of the lower crust. This mode is directed along the valleys whereas the minor mode is directed across the valleys. The minor mode is of secondary importance to this study because it is not as sensitive to anomalous zones in the lower crust.

In Figures 4-40, 4-41, and 4-42, we have plotted the apparent resistivity and phase versus frequency for three transects across the California Basin and Range and the northern Mojave. We have normalized the apparent resistivities to a constant value at the shortest period since with these plots we are mainly concerned with the slopes of the curves and not their actual amplitudes. Figure 4-40 shows data south to north from Garlock, Searles Valley, Panamint Valley, and Eureka Valley. What is most striking about this plot is the systematic change in the slope of the apparent resistivity curves and the systematic shift in the phases from south to north. Notice that this is very similar to the leakage effects seen in the 2D TM mode responses shown earlier in Figure 4-5. We believe these data are showing a loss of excess ocean current as one progresses north along this profile and further away from the ocean. Figure 4-41 shows data south to north in Death Valley, although these data are not of the highest quality, and Figure 4-42 shows data west to east across the northern Mojave. Again we believe these two figures show a loss of ocean current as one progresses south to north in Death Valley and west to east across the northern Mojave, in both cases further away from the ocean.

A closer examination of these three plots and the data plots in Figures 4-11 to 4-36 reveals several additional features that we interpret in the context of excess ocean currents as follows. The responses in the northern Mojave do not show as much retardation of their mantle branches as do the stations along the southern edge of the Basin and Range, but the

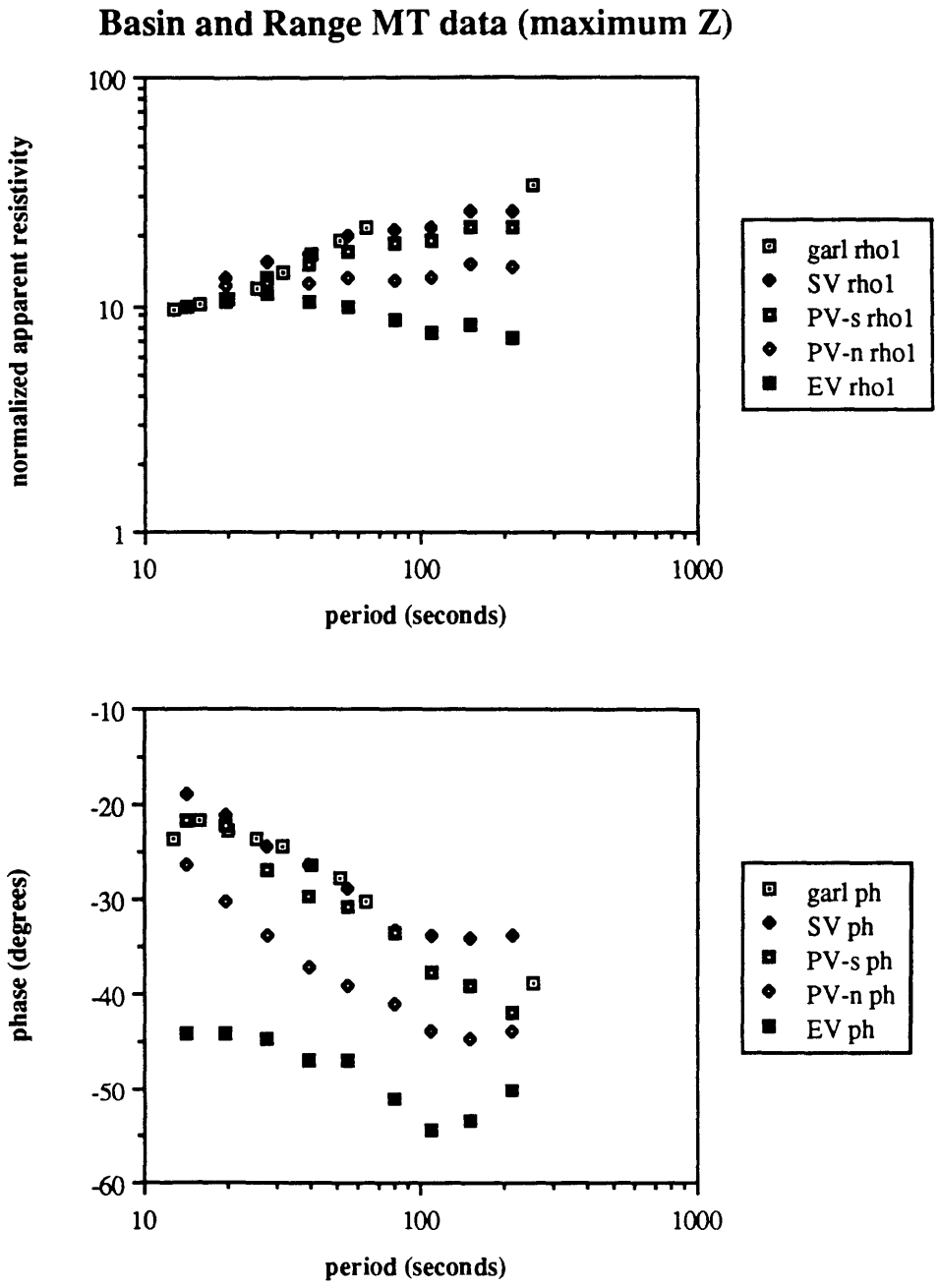


**Figure 4-40.** A plot of the apparent resistivity and phase for sites along a north-trending traverse in the California Basin and Range. We have plotted the data south to north from Garlock, Searles Valley, Panamint Valley, and Eureka Valley. We have normalized the apparent resistivity curves to a value of 10 ohm-m at the shortest period since we are concerned with the slopes of the curves and not their actual amplitudes.

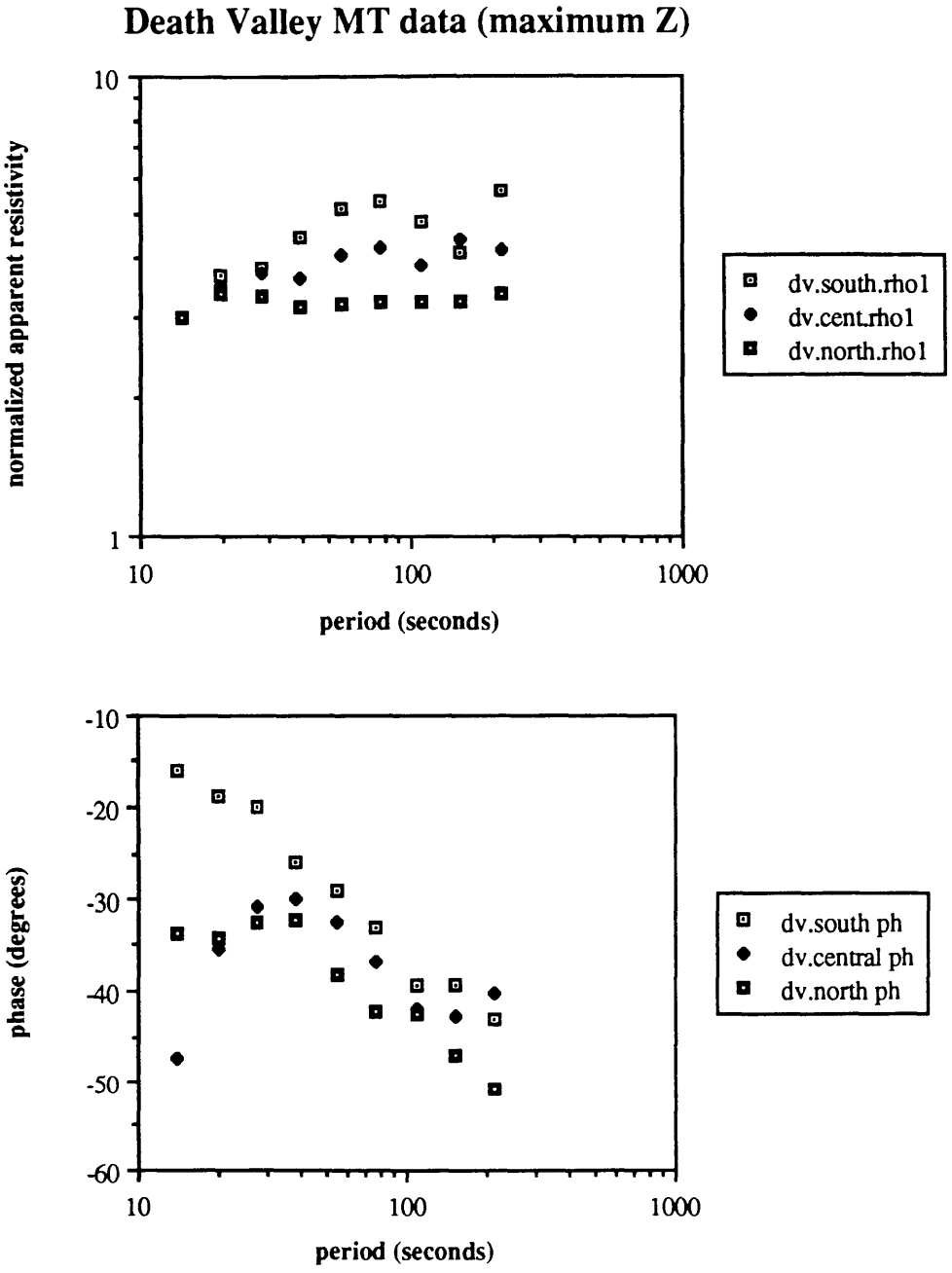


**Figure 4-41.** A plot of the apparent resistivity and phase for sites along a north-trending traverse in Death Valley. We have plotted the data south to north from southern Death Valley, central Death Valley, and northern Death Valley. We have normalized the apparent resistivity curves to a value of 3 ohm-m at the shortest period since we are concerned with the slopes of the curves and not their actual amplitudes.

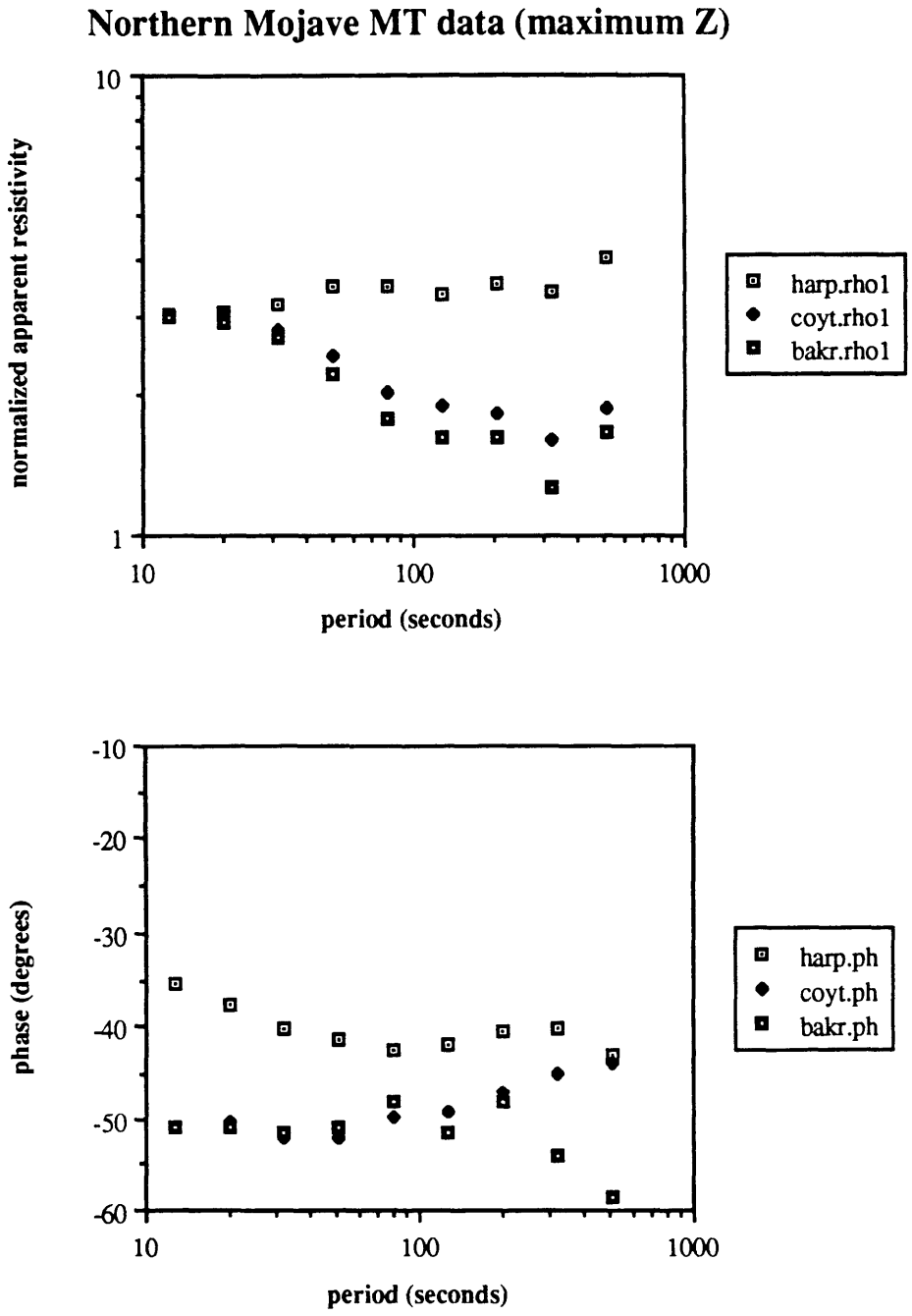


**Figure 4-42.** A plot of the apparent resistivity and phase for sites along an east-trending traverse across the northern Mojave Desert. We have plotted the data west to east from Harper Lake, Coyote Lake, and Baker. We have normalized the apparent resistivity curves to a value of 3 ohm-m at the shortest period since we are concerned with the slopes of the curves and not their actual amplitudes.

Garlock site seems to have more excess ocean current than any other site. This seems to indicate that the excess ocean current seen in the California Basin and Range does not come up from the Salton Sea to the south, but rather, is channelled along the Garlock Fault zone from the west and then up into the California Basin and Range through Searles Valley and Death Valley. The Peninsular Ranges, which run along the western edge of California south of Los Angeles, may also act to partially block some of the current from reaching those sites in the northern Mojave. Additionally, the response at the western edge of Indian Wells Valley (site 10) seems to be entirely in the mantle branch, but the response south of Owens Lake (site 8) shows some effect of ocean currents, although to a degree less than seen in Panamint Valley. We believe that the mountains just north of the Garlock Fault zone at the southern edge of Indian Wells Valley, and the Sierra Nevada, may block off any excess current from Indian Wells Valley, but that some of the ocean current gets into southern Owens Valley from Panamint Valley and Searles Valley. The responses in Death Valley do not show as much ocean effect as the responses in Panamint and Searles Valley, but this is probably because it is simply further away from the ocean and more current has leaked off by the time it has reached Death Valley.

Up to this point, we have concentrated primarily on the major impedance response, but the minor impedance response also has some interesting characteristics. This impedance mode at all sites is in the mantle branch. However, high phases at short periods are found at many sites (e.g., sites 2, 3, 6, 7, 8, 12, 17, 20, 22). These phases decrease at the longer periods as the slopes of the apparent resistivity curves decrease. We believe that some of this effect at these sites may be due to highly conductive sediments in the shallow upper crust that give way to more resistive sediments deeper in the crust.

### *3D modeling of the data*

The data we have taken in the California Basin and Range is obviously very three-dimensional in nature. Trying to model the data using 1D or 2D algorithms would not allow

us to accurately characterize the resistivity structure of the area. On the other hand, trial-and-error forward modeling of the data using a 3D algorithm is a very time-consuming and difficult problem. In this situation, we had little choice but to proceed with the 3D modeling to see how much of the data we could explain with the simplest models possible. All of the preliminary modeling used the multiple scaling relaxation routine on the NCUBE computer at the Earth Resources Laboratory and the MINRTRACC routine on the MIT Cray Supercomputer. The last few models, and the predictions we show, were all computed using the direct solution algorithm on the MIT Cray.

As a prelude to the 3D modeling, we ran several 2D inversions of both modes of the data to use as a starting point for the 3D model. Once we had done this, we proceeded systematically to fit the data by trial-and-error 3D forward modeling. We did not attempt to fit the data at every site - the geologic complexity of the area would have required too large a 3D model to be realistic. Our 3D models had to cover a large area, from the Pacific Ocean to the Basin and Range, yet be detailed enough to accurately model the data at sites within the Basin and Range. Since most of the data that was collected is bounded between the Garlock Fault, the Sierra Nevada, Death Valley, and south of Panamint Valley, we chose to concentrate our modeling efforts on this region.

In our modeling efforts, we did not concentrate very much on fitting the amplitudes exactly at each site. We are somewhat at a disadvantage because we do not have higher frequency data to constrain the statics of the upper crust. We have no way of knowing whether one or both apparent resistivity curves at each site are static-shifted up or down due to local conductivity anomalies. Static shifts affect primarily the interpretation of the upper crustal resistivity structure, and their effect on the lower crustal resistivity structure, we believe, would be minimal. Therefore, we were concerned primarily with the phases and the slopes of the apparent resistivity curves.

Our first 3D model is given in Appendix A (this is actually a resistivity map for each layer of the model, and is explained in more detail in the appendix). In our model, we have

aligned the y-axis with the structural grain of the Sierra Nevada-Great Valley trend, and the x-axis is perpendicular to that grain. As mentioned previously, we had to balance the need for covering a large area with accurate modeling of the responses in a smaller detailed area. We have attempted to include as many of the major geologic features of California as possible. We have included the Great Valley, the Sierra Nevada, the Penninsular Ranges, the San Bernardino Mountains, the Garlock Fault zone, and as much detail as possible in the California Basin and Range.

This model, in general, has valleys containing conductive sediments down to a few kilometers and mountain ranges that are much more resistive down through the crust. The most important feature of this model is the *change* in lower crustal resistivity from the ocean and western California to the California Basin and Range. We set the resistivity of the lower crust under the ocean and western California into the Mojave Desert region to a value of 80,000 ohm-m from 12 km to 32 km depth. This gives that part of the lower crust a resistivity-thickness product of $1.6 \times 10^6$ ohm-m-km, which is in keeping with those values deduced by *Bennett* (1986), *Mackie et al.* (1988), and *Park et al.* (1990). This value contrasts *dramatically* with that needed in the California Basin and Range. There, the lower crust has a resistivity of 5000 ohm-m between 12 km and 32 km depth, with a zone in Panamint Valley of 3000 ohm-m at the same depths. This gives the lower crust in the California Basin and Range a resistivity-thickness product of $1 \times 10^5$ ohm-m-km, which corresponds to an increase in the lower crustal conductance by a factor of 16. In addition, we have made the Garlock Fault zone fairly conductive in order to attract the current from the coast and channel it up into the Basin and Range.

In Figures 4-43 to 4-46, we show the model predictions for this model compared with the data. The model predictions were computed for four periods - 10, 30, 100, and 300 seconds. The solid lines represent the model predictions for this model (dashed lines represent the results for a second model that we will discuss shortly). We do not show predictions for all the data we took because, as mentioned previously, the 3D model

**Figures 4-43 to 4-46**. The model predictions for the models given in Appendices A and B are shown in comparison with the actual field data for several of the sites within the study area. The model predictions for the first model given in Appendix A are shown by the solid lines, and the model predictions for the second model shown in Appendix B are shown by the dashed lines. The model predictions were computed using the direct solution algorithm at periods of 10, 30, 100 and 300 seconds.

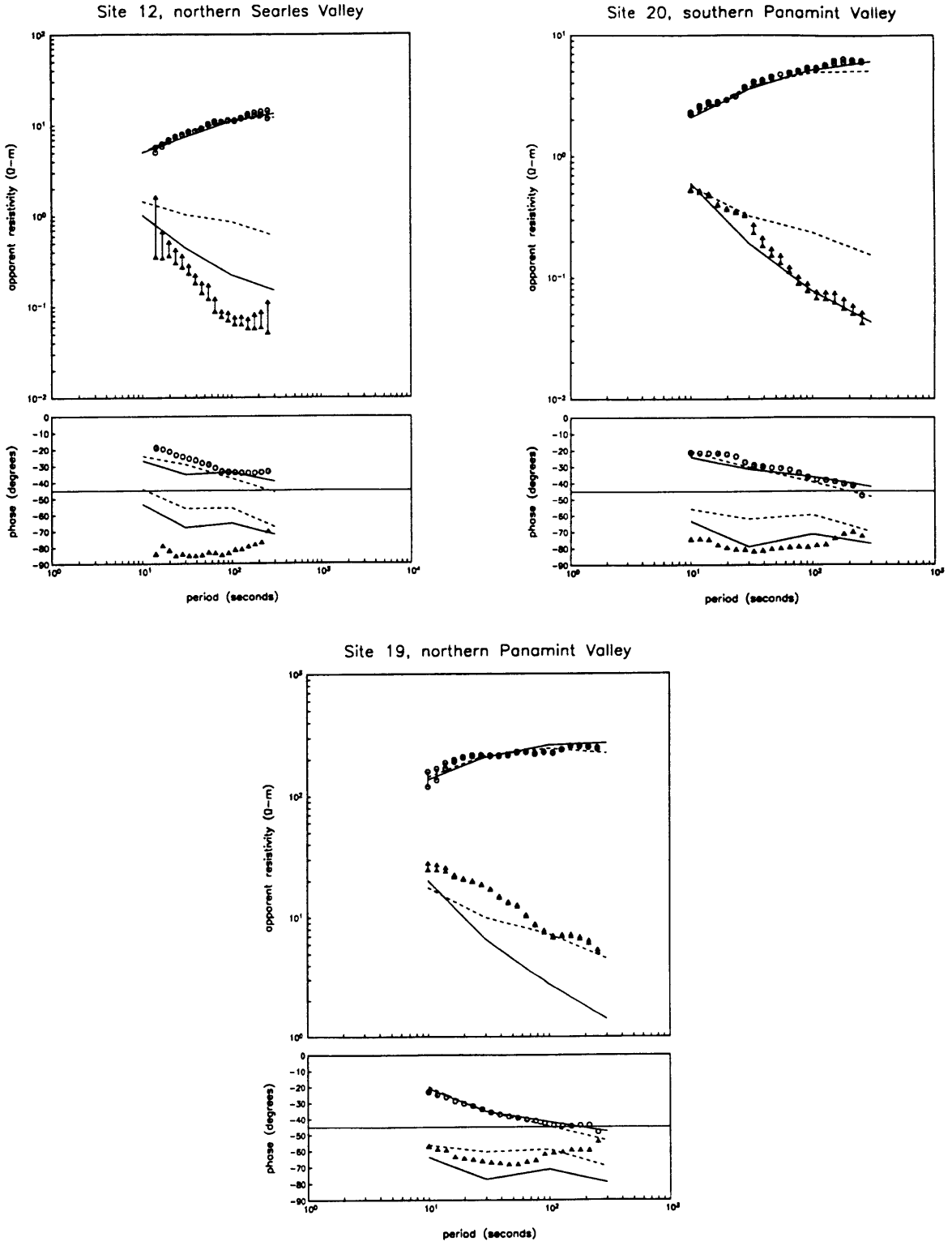
Site 12, northern Searles Valley
Site 20, southern Panamint Valley
Site 19, northern Panamint Valley
apparent resistivity (Ω-m)
phase (degrees)
period (seconds)

Figure 4-43.

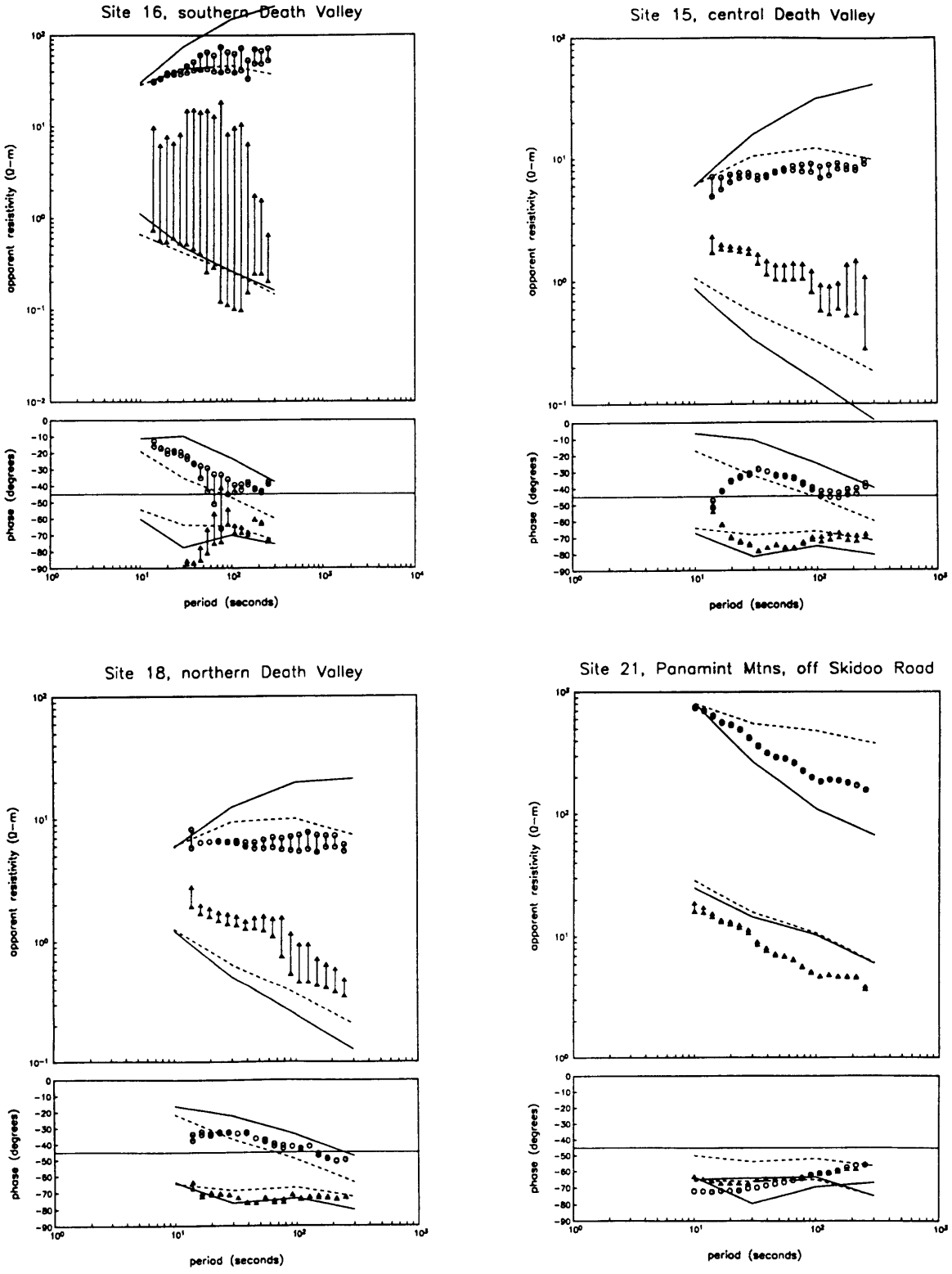
Site 16, southern Death Valley
Site 15, central Death Valley
Site 18, northern Death Valley
Site 21, Panamint Mtns, off Skidoo Road
apparent resistivity (Ω-m)
phase (degrees)
period (seconds)

**Figure 4-44.**

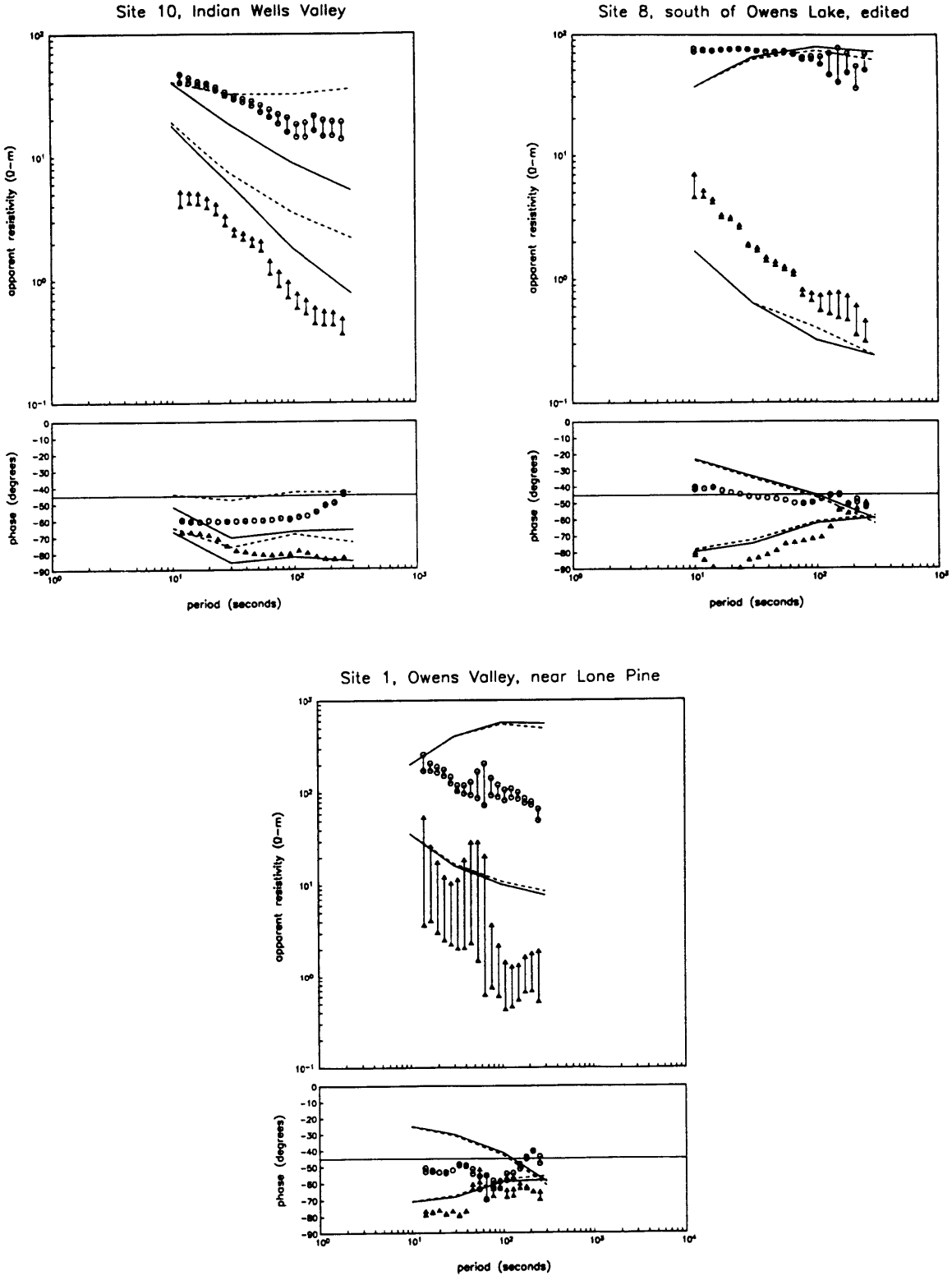
Site 10, Indian Wells Valley
Site 8, south of Owens Lake, edited
Site 1, Owens Valley, near Lone Pine
apparent resistivity (Ω-m)
phase (degrees)
period (seconds)

Figure 4-45.

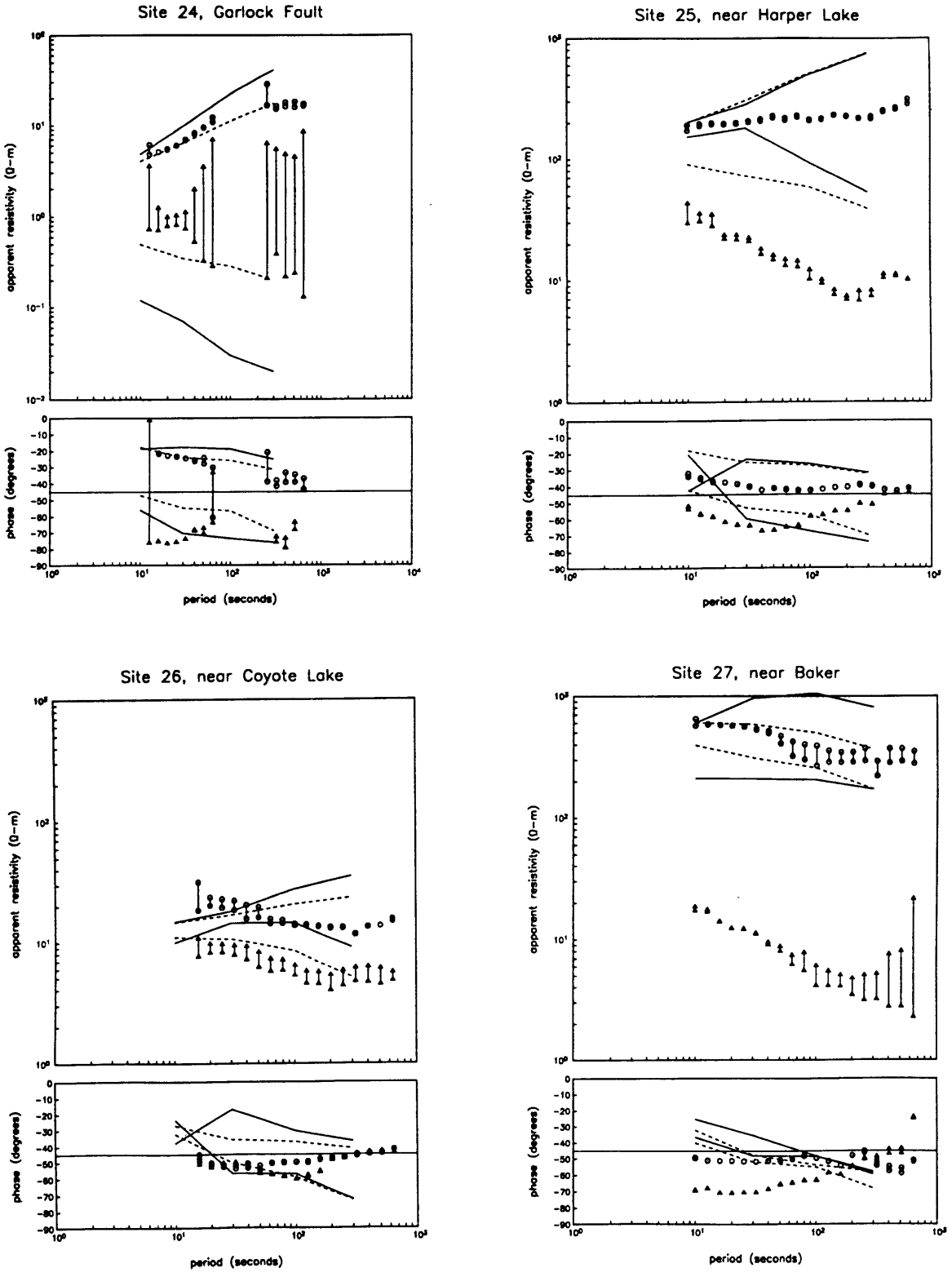
Site 24, Garlock Fault
Site 25, near Harper Lake
Site 26, near Coyote Lake
Site 27, near Baker
apparent resistivity (Ω-m)
phase (degrees)
period (seconds)

**Figure 4-46.**

required to describe the local physiography of all stations would simply require too large a model to be manageable. We have shifted the predictions plotted in Figures 4-43 to 4-46 by an amount needed to get the major impedance response to agree in amplitude with the actual field data. This could have been accomplished by minor adjustments in the near surface resistivities at each data site, but given the computational time and costs of 3D modeling, we felt we were justified to simply shift the curves ourselves. Furthermore, minor adjustments in the near surface resistivities would not really affect our interpretation of the lower crustal resistivity structure.

We have fit the major impedance response very well at Searles Valley and Panamint Valley. Even the minor impedance responses are fit fairly well in both valleys. This model has too much current channelled up into the Death Valley region as evidenced by the steeply rising apparent resistivity curves for sites within Death Valley. The minor impedance responses are fit fairly well there, however. The fits at the other data sites are not as good. For example, this model has too much current in Owens Valley and in the northern Mojave Desert (Harper Lake, Coyote Lake, and Baker). We believe that the excess current at Owens Valley could be leaked out by a local zone in the lower crust of increased conductivity. Likewise, increased leakage in the Mojave would help to get the model predictions there more in line with the data. The major impedance response is fit fairly well at Garlock, however. We were not able to fit the northern Mojave Desert data very well because we just did not have the detail there necessary to model the effects of the ranges and valleys which, as in the California Basin and Range, is an important consideration.

In some instances, which we do not show, the modeling would predict non-minimum phase behavior in the minor impedance response (that is, the slope of the apparent resisitivity would be greater than -1 and the phase would be greater than 90°). We believe that this is a feature of the modeling algorithms that we have little experience in dealing with, and that it is caused by sharp corners and dramatic conductivity contrasts across the corners. This behavior was particularly noticeable in areas where the Earth

model was very complicated, such as around the Searles Valley-Panamint Valley area. At the sites where this happened, we were able to go just one model block away and obtain a more reasonable curve for the minor response without changing the major response. This behavior was probably accentuated by the dramatic split in the amplitudes of the fields at these longer periods. This points out the difficulty associated with trying to model a complex region with the crudeness that we have put into our Earth models.

Overall, we feel that we have done a reasonable job in predicting the major response at several of the data locations. We believe our modeling supports our hypothesis that the lower crust in the California Basin and Range must be much more conductive than that found in surrounding areas in order to attract enough ocean current. Recall that the lower crust under the ocean and the continent into the western edge of the Mojave had a resistivity-thickness product of $1.6 \times 10^6$ ohm-m-km whereas the resisitivity-thickness product in the California Basin and Range was $1 \times 10^5$ ohm-m-km. This represents a 16 fold change in resistivity-thickness product from the lower crust in western California to that in the California Basin and Range. This is a very non-unique problem, however, with many tradeoffs. For example, the resistivity of the lower crust in the Basin and Range could be increased, but then either the oceanic crust would have to be made more resistive, or the Garlock Fault zone would have to be made more conductive in order to get enough current into the Basin and Range. However, we find it difficult to believe that a 16 fold change in the resisitivity-thickness product of the lower crust could be realistically compensated for by a 16 fold increase in the conductivity-thickness product of the continental upper crust, or by similar changes in the resistivity-thickness product elsewhere. Higher frequency measurements (or DC resistivity or shallow electromagnetic measurements) would help to constrain the conductivity structure of the upper crust, but the dramatic change in lower crustal resistivity is a feature that is probably fairly robust. We should mention that we can do a better job at modeling the minor impedance responses using 2D TM mode inversion algorithms. The minor impedance response is associated with the current system across the

valley, but one does not have the ability to take into account the finite strike length of the ranges and valleys. It is difficult, however, to completely resolve the 2D models with the 3D model, so for simplicity and brevity, we show only the 3D responses here.

It is useful to compare the responses from the previous model to one in which we have made some minor adjustments in some of the features that control the leakage of the excess ocean current. This not only demonstrates how minor changes can dramatically affect the responses at many locations far removed from where the change was made, but it also demonstrates the sensitivity we have in determining the leakage properties of the lower crust.

For the second model, shown in Appendix B, we increased the resisitivity of the Garlock Fault zone. We also decreased the resistivity of the lower crust around the southern end of the Death Valley region and in the western Mojave Desert region. The upper crustal conductivity in Death Valley was also decreased slightly. All other features remained the same. We expect that these changes should cause the Garlock Fault to attract less current, and should cause more leakage to occur before the current reaches Death Valley. The predictions for this model are shown in Figures 4-43 to 4-46 as dashed lines.

Note that the major impedance responses were changed only slightly in Searles Valley and Panamint Valley, but changed quite dramatically in Death Valley. The major impedance responses in Death Valley are now better fit by the model, but there are large changes in the minor impedance responses in Panamint Valley, Searles Valley, and Death Valley. These changes in the slopes of the minor impedance responses are probably due to the fact that there is less excess ocean current in these areas, which causes less of a split between the two modes. This model does a better job at predicting the responses at Garlock and in the northern Mojave than the first model.

Both models are fairly robust in needing a conductive lower crust in the Basin and Range. We saw that minor changes in the lower crustal resisitivity structure could produce dramatic changes in both the major and minor impedance responses. Although the numbers

we have obtained are not unique, the *change* in lower crustal resisitivity from the ocean and western California into the Mojave and the Basin and Range is necessary to attract enough excess ocean current. It is obvious that 1D or 2D interpretation of these curves could lead to very erroneous results. In the case of the major response, the lower crustal resistivity would be severely over-estimated, while in the case of the minor response, the lower crustal resistivity would be severely under-estimated. The fact that the lower crust in the California Basin and Range is so conductive may have important implications for the mechanical state of the crust there.

### *Geophysical and geological implications*

Our data and modeling results, though intriguing, do not allow us to resolve any particular mechanism of extension in the California Basin and Range along the Death Valley-Sierra Nevada transect. Unfortunately, our data are not very sensitive to the upper mantle resistivity structure, so we are not able to determine any structure associated with the crust-mantle boundary or any thermal anomalies. However, the lower crust under Panamint Valley seems to be somewhat more conductive than the rest of the California Basin and Range. This may be related to the Death Valley extensional system, or may be a manifestation of the more recent extension occurring in Panamint Valley. If it is related to the Death Valley extension, it seems to indicate that deformation in the upper crust at Death Valley gives way to some form of deformation in the lower crust under Panamint Valley (the deformation in the lower crust would necessarily need to increase the porosity there). Such a scenario seems to favor the simple shear model for extension, but we cannot catagorically state that this must be the case. The extremely low resistivities modeled for the California Basin and Range may, however, provide some insight into the mechanical properties of the lower crust there. The value of 5000 ohm-m down to 32 km depth is much more conductive than we might normally expect for those depths in the crust.

The electrical conductivity of the lower crust has always been somewhat of an enigma. It is well known that the electrical conduction in upper crustal rocks is controlled by the presence of a fluid-filled interconnected porosity, and that the conductivity is dominated by the porosity and salinity of fluids whereas other factors such as grain size and mineralogy have little or no effect (*Brace*, 1971). Within the mantle, temperatures are high enough so that normally insulating silicate minerals become good conductors of electricity by dint of thermally-activated semi-conduction processes (*Hughes*, 1955; *Runcorn and Tozer*, 1955). In the lower crust, however, the controls of electrical conductivity are not quite so clear.

Laboratory measurements on crystalline rocks to 10 kbar of confining pressure (approximately 30 km depth within the Earth), and at a constant temperature of 20°C yielded resistivities ranging from $10^4$ ohm-m to $10^6$ ohm-m (*Brace et al.*, 1965). They suggested that the high confining pressures closed up much of the available porosity, thus increasing the electrical resisitivity, and that a similar scenario might be expected in the lower crust More recent laboratory studies (*Lee et al.*, 1983) corroborate these results and again suggest that saline volatiles in the crust are largely responsible for its electrical conductivity. These studies, however, did not take into account the effect of temperature on the mechanics of lower crustal rocks, nor did they take into account how crustal fluids and wetting angles affected the conductivity.

Because of the increased temperatures in the lower crust as compared to the upper crust, it is commonly believed that rocks deform ductilely rather than brittlely (e.g., *Heard*, 1976), although the mid to lower crust may actually be in the semi-brittle regime (*Carter and Tsenn*, 1987; *Evans et al.*, 1990). Because ductile deformation processes are thought to eliminate much of the porosity (*Brace and Kohlstedt*, 1980), the lower crust, in general, should be very resistive.

Indeed, deep resistivity measurements in Massachusetts (*Schlichter*, 1934), South Africa (*Van Zijl*, 1969), and in the Pacific Northwest (*Cantwell et al.*, 1965; *Cantwell and*

*Orange*, 1965) have required lower crustal resistivity-thickness products on the order of $10^6$ ohm-m-km to fit their data. Magnetotelluric measurements made near ocean-continent boundaries (and therefore very sensitive to the lower crustal resistivity) have also required similarly high resistivity-thickness products to fit the observed data. This is seen in data taken across New England (*Kasameyer*, 1974), and in data taken in California (*Bennett*, 1986; *Mackie et al.*, 1988; *Park et al.*, 1990). These values for the lower crustal resistivity-thickness product agree remarkably well with an independent study carried out by *Cox et al.* (1986) who made controlled-source electromagnetic measurements in the Pacific ocean with the transmitter and receiver antennas directly on the ocean floor. They were able to model their data with a lower crustal resistivity-thickness product of $2x10^6$ ohm-m-km.

However, there are a plethora of journal articles (a summary is given in *Haak and Hutton*, 1986) that suggest that the electrical resistivity of the lower crust is much lower than the values found from these other studies we have just mentioned. Many of these studies, however, were based on 1D or 2D TE mode interpretations of the data, which are biased to lower resistivity values. In general, it is difficult to resolve the resistivity of the lower crust from MT measurements. It is well known that in 1D geometries, one cannot determine the resistivity of a highly resistive layer, but can resolve only its thickness (*Madden,* 1971). And even in 2D environments, only very special circumstances allow one to adequately resolve zones of high resistivity because current simply flows around rather than through these features. Only when current is forced to cross a resistive zone can one begin to determine how resistive these zones actually are. One example of this that we discussed earlier occurs near ocean-continent boundaries.

The point of this discussion is not to imply that all studies that suggest the lower crust is conductive are wrong, for we believe there are situations in which the lower crust will be anomalously conductive. Rather, our point is simply that the lower crust has a finite resistivity. This most likely implies that the lower crust has a small porosity, but that this

porosity is connected and filled with saline solutions (*Brace et al.*, 1965; *Lee et al.*, 1983; *Shankland and Ander*, 1983). *Shankland and Ander* (1983) have suggested fracture porosities on the order of 0.01-0.1% could explain the high conductivities in the lower crust implied by some field studies.

There are many lines of evidence suggesting that free water is present to at least moderate depths within the crust. These include electromagnetic field studies (as detailed earlier), isotopic studies of batholithic rocks (e.g. *Taylor*, 1977), geochemical studies (e.g. *Kerrich et al.*, 1984; *Kerrich*, 1986), analyses of metamorphic rocks (e.g. *Etheridge et al.*, 1984), and seismic studies (e.g. *Nur and Simmons*, 1969; *Jones and Nur*, 1982).

Even if free water does exist in the lower crust, it may not necessarily exist in a connected form; rather, because lower crustal rocks are believed to undergo ductile deformation, it is conceivable that the water may exist only in isolated pockets or in absorbed hydrous phases unless the wetting angles are low enough (*Watson and Brenan*, 1987), or unless fluid pressures can be maintained at greater than hydrostatic for geologically significant times (see *Walder and Nur*, 1984 for a discussion of this idea). It is also highly likely that the amount of free water in the lower crust, and the state in which it exists, is variable from area to area and may depend on many factors including the state of stress to which the region is being subjected.

The crustal state of stress in a particular region controls the deformation occurring there, and may also control the magnitude of fluid flow (*Torgensen*, 1990). Thus, large-scale fluid transport may be important in tectonically active areas. Specifically, fluid transport in fault zones and into deeper shear zones has been evidenced by geochemical studies of metamorphosed rocks in several different localities (*Kerrich et al.*, 1984; *Kerrich*, 1986), although the fluid origin, temperature regime, or amount of fluid infiltration are not well understood. *Sibson* (1981,1988) suggests that high fluid pressures, greater than hydrostatic, may be responsible for activation of faulting along high-angle reverse faults. *Etheridge et al.* (1984) present evidence, from the studies of rocks having

undergone low to medium grade metamorphism, that a high-pressure, mobile fluid phase exists at least to moderate depths in the crust during regional metamorphism. Even though the porosity in these regimes is likely to be very low, less than 0.1%, *Etheridge et al.* (1984) suggest that the high fluid pressures cause microcracking which in turn forms an interconnected porosity. A high pore fluid pressure would necessarily need to be maintained by the constant infiltration of fluids from below the crust. Although high fluid pressures may be present during regional metamorphism, and even though this may be one mechanism for producing an interconnected porosity in the lower crust, it is by no means the only mechanism.

Another way in which a fluid phase can be interconnected in a crustal environment without having to rely on high fluid pressures is simply to have the wetting angles (which are the angles between the crystal faces) low enough so that the energetics of the system will favor a wet connected configuration (*Watson and Brenan*, 1987). In a polycrystalline aggregate, the 3D interconnectivity of a fluid phase is controlled almost entirely by the wetting angle and not by the shape of the pore cross-section (*Watson and Brenan*, 1987; *Hay and Evans*, 1988). If the wetting angles are less than 60°, then the channels formed by the pore space remain open, and likewise, if the wetting angles are greater than 60°, then the channels close off and the fluid collects at grain corners. This 60° criteria is valid only when the volume fraction of fluid is less than about 1%, which is almost certainly the case for the lower crust.

Wetting angles for single phase systems are dependent upon the crystalline material. *Hay and Evans* (1988) found that interconnected pore fluid networks were unstable in polycrystalline calcite at high temperatures. *Watson and Brenan* (1987) found that for quartz-water systems at 1000°C, the wetting angles are generally too high for interconnectivity (the wetting angle $\theta$ is approximately 60° for pure water) unless salts were added to the fluids (a solution that is 0.4 mg NaCl/mg of solution reduces the wetting angle for quartz to around 40°. The wetting angles for olivine were generally greater than

70°, and were not reduced when aqueous salt solutions were added. There is evidence that any fluid present in the lower crust will contain dissolved salts, but it is not clear from the experimental data what effect this will have on the wetting angles of lower crustal rocks (this is complicated by the fact that there have been no wetting angle experiments carried out on multiphase aggregates). High concentrations of dissolved salts are commonly found in hydrothermal systems (*Ellis and Mahon*, 1964) and although these hydrothermal systems commonly occur at shallow depths within the crust, their fluids may originate from deeper in the crust. Additionally, fluid inclusions found in quartz and other minerals often contain highly concentrated salt solutions (*Orville,* 1963) indicating that the crystallization of these rocks has taken place in the presence of a vapor phase containing salts in solution. This would seem to suggest that at least to moderate depths in the crust, and quite likely to deeper depths, fluids exist and contain dissolved salts. Whether this allows for interconnectivity of the fluids in the lower crust is debatable given the current experimental evidence.

However, as Brian Evans pointed out (1990, personal communication), even if the pore space in the lower crust were extensively connected, the pores would eventually be eliminated by non-hydrostatic stresses that would cause the solid framework to creep shut unless the fluid pressures were at or near lithostatic pressure. Once the pore spaces were closed off, the pore pressures would increase and thus increase the likelihood of semi-brittle failure. Such cycles of cracking and healing are discussed in *Walder and Nur* (1984) and *Nur and Walder* (1990).

Thus, we have seen that there is evidence for the connectivity of saline fluids in the lower crust, but in general, the connected porosity would be very small (*Shankland and Ander*, 1983). To obtain dramatically increased lower crustal resistivities, such as we find in the California Basin and Range, some mechanism must be acting to produce increased porosity in the lower crust. We mentioned earlier that in metamorphic regions, elevated fluid pressures can cause microcracking that in turn would lead to an increased porosity.

However, we believe that in the case of the California Basin and Range, the increased porosity is probably related to the dramatic extension that has been occurring recently.

Most of the models suggested for deformation in the Basin and Range have the deformation in the lower crust occurring through ductile deformation processes. However, because the lower crust consists of many different minerals, it is not unreasonable to expect that the type of deformation occurring, even though it is primarily ductile, has some small component of brittle behavior. In this semi-brittle regime, deformation occurs by crystal plasticity and microcracking (*Evans et al.*, 1990). Even though the geothermal gradients are believed to be large in the Basin and Range, we believe that there may be some component of brittle failure (microcracking) in the lower crust that is enhanced by the extensional stress field. This may be helped by the fact that mafic minerals, which make up a large part of the lower crust, undergo the transition to ductile deformation at higher temperatures than the less mafic minerals. Of course, it would not take a much increased porosity to give dramatically increased lower crustal conductivities. At this point, we are beginning to get onto very tenuous ground as we can only speculate about what might be leading to the increased conductivity of the lower crust in the California Basin and Range. There are many deformation and healing mechanisms, and their interactions and behaviors in polymineral rocks such as the lower crust are not well understood. Even if there was some small component of brittle behavior in the lower crust, this would not preclude the lower crust as a whole from deforming ductilely over geologically significant time periods.

## *Conclusions*

In this chapter, we have interpreted short-band magnetotelluric data collected primarily in the California Basin and Range. The data are very three-dimensional in nature and are influenced by excess ocean electrical currents that get trapped in the continental upper crust. Much of the data can be predicted by models that have a very conductive lower crust in the California Basin and Range as compared to the crust further west in California.

We interpret the increased conductivity in the Basin and Range lower crust to result from an increased porosity due to the extension that is ongoing there. We believe that the lower crust must have some small component of brittle failure, perhaps microcracking, that increases the porosity during tectonic deformation. The existence of a small component of brittle failure in the lower crust does not necessarily preclude any extensional models that have lower crustal flow as the deformation mechanism.

***References***

Atwater, T., 1970. Implications of plate tectonics for the Cenozoic tectonic evolution of western North America, *Geol. Soc. Am. Bull.*, **81**, 3513-3536.

Bennett, B.R., 1985. A long-period magnetotelluric study in California, *MSc dissertation*, MIT.

Buck, W.R., Martinez, F., Steckler, M.S., and Cochran, J.R., 1988. Thermal consequences of lithospheric extension: pure and simple, *Tectonics*, **7**, 213-234.

Brace, W.F., Orange, A.S., and Madden, T.R., 1965. The effect of pressure on the electrical resistivity of water-saturated crystalline rocks, *J. Geophys. Res.*, **70**, 5669-5678.

Brace, W.F., 1971. Resistivity of saturated crustal rocks to 40 km based on laboratory measurements, *The Structure and Physical Properties of the Earth's Crust*, AGU Geophysical Monograph 14, 243-255.

Brace, W.F., and Kohlstedt, D.L., 1980. Limits on lithospheric stress imposed by laboratory experiments, *J. Geophys. Res.*, **85**, 6248-6252.

Burchfiel, B.C., and Davis, G.A., 1972. Structural framework and evolution of the southern part of the cordilleran orogen, western United States, *Am. J. Sci.*, **272**, 97-118.

Burchfiel, B.C., and Davis, G.A., 1975. Nature and controls of cordilleran orogenesis, western United States: extensions of an earlier systhesis, *Am. J. Sci.*, **275-A**, 363-396.

Burchfiel, B.C., Hodges, K.V., and Royden, L.H., 1987. Geology of Panamint Valley-Saline Valley pull-apart system, California: palinspastic evidence for low-angle geometry of a Neogene range-bounding fault, *J. Geophys. Res.*, **92**, 10422-10426.

Cantwell, T., 1960. Detecation and analysis of of low frequency magnetotelluric signals, *Ph.D. dissertation*, MIT.

Cantwell, T., Nelson, P., and Webb, J., 1965. Deep resistivity measurements in the Pacific Northwest, *J. Geophys. Res.*, **70**, 1931-1937.

Cantwell, T., and Orange, A., 1965. Further deep resistivity measurements in the Pacific Northwest, *J. Geophys. Res.*, **70**, 4068-4072.

Carter, N.L., and Tsenn, M.C., 1987. Flow properties of continental lithosphere, *Tectonophysics*, **136**, 27-63.

Chave, A.D., and Thomson, D.J., 1989. Some comments of magnetotelluric response function estimation, *J. Geophys. Res.*, **94**, 14215-14225.

Cox, C.S., Constable, S.C., Chave, A.D., and Webb, S.C., 1986. Controlled-source electromagnetic sounding of the oceanic lithosphere, *Nature*, **320**, 52-54.

Davis, R.A., 1979. A bandlimited magnetotelluric study of an area in Harvard, Massachusetts, *S.M. dissertation*, MIT.

Eaton, G.P., Wahl, R.R., Prostka, H.J., Mabey, D.R., and Kleinkopf, M.D., 1978. Regional gravity and tectonic patterns: their relation to late Cenozoic epeirogeny and lateral spreading in the western Cordillera, in *Cenozoic Tectonics and Regional Geophysics of the Western Cordillera*, ed. R.B. Smith and G.P. Eaton, 51-92, *Geol. Soc. Am. Mem. 152.*

Eaton, G.P., 1982. The Basin and Range province: origin and tectonic significance, *Ann. Rev. Earth Planet. Sci.*, **10**, 409-440.

Egbert, G.D., and Booker, J.R., 1986. Robust estimation of geomagnetic transfer functions, *Geophys. J. R. Astron. Soc.*, **87**, 173-194.

Ellis, A.J., and Mahon, W.A.J., 1964. Natural hydrothermal systems and experimental hot-water/rock interactions, *Geochim. Cosmo. Acta*, **28**, 1323-1357.

Etheridge, M.A., Wall, V.J., Cox, S.F., and Vernon, R.H., 1984. High fluid pressures during regional metamorphism and deformation: implications for mass transport and deformation mechanisms, *J. Geophys. Res.*, **89**, 4344-4358.

Evans, B.R., Fredrich, J.T., and Wong, T.W., 1990. The brittle-ductile transition in rocks: recent experimental and theoretical progress, in *Geophys. Monogr. Ser. 56, The Heard Volume*, Amer. Geophys.Un.

Froidevaux, C., 1986. Basin and Range large-scale tectonics: constraints from gravity and reflection seismology, *J. Geophys. Res.*, **91**, 3625-3632.

Haak, V., and Hutton, R., 1986. Electrical resistivity in continental lower crust, in *The Nature of the Lower Continental Crust*, Geological Society Special Publication 24, 35-49.

Hay, R.S., and Evans, B., 1988. Intergranular distribution of pore fluid and the nature of high-angle grain boundaries in limestone and marble, *J. Geophys. Res.*, **93**, 8959-8974.

Heard, H.C., 1976. Comparison of the flow properties of rocks at crustal conditions, *Phil. Trans. R. Soc. Lond.*, **A283**, 173-186.

Hughes, H., 1955. The pressure effect on the electrical conductivity of peridot, *J. Geophys. Res.*, **60**, 187-191.

Jones, A.G., 1981. Transformed coherence functions for multivariate studies, *IEEE Trans. Ac., Speech, and Sig. Proc.*, **ASSP-29**, 317-319.

Jones, A.G., 1984. Magnetotelluric transfer function estimation improvement by a coherence based rejection technique, *SEG Expanded Abstracts, 54th meeting*, 51-55.

Jones, A.G., Chave, A.D., Egbert, G., Auld, D., and Bahr, K., 1989. A comparison of techniques for magnetotelluric response funtion estimation, *J. Geophys. Res.*, **94**, 14201-14213.

Jones, C.H., 1987. Is extension in Death Valley accommodated by thinning of the mantle lithosphere beneath the Sierra Nevada, California?, *Tectonics*, **6**, 449-473.

Jones, T.D., and Nur, A., 1982. Seismic velocity and anisotropy in mylonite and the reflectivity of deep crustal fault zones, *Geology*, **10**, 260-263.

Kasameyer, P., 1974. Low frequency magnetotelluric survey of New England, *Ph.D. dissertation*, MIT.

Kaufman, A.A., and Keller, G.V., 1981. *The Magnetotelluric Sounding Method*, Elsevier Scientific Publishing Co.

Kerrich, R., LaTour, T.E., and Willmore, L., 1984. Fluid participation in deep fault zones: evidence from geological, geochemical, and $^{18}O/^{16}O$ relations, *J. Geophys. Res.*, **89**, 4331-4343.

Kerrich, R., 1986. Fluid transport in lineaments, *Phil. Trans. R. Soc. Lond.*, A**317**, 219-251.

LaTorraca, G.A., Madden, T.R., and Korringa, J., 1986. An analysis of the magnetotelluric impedance for three-dimensional conductivity structures, *Geophysics*, **51**, 1819-1829.

Lee, C.D., Vine, F.J., and Ross, R.G., 1983. Electrical conductivity models for the continental crust based on laboratory measurements on high-grade metamorphic rocks, *Geophys. J. R.astr. Soc.*, **72**, 353-371.

Lienert, B.R., Whitcomb, J.H., Phillips, R.J., Reddy, I.K., and Taylor, R.A., 1980. Long term variations in magnetotelluric apparent resistivities observed near the San Andreas fault in southern California, *J. Geomag. Geoelectr.*, **32**, 757-775.

Mackie, R.L., Bennett, B.R., and Madden, T.R., 1988. Long-period magnetotelluric measurements near the central California coast: a land-locked view of the conductivity structure under the Pacific Ocean, *Geophys. J.*, **95**, 181-194.

Madden, T.R., 1971. The resolving power of geoelectric measurements for delineating resistive zones within the crust, in *The Structure and Physical Properties of the Earth's Crust*, Geophysical Monograph Series 14, American Geophysical Union, 95-105.

Madden, T.R., LaTorraca, G.A., and Park, S.K., 1990. Resistivity variations around the Palmdale section of the San Andreas, *to be submitted.*

Menvielle, M., Rossignol, J.C., and Tarits, P., 1982. The coast effect in terms of deviated electric currents: a numerical study, *Phys. Earth Planet. Int.*, **28**, 118-128.

Nur, A., and Simmons, G., 1969. The effect of saturation on velocity in low porosity rocks, *Earth Planet. Sci. Lett.*, **7**, 183-193.

Nur, A., and Walder, J., 1990. Hydraulic pulses in the Earth's crust, *W.F. Brace Special Volume*, **in press.**

Orville, P.M., 1963. Alkali ion exchange between vapor and feldspar phases, *Am. J. Sci.*, **261**, 201-237.

Park, S.K, and Torres-Verdin, C., 1988. A systematic approach to the interpretation of magnetotelluric data in volcanic environments with applications to the quest for magma in Long Valley, California, *J. Geophys. Res.*, **93**, 13265-13283.

Park, S.K., Biasi, G.P., Mackie, R.L., and Madden, T.R., 1990. Magnetotelluric evidence for crustal suture zones bounding the southern Great Valley, California, *J. Geophys. Res.*, **in press**.

Parkinson, W.D., 1962. The influence of continents and oceans on geomagnetic variations, *Geophys. J.*, **6**, 441-449.

Ranganayaki, R.P., 1978. Generalized thin sheet approximation for magnetotelluric modeling, *Ph.D. dissertation*, MIT.

Ranganayaki, R.P., and Madden, T.R., 1980. Generalized thin sheet analysis in magnetotellurics, an extension of Price's analysis, *Geophys. J. R. astr. Soc.*, **60**, 445-457.

Reddy, I.K, Phillips, R.J., Whitcomb, J.H., and Rankin, D., 1977. Electrical structure in a region of the Transverse Ranges, southern California, *Earth and Planet. Sci. Ltrs*, **34**, 313-320.

Runcorn, S.K., and Tozer, D.C., 1955. The electrical conductivity of olivine at high temperatures and pressures, *Ann. de Geophysique*, **11**, 98-102.

Schlichter, L.B., 1934. An electrical problem in geophysics, *Tech Eng. News*, MIT.

Schmucker, U., 1963. Anomalies of geomagnetic variations in the southwestern United States, *J. Geomagn. Geoelectr.*, **15**, 193-221.

Schmucker, U., 1970. *Anomalies of Geomagnetic Variations in the southwestern United States*, Bull. of the Scripps Inst. of Oceanography, **13**, University of California Press.

Shankland, T.J., and Ander, M.E., 1983. Electrical conductivity, temperatures, and fluids in the lower crust, *J. Geophys. Res.*, **88**, 9475-9484.

Sibson, R.H., 1981. Fluid flow accompanying faulting: field evidence and models, in *Earthquake Prediction: An International Review*, American Geophysical Union, Maurice Ewing Series, v. 4.

Sibson, R.H., Robert, F., and Poulsen, K.H., 1988. High-angle reverse faults, fluid-pressure cycling, and mesothermal gold-quartz deposits, *Geology*, **16**, 551-555.

Sims, W.E., Bostick, F.X., and Smith, H.W., 1971. The estimation of magnetotelluric impedance tensor elements from the measured data, *Geophysics*, **36**, 938-942.

Stewart, J.H., 1971. Basin and Range structure - a system of horsts and grabens produced by deep-seated extension, *Geol. Soc. Am. Bull.*, **82**, 1019-1044.

Swift, C.M., 1967. A magnetotelluric investigation of an electrical conductivity anomaly in the southwestern United States, *Ph.D. dissertation*, MIT.

Taylor, H.P., Jr., 1977. Water/rock interaction and the origin of $H_2O$ in granitic batholiths, *J. Geol. Soc. London*, **133**, 509-558.

Torgensen, T., 1990, Crustal-scale fluid transport, *Eos*, Transactions, American Geophysical Union, **71**, 1-4.

Towle, J.N., 1980. Observations of a direct current concentration on the eastern Sierran front: evidence for shallow crustal conductors on the eastern Sierran front and beneath the Coso Range, *J. Geophys. Res.*, **85**, 2484-2490.

Van Zijl, J.S.V., 1969. A deep schlumberger sounding to investigate the electrical structure of the crust and upper mantle in South Africa, *Geophysics*, **34**, 450-462.

Vozoff, K., 1972. The magnetotelluric method in the exploration of sedimentary basins, *Geophysics*, **37**, 98-141.

Walder, J., and Nur, A., 1984. Porosity reduction and crustal pore pressure development, *J. Geophys. Res.*, **89**, 11539-11548.

Wannamaker, P.E., 1983. Resistivity structure of the northern Basin and Range, *Geothermal Resources Council, Special Report 13*, 345-362.

Watson, E.B., and Brenan, J.M., 1987. Fluids in the lithosphere, 1. Experimentally-determined wetting characteristics of $CO_2$-$H_2O$ fluids and their implications for fluid transport, host-rock physical properties, and fluid inclusion formation, *Earth Planet. Sc. Lettr.*, **85**, 497-515.

Wernicke, B., 1985. Uniform-sense normal simple shear of the continental lithosphere, *Canadian J. Earth Sc.*, **22**, 108-125.

Wernicke, B.P., Christiansen, R.L., England, P.C., and Sonder, L.J., 1987. Tectonomagmatic evolution of Cenozoic extension in the North America Cordillera, in *Continental Extensional Tectonics*, Geological Society Special Publication No. 28, 203-221.

Zoback, M.L., Anderson, R.E., and Thompson, G.A., 1981. Cainozoic evolution of the state of stress and style of tectonism of the Basin and Range province of the western United States, *Phil. Trans. R. Soc. Lond.*, **A300**, 407-434.

Zuber, M.T., Parmentier, E.M., and Fletcher, R.C., 1986. Extension of continental lithosphere: a model for two scales of Basin and Range deformation, *J. Geophys. Res.*, **91**, 4826-4838.

## *Appendix A*

In this appendix, we present the first 3D model for which model predictions are shown earlier in the chapter. We present for each level in the model a resistivity map. The numbers in the map correspond to a particular resistivity value, which we give below. In general, the resistivity is approximately equal to $2^n/4$ where $n$ is the number in the map. Therefore, a map value of 2 corresponds to a resistivity of 1 ohm-m. In this fashion, there is approximately a factor of 2 increase in resistivity for each increase in map number. The y-axis, which runs down the page, is aligned with the structural grain of the Sierra Nevada. The x-axis, which runs horizontally across the page, is perpendicular to the structural grain of the Sierra Nevada. The model was 27 blocks in the x-direction, 18 in the y-direction, and 13 Earth layers vertically (7 graded air layers are put on top of the model).

The widths, in kilometers, of the blocks in the x-directions are (from left to right):

4500, 1500, 500, 180, 60, 60, 80, 80, 40, 20, 20, 5, 5, 5, 15, 15, 5, 10, 5, 20, 5, 10, 5, 20, 100, 300, 1000

The widths, in kilometers, of the blocks in the y-directions are (from top to bottom):

1000, 300, 100, 60, 30, 20, 20, 10, 10, 20, 10, 15, 20, 20, 30, 100, 300, 1000

The thickness, in kilometers, of the layers in the z-direction are (from the surface down):

0.1, 0.2, 0.4, 0.8, 1.5, 2.5, 2.5, 4, 10, 10, 20, 50, 100

The resistivity map values correspond to the following resistivities (in ohm-m)

| | | | |
|---|---|---|---|
| 0 = 0.3 | 5 = 8.5 | 10 = 300 | 15 = 10000 |
| 1 = 0.5 | 6 = 20 | 11 = 500 | 16 = 16000 |
| 2 = 1.0 | 7 = 30 | 12 = 1000 | 17 = 30000 |
| 3 = 2.0 | 8 = 55 | 13 = 3000 | 18 = 80000 |
| 4 = 5.0 | 9 = 100 | 14 = 5000 | |

The data sites have the following correspondence to the model locations (xblock, yblock):

| | |
|---|---|
| Site 1, Owens Valley = | (12,5) |
| Site 8, south of Owens Lake = | (12,7) |
| Site 10, Indian Wells Valley = | (12,11) |
| Site 12, Searles Valley = | (19,11) |
| Site 15, central Death Valley = | (22,9) |
| Site 16, southern Death Valley = | (23,11) |
| Site 18, northern Death Valley = | (22,6) |
| Site 19, northern Panamint Valley = | (19,7) |
| Site 20, southern Panamint Valley = | (19,9) |
| Site 21, Panamint Mtns = | (20,7) |
| Site 24, Garlock Fault = | (13,13) |
| Site 25, near Harper Lake = | (14,14) |
| Site 26, near Coyote Lake = | (18,14) |
| Site 27, Baker = | (23,14) |

The resistivity maps for each layer in the model are as follows:

layer 1

| | | | | | | | | | | | | | | | | | | | | | | | | | |
|---|---|---|---|---|---|---|---|---|---|---|---|---|---|---|---|---|---|---|---|---|---|---|---|---|---|
| 0 | 0 | 0 | 0 | 0 | 0 | 8 | 8 | 8 | 8 | 8 | 8 | 8 | 8 | 8 | 8 | 8 | 8 | 8 | 8 | 8 | 8 | 8 | 8 | 8 | 8 |
| 0 | 0 | 0 | 0 | 0 | 0 | 8 | 3 | 13 | 13 | 13 | 8 | 8 | 8 | 8 | 8 | 8 | 8 | 8 | 8 | 8 | 8 | 8 | 8 | 8 | 8 |
| 0 | 0 | 0 | 0 | 0 | 0 | 8 | 3 | 13 | 13 | 13 | 8 | 8 | 8 | 8 | 8 | 8 | 8 | 8 | 8 | 8 | 8 | 8 | 8 | 8 | 8 |
| 0 | 0 | 0 | 0 | 0 | 0 | 8 | 3 | 13 | 13 | 13 | 6 | 6 | 8 | 8 | 8 | 12 | 12 | 12 | 12 | 12 | 12 | 12 | 12 | 8 | 8 |
| 0 | 0 | 0 | 0 | 0 | 0 | 8 | 3 | 13 | 13 | 13 | 6 | 6 | 8 | 8 | 8 | 12 | 12 | 12 | 12 | 3 | 3 | 3 | 12 | 8 | 8 |
| 0 | 0 | 0 | 0 | 0 | 0 | 8 | 3 | 13 | 13 | 13 | 5 | 5 | 5 | 8 | 8 | 7 | 7 | 7 | 12 | 3 | 3 | 3 | 12 | 8 | 8 |
| 0 | 0 | 0 | 0 | 0 | 0 | 8 | 3 | 13 | 13 | 13 | 5 | 5 | 8 | 5 | 8 | 7 | 7 | 7 | 12 | 3 | 3 | 3 | 12 | 8 | 8 |
| 0 | 0 | 0 | 0 | 0 | 0 | 8 | 3 | 13 | 13 | 13 | 5 | 8 | 8 | 8 | 12 | 7 | 7 | 7 | 12 | 3 | 3 | 3 | 12 | 8 | 8 |
| 0 | 0 | 0 | 0 | 0 | 0 | 8 | 3 | 13 | 13 | 13 | 8 | 8 | 8 | 8 | 12 | 7 | 7 | 7 | 12 | 3 | 3 | 3 | 12 | 8 | 8 |
| 0 | 0 | 0 | 0 | 0 | 0 | 8 | 3 | 13 | 13 | 13 | 5 | 5 | 5 | 5 | 12 | 7 | 7 | 7 | 12 | 3 | 3 | 3 | 12 | 8 | 8 |
| 0 | 0 | 0 | 0 | 0 | 0 | 8 | 3 | 13 | 13 | 5 | 5 | 5 | 5 | 5 | 7 | 7 | 7 | 7 | 12 | 3 | 3 | 3 | 12 | 8 | 8 |
| 0 | 0 | 0 | 0 | 0 | 0 | 8 | 8 | 13 | 13 | 12 | 12 | 12 | 12 | 7 | 7 | 7 | 7 | 7 | 12 | 3 | 3 | 3 | 12 | 8 | 8 |
| 0 | 0 | 0 | 0 | 0 | 0 | 0 | 8 | 8 | 3 | 3 | 3 | 3 | 3 | 3 | 3 | 3 | 3 | 3 | 3 | 3 | 3 | 3 | 12 | 12 | 8 |
| 0 | 0 | 0 | 0 | 0 | 0 | 0 | 0 | 8 | 8 | 3 | 3 | 6 | 6 | 6 | 6 | 6 | 6 | 6 | 6 | 6 | 6 | 6 | 6 | 12 | 8 |
| 0 | 0 | 0 | 0 | 0 | 0 | 0 | 0 | 8 | 8 | 6 | 6 | 6 | 6 | 6 | 6 | 6 | 6 | 6 | 6 | 6 | 6 | 6 | 6 | 12 | 8 |
| 0 | 0 | 0 | 0 | 0 | 0 | 0 | 0 | 12 | 12 | 9 | 9 | 9 | 9 | 9 | 9 | 9 | 9 | 9 | 9 | 9 | 9 | 9 | 11 | 8 | 8 |
| 0 | 0 | 0 | 0 | 0 | 0 | 0 | 0 | 12 | 12 | 8 | 8 | 8 | 8 | 8 | 8 | 8 | 8 | 8 | 8 | 8 | 8 | 8 | 8 | 8 | 8 |
| 0 | 0 | 0 | 0 | 0 | 0 | 0 | 0 | 8 | 8 | 8 | 8 | 8 | 8 | 8 | 8 | 8 | 8 | 8 | 8 | 8 | 8 | 8 | 8 | 8 | 8 |

layer 2

| | | | | | | | | | | | | | | | | | | | | | | | | | |
|---|---|---|---|---|---|---|---|---|---|---|---|---|---|---|---|---|---|---|---|---|---|---|---|---|---|
| 0 | 0 | 0 | 0 | 0 | 0 | 8 | 8 | 8 | 8 | 8 | 8 | 8 | 8 | 8 | 8 | 8 | 8 | 8 | 8 | 8 | 8 | 8 | 8 | 8 | 8 |
| 0 | 0 | 0 | 0 | 0 | 0 | 8 | 3 | 13 | 13 | 13 | 8 | 8 | 8 | 8 | 8 | 8 | 8 | 8 | 8 | 8 | 8 | 8 | 8 | 8 | 8 |
| 0 | 0 | 0 | 0 | 0 | 0 | 8 | 3 | 13 | 13 | 13 | 8 | 8 | 8 | 8 | 8 | 8 | 8 | 8 | 8 | 8 | 8 | 8 | 8 | 8 | 8 |
| 0 | 0 | 0 | 0 | 0 | 0 | 8 | 3 | 13 | 13 | 13 | 5 | 5 | 11 | 11 | 12 | 12 | 12 | 12 | 12 | 12 | 12 | 12 | 8 | 8 | 8 |
| 0 | 0 | 0 | 0 | 0 | 0 | 8 | 3 | 13 | 13 | 13 | 5 | 5 | 11 | 11 | 12 | 12 | 12 | 12 | 3 | 3 | 3 | 12 | 8 | 8 | 8 |
| 0 | 0 | 0 | 0 | 0 | 0 | 8 | 3 | 13 | 13 | 13 | 5 | 5 | 5 | 11 | 12 | 3 | 3 | 3 | 12 | 3 | 3 | 3 | 12 | 8 | 8 |
| 0 | 0 | 0 | 0 | 0 | 0 | 8 | 3 | 13 | 13 | 13 | 5 | 5 | 11 | 11 | 12 | 3 | 3 | 3 | 12 | 3 | 3 | 3 | 12 | 8 | 8 |
| 0 | 0 | 0 | 0 | 0 | 0 | 8 | 3 | 13 | 13 | 13 | 5 | 11 | 11 | 11 | 12 | 5 | 5 | 5 | 12 | 3 | 3 | 3 | 12 | 8 | 8 |
| 0 | 0 | 0 | 0 | 0 | 0 | 8 | 3 | 13 | 13 | 13 | 11 | 11 | 11 | 11 | 12 | 5 | 5 | 5 | 12 | 3 | 3 | 3 | 12 | 8 | 8 |
| 0 | 0 | 0 | 0 | 0 | 0 | 8 | 3 | 13 | 13 | 13 | 5 | 5 | 5 | 5 | 12 | 5 | 5 | 5 | 12 | 3 | 3 | 3 | 12 | 8 | 8 |
| 0 | 0 | 0 | 0 | 0 | 0 | 8 | 3 | 13 | 13 | 5 | 5 | 5 | 5 | 5 | 5 | 5 | 5 | 5 | 12 | 3 | 3 | 3 | 12 | 8 | 8 |
| 0 | 0 | 0 | 0 | 0 | 0 | 8 | 8 | 13 | 13 | 12 | 12 | 12 | 12 | 5 | 5 | 5 | 5 | 5 | 12 | 3 | 3 | 3 | 12 | 8 | 8 |
| 0 | 0 | 0 | 0 | 0 | 0 | 0 | 8 | 8 | 3 | 3 | 3 | 3 | 3 | 3 | 3 | 3 | 3 | 3 | 3 | 3 | 3 | 3 | 12 | 12 | 8 |
| 0 | 0 | 0 | 0 | 0 | 0 | 0 | 0 | 8 | 8 | 6 | 6 | 6 | 6 | 6 | 6 | 6 | 6 | 6 | 6 | 6 | 6 | 6 | 6 | 12 | 8 |
| 0 | 0 | 0 | 0 | 0 | 0 | 0 | 0 | 8 | 8 | 6 | 6 | 6 | 6 | 6 | 6 | 6 | 6 | 6 | 6 | 6 | 6 | 6 | 6 | 12 | 8 |
| 0 | 0 | 0 | 0 | 0 | 0 | 0 | 0 | 12 | 12 | 12 | 12 | 12 | 12 | 12 | 12 | 12 | 12 | 12 | 12 | 12 | 12 | 12 | 12 | 12 | 8 |
| 0 | 0 | 0 | 0 | 0 | 0 | 0 | 0 | 12 | 12 | 8 | 8 | 8 | 8 | 8 | 8 | 8 | 8 | 8 | 8 | 8 | 8 | 8 | 8 | 8 | 8 |
| 0 | 0 | 0 | 0 | 0 | 0 | 0 | 0 | 8 | 8 | 8 | 8 | 8 | 8 | 8 | 8 | 8 | 8 | 8 | 8 | 8 | 8 | 8 | 8 | 8 | 8 |

layer 3

| | | | | | | | | | | | | | | | | | | | | | | | | | |
|---|---|---|---|---|---|---|---|---|---|---|---|---|---|---|---|---|---|---|---|---|---|---|---|---|---|
| 0 | 0 | 0 | 0 | 0 | 0 | 8 | 8 | 8 | 8 | 8 | 8 | 8 | 8 | 8 | 8 | 8 | 8 | 8 | 8 | 8 | 8 | 8 | 8 | 8 | 8 |
| 0 | 0 | 0 | 0 | 0 | 0 | 8 | 3 | 13 | 13 | 13 | 8 | 8 | 8 | 8 | 8 | 8 | 8 | 8 | 8 | 8 | 8 | 8 | 8 | 8 | 8 |
| 0 | 0 | 0 | 0 | 0 | 0 | 8 | 3 | 13 | 13 | 13 | 8 | 8 | 8 | 8 | 8 | 8 | 8 | 8 | 8 | 8 | 8 | 8 | 8 | 8 | 8 |
| 0 | 0 | 0 | 0 | 0 | 0 | 8 | 3 | 13 | 13 | 13 | 0 | 0 | 12 | 12 | 12 | 12 | 12 | 12 | 12 | 12 | 12 | 12 | 8 | 8 | 8 |
| 0 | 0 | 0 | 0 | 0 | 0 | 8 | 3 | 13 | 13 | 13 | 0 | 0 | 12 | 12 | 12 | 12 | 12 | 12 | 12 | 3 | 3 | 3 | 12 | 8 | 8 |
| 0 | 0 | 0 | 0 | 0 | 0 | 8 | 3 | 13 | 13 | 13 | 0 | 0 | 0 | 12 | 12 | 4 | 4 | 4 | 12 | 3 | 3 | 3 | 12 | 8 | 8 |
| 0 | 0 | 0 | 0 | 0 | 0 | 8 | 3 | 13 | 13 | 13 | 0 | 0 | 12 | 12 | 12 | 4 | 4 | 4 | 12 | 3 | 3 | 3 | 12 | 8 | 8 |
| 0 | 0 | 0 | 0 | 0 | 0 | 8 | 3 | 13 | 13 | 13 | 3 | 12 | 12 | 12 | 12 | 3 | 3 | 3 | 12 | 3 | 3 | 3 | 12 | 8 | 8 |
| 0 | 0 | 0 | 0 | 0 | 0 | 8 | 3 | 13 | 13 | 13 | 12 | 12 | 12 | 12 | 12 | 3 | 3 | 3 | 12 | 3 | 3 | 3 | 12 | 8 | 8 |
| 0 | 0 | 0 | 0 | 0 | 0 | 8 | 3 | 13 | 13 | 13 | 5 | 5 | 5 | 5 | 12 | 3 | 3 | 3 | 12 | 3 | 3 | 3 | 12 | 8 | 8 |
| 0 | 0 | 0 | 0 | 0 | 0 | 8 | 3 | 13 | 13 | 5 | 5 | 5 | 5 | 5 | 12 | 3 | 3 | 3 | 12 | 3 | 3 | 3 | 12 | 8 | 8 |
| 0 | 0 | 0 | 0 | 0 | 0 | 8 | 8 | 13 | 13 | 12 | 12 | 12 | 12 | 3 | 3 | 3 | 3 | 3 | 12 | 3 | 3 | 3 | 12 | 12 | 8 |
| 0 | 0 | 0 | 0 | 0 | 0 | 0 | 8 | 8 | 3 | 3 | 3 | 3 | 3 | 3 | 3 | 3 | 3 | 3 | 3 | 3 | 3 | 3 | 3 | 12 | 8 |
| 0 | 0 | 0 | 0 | 0 | 0 | 0 | 0 | 8 | 8 | 3 | 3 | 3 | 3 | 3 | 3 | 3 | 3 | 3 | 3 | 3 | 3 | 3 | 3 | 12 | 8 |
| 0 | 0 | 0 | 0 | 0 | 0 | 0 | 0 | 8 | 8 | 3 | 3 | 3 | 3 | 3 | 3 | 3 | 3 | 3 | 3 | 3 | 3 | 3 | 3 | 12 | 8 |
| 0 | 0 | 0 | 0 | 0 | 0 | 0 | 0 | 12 | 12 | 12 | 12 | 12 | 12 | 12 | 12 | 12 | 12 | 12 | 12 | 12 | 12 | 12 | 12 | 12 | 8 |
| 0 | 0 | 0 | 0 | 0 | 0 | 0 | 0 | 12 | 12 | 8 | 8 | 8 | 8 | 8 | 8 | 8 | 8 | 8 | 8 | 8 | 8 | 8 | 8 | 8 | 8 |
| 0 | 0 | 0 | 0 | 0 | 0 | 0 | 0 | 8 | 8 | 8 | 8 | 8 | 8 | 8 | 8 | 8 | 8 | 8 | 8 | 8 | 8 | 8 | 8 | 8 | 8 |

* Several of the major physiographic provinces are outlined for reference on the resistivity map for layer 1. The 4 areas outlined from left to right are the Sierra Nevada, Owens Valley, Searles Valley and Panamint Valley, and Death Valley. The long, thin box outlined just below these 4 areas represents the Garlock Fault zone.

layer 4

```
0  0  0  0  0  0  11 11 11 11 11 11 11 11 11 11 11 11 11 11 11 11 11 11 11 11 11 11
0  0  0  0  0  0  11 5  13 13 13 11 11 11 11 11 11 11 11 11 11 11 11 11 11 11 11 11
0  0  0  0  0  0  11 5  13 13 13 11 11 11 11 11 11 11 11 11 11 11 11 11 11 11 11 11
0  0  0  0  0  0  11 5  13 13 13 5  5  12 12 12 12 12 12 12 12 12 12 11 11 11
0  0  0  0  0  0  11 5  13 13 13 5  5  12 12 12 12 12 12 12 5  5  5  12 11 11 11
0  0  0  0  0  0  11 5  13 13 13 5  5  5  12 12 8  8  8  12 5  5  5  12 11 11 11
0  0  0  0  0  0  11 5  13 13 13 5  5  12 12 12 8  8  8  12 5  5  5  12 11 11 11
0  0  0  0  0  0  11 5  13 13 13 5  12 12 12 12 5  5  5  12 5  5  5  12 11 11 11
0  0  0  0  0  0  11 5  13 13 13 12 12 12 12 12 5  5  5  12 5  5  5  12 11 11 11
0  0  0  0  0  0  11 5  13 13 13 5  5  5  5  12 5  5  5  12 5  5  5  12 11 11 11
0  0  0  0  0  0  11 5  13 13 5  5  5  5  5  5  5  5  5  12 5  5  5  12 11 11 11
0  0  0  0  0  0  11 11 13 13 12 12 12 12 5  5  5  5  5  12 5  5  5  12 12 11 11
0  0  0  0  0  0  0  11 11 5  5  5  5  5  5  5  5  5  5  5  5  5  5  11 12 11 11
0  0  0  0  0  0  0  0  11 11 5  5  5  5  5  5  5  5  5  5  5  5  5  11 12 11 11
0  0  0  0  0  0  0  0  11 11 5  5  5  5  5  5  5  5  5  5  5  5  5  11 12 11 11
0  0  0  0  0  0  0  0  12 12 12 12 12 12 12 12 12 12 12 12 12 12 12 12 12 11 11
0  0  0  0  0  0  0  0  12 12 11 11 11 11 11 11 11 11 11 11 11 11 11 11 11 11 11
0  0  0  0  0  0  0  0  11 11 11 11 11 11 11 11 11 11 11 11 11 11 11 11 11 11 11
```

layer 5

```
0  0  0  0  0  11 11 11 11 11 11 11 11 11 11 11 11 11 11 11 11 11 11 11 11 11 11 11
0  0  0  0  0  11 11 5  13 13 13 11 11 11 11 11 11 11 11 11 11 11 11 11 11 11 11 11
0  0  0  0  0  11 11 5  13 13 13 11 11 11 11 11 11 11 11 11 11 11 11 11 11 11 11 11
0  0  0  0  0  11 11 5  13 13 13 6  6  13 13 13 13 13 13 13 13 13 13 11 11 11
0  0  0  0  0  11 11 5  13 13 13 6  6  13 13 13 13 13 13 13 6  6  6  13 11 11 11
0  0  0  0  0  11 11 5  13 13 13 6  6  6  13 13 9  9  9  13 6  6  6  13 11 11 11
0  0  0  0  0  11 11 5  13 13 13 6  6  13 13 13 9  9  9  13 6  6  6  13 11 11 11
0  0  0  0  0  11 11 5  13 13 13 6  13 13 13 13 6  6  6  13 6  6  6  13 11 11 11
0  0  0  0  0  11 11 5  13 13 13 13 13 13 13 13 6  6  6  13 6  6  6  13 11 11 11
0  0  0  0  0  11 11 5  13 13 13 5  5  5  5  13 6  6  6  13 6  6  6  13 11 11 11
0  0  0  0  0  11 11 5  13 13 5  5  5  5  6  6  6  6  6  13 6  6  6  13 11 11 11
0  0  0  0  0  11 11 11 13 13 13 13 13 13 6  6  6  6  6  13 6  6  6  13 13 11 11
0  0  0  0  0  0  11 11 11 5  5  5  5  5  5  5  5  5  5  5  5  5  5  11 13 11 11
0  0  0  0  0  0  0  11 11 11 6  6  6  6  6  6  6  6  6  6  6  6  6  6  13 11 11
0  0  0  0  0  0  0  11 11 11 6  6  6  6  6  6  6  6  6  6  6  6  6  6  13 11 11
0  0  0  0  0  0  0  11 13 13 13 13 13 13 13 13 13 13 13 13 13 13 13 13 13 11 11
0  0  0  0  0  0  0  11 13 13 11 11 11 11 11 11 11 11 11 11 11 11 11 11 11 11 11
0  0  0  0  0  0  0  11 11 11 11 11 11 11 11 11 11 11 11 11 11 11 11 11 11 11 11
```

layer 6

```
0  0  0  0  11 11 11 11 11 11 11 11 11 11 11 11 11 11 11 11 11 11 11 11 11 11 11 11
0  0  0  0  11 11 11 5  14 14 14 11 11 11 11 11 11 11 11 11 11 11 11 11 11 11 11 11
0  0  0  0  11 11 11 5  14 14 14 11 11 11 11 11 11 11 11 11 11 11 11 11 11 11 11 11
0  0  0  0  11 11 11 5  14 14 14 11 11 13 13 13 13 13 13 13 13 13 13 11 11 11
0  0  0  0  11 11 11 5  14 14 14 11 11 13 13 13 13 13 13 13 11 11 11 13 11 11 11
0  0  0  0  11 11 11 5  14 14 14 11 11 11 13 13 11 11 11 13 11 11 11 13 11 11 11
0  0  0  0  11 11 11 5  14 14 14 11 11 13 13 13 13 11 11 11 13 11 11 11 13 11 11 11
0  0  0  0  11 11 11 5  14 14 14 11 13 13 13 13 11 11 11 13 11 11 11 13 11 11 11
0  0  0  0  11 11 11 5  14 14 14 13 13 13 13 13 11 11 11 13 11 11 11 13 11 11 11
0  0  0  0  11 11 11 5  14 14 14 5  5  5  5  13 11 11 11 13 11 11 11 13 11 11 11
0  0  0  0  11 11 11 5  14 14 5  5  5  5  11 11 11 11 11 13 11 11 11 13 11 1: 11
0  0  0  0  11 11 11 11 14 14 13 13 13 13 11 11 11 11 11 13 11 11 11 13 13 11 11
0  0  0  0  0  11 11 11 11 5  5  5  5  5  5  5  5  5  5  5  5  5  5  11 13 11 11
0  0  0  0  0  0  11 11 11 11 11 11 11 11 11 11 11 11 11 11 11 11 11 11 11 13 11 11
0  0  0  0  0  0  11 11 11 11 11 11 11 11 11 11 11 11 11 11 11 11 11 11 13 11 11
0  0  0  0  0  0  11 11 14 14 13 13 13 13 13 13 13 13 13 13 13 13 13 13 11 11
0  0  0  0  0  0  11 11 14 14 11 11 11 11 11 11 11 11 11 11 11 11 11 11 11 11 11
0  0  0  0  0  0  11 11 11 11 11 11 11 11 11 11 11 11 11 11 11 11 11 11 11 11 11
```

layer 7

```
11 11 11 11 11 11 11 11 11 11 11 11 11 11 11 11 11 11 11 11 11 11 11 11 11 11 11 11
11 11 11 11 11 11 11 11 14 14 14 11 11 11 11 11 11 11 11 11 11 11 11 11 11 11 11 11
11 11 11 11 11 11 11 11 14 14 14 11 11 11 11 11 11 11 11 11 11 11 11 11 11 11 11 11
11 11 11 11 11 11 11 11 14 14 14 11 11 14 14 14 14 14 14 14 14 14 14 14 11 11 11 11
11 11 11 11 11 11 11 11 14 14 14 11 11 14 14 14 14 14 14 14 11 11 11 14 11 11 11 11
11 11 11 11 11 11 11 11 14 14 14 11 11 11 14 14 11 11 11 14 11 11 11 14 11 11 11 11
11 11 11 11 11 11 11 11 14 14 14 11 11 14 14 14 14 11 11 11 14 11 11 11 14 11 11 11
11 11 11 11 11 11 11 11 14 14 14 11 14 14 14 14 11 11 11 14 11 11 11 14 11 11 11 11
11 11 11 11 11 11 11 11 14 14 14 14 14 14 14 14 11 11 11 14 11 11 11 14 11 11 11 11
11 11 11 11 11 11 11 11 14 14 14 8  8  8  8  14 11 11 11 14 11 11 11 14 11 11 11 11
11 11 11 11 11 11 11 11 14 14 8  8  8  8  8  11 11 11 11 14 11 11 11 14 11 11 11 11
11 11 11 11 11 11 11 11 14 14 14 14 14 14 11 11 11 11 11 14 11 11 11 14 11 11 11 11
11 11 11 11 11 11 11 11 11 8  8  8  8  8  8  8  8  8  8  8  8  8  14 14 11 11 11 11
11 11 11 11 11 11 11 11 11 11 11 11 11 11 11 11 11 11 11 11 11 11 11 11 11 14 11 11
11 11 11 11 11 11 11 11 11 11 11 11 11 11 11 11 11 11 11 11 11 11 11 11 11 14 11 11
11 11 11 11 11 11 11 11 14 14 14 14 14 14 14 14 14 14 14 14 14 14 14 14 14 14 11 11
11 11 11 11 11 11 11 11 14 14 11 11 11 11 11 11 11 11 11 11 11 11 11 11 11 11 11 11
11 11 11 11 11 11 11 11 11 11 11 11 11 11 11 11 11 11 11 11 11 11 11 11 11 11 11 11
```

layer 8

```
12 12 12 12 12 12 12 12 12 12 12 12 12 12 12 12 12 12 12 12 12 12 12 12 12 12 12 12
12 12 12 12 12 12 12 12 14 14 14 12 12 12 12 12 12 12 12 12 12 12 12 12 12 12 12 12
12 12 12 12 12 12 12 12 14 14 14 12 12 12 12 12 12 12 12 12 12 12 12 12 12 12 12 12
12 12 12 12 12 12 12 12 14 14 14 12 12 14 14 14 14 14 14 14 14 14 14 14 12 12 12 12
12 12 12 12 12 12 12 12 14 14 14 12 12 14 14 14 14 14 14 12 12 12 14 12 12 12 12 12
12 12 12 12 12 12 12 12 14 14 14 12 12 12 14 14 12 12 12 14 12 12 12 14 12 12 12 12
12 12 12 12 12 12 12 12 14 14 14 12 12 14 14 14 12 12 12 14 12 12 12 14 12 12 12 12
12 12 12 12 12 12 12 12 14 14 14 12 14 14 14 14 12 12 12 14 12 12 12 14 12 12 12 12
12 12 12 12 12 12 12 12 14 14 14 14 14 14 14 14 12 12 12 14 12 12 12 14 12 12 12 12
12 12 12 12 12 12 12 12 14 14 14 12 12 12 12 14 12 12 12 12 12 12 12 14 12 12 12 12
12 12 12 12 12 12 12 12 14 14 14 14 14 14 12 12 12 12 12 12 12 12 12 14 12 12 12 12
12 12 12 12 12 12 12 12 12 12 12 12 12 12 12 12 12 12 12 12 12 12 12 14 14 12 12 12
12 12 12 12 12 12 12 12 12 12 12 12 12 12 12 12 12 12 12 12 12 12 12 12 14 12 12 12
12 12 12 12 12 12 12 12 12 12 12 12 12 12 12 12 12 12 12 12 12 12 12 12 14 12 12 12
12 12 12 12 12 12 12 12 14 14 14 14 14 14 14 14 14 14 14 14 14 14 14 14 14 12 12 12
12 12 12 12 12 12 12 12 14 14 12 12 12 12 12 12 12 12 12 12 12 12 12 12 12 12 12 12
12 12 12 12 12 12 12 12 12 12 12 12 12 12 12 12 12 12 12 12 12 12 12 12 12 12 12 12
```

layer 9

```
18 18 18 18 18 18 18 18 18 18 18 18 18 18 18 18 18 18 18 18 18 18 18 18 18 18 18 18
18 18 18 18 18 18 18 18 18 18 18 15 15 15 15 15 15 15 15 15 15 15 15 15 15 15 15 18
18 18 18 18 18 18 18 13 18 18 18 15 15 14 14 14 14 14 14 14 14 14 14 14 14 14 15 18
18 18 18 18 18 18 18 13 18 18 18 15 15 14 14 14 14 14 14 14 14 14 14 14 14 14 15 18
18 18 18 18 18 18 18 13 18 18 18 14 14 14 14 14 14 14 14 14 14 14 14 14 14 14 15 18
18 18 18 18 18 18 18 13 18 18 18 14 14 14 14 14 13 13 13 14 14 14 14 14 14 14 15 18
18 18 18 18 18 18 18 13 18 18 18 14 14 14 14 14 13 13 13 14 14 14 14 14 14 14 15 18
18 18 18 18 18 18 18 13 18 18 18 14 14 14 14 14 13 13 13 14 14 14 14 14 14 14 15 18
18 18 18 18 18 18 18 18 18 18 18 14 14 14 14 14 14 14 14 14 14 14 14 14 14 14 15 18
18 18 18 18 18 18 18 18 18 15 15 15 15 15 15 15 15 15 15 15 15 14 14 14 14 14 15 18
18 18 18 18 18 18 18 18 18 14 15 18 18 18 18 18 15 15 15 15 15 15 14 14 14 14 15 18
18 18 18 18 18 18 18 18 18 14 15 18 18 18 18 18 15 15 15 15 15 15 14 14 14 14 15 18
18 18 18 18 18 18 18 18 18 14 15 18 18 18 18 18 15 15 15 15 15 15 14 14 14 14 15 18
18 18 18 18 18 18 18 18 18 14 15 18 18 18 18 18 15 15 15 15 15 15 15 15 15 15 15 18
18 18 18 18 18 18 18 18 18 18 18 18 18 18 18 18 18 18 18 18 18 18 18 18 18 18 18 18
```

layer 10

```
18 18 18 18 18 18 18 18 18 18 18 18 18 18 18 18 18 18 18 18 18 18 18 18 18 18 18 18
18 18 18 18 18 18 18 18 18 18 18 15 15 15 15 15 15 15 15 15 15 15 15 15 15 15 15 18
18 18 18 18 18 18 18 13 18 18 18 15 15 14 14 14 14 14 14 14 14 14 14 14 14 14 15 18
18 18 18 18 18 18 18 13 18 18 18 15 15 14 14 14 14 14 14 14 14 14 14 14 14 14 15 18
18 18 18 18 18 18 18 13 18 18 18 14 14 14 14 14 14 14 14 14 14 14 14 14 14 14 15 18
18 18 18 18 18 18 18 13 18 18 18 14 14 14 14 14 13 13 13 14 14 14 14 14 14 14 15 18
18 18 18 18 18 18 18 13 18 18 18 14 14 14 14 14 13 13 13 14 14 14 14 14 14 14 15 18
18 18 18 18 18 18 18 13 18 18 18 14 14 14 14 14 13 13 13 14 14 14 14 14 14 14 15 18
18 18 18 18 18 18 18 13 18 18 18 14 14 14 14 14 14 14 14 14 14 14 14 14 14 14 15 18
18 18 18 18 18 18 18 18 18 18 18 14 14 14 14 14 14 14 14 14 14 14 14 14 14 14 15 18
18 18 18 18 18 18 18 18 18 15 15 15 15 15 15 15 15 15 15 15 15 14 14 14 14 14 15 18
18 18 18 18 18 18 18 18 18 14 15 18 18 18 18 15 15 15 15 15 15 14 14 14 14 14 15 18
18 18 18 18 18 18 18 18 18 14 15 18 18 18 18 15 15 15 15 15 15 14 14 14 14 14 15 18
18 18 18 18 18 18 18 18 18 14 15 18 18 18 18 15 15 15 15 15 15 14 14 14 14 14 15 18
18 18 18 18 18 18 18 18 18 14 15 18 18 18 18 15 15 15 15 15 15 14 14 14 14 14 15 18
18 18 18 18 18 18 18 18 18 14 15 18 18 18 18 15 15 15 15 15 15 14 14 14 14 14 15 18
18 18 18 18 18 18 18 18 18 14 15 18 18 18 18 15 15 15 15 15 15 15 15 15 15 15 15 18
18 18 18 18 18 18 18 18 18 18 18 18 18 18 18 18 18 18 18 18 18 18 18 18 18 18 18 18
```

layer 11

```
15 15 15 15 15 15 15 15 15 15 15 15 15 15 15 15 15 15 15 15 15 15 15 15 15 15 15 15
15 15 15 15 15 15 15 15 15 15 15 14 14 14 14 14 14 14 14 14 14 14 14 14 14 14 14 15
15 15 15 15 15 15 15 12 15 15 15 14 14 14 13 13 13 13 13 13 13 13 13 13 13 13 14 15
15 15 15 15 15 15 15 12 15 15 15 14 14 14 13 13 13 13 13 13 13 13 13 13 13 13 14 15
15 15 15 15 15 15 15 12 15 15 15 14 14 14 13 13 13 13 13 13 13 13 13 13 13 13 14 15
15 15 15 15 15 15 15 12 15 15 15 13 13 13 13 13 13 12 12 12 13 13 13 13 13 13 14 15
15 15 15 15 15 15 15 12 15 15 15 13 13 13 13 13 13 12 12 12 13 13 13 13 13 13 14 15
15 15 15 15 15 15 15 12 15 15 15 14 14 14 13 13 12 12 12 13 13 13 13 13 13 14 15
15 15 15 15 15 15 15 12 15 15 15 14 14 14 13 13 13 13 13 13 13 13 13 13 13 13 14 15
15 15 15 15 15 15 15 15 15 15 15 14 14 14 14 14 14 14 14 14 14 14 14 14 14 14 14 15
15 15 15 15 15 15 15 15 15 15 15 14 14 14 14 14 14 14 14 14 14 14 14 14 14 14 14 15
15 15 15 15 15 15 15 15 15 15 15 15 15 15 15 15 14 14 14 14 14 14 14 14 14 14 14 15
15 15 15 15 15 15 15 15 15 15 15 15 15 15 15 15 14 14 14 14 14 14 14 14 14 14 14 15
15 15 15 15 15 15 15 15 15 15 15 15 15 15 15 15 14 14 14 14 14 14 14 14 14 14 14 15
15 15 15 15 15 15 15 15 15 15 15 15 15 15 15 15 14 14 14 14 14 14 14 14 14 14 14 15
15 15 15 15 15 15 15 15 15 15 15 15 15 15 15 15 14 14 14 14 14 14 14 14 14 14 14 15
15 15 15 15 15 15 15 15 15 15 15 15 15 15 15 15 14 14 14 14 14 14 14 14 14 14 14 15
15 15 15 15 15 15 15 15 15 15 15 15 15 15 15 15 15 15 15 15 15 15 15 15 15 15 15 15
```

layer 12

```
10 10 10 10 10 10 10 10 10 10 10 10 10 10 10 10 10 10 10 10 10 10 10 10 10 10 10 10
10 10 10 10 10 10 10 10 10 10 10 10 10 10 10 10 10 10 10 10 10 10 10 10 10 10 10 10
10 10 10 10 10 10 10 10 10 10 10 10 10 10 10 10 10 10 10 10 10 10 10 10 10 10 10 10
10 10 10 10 10 10 10 10 10 10 10 10 10 10 10 10 10 10 10 10 10 10 10 10 10 10 10 10
10 10 10 10 10 10 10 10 10 10 10 10 10 10 10 10 10 10 10 10 10 10 10 10 10 10 10 10
10 10 10 10 10 10 10 10 10 10 10 10 10 10 10 10 10 10 10 10 10 10 10 10 10 10 10 10
10 10 10 10 10 10 10 10 10 10 10 10 10 10 10 10 10 10 10 10 10 10 10 10 10 10 10 10
10 10 10 10 10 10 10 10 10 10 10 10 10 10 10 10 10 10 10 10 10 10 10 10 10 10 10 10
10 10 10 10 10 10 10 10 10 10 10 10 10 10 10 10 10 10 10 10 10 10 10 10 10 10 10 10
10 10 10 10 10 10 10 10 10 10 10 10 10 10 10 10 10 10 10 10 10 10 10 10 10 10 10 10
10 10 10 10 10 10 10 10 10 10 10 10 10 10 10 10 10 10 10 10 10 10 10 10 10 10 10 10
10 10 10 10 10 10 10 10 10 10 10 10 10 10 10 10 10 10 10 10 10 10 10 10 10 10 10 10
10 10 10 10 10 10 10 10 10 10 10 10 10 10 10 10 10 10 10 10 10 10 10 10 10 10 10 10
10 10 10 10 10 10 10 10 10 10 10 10 10 10 10 10 10 10 10 10 10 10 10 10 10 10 10 10
10 10 10 10 10 10 10 10 10 10 10 10 10 10 10 10 10 10 10 10 10 10 10 10 10 10 10 10
10 10 10 10 10 10 10 10 10 10 10 10 10 10 10 10 10 10 10 10 10 10 10 10 10 10 10 10
10 10 10 10 10 10 10 10 10 10 10 10 10 10 10 10 10 10 10 10 10 10 10 10 10 10 10 10
10 10 10 10 10 10 10 10 10 10 10 10 10 10 10 10 10 10 10 10 10 10 10 10 10 10 10 10
```

layer 13

8 8 8 8 8 8 8 8 8 8 8 8 8 8 8 8 8 8 8 8 8 8 8 8 8 8
8 8 8 8 8 8 8 8 8 8 8 8 8 8 8 8 8 8 8 8 8 8 8 8 8 8
8 8 8 8 8 8 8 8 8 8 8 8 8 8 8 8 8 8 8 8 8 8 8 8 8 8
8 8 8 8 8 8 8 8 8 8 8 8 8 8 8 8 8 8 8 8 8 8 8 8 8 8
8 8 8 8 8 8 8 8 8 8 8 8 8 8 8 8 8 8 8 8 8 8 8 8 8 8
8 8 8 8 8 8 8 8 8 8 8 8 8 8 8 8 8 8 8 8 8 8 8 8 8 8
8 8 8 8 8 8 8 8 8 8 8 8 8 8 8 8 8 8 8 8 8 8 8 8 8 8
8 8 8 8 8 8 8 8 8 8 8 8 8 8 8 8 8 8 8 8 8 8 8 8 8 8
8 8 8 8 8 8 8 8 8 8 8 8 8 8 8 8 8 8 8 8 8 8 8 8 8 8
8 8 8 8 8 8 8 8 8 8 8 8 8 8 8 8 8 8 8 8 8 8 8 8 8 8
8 8 8 8 8 8 8 8 8 8 8 8 8 8 8 8 8 8 8 8 8 8 8 8 8 8
8 8 8 8 8 8 8 8 8 8 8 8 8 8 8 8 8 8 8 8 8 8 8 8 8 8
8 8 8 8 8 8 8 8 8 8 8 8 8 8 8 8 8 8 8 8 8 8 8 8 8 8
8 8 8 8 8 8 8 8 8 8 8 8 8 8 8 8 8 8 8 8 8 8 8 8 8 8
8 8 8 8 8 8 8 8 8 8 8 8 8 8 8 8 8 8 8 8 8 8 8 8 8 8
8 8 8 8 8 8 8 8 8 8 8 8 8 8 8 8 8 8 8 8 8 8 8 8 8 8
8 8 8 8 8 8 8 8 8 8 8 8 8 8 8 8 8 8 8 8 8 8 8 8 8 8
8 8 8 8 8 8 8 8 8 8 8 8 8 8 8 8 8 8 8 8 8 8 8 8 8 8

## *Appendix B*

In this appendix, we present the second 3D model for which model predictions are shown earlier in the chapter. Again, a resistivity map is presented for each layer of the model. The dimensions and resistivities given in Appendix A apply here also and will not be repeated.

layer 1

```
0  0  0  0  0  0  8  8  8  8  8  8  8  8  8  8  8  8  8  8  8  8  8  8  8  8
0  0  0  0  0  0  8  3  13 13 13 8  8  8  8  8  8  8  8  8  8  8  8  8  8  8
0  0  0  0  0  0  8  3  13 13 13 8  8  8  8  8  8  8  8  8  8  8  8  8  8  8
0  0  0  0  0  0  8  3  13 13 13 6  6  8  8  8  12 12 12 12 12 12 12 8  8  8
0  0  0  0  0  0  8  3  13 13 13 6  6  8  8  8  12 12 12 12 5  5  5  12 8  8
0  0  0  0  0  0  8  3  13 13 13 5  5  5  8  8  7  7  7  12 5  5  5  12 8  8
0  0  0  0  0  0  8  3  13 13 13 5  5  8  5  8  7  7  7  12 5  5  5  12 8  8
0  0  0  0  0  0  8  3  13 13 13 5  8  8  8  12 7  7  7  12 5  5  5  12 8  8
0  0  0  0  0  0  8  3  13 13 13 8  8  8  8  12 7  7  7  12 5  5  5  12 8  8
0  0  0  0  0  0  8  3  13 13 13 5  5  5  5  12 7  7  7  12 5  5  5  12 8  8
0  0  0  0  0  0  8  3  13 13 5  5  5  5  5  7  7  7  7  12 5  5  5  12 8  8
0  0  0  0  0  0  8  8  13 13 12 12 12 12 7  7  7  7  7  12 6  6  6  12 8  8
0  0  0  0  0  0  0  8  8  6  6  6  6  6  6  6  6  6  6  6  6  6  6  12 12 8
0  0  0  0  0  0  0  0  8  8  6  6  6  6  6  6  6  6  6  6  6  6  6  6  12 8
0  0  0  0  0  0  0  0  8  8  6  6  6  6  6  6  6  6  6  6  6  6  6  6  12 8
0  0  0  0  0  0  0  0  12 12 9  9  9  9  9  9  9  9  9  9  9  9  9  11 8  8
0  0  0  0  0  0  0  0  12 12 8  8  8  8  8  8  8  8  8  8  8  8  8  8  8  8
0  0  0  0  0  0  0  0  8  8  8  8  8  8  8  8  3  8  8  8  8  8  8  8  8  8
```

layer 2

```
0  0  0  0  0  0  8  8  8  8  8  8  8  8  8  8  8  8  8  8  8  8  8  8  8  8
0  0  0  0  0  0  8  3  13 13 13 8  8  8  8  8  8  8  8  8  8  8  8  8  8  8
0  0  0  0  0  0  8  3  13 13 13 8  8  8  8  8  8  8  8  8  8  8  8  8  8  8
0  0  0  0  0  0  8  3  13 13 13 5  5  11 11 12 12 12 12 12 12 12 12 8  8  8
0  0  0  0  0  0  8  3  13 13 13 5  5  11 11 12 12 12 12 12 5  5  5  12 8  8
0  0  0  0  0  0  8  3  13 13 13 5  5  5  11 12 3  3  3  12 5  5  5  12 8  8
0  0  0  0  0  0  8  3  13 13 13 5  5  11 11 12 3  3  3  12 5  5  5  12 8  8
0  0  0  0  0  0  8  3  13 13 13 5  11 11 11 12 5  5  5  12 5  5  5  12 8  8
0  0  0  0  0  0  8  3  13 13 13 11 11 11 11 12 5  5  5  12 5  5  5  12 8  8
0  0  0  0  0  0  8  3  13 13 13 5  5  5  5  12 5  5  5  12 5  5  5  12 8  8
0  0  0  0  0  0  8  3  13 13 5  5  5  5  5  5  5  5  5  12 5  5  5  12 8  8
0  0  0  0  0  0  8  8  13 13 12 12 12 12 5  5  5  5  5  12 6  6  6  12 8  8
0  0  0  0  0  0  0  8  8  6  6  6  6  6  6  6  6  6  6  6  6  6  6  12 12 8
0  0  0  0  0  0  0  0  8  8  6  6  6  6  6  6  6  6  6  6  6  6  6  6  12 8
0  0  0  0  0  0  0  0  8  8  6  6  6  6  6  6  6  6  6  6  6  6  6  6  12 8
0  0  0  0  0  0  0  0  12 12 12 12 12 12 12 12 12 12 12 12 12 12 12 12 12 8
0  0  0  0  0  0  0  0  12 12 8  8  8  8  8  8  8  8  8  8  8  8  8  8  8  8
0  0  0  0  0  0  0  0  8  8  8  8  8  8  8  8  8  8  8  8  8  8  8  8  8  8
```

layer 3

```
0  0  0  0  0  0  8  8  8  8  8  8  8  8  8  8  8  8  8  8  8  8  8  8  8  8
0  0  0  0  0  0  8  3  13 13 13 8  8  8  8  8  8  8  8  8  8  8  8  8  8  8
0  0  0  0  0  0  8  3  13 13 13 8  8  8  8  8  8  8  8  8  8  8  8  8  8  8
0  0  0  0  0  0  8  3  13 13 13 0  0  12 12 12 12 12 12 12 12 12 12 8  8  8
0  0  0  0  0  0  8  3  13 13 13 0  0  12 12 12 12 12 12 12 3  3  3  12 8  8
0  0  0  0  0  0  8  3  13 13 13 0  0  0  12 12 4  4  4  12 3  3  3  12 8  8
0  0  0  0  0  0  8  3  13 13 13 0  0  12 12 12 4  4  4  12 3  3  3  12 8  8
0  0  0  0  0  0  8  3  13 13 13 3  12 12 12 12 3  3  3  12 3  3  3  12 8  8
0  0  0  0  0  0  8  3  13 13 13 12 12 12 12 12 3  3  3  12 3  3  3  12 8  8
0  0  0  0  0  0  8  3  13 13 13 5  5  5  5  12 3  3  3  12 3  3  3  12 8  8
0  0  0  0  0  0  8  3  13 13 5  5  5  5  5  12 3  3  3  12 3  3  3  12 8  8
0  0  0  0  0  0  8  8  13 13 12 12 12 12 3  3  3  3  3  12 8  8  8  12 12 8
0  0  0  0  0  0  0  0  8  8  8  8  8  8  8  8  8  8  8  8  8  8  8  8  12 8
0  0  0  0  0  0  0  0  8  8  8  8  8  8  8  8  8  8  8  8  8  8  8  8  12 8
0  0  0  0  0  0  0  0  8  8  8  8  8  8  8  8  8  8  8  8  8  8  8  8  12 8
0  0  0  0  0  0  0  0  12 12 12 12 12 12 12 12 12 12 12 12 12 12 12 12 12 8
0  0  0  0  0  0  0  0  12 12 8  8  8  8  8  8  8  8  8  8  8  8  8  8  8  8
0  0  0  0  0  0  0  0  8  8  8  8  8  8  8  8  8  8  8  8  8  8  8  8  8  8
```

layer 4

```
0  0  0  0  0  0  11 11 11 11 11 11 11 11 11 11 11 11 11 11 11 11 11 11 11 11 11
0  0  0  0  0  0  11 5  13 13 13 11 11 11 11 11 11 11 11 11 11 11 11 11 11 11 11
0  0  0  0  0  0  11 5  13 13 13 11 11 11 11 11 11 11 11 11 11 11 11 11 11 11 11
0  0  0  0  0  0  11 5  13 13 13 5  5  12 12 12 12 12 12 12 12 12 12 11 11 11
0  0  0  0  0  0  11 5  13 13 13 5  5  12 12 12 12 12 12 12 5  5  5  12 11 11 11
0  0  0  0  0  0  11 5  13 13 13 5  5  5  12 12 8  8  8  12 5  5  5  12 11 11 11
0  0  0  0  0  0  11 5  13 13 13 5  5  12 12 12 8  8  8  12 5  5  5  12 11 11 11
0  0  0  0  0  0  11 5  13 13 13 5  12 12 12 12 5  5  5  12 5  5  5  12 11 11 11
0  0  0  0  0  0  11 5  13 13 13 12 12 12 12 12 5  5  5  12 5  5  5  12 11 11 11
0  0  0  0  0  0  11 5  13 13 13 5  5  5  5  12 5  5  5  12 5  5  5  12 11 11 11
0  0  0  0  0  0  11 5  13 13 5  5  5  5  5  5  5  5  5  12 5  5  5  12 11 11 11
0  0  0  0  0  0  11 11 13 13 12 12 12 12 5  5  5  5  5  12 9  9  9  12 12 11 11
0  0  0  0  0  0  0  11 11 9  9  9  9  9  9  9  9  9  9  9  9  9  9  11 12 11 11
0  0  0  0  0  0  0  0  11 11 9  9  9  9  9  9  9  9  9  9  9  9  9  11 12 11 11
0  0  0  0  0  0  0  0  11 11 9  9  9  9  9  9  9  9  9  9  9  9  9  11 12 11 11
0  0  0  0  0  0  0  0  12 12 12 12 12 12 12 12 12 12 12 12 12 12 12 12 12 11 11
0  0  0  0  0  0  0  0  12 12 11 11 11 11 11 11 11 11 11 11 11 11 11 11 11 11 11
0  0  0  0  0  0  0  0  11 11 11 11 11 11 11 11 11 11 11 11 11 11 11 11 11 11 11
```

layer 5

```
0  0  0  0  0  11 11 11 11 11 11 11 11 11 11 11 11 11 11 11 11 11 11 11 11 11 11
0  0  0  0  0  11 11 5  13 13 13 11 11 11 11 11 11 11 11 11 11 11 11 11 11 11 11
0  0  0  0  0  11 11 5  13 13 13 11 11 11 11 11 11 11 11 11 11 11 11 11 11 11 11
0  0  0  0  0  11 11 5  13 13 13 6  6  13 13 13 13 13 13 13 13 13 13 11 11 11
0  0  0  0  0  11 11 5  13 13 13 6  6  13 13 13 13 13 13 13 6  6  6  13 11 11 11
0  0  0  0  0  11 11 5  13 13 13 6  6  6  13 13 9  9  9  13 6  6  6  13 11 11 11
0  0  0  0  0  11 11 5  13 13 13 6  6  13 13 13 9  9  9  13 6  6  6  13 11 11 11
0  0  0  0  0  11 11 5  13 13 13 6  13 13 13 13 6  6  6  13 6  6  6  13 11 11 11
0  0  0  0  0  11 11 5  13 13 13 13 13 13 13 13 6  6  6  13 6  6  6  13 11 11 11
0  0  0  0  0  11 11 5  13 13 13 5  5  5  5  13 6  6  6  13 6  6  6  13 11 11 11
0  0  0  0  0  11 11 5  13 13 5  5  5  5  6  6  6  6  6  13 6  6  6  13 11 11 11
0  0  0  0  0  11 11 11 13 13 13 13 13 13 6  6  6  6  6  13 11 11 11 13 13 11 11
0  0  0  0  0  0  11 11 11 11 11 11 11 11 11 11 11 11 11 11 11 11 11 11 11 11 11
0  0  0  0  0  0  0  11 11 11 11 11 11 11 11 11 11 11 11 11 11 11 11 11 11 13 11
0  0  0  0  0  0  0  11 11 11 11 11 11 11 11 11 11 11 11 11 11 11 11 11 11 13 11
0  0  0  0  0  0  0  11 13 13 13 13 13 13 13 13 13 13 13 13 13 13 13 13 13 11 11
0  0  0  0  0  0  0  11 13 13 11 11 11 11 11 11 11 11 11 11 11 11 11 11 11 11 11
0  0  0  0  0  0  0  11 11 11 11 11 11 11 11 11 11 11 11 11 11 11 11 11 11 11 11
```

layer 6

```
0  0  0  0  11 11 11 11 11 11 11 11 11 11 11 11 11 11 11 11 11 11 11 11 11 11 11
0  0  0  0  11 11 11 5  14 14 14 11 11 11 11 11 11 11 11 11 11 11 11 11 11 11 11
0  0  0  0  11 11 11 5  14 14 14 11 11 11 11 11 11 11 11 11 11 11 11 11 11 11 11
0  0  0  0  11 11 11 5  14 14 14 11 11 13 13 13 13 13 13 13 13 13 13 11 11 11
0  0  0  0  11 11 11 5  14 14 14 11 11 13 13 13 13 13 13 11 11 11 13 11 11 11
0  0  0  0  11 11 11 5  14 14 14 11 11 13 13 13 11 11 11 13 11 11 13 11 11 11
0  0  0  0  11 11 11 5  14 14 14 11 11 13 13 13 11 11 11 13 11 11 13 11 11 11
0  0  0  0  11 11 11 5  14 14 14 11 13 13 13 13 11 11 11 13 11 11 13 11 11 11
0  0  0  0  11 11 11 5  14 14 14 13 13 13 13 13 11 11 11 13 11 11 13 11 11 11
0  0  0  0  11 11 11 5  14 14 14 5  5  5  5  13 11 11 11 13 11 11 13 11 11 11
0  0  0  0  11 11 11 5  14 14 5  5  5  5  11 11 11 11 11 13 11 11 13 11 11 11
0  0  0  0  11 11 11 11 14 14 13 13 13 13 11 11 11 11 11 13 11 11 13 13 11 11
0  0  0  0  0  11 11 11 11 11 11 11 11 11 11 11 11 11 11 11 11 11 11 13 11 11
0  0  0  0  0  0  11 11 11 11 11 11 11 11 11 11 11 11 11 11 11 11 11 13 11 11
0  0  0  0  0  0  11 11 11 11 11 11 11 11 11 11 11 11 11 11 11 11 11 13 11 11
0  0  0  0  0  0  11 11 14 14 13 13 13 13 13 13 13 13 13 13 13 13 13 13 11 11
0  0  0  0  0  0  11 11 14 14 11 11 11 11 11 11 11 11 11 11 11 11 11 11 11 11
0  0  0  0  0  0  11 11 11 11 11 11 11 11 11 11 11 11 11 11 11 11 11 11 11 11
```

layer 7

```
11 11 11 11 11 11 11 11 11 11 11 11 11 11 11 11 11 11 11 11 11 11 11 11 11 11 11 11 11
11 11 11 11 11 11 11 11 14 14 14 11 11 11 11 11 11 11 11 11 11 11 11 11 11 11 11 11 11
11 11 11 11 11 11 11 11 14 14 14 11 11 11 11 11 11 11 11 11 11 11 11 11 11 11 11 11 11
11 11 11 11 11 11 11 11 14 14 14 11 11 14 14 14 14 14 14 14 14 14 14 14 14 11 11 11 11
11 11 11 11 11 11 11 11 14 14 14 11 11 14 14 14 14 14 14 14 11 11 11 14 11 11 11 11 11
11 11 11 11 11 11 11 11 14 14 14 11 11 11 14 14 11 11 11 14 11 11 11 14 11 11 11 11 11
11 11 11 11 11 11 11 11 14 14 14 11 11 14 14 14 11 11 11 14 11 11 11 14 11 11 11 11 11
11 11 11 11 11 11 11 11 14 14 14 11 14 14 14 14 11 11 11 14 11 11 11 14 11 11 11 11 11
11 11 11 11 11 11 11 11 14 14 14 14 14 14 14 14 11 11 11 14 11 11 11 14 11 11 11 11 11
11 11 11 11 11 11 11 11 14 14 14 8  8  8  8  14 11 11 11 14 11 11 11 14 11 11 11 11 11
11 11 11 11 11 11 11 11 14 14 8  8  8  8  8  11 11 11 11 14 11 11 11 14 11 11 11 11 11
11 11 11 11 11 11 11 11 14 14 14 14 14 14 11 11 11 11 11 14 11 11 11 14 11 11 11 11 11
11 11 11 11 11 11 11 11 11 11 11 11 11 11 11 11 11 11 11 11 11 11 11 11 11 14 14 11 11
11 11 11 11 11 11 11 11 11 11 11 11 11 11 11 11 11 11 11 11 11 11 11 11 11 14 14 11 11
11 11 11 11 11 11 11 11 11 11 11 11 11 11 11 11 11 11 11 11 11 11 11 11 11 14 14 11 11
11 11 11 11 11 11 11 11 14 14 14 14 14 14 14 14 14 14 14 14 14 14 14 14 14 14 14 11 11
11 11 11 11 11 11 11 11 14 14 11 11 11 11 11 11 11 11 11 11 11 11 11 11 11 11 11 11 11
11 11 11 11 11 11 11 11 11 11 11 11 11 11 11 11 11 11 11 11 11 11 11 11 11 11 11 11 11
```

layer 8

```
12 12 12 12 12 12 12 12 12 12 12 12 12 12 12 12 12 12 12 12 12 12 12 12 12 12 12 12 12
12 12 12 12 12 12 12 12 14 14 14 12 12 12 12 12 12 12 12 12 12 12 12 12 12 12 12 12 12
12 12 12 12 12 12 12 12 14 14 14 12 12 12 12 12 12 12 12 12 12 12 12 12 12 12 12 12 12
12 12 12 12 12 12 12 12 14 14 14 12 12 14 14 14 14 14 14 14 14 14 14 14 14 12 12 12 12
12 12 12 12 12 12 12 12 14 14 14 12 12 14 14 14 14 14 14 14 12 12 12 14 12 12 12 12 12
12 12 12 12 12 12 12 12 14 14 14 12 12 12 14 14 12 12 12 14 12 12 12 14 12 12 12 12 12
12 12 12 12 12 12 12 12 14 14 14 12 12 14 14 14 12 12 12 14 12 12 12 14 12 12 12 12 12
12 12 12 12 12 12 12 12 14 14 14 12 14 14 14 14 12 12 12 14 12 12 12 14 12 12 12 12 12
12 12 12 12 12 12 12 12 14 14 14 14 14 14 14 14 14 12 12 14 12 12 12 14 12 12 12 12 12
12 12 12 12 12 12 12 12 14 14 14 12 12 12 12 12 12 12 12 12 12 12 12 12 12 14 12 12 12
12 12 12 12 12 12 12 12 14 14 12 12 12 12 12 12 12 12 12 12 12 12 12 12 12 14 12 12 12
12 12 12 12 12 12 12 12 14 14 14 14 14 14 12 12 12 12 12 12 12 12 12 12 12 14 12 12 12
12 12 12 12 12 12 12 12 12 12 12 12 12 12 12 12 12 12 12 12 12 12 12 12 12 14 14 12 12
12 12 12 12 12 12 12 12 12 12 12 12 12 12 12 12 12 12 12 12 12 12 12 12 12 12 14 12 12
12 12 12 12 12 12 12 12 12 12 12 12 12 12 12 12 12 12 12 12 12 12 12 12 12 14 12 12 12
12 12 12 12 12 12 12 12 14 14 14 14 14 14 14 14 14 14 14 14 14 14 14 14 14 14 14 12 12
12 12 12 12 12 12 12 12 14 14 12 12 12 12 12 12 12 12 12 12 12 12 12 12 12 12 12 12 12
12 12 12 12 12 12 12 12 12 12 12 12 12 12 12 12 12 12 12 12 12 12 12 12 12 12 12 12 12
```

layer 9

```
18 18 18 18 18 18 18 18 18 18 18 18 18 18 18 18 18 18 18 18 18 18 18 18 18 18 18 18 18
18 18 18 18 18 18 18 18 18 18 18 15 15 15 15 15 15 15 15 15 15 15 15 15 15 15 15 15 18
18 18 18 18 18 18 18 13 18 18 18 15 15 14 14 14 14 14 14 14 14 14 14 14 14 14 15 15 18
18 18 18 18 18 18 18 13 18 18 18 15 15 14 14 14 14 14 14 14 14 14 14 14 14 14 15 15 18
18 18 18 18 18 18 18 13 18 18 18 14 14 14 14 14 14 14 14 14 14 14 14 14 14 14 15 15 18
18 18 18 18 18 18 18 13 18 18 18 14 14 14 14 14 14 13 13 13 14 14 14 14 14 14 15 15 18
18 18 18 18 18 18 18 13 18 18 18 14 14 14 14 14 14 13 13 13 14 14 14 14 14 14 15 15 18
18 18 18 18 18 18 18 13 18 18 18 14 14 14 14 14 14 13 13 13 14 14 14 14 14 14 15 15 18
18 18 18 18 18 18 18 13 18 18 18 14 14 14 14 14 14 14 14 14 14 14 14 14 14 14 15 15 18
18 18 18 18 18 18 18 18 18 18 18 18 14 14 14 14 14 14 14 14 14 14 14 14 14 14 15 15 18
18 18 18 18 18 18 18 18 18 15 15 15 14 14 14 14 14 14 14 14 14 14 14 14 14 14 15 15 18
18 18 18 18 18 18 18 18 18 15 15 15 15 14 14 14 14 14 14 14 14 14 14 14 14 14 15 15 18
18 18 18 18 18 18 18 18 18 15 15 15 15 15 14 14 14 14 14 14 14 14 14 14 14 14 15 15 18
18 18 18 18 18 18 18 18 18 15 15 15 15 15 15 14 14 14 14 14 14 14 14 14 14 14 15 15 18
18 18 18 18 18 18 18 18 18 15 15 15 15 15 15 15 15 15 15 15 15 14 14 14 14 14 15 15 18
18 18 18 18 18 18 18 18 18 15 15 15 15 15 15 15 15 15 15 15 15 15 15 15 15 15 15 15 18
18 18 18 18 18 18 18 18 18 18 18 18 18 18 18 18 18 18 18 18 18 18 18 18 18 18 18 18 18
```

layer 10

```
18 18 18 18 18 18 18 18 18 18 18 18 18 18 18 18 18 18 18 18 18 18 18 18 18 18 18
18 18 18 18 18 18 18 18 18 18 18 15 15 15 15 15 15 15 15 15 15 15 15 15 15 15 18
18 18 18 18 18 18 18 13 18 18 18 15 15 14 14 14 14 14 14 14 14 14 14 14 14 15 18
18 18 18 18 18 18 18 13 18 18 18 15 15 14 14 14 14 14 14 14 14 14 14 14 14 15 18
18 18 18 18 18 18 18 13 18 18 18 14 14 14 14 14 14 14 14 14 14 14 14 14 14 15 18
18 18 18 18 18 18 18 13 18 18 18 14 14 14 14 14 13 13 13 14 14 14 14 14 14 15 18
18 18 18 18 18 18 18 13 18 18 18 14 14 14 14 14 13 13 13 14 14 14 14 14 14 15 18
18 18 18 18 18 18 18 13 18 18 18 14 14 14 14 14 13 13 13 14 14 14 14 14 14 15 18
18 18 18 18 18 18 18 13 18 18 18 14 14 14 14 14 14 14 14 14 14 14 14 14 14 15 18
18 18 18 18 18 18 18 18 18 18 18 14 14 14 14 14 14 14 14 14 14 14 14 14 14 15 18
18 18 18 18 18 18 18 18 18 15 15 15 14 14 14 14 14 14 14 14 14 14 14 14 14 15 18
18 18 18 18 18 18 18 18 18 15 15 15 15 14 14 14 14 14 14 14 14 14 14 14 14 15 18
18 18 18 18 18 18 18 18 18 15 15 15 15 15 14 14 14 14 14 14 14 14 14 14 14 15 18
18 18 18 18 18 18 18 18 18 15 15 15 15 15 15 15 15 15 15 15 14 14 14 14 14 15 18
18 18 18 18 18 18 18 18 18 15 15 15 15 15 15 15 15 15 15 15 15 15 15 15 15 15 18
18 18 18 18 18 18 18 18 18 18 18 18 18 18 18 18 18 18 18 18 18 18 18 18 18 18 18
```

layer 11

```
15 15 15 15 15 15 15 15 15 15 15 15 15 15 15 15 15 15 15 15 15 15 15 15 15 15 15
15 15 15 15 15 15 15 15 15 15 15 14 14 14 14 14 14 14 14 14 14 14 14 14 14 14 15
15 15 15 15 15 15 15 12 15 15 15 14 14 14 13 13 13 13 13 13 13 13 13 13 13 14 15
15 15 15 15 15 15 15 12 15 15 15 14 14 14 13 13 13 13 13 13 13 13 13 13 13 14 15
15 15 15 15 15 15 15 12 15 15 15 14 14 14 13 13 13 13 13 13 13 13 13 13 13 14 15
15 15 15 15 15 15 15 12 15 15 15 13 13 13 13 13 12 12 12 13 13 13 13 13 13 14 15
15 15 15 15 15 15 15 12 15 15 15 13 13 13 13 13 12 12 12 13 13 13 13 13 13 14 15
15 15 15 15 15 15 15 12 15 15 15 14 14 14 13 13 12 12 12 13 13 13 13 13 13 14 15
15 15 15 15 15 15 15 12 15 15 15 14 14 14 13 13 13 13 13 13 13 13 13 13 13 14 15
15 15 15 15 15 15 15 15 15 15 15 14 14 14 14 14 13 13 13 13 13 13 13 13 13 14 15
15 15 15 15 15 15 15 15 15 15 15 14 14 14 14 14 14 13 13 13 13 13 13 13 13 14 15
15 15 15 15 15 15 15 15 15 15 15 14 14 14 14 14 14 14 13 13 13 13 13 13 13 14 15
15 15 15 15 15 15 15 15 15 15 15 14 14 14 14 14 14 14 14 13 13 13 13 13 13 14 15
15 15 15 15 15 15 15 15 15 15 15 14 14 14 14 14 14 14 14 14 14 14 14 14 14 14 15
15 15 15 15 15 15 15 15 15 15 15 14 14 14 14 14 14 14 14 14 14 14 14 14 14 14 15
15 15 15 15 15 15 15 15 15 15 15 14 14 14 14 14 14 14 14 14 14 14 14 14 14 14 15
15 15 15 15 15 15 15 15 15 15 15 15 15 15 15 15 15 15 15 15 15 15 15 15 15 15 15
```

layer 12

```
10 10 10 10 10 10 10 10 10 10 10 10 10 10 10 10 10 10 10 10 10 10 10 10 10 10 10
10 10 10 10 10 10 10 10 10 10 10 10 10 10 10 10 10 10 10 10 10 10 10 10 10 10 10
10 10 10 10 10 10 10 10 10 10 10 10 10 10 10 10 10 10 10 10 10 10 10 10 10 10 10
10 10 10 10 10 10 10 10 10 10 10 10 10 10 10 10 10 10 10 10 10 10 10 10 10 10 10
10 10 10 10 10 10 10 10 10 10 10 10 10 10 10 10 10 10 10 10 10 10 10 10 10 10 10
10 10 10 10 10 10 10 10 10 10 10 10 10 10 10 10 10 10 10 10 10 10 10 10 10 10 10
10 10 10 10 10 10 10 10 10 10 10 10 10 10 10 10 10 10 10 10 10 10 10 10 10 10 10
10 10 10 10 10 10 10 10 10 10 10 10 10 10 10 10 10 10 10 10 10 10 10 10 10 10 10
10 10 10 10 10 10 10 10 10 10 10 10 10 10 10 10 10 10 10 10 10 10 10 10 10 10 10
10 10 10 10 10 10 10 10 10 10 10 10 10 10 10 10 10 10 10 10 10 10 10 10 10 10 10
10 10 10 10 10 10 10 10 10 10 10 10 10 10 10 10 10 10 10 10 10 10 10 10 10 10 10
10 10 10 10 10 10 10 10 10 10 10 10 10 10 10 10 10 10 10 10 10 10 10 10 10 10 10
10 10 10 10 10 10 10 10 10 10 10 10 10 10 10 10 10 10 10 10 10 10 10 10 10 10 10
10 10 10 10 10 10 10 10 10 10 10 10 10 10 10 10 10 10 10 10 10 10 10 10 10 10 10
10 10 10 10 10 10 10 10 10 10 10 10 10 10 10 10 10 10 10 10 10 10 10 10 10 10 10
10 10 10 10 10 10 10 10 10 10 10 10 10 10 10 10 10 10 10 10 10 10 10 10 10 10 10
```

layer 13

8 8 8 8 8 8 8 8 8 8 8 8 8 8 8 8 8 8 8 8 8 8 8 8 8 8
8 8 8 8 8 8 8 8 8 8 8 8 8 8 8 8 8 8 8 8 8 8 8 8 8 8
8 8 8 8 8 8 8 8 8 8 8 8 8 8 8 8 8 8 8 8 8 8 8 8 8 8
8 8 8 8 8 8 8 8 8 8 8 8 8 8 8 8 8 8 8 8 8 8 8 8 8 8
8 8 8 8 8 8 8 8 8 8 8 8 8 8 8 8 8 8 8 8 8 8 8 8 8 8
8 8 8 8 8 8 8 8 8 8 8 8 8 8 8 8 8 8 8 8 8 8 8 8 8 8
8 8 8 8 8 8 8 8 8 8 8 8 8 8 8 8 8 8 8 8 8 8 8 8 8 8
8 8 8 8 8 8 8 8 8 8 8 8 8 8 8 8 8 8 8 8 8 8 8 8 8 8
8 8 8 8 8 8 8 8 8 8 8 8 8 8 8 8 8 8 8 8 8 8 8 8 8 8
8 8 8 8 8 8 8 8 8 8 8 8 8 8 8 8 8 8 8 8 8 8 8 8 8 8
8 8 8 8 8 8 8 8 8 8 8 8 8 8 8 8 8 8 8 8 8 8 8 8 8 8
8 8 8 8 8 8 8 8 8 8 8 8 8 8 8 8 8 8 8 8 8 8 8 8 8 8
8 8 8 8 8 8 8 8 8 8 8 8 8 8 8 8 8 8 8 8 8 8 8 8 8 8
8 8 8 8 8 8 8 8 8 8 8 8 8 8 8 8 8 8 8 8 8 8 8 8 8 8
8 8 8 8 8 8 8 8 8 8 8 8 8 8 8 8 8 8 8 8 8 8 8 8 8 8
8 8 8 8 8 8 8 8 8 8 8 8 8 8 8 8 8 8 8 8 8 8 8 8 8 8
8 8 8 8 8 8 8 8 8 8 8 8 8 8 8 8 8 8 8 8 8 8 8 8 8 8
8 8 8 8 8 8 8 8 8 8 8 8 8 8 8 8 8 8 8 8 8 8 8 8 8 8

# Chapter 5
## Summary

"There is no doubt that the first positive success in geophysical prospecting was obtained by electrical methods."
-*Cagniard* (1953)

In this thesis, we developed several 3D magnetotelluric modeling algorithms. All of our algorithms are finite difference algorithms that are based on the integral forms of Maxwell's equations rather than the differential forms. We developed a direct solution algorithm and several approximate solution algorithms. Our direct solution algorithm is similar to propagator matrix techniques, and the results from this algorithm compare very well with those from an independent algorithm that uses integral equation techniques. The approximate solution algorithms employ conjugate direction relaxation methods. These algorithms are quick and do not require large amounts of computer memory, but they sometimes give inaccurate results. A technique that uses multiple scaling in conjunction with conjugate direction relaxation seems to give results that compare well with the direct solution results, at least for modest 3D Earth models.

We also made considerable progress in the development of a 3D magnetotelluric inversion algorithm. This problem in non-linear and although there are many schemes for obtaining the solution to a non-linear inverse problem, we prefer to use the maximum likelihood inverse. However, instead of solving the maximum likelihood equations directly at each step of the non-linear inversion, we use conjugate gradient relaxation to obtain an approximate solution. This allowed us to bypass a traditional sensitivity analysis and resulted in a considerable computational time savings. We were encouraged by the results of this scheme for simple 3D Earth models and synthetic, noise-free data.

Finally, using the forward modeling codes developed in this thesis, we interpreted magnetotelluric data collected in the California Basin and Range Province. These data are very three-dimensional and their proper interpretation required the use of 3D forward modeling algorithms. We believe that these data are contaminated by excess ocean electrical currents trapped

in the continental upper crust even though the data sites are located 200-300 km away from the ocean. We observed a very systematic leakage effect in the data northwards into the California Basin and Range and eastwards across the northern Mojave Desert. We believe the excess ocean current is channelled along the Garlock Fault zone, then up into the California Basin and Range through Searles Valley - Panamint Valley and Death Valley. Three-dimensional modeling of these data required the lower crust in the California Basin and Range to have 16 times more conductance than the lower crust further west in California and under the ocean. We interpreted this to result from the ongoing extension in the area and a small component of brittle deformation in the otherwise ductilely deforming lower crust. Issues of porosity, connectivity, deformation, and fluids in the lower crust are still in debate and are yet to be fully resolved.

## Acknowledgements

This thesis brings to a close another chapter in my life, but it is not without fond memories, experiences, and friends. The last six years I have spent here at M.I.T. have enriched me not only intellectually, but personally and emotionally as well. I made many good friends, enjoyed many good times, and was exposed to many new and challenging ideas. My only regret is that the time seems to have gone by so quickly.

Much of the work in this thesis would not have been possible without the guidance of my advisor, Ted Madden. Not only has he been constant source of ideas, but he has also become a very good friend. Whether it was drinking sherry before dinner, camping in Maine, or talking politics, it was always enjoyable spending time with him. I have also benefitted from the many interactions and discussions with the other graduate students in the department, especially the meteorology students and my officemates, and I have enjoyed their friendships. I know that their feelings will not be hurt if I do not explicitly name all of them here.

Phil Wannamaker generously supplied me with the modeling results from his integral equation algorithm. Steve Park stored a lot of our field equipment and helped in the logistics of the field operations. I had several field assistants who helped collect the data, and their assistance is gratefully appreciated.

I would like to thank my parents for supporting me in everything I have chosen to do. Their love and support has always meant a great deal to me.

And finally, to Imtiyaz Hussein - words cannot describe my feelings for you. You have loved me and supported me through the good times and bad, and I'm truly lucky that you are such an important person in my life.

Much of this work was financially supported by an industrial consortium of oil companies: Amoco, Chevron, Standard Oil Production Co., Sun, and Texaco. Some of the work was also supported under an NSF grant, #8817149-EAR. The Department of Earth, Atmospheric, and Planetary Sciences also provided several semesters of TA funds when our other funds were

running low. A lot of the computational work in this thesis was performed on the M.I.T. Supercomputer Facility CRAY-2. The use of the NCUBE computer at the Earth Resources Lab was a tremendous help in modeling the California magnetotelluric data..